
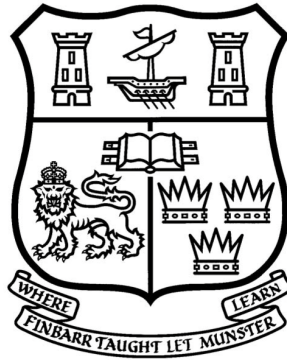


<b>Title</b>	Open-source virtual bronchoscopy for image guided navigation
<b>Author(s)</b>	Nardelli, Pietro
<b>Publication date</b>	2016
<b>Original citation</b>	Nardelli, P. 2016. Open-source virtual bronchoscopy for image guided navigation. PhD Thesis, University College Cork.
<b>Type of publication</b>	Doctoral thesis
<b>Rights</b>	<p>© 2016, Pietro Nardelli.</p> <p><a href="http://creativecommons.org/licenses/by-nc-nd/3.0/">http://creativecommons.org/licenses/by-nc-nd/3.0/</a></p> 
<b>Embargo information</b>	No embargo required
<b>Item downloaded from</b>	<a href="http://hdl.handle.net/10468/2596">http://hdl.handle.net/10468/2596</a>

Downloaded on 2017-02-12T10:15:24Z



# Open-source Virtual Bronchoscopy for Image Guided Navigation

Pietro Nardelli, M.Eng.Sc.

A thesis presented to the National University of Ireland for  
the degree of Doctor of Philosophy

February, 2016

Supervised by Dr. Pádraig Cantillon-Murphy  
School of Engineering  
University College Cork  
Ireland





# Declaration

I hereby declare that I am the sole author of this thesis and all of the work undertaken in this thesis is original in content and was carried out by the author. Work carried out by others has been duly acknowledged in the thesis. This is a true copy of the thesis, including any required final revisions, as accepted by my examiners. The work presented has not been accepted in any previous application for a degree.

Signed: \_\_\_\_\_

Date: \_\_\_\_\_

# Abstract

This thesis describes the development of an open-source system for virtual bronchoscopy used in combination with electromagnetic instrument tracking. The end application is virtual navigation of the lung for biopsy of early stage cancer nodules. The open-source platform 3D Slicer was used for creating freely available algorithms for virtual bronchoscopy.

Firstly, the development of an open-source semi-automatic algorithm for prediction of solitary pulmonary nodule malignancy is presented. This approach may help the physician decide whether to proceed with biopsy of the nodule. The user-selected nodule is segmented in order to extract radiological characteristics (i.e., size, location, edge smoothness, calcification presence, cavity wall thickness) which are combined with patient information to calculate likelihood of malignancy. The overall accuracy of the algorithm is shown to be high compared to independent experts' assessment of malignancy. The algorithm is also compared with two different predictors, and our approach is shown to provide the best overall prediction accuracy.

The development of an airway segmentation algorithm which extracts the airway tree from surrounding structures on chest Computed Tomography (CT) images is then described. This represents the first fundamental step toward the creation of a virtual bronchoscopy system. Clinical and *ex-vivo* images are used to evaluate performance of the algorithm. Different CT scan parameters are investigated and parameters for successful airway segmentation are optimized. Slice thickness is the most affecting parameter, while variation of reconstruction kernel and radiation dose is shown to be less critical. Airway segmentation is used to create a 3D rendered model of the airway tree for virtual navigation.

Finally, the first open-source virtual bronchoscopy system was combined with electromagnetic tracking of the bronchoscope for the development of a GPS-like system for navigating within the lungs. Tools for

pre-procedural planning and for helping with navigation are provided. Registration between the lungs of the patient and the virtually reconstructed airway tree is achieved using a landmark-based approach. In an attempt to reduce difficulties with registration errors, we also implemented a landmark-free registration method based on a balanced airway survey. *In-vitro* and *in-vivo* testing showed good accuracy for this registration approach.

The centreline of the 3D airway model is extracted and used to compensate for possible registration errors. Tools are provided to select a target for biopsy on the patient CT image, and pathways from the trachea towards the selected targets are automatically created. The pathways guide the physician during navigation, while distance to target information is updated in real-time and presented to the user. During navigation, video from the bronchoscope is streamed and presented to the physician next to the 3D rendered image. The electromagnetic tracking is implemented with 5 DOF sensing that does not provide roll rotation information. An intensity-based image registration approach is implemented to rotate the virtual image according to the bronchoscope's rotations. The virtual bronchoscopy system is shown to be easy to use and accurate in replicating the clinical setting, as demonstrated in the pre-clinical environment of a breathing lung method. Animal studies were performed to evaluate the overall system performance.

# Acknowledgements

In presenting this work, I would like to acknowledge all the people who helped and contributed to my work over the course of my PhD. This thesis would not have been possible without their support and guidance. Firstly, I am sincerely grateful to my academic supervisor, Dr. Pádraig Cantillon-Murphy, for welcoming me warmly when I started working at UCC, and whose generous support, guidance, enthusiasm, and invaluable patience helped me hugely during the thesis. It has been a honour to work with him, and I wish to continue our collaboration in the future. I also wish to thank Professor Liam Mar-nane and Dr. Peter Culmer for examining my thesis as well as Dr. Marcus Kennedy and Dr. Kashif Ali Khan from the Department of Pulmonology in Cork University Hospital for all their contributions. Special thanks go to Professor Raúl San Jose Estépar, who gave me the opportunity to live an amazing experience at the Surgical and Planning Laboratory, in Boston.

I would also like to thank my fellow students at the Bioelectromag-netics Group, Kilian, Conor, and Alex. Cheers for all your support and the great, funny, and sometimes stressful moments we shared together.

A huge thank goes to my friends, Cri, Eli, and Harsh. Thank you for loving me so much and for all the laughs we had together. You have been my family in Ireland, and I will miss you tremendously in Boston. I extend a big thank you to Pablo, Ale, Gagge and all the guys I shared my Irish experience with. I will never forget our moments together.

I am truly thankful to my mum and dad for their unconditional sup-port and patience, their incredible love and for always encouraging me to try new experiences and adventures. A great thank you goes to Giulia, Paolo, Niels, and Luigi for always giving me strength and love. I would not have been able to complete this thesis without the support and love of my family.

Finally, the biggest thank you goes to the girl who changed my life with her incredible smile and happiness. Raquel, I thank you for being the person you are and for giving me the opportunity to live a dream with you. Thanks for all our interesting discussions and for always encouraging and sustaining me. I am sorry for the long hours of work, especially in the last period, that I did not dedicate to you, but you never complained, you always understood me, and I know that at the end you will say to me: Bravo Piccolino!

# List of Publications

1. P. Nardelli, R. S. J. Estépar and P. Cantillon-Murphy, “Semi-automated Airway Segmentation for Lung CT Datasets”, Computer Assisted Radiology and Surgery (CARS), Heidelberg, 2013.
2. K. O’Donoghue, A. Corvó, P. Nardelli, C. O’Shea, K. A. Khan, M. Kennedy and P. Cantillon-Murphy, “Evaluation of a Novel Tracking System in a Breathing Lung Model”, 36th Annual International Conference of the IEEE Engineering in Medicine and Biology Society, 2014.
3. P. Nardelli, K. A. Khan, A. Corvó, N. Moore, M. J. Murphy, M. Twomey, O. J. O’Connor, M. P. Kennedy, R. S. J. Estépar, M. M. Maher, P. Cantillon-Murphy, “Optimizing parameters of an opensource airway segmentation algorithm using different CT images”, Biomedical Engineering Online, 14(1), 62, 2015.
4. P. Nardelli, M. P. Kennedy and P. Cantillon-Murphy, “Airway Segmentation Algorithm Starting From Chest CT Images”, Irish Thoracic Society ASM, Cork, 2015.
5. P. Nardelli, H. A Jaeger, C. O’Shea, K. A. Khan, M. P. Kennedy and P. Cantillon-Murphy, “Open-source Virtual Bronchoscopy in Pre-clinical Validation Using 3D Slicer”, International Journal of Computer Assisted Radiology and Surgery, [Under Review], 2016.
6. P. Nardelli, H. A Jaeger, C. O’Shea, K. A. Khan, M. P. Kennedy and P. Cantillon-Murphy, “Open-source Virtual Bronchoscopy in Pre-clinical Validation”, World Congress for Bronchology and Interventional Pulmonology, Florence, 2016.
7. P. Nardelli, R. Volpi, A. Jaeger, C. O’Shea, K.A. Khan, M. P. Kennedy, P. Cantillon-Murphy, “Open-source Image-guided system for Virtual Bronchoscopy”, Medical Image Computing and Computer Assisted Intervention (MICCAI), [Under review], 2016.

8. H. A. Jaeger, P. Nardelli, C. O'Shea, J. Tugwell, K. A. Khan, T. Power, M. O'Shea, M. P. Kennedy and P. Cantillon-Murphy, "Automated Catheter Navigation with Electromagnetic Image Guidance", IEEE Transaction on Biomedical Engineering, [Under review], 2016.
9. K. A. Khan, P. Nardelli, H. A. Jeager, C. O'Shea, P. Cantillon-Murphy, M. P. Kennedy, "Navigational Bronchoscopy for Early Lung Cancer- A Road to Therapy", Advances in Therapy (ADTH), 1-17, 2016.



# Table of Contents

<b>Declaration</b>	<b>iv</b>
<b>Abstract</b>	<b>vi</b>
<b>Acknowledgements</b>	<b>viii</b>
<b>List of Publications</b>	<b>x</b>
<b>List of Figures</b>	<b>xvi</b>
<b>List of Tables</b>	<b>xxiv</b>
<b>List of Abbreviations</b>	<b>xxix</b>
<b>1 Introduction</b>	<b>1</b>
1.1 Overview . . . . .	1
1.2 Thesis Objectives . . . . .	4
1.3 Thesis Structure . . . . .	6
1.4 Key Contributions . . . . .	7
<b>2 Background</b>	<b>9</b>
2.1 Overview . . . . .	9
2.2 Human Lung and Airways Tree . . . . .	9
2.3 Lung Cancer and Diseases . . . . .	11
2.4 X-ray Computed Tomography (CT) . . . . .	12
2.4.1 Historical Background . . . . .	13
2.4.2 Operating Principles . . . . .	14

2.4.2.1	X-ray Source and Detector . . . . .	16
2.4.2.2	Absorption and Hounsfield Unit . . . . .	18
2.4.2.3	Parameters . . . . .	19
2.5	3D Slicer . . . . .	20
2.6	Electromagnetic Navigation Systems . . . . .	22
2.6.1	Superdimension iLogic System . . . . .	23
2.6.2	Veran SPINDrive . . . . .	23
2.6.3	Electromagnetic Navigation at University College Cork . .	24
<b>3</b>	<b>Solitary Pulmonary Nodules Malignancy</b>	<b>28</b>
3.1	Overview . . . . .	28
3.2	Introduction . . . . .	29
3.2.1	Nodule Classification . . . . .	30
3.2.2	Computer-aided Detection . . . . .	30
3.3	Solitary Pulmonary Nodule . . . . .	31
3.4	Literature Review . . . . .	33
3.4.1	CAD Methods . . . . .	34
3.4.2	Systems for Probability of Malignancy . . . . .	36
3.5	Algorithm Implementation . . . . .	37
3.5.1	Overview . . . . .	37
3.5.2	Lung Segmentation . . . . .	38
3.5.2.1	Related Work . . . . .	39
3.5.2.2	Algorithm Description . . . . .	41
3.5.3	Nodule Segmentation . . . . .	46
3.5.3.1	Related Work . . . . .	47
3.5.3.2	Algorithm Description . . . . .	50
3.5.4	Lung Fissures Segmentation . . . . .	57
3.5.4.1	Previous Work . . . . .	57
3.5.4.2	Algorithm Description . . . . .	59
3.5.5	Lung Lobes Segmentation . . . . .	63
3.5.5.1	Lobe Segmentation Algorithm . . . . .	64
3.5.5.2	Fissure Points Extraction . . . . .	64
3.5.6	Nodule Diagnosis . . . . .	65

3.6	Algorithm Performance . . . . .	68
3.6.1	Overview . . . . .	68
3.6.2	CT Datasets . . . . .	68
3.6.3	Algorithm Testing Approach . . . . .	70
3.6.4	Results . . . . .	72
3.6.5	Discussion . . . . .	74
3.7	Summary . . . . .	77
<b>4</b>	<b>Airway Segmentation</b>	<b>78</b>
4.1	Overview . . . . .	78
4.2	Medical Image Segmentation . . . . .	79
4.2.1	Thresholding . . . . .	80
4.2.2	Edge Based Segmentation . . . . .	81
4.2.3	Region Growing Segmentation . . . . .	81
4.2.4	Level Set Segmentation . . . . .	82
4.2.5	Atlas Based Segmentation . . . . .	83
4.3	Airway Segmentation Methods: Background . . . . .	84
4.3.1	Overview . . . . .	84
4.3.2	Principal Limitations of Airway Segmentation . . . . .	84
4.4	Background . . . . .	87
4.5	Airway Segmentation: Implementation . . . . .	89
4.5.1	Introduction . . . . .	89
4.5.2	Overview of Algorithm Versions . . . . .	90
4.5.3	Algorithm Implementation . . . . .	93
4.5.3.1	Overview . . . . .	93
4.5.3.2	Volume cropping . . . . .	94
4.5.3.3	Trachea Segmentation . . . . .	96
4.5.3.4	Right and Left Airways Segmentation . . . . .	98
4.5.3.5	Binary Image Closing . . . . .	102
4.5.3.6	Binary Voting Fill Hole Filter . . . . .	104
4.5.4	Algorithm Performance . . . . .	104
4.5.4.1	Overview . . . . .	104
4.5.4.2	CT Datasets . . . . .	104

4.5.4.3	Evaluation Methods . . . . .	108
4.5.4.4	Leakage Evaluation Method . . . . .	110
4.5.5	Results . . . . .	110
4.5.5.1	Results on Clinical Cases . . . . .	111
4.5.5.2	Results on Breathing Pig Lung Model . . . . .	118
4.5.5.3	Correlation Between Segmentation Metrics and CT Acquisition Parameters . . . . .	122
4.5.6	Discussion and Future Work . . . . .	124
4.6	Summary . . . . .	125
<b>5</b>	<b>Virtual Bronchoscopy</b>	<b>126</b>
5.1	Overview . . . . .	126
5.2	Introduction . . . . .	127
5.3	Literature Review . . . . .	128
5.4	Algorithm Implementation . . . . .	131
5.4.1	Overview . . . . .	131
5.4.2	Centreline Extraction . . . . .	134
5.4.2.1	Overview . . . . .	134
5.4.2.2	Centerline Extraction Method . . . . .	135
5.4.3	Procedure Planning . . . . .	139
5.4.3.1	Overview . . . . .	139
5.4.3.2	Route Extraction Implementation . . . . .	139
5.4.4	Registration . . . . .	140
5.4.4.1	Overview . . . . .	140
5.4.4.2	Landmark-free Registration . . . . .	142
5.4.5	Image-Guided Bronchoscopy . . . . .	156
5.4.5.1	Overview . . . . .	156
5.4.5.2	MATLAB-Slicer Bridge Connection . . . . .	156
5.4.5.3	Centreline Compensation . . . . .	158
5.4.5.4	Roll Rotation Compensation . . . . .	160
5.4.5.5	Video Streaming . . . . .	165
5.5	Summary . . . . .	165

<b>6</b>	<b>Pre-clinical Testing and Results</b>	<b>167</b>
6.1	Overview . . . . .	167
6.2	Breathing Lung Model Evaluation . . . . .	168
6.2.1	Bronchoscope . . . . .	168
6.2.2	EM Tracker . . . . .	168
6.2.3	Airways 3D Model . . . . .	169
6.2.4	Breathing Lung Model . . . . .	172
6.2.5	Virtual Bronchoscopy: Pre-Processing . . . . .	172
6.2.6	Virtual Bronchoscopy: Image-Guided Navigation . . . . .	172
6.2.7	System Usability Scale Questionnaire . . . . .	174
6.2.8	Results . . . . .	176
6.3	Tests in Live Animal Setting . . . . .	177
6.3.1	Protocol and Methods . . . . .	179
6.3.1.1	Endoscopic Placement of Tumour Models . . . . .	180
6.3.1.2	Airways Segmentation . . . . .	181
6.3.1.3	Pre-Procedure . . . . .	182
6.3.1.4	Registration . . . . .	183
6.3.1.5	Image-Guided Navigation to Targets . . . . .	184
6.3.1.6	Automated Navigation . . . . .	185
6.3.2	Results: First Study . . . . .	188
6.3.3	Results: Second Study . . . . .	189
6.3.4	Conclusions . . . . .	189
<b>7</b>	<b>Summary and Future Work</b>	<b>192</b>
7.1	Summary of Thesis Contributions . . . . .	192
7.2	Proposals for Future Work . . . . .	194
7.2.1	CT Images Noise Removal . . . . .	194
7.2.2	Airway Segmentation Improvement . . . . .	194
7.2.3	Registration Improvement . . . . .	195
7.2.4	5 DOF Sensor Compensation . . . . .	195
7.2.5	Real-time Pathway Updating . . . . .	196
7.2.6	Nodule Computer-aided Detection System . . . . .	196



# List of Figures

1.1	Example of a standard bronchoscope. . . . .	2
1.2	A typical chest fluoroscopy 2D image. Overlap of different structures appears evident. . . . .	3
2.1	The human respiratory system [31]. . . . .	10
2.2	This figure shows an axial CT image of a patient presenting a malignant nodule (red arrow). . . . .	12
2.3	A reconstructed CT image as shown to physicians. Axial (red), sagittal (yellow), and coronal (green) views of the same patient are shown. . . . .	13
2.4	A representation of a CT scanner with x-ray source and detectors shown in three different positions [45]. . . . .	15
2.5	Block-diagram of the main steps for the creation of a CT image. Parameters that can be modified at every step are specified. FOV stands for field of view, FBP for filtered back-projection, while IR is used for iterative reconstruction. . . . .	16
2.6	The SuperDimension transmitter board [65]. . . . .	23
2.7	(a) EM transmitter and (b) working station of the Veran SPIN-Drive system [67]. . . . .	24
2.8	The tracking system as developed at University College Cork. . .	25
2.9	The breathing pig lung model as used in our research. . . . .	26
3.1	Example of nodule shown on a axial CT image. The nodule is indicated by the yellow arrow. . . . .	29
3.2	Scheme of benign calcification patterns. . . . .	33

3.3	Modularity scheme of nodule diagnosis extension. The different tools are executed individually. . . . .	38
3.4	Block diagram of the different steps involved in lung segmentation.	41
3.5	Typical histogram of a chest CT image (size $512 \times 512 \times 480$ ). . .	42
3.6	An example of thin lung separation in the anterior and posterior junctions. a) Shows the anterior (blue square) and posterior (orange square) junctions on a axial CT image. In b) the result after lung segmentation (green) of the same image is presented. As shown, when the junctions are thin, segmentation might consider the two lungs as one. . . . .	45
3.7	Example of lung label map as roughly divided into thirds. . . . .	46
3.8	Steps involved in nodule segmentation. RG stands for region growing, where ROI is the region of interest. . . . .	50
3.9	Example of region of interest extraction and enhancement. a) The nodule is selected by the user on the CT image (red point). b) A region of $4 \times 4 \times 4$ cm including the whole nodule is extracted. c) The extracted region is enhanced using a blob-like multiscale enhancement. . . . .	52
3.10	Example of nodule segmentation results. On the three CT views, the nodule label is represented in light blue and is imposed on the nodule. As shown, the cavity of the nodule is preserved (axial view). The CT image is the same as in Figure 3.9 . . . . .	56
3.11	Steps involved in fissure segmentation. . . . .	60
3.12	Representation of the eigenvalues of plate-like structures [147]. . .	61
3.13	An example of fissure enhancement as it appears on a sagittal CT slice. The right fissures are clearly visible on the enhanced image (right). However, other structures are also still present in the enhanced image. The thorax is excluded using the lung label map previously segmented as a mask prior to the enhancement. .	62
3.14	Example of a fissure segmentation result. The fissures label is imposed on the three views of the CT image in a light blue colour.	63



3.15	Example of a lobe segmentation result. The three different lobes are assigned a different label. Blue, red, and green represent the right upper, middle, and lower lobes, respectively. Light blue and yellow are the colour used for the labels of the left upper and lower lobes, respectively. . . . .	65
3.16	ROC curves comparing the different results from the four radiologists and the described algorithm from the LIDC.B dataset. . . .	73
3.17	ROC curves comparing results from the algorithm compared to Swensen's and McWilliams' methods for the CUH dataset. . . . .	75
4.1	Region growing segmentation scheme. (a) A seed pixel (red) is selected and the algorithm starts checking neighbouring pixels (blue arrows). (b) The pixels around the grown region (red) are assessed.	82
4.2	Example of airways (red arrows) and vessels (yellow arrow) on a axial chest CT image. . . . .	85
4.3	Example of leakage on a axial chest CT image. The segmentation (pink) "explodes" including pixels of the lung tissue surrounding the airways. . . . .	85
4.4	Airway segmentation algorithm interface of (a) version 1.0 and (b) version 1.2. In (a) seeds, input and label volumes had to be created and selected. With the new version (b) Only input volume and seed point have to be selected. In both cases the label value can be manually changed (default = 2). . . . .	91
4.5	Coronal CT image showing a pig lung. The additive bronchus coming out of the trachea above the carina is indicated in the red circle. . . . .	93
4.6	Scheme of the steps involved in airway segmentation. . . . .	94
4.7	Example of volume cropping in version 1.0 of the algorithm. The seeds point are represented by the circles, while the trachea volume as it would be cropped by the approach is showed on the blue rectangle. In this case, due to the seeds' position the entire trachea is included in the cropped volume, but a slightly different position of the purple seed might exclude some part. . . . .	95

4.8	Representation of length, width and height in a 3D volume as utilised in this approach. . . . .	95
4.9	CT axial slice showing (a) the carina slice as found by the presented approach and (b) seed points representation (red circles) of seed points as automatically identified and placed on the main bronchi. . . . .	96
4.10	Block diagram of the implementation of trachea segmentation. T stands for threshold, CL and PCL for coronal length and previous coronal length, while AW and PAW are used for axial width and previous axial width. Finally, V stands for volume. . . . .	97
4.11	Example of “masking” as it appears on a sagittal slice. Half trachea label is used to turn values where the half trachea overlays to 0 HU (yellow voxels). In the picture, the left part of the trachea is masked, to allow segmentation of the right lung. A closing process is also used to make sure that no spreading within the left lung is obtained. . . . .	99
4.12	Example of small holes on the airways label due to noise. The label (pink) is showed overlaid on an axial CT image zoomed on the area of interest. . . . .	102
4.13	Morphological closing scheme. (a) A region with small holes (white parts inside the red region). (b) After the closing operation the red region has grown and the holes become smaller. . . . .	103
4.14	Breathing pig lung model. (a) Scheme representing the breathing pig lung model. (b) Plasticised pig lung when fully inflated [30]. . . . .	107
4.15	Leakage scoring scheme as presented to clinical experts. A score of 5 is given to an image with significant leakage present, while 1 represents an image with no leakage. . . . .	111

4.16	Representative 3D constructions of results obtained from (a-d) CUH cases (acquired with 1.25 mm slice thickness), from (e,f) EX-ACT'09 cases 24 and 25 (1.0 mm slice thickness), and from (g-l) six pig lung breathing model cases acquired using 0.625 mm slice thickness, during inspiration. (g-i) were reconstructed using a lung convolution kernel, varying dose from high to low, respectively. (j-l) were reconstructed with a standard convolution kernel, varying dose from high to low, respectively. . . . .	112
4.17	Results for the EXACT'09 challenge. In airway segmentation, having a good trade-off between tree length and leakage volume is essential. . . . .	113
4.18	Results for the breathing pig lung model during inspiration (blue) and expiration (red), when varying (a-d) slice thickness (computing the average values among dose and kernel) and (e-h) radiation dose (computing the average values among slice thickness and kernel). .	120
4.19	Correlation between image quality and metrics for the breathing pig lung model during (a) inspiration and (b) expiration phases. .	122
5.1	Block diagram of system hardware. . . . .	132
5.2	Block-diagram of the steps involved in centreline extraction. For each step the resulting image is shown. . . . .	136
5.3	Example of centreline extraction from a pig lung 3D model. a) Shows the extracted centreline alone, whereas in b) the centreline is imposed on the lung model. . . . .	138
5.4	Example of routes as created from an pig airway model. The different routes are shown in blue. The red dots represent 5 different targets selected by the user. . . . .	141
5.5	Scheme representing yaw, pitch, and roll rotations. . . . .	144
5.6	The model used for the first test. In a) the portion of centreline used to run the registration is shown. In b) the centreline (black) and the point cloud (red) generated by adding random values are presented. The origin of the reference system is represented by the carina centreline. . . . .	147

5.7	Portion of centreline extracted for the registration algorithm. Different labels are automatically associated with trachea, left main bronchus and right main bronchus, shown in red, green and blue, respectively. . . . .	148
5.8	Generation of simulated probe data. In (a) the centreline (black) and the generated point cloud after a rotation of yaw = roll = pitch = $\pi$ is applied. (b) Shows the centreline (black) and the point cloud generated after an arbitrary translation is applied. The origin of the reference system is the original carina centreline. . . . .	148
5.9	The perspex model used for the second test. The blue line highlights the path followed to simulate a balanced survey. . . . .	150
5.10	Two different views of initial conditions for registration testing with the plastic phantom model. Centreline points are shown in black, while probe data points are shown in red. . . . .	150
5.11	Initial condition for registration testing with data acquired using a balanced surveillance bronchoscopy. The airway 3D model is shown in black, whereas centreline points are shown in green and experimentally recorded probe points are shown in red. . . . .	151
5.12	Correlation between Euclidean distance at the beginning of registration and the registration accuracy, achieved in 100 different trials. . . . .	153
5.13	Example of registration trial between the centreline (black) and a point cloud (red) generated without adding the initial random value. (a) Shows the initial condition: the Euclidean distance between the two carinae is 8.6 mm. (b) Shows the registration achieved. The process took 9.88 seconds, with an error of $5.40 \times 10^{-4}$ mm. . . . .	154
5.14	Two different views of result achieved using the perspex model. Centreline points are shown in black, while probe points are shown in red. . . . .	155
5.15	Registration results achieved on the breathing pig lung model. Two views from two different perspective are shown. . . . .	156
5.16	The OpenIGTLink extension interface as it appears in 3D Slicer. .	157

5.17	If registration is not adequately executed, the probe model position (indicated by the purple marker) will be completely outside the airways model. . . . .	159
5.18	Representation of the centreline compensated navigation. Two views of the same frame from two different perspective are shown. The blue stick indicates the actual position as received from the tracking system. The purple stick represents the corrected position of the probe. . . . .	160
5.19	Example of roll misalignment between the real and virtual video frames. On the left side the actual view from the bronchoscope is presented, while the picture on the right side shows the virtual image. The green line indicates the path to reach the selected target.	161
5.20	Block diagram of the roll rotation compensation steps. Extraction of branching points is computed prior to the procedure, while registration steps are executed at every bifurcation during navigation.	162
5.21	Scheme of the multiresolution pyramid method [248]. . . . .	163
5.22	After the image registration process, the virtual image is rotated to match the real image. . . . .	165
6.1	Diagram of the system in the operating setup. In the figure, the automated navigation system described in Section 6.3.1.6 is also shown. This was not used for testing with the breathing pig lung model. . . . .	169
6.2	GE Discovery CT750 CT scanner with the inflated pig lung model.	170
6.3	The inflatable lung model setup for the CT scan when (a) inflated and (b) deflated. Below each lung there is a laminated scaled image of the deflated lungs used for lining up the model in a repeatable manner. . . . .	171
6.4	3D model of the inflated pig lung model (0.625 slice thickness, 60 mA radiation dose, LUNG convolution kernel). . . . .	171

6.5	Position of the three targets inside the airways. Two different views are shown. The first, second, and third targets are indicated in red, blue, and green, respectively. First and third targets were placed in the right lung. The second target was in the left lung. .	173
6.6	The pig during one of the scanning processes. . . . .	180
6.7	Tripe tumour models visible in lower right and left lobes. A coronal CT slice, a C-arm X-ray image taken in real time while placing the models, and images of the tripe models prior to insertion and positioned <i>in-vivo</i> are shown. The 3D airway model is also visible overlaid to the CT scout image [254]. . . . .	181
6.8	The 3D rendered airway model as obtained during (a) the first and (b) the second study. . . . .	182
6.9	A 2D view of the airway model showing the position of the placed tumour markers for the (a) first and (b) second study. The different colours are used here to distinguish the targets. . . . .	184
6.10	The VB system as used by the physician during the first animal study. . . . .	185
6.11	The semi-automated joystick-based navigation system as used by the physician in combination with VB. . . . .	186
6.12	Example of forceps as utilised to biopsy the different targets. . . .	186
6.13	The physician used the joystick to navigate inside the lung. . . .	187
6.14	The catheter is connected to a motorised system where four force sensing loadcells apply a different tension on the four wires connected to the catheter's tip based on the position of the joystick. .	187

# List of Tables

2.1	This table shows the typical Hounsfield values of some body tissues and substances. . . . .	19
2.2	This table shows the typical parameters of a CT scan. . . . .	19
3.1	List of the single algorithms composing the method to determine probability of malignancy. . . . .	38
3.2	Possible structures enhancement based on the Hessian eigenvalues $\lambda_0$ . Neg/Pos indicates if the eigenvalue has a negative or positive value. . . . .	54
3.3	Likelihood ratios for malignancy in SPNs as found in [38]. . . . .	67
3.4	Average times to compute the different steps for prediction of likelihood of malignancy for 175 cases. . . . .	72
3.5	Comparison of prediction performance of radiologists and algorithm from the LIDC.B dataset. . . . .	73
3.6	Individual ROC outcomes for the first ROC curve analysis (LIDC.A). T stands for threshold, SN for sensitivity (true positive rate), and SP for specificity (1 - false positive rate). . . . .	74
3.7	Comparison of the performance of the algorithm, compared to Swensen's [90] and McWilliams' [110] methods using the CUH dataset. . . . .	75
3.8	Individual ROC outcomes for the second ROC curve analysis (LIDC.B). T stands for threshold, SN for sensitivity, and SP for specificity. . . . .	75
4.1	Airway segmentation algorithm versions. . . . .	93

4.2	Percentage of trachea voxels used for different reconstruction kernels and slice thicknesses. $S$ is used to take into account the different slice thicknesses. (a) Kernels: GE Medical System Standard, Siemens B20f and B30f, Philips B and C, Toshiba FC10 and FC12; (b) Kernels: GE Medical System Lung, Siemens B50f, Toshiba FC50 and FC52; (c) Kernels: Siemens B60f, B70f and B70s, and Philips D; (d) Any other kernel. . . . .	101
4.3	Acquisition parameters of the scans provided by CUH. I/E indicates full-inspiration (I) or full-expiration (E) breath-hold. . . . .	106
4.4	Acquisition parameters of the twenty cases from the EXACT'09 dataset. I/E indicates full-inspiration (I) or full-expiration (E) breath-hold. Asterisk * indicates that a scan was acquired from the same subject as the previous one. . . . .	106
4.5	Optimal thresholds (in HU) identified by the algorithm for airway segmentation of human cases. Thresholds are chosen independently for trachea, right and left lungs. Asterisk * indicates that a scan was acquired from the same subject as the previous one.	114
4.6	Results obtained from the twenty test cases of the EXACT'09 project.	115
4.7	Mean results of the teams taking part in the EXACT'09 challenge. The last row reports mean results obtained with the described approach. . . . .	116
4.8	Results obtained for human cases. (a) Cases provided by CUH. (b) Cases selected from the EXACT'09 cases. Asterisk * indicates that a scan was acquired from the same subject as the previous ones.	117
4.9	Results obtained on the breathing pig lung model for kernel variation in inspiration and expiration. . . . .	119
4.10	Parameters and results for pig lung breathing model during half-inflation. . . . .	119
5.1	Summary of algorithms involved in the VB procedure. (a) Pre-procedure operations. (b) Operations for image-guided navigation.	133



5.2	Registration trials between the centreline extracted from the pig (299 points) and the point clouds generated with the method proposed without adding the random values. . . . .	152
5.3	Registration trials between the centreline extracted from the pig (299 points) and the simulated point clouds. $\text{RMSD}_f$ is the RMSD computed after registration, while $\text{RMSD}_i$ represents the initial RMSD. . . . .	152
5.4	Ten different registration problems. Initial condition, registration error and time of convergence are reported. . . . .	154
6.1	Details of volunteers participating to the VB system test. SHO stands for senior house officer, while Reg indicates registrar physician (junior clinical fellow). . . . .	173
6.2	Time (in seconds) required to each participant to reach the three targets. . . . .	176
6.3	Results of overall satisfaction of participants. For all questions a score 1-5 was requested. For question 1 (Q1), 1 represented poor and 5 excellent. For Q2, 1 was not at all, whereas 5 stood for excellent. For Q3 and Q4 scores ranged from not at all (1) to extremely valuable. The test aimed at evaluating the entire system, composed of both the EM tracking and VB. In this sense, physical setup deficiencies cannot be addressed separately to VB. . . . .	178
6.4	System usability for all participants. Each question was given a score from 1 to 5, with 1 indicating strongly disagree, and 5 strongly agree. Final usability score for each volunteer was given by multiply by 2.5 the sum of individual scores. Scores higher than 68 indicate usability above average. . . . .	179
6.5	Distance (in mm) of the targets from the bronchus sus and location in the pig lungs for the (a) first and (b) second study. . . . .	183
6.6	Time (in seconds) required to reach every target using VB. . . . .	188
6.7	Time (in seconds) required to reach every target using robotic steering and VB. Targets 3 and 6 were not reached. . . . .	190

# List of Abbreviations

<b>3D</b>	Three Dimensional
<b>AUF</b>	Average Outward Flux
<b>BSD</b>	Berkeley Software Distribution
<b>CAD</b>	Computer Aided Detection
<b>CIP</b>	Chest Imaging Platform
<b>CLI</b>	Common Language Interface
<b>COPD</b>	Chronic Obstructive Pulmonary Disease
<b>CT</b>	Computed Tomography
<b>CUH</b>	Cork University Hospital
<b>DICOM</b>	Digital Imaging and Communication in Medicine
<b>DOF</b>	Degree of Freedom
<b>EM</b>	Electromagnetic
<b>ENB</b>	Electromagnetic Navigation Bronchoscopy
<b>FLTK</b>	Fast Light Toolkit
<b>HRCT</b>	High Resolution Computed Tomography
<b>ITS</b>	Irish Thoracic Society
<b>IVM</b>	In Volume Maximization
<b>GUI</b>	Graphical User Interface
<b>HU</b>	Hounsfield Unit
<b>ICP</b>	Iterative Closest Point
<b>ITK</b>	Insight Toolkit
<b>MRI</b>	Magnetic Resonance Imaging
<b>NBIA</b>	National Biomedical Imaging Archive
<b>NCI</b>	National Cancer Institute
<b>NEMA</b>	National Electrical Manufacturers Association
<b>NMI</b>	Normalized Mutual Information
<b>NN</b>	Neural Network
<b>PACS</b>	Picture Archiving and Communication System
<b>PC</b>	Personal Computer
<b>PCB</b>	Printed Circuit Board
<b>PDE</b>	Partial Differential Equation

<b>PLUS</b>	Public Software Library for Ultrasound Imaging
<b>RMSD</b>	Root Mean Squared Distance
<b>SFS</b>	Shape From Shading
<b>SPL</b>	Surgical Planning Laboratory
<b>SPN</b>	Solitary Pulmonary Nodule
<b>SVD</b>	Single Value Decomposition
<b>SVM</b>	Support Vector Machine
<b>TPS</b>	Thin Plate Spin
<b>UCC</b>	University College Cork
<b>USB</b>	Universal Serial Bus
<b>VB</b>	Virtual Bronchoscopy
<b>VOI</b>	Volume Of Interest
<b>VMTK</b>	Vascular Model Toolkit
<b>VTK</b>	Visualization Toolkit
<b>WHO</b>	World Health Organization



# Chapter 1

## Introduction

### 1.1 Overview

This chapter provides an introduction to the research work presented in this thesis. It explains the motivation for this work and the relevant background information. It presents the objectives of the thesis as well as the thesis structure.

#### **Introduction to Bronchoscopy**

Endoscopy is the descriptive term for a minimally invasive medical procedure used to directly look inside hollow organs or cavities of the body using an endoscope, that is a flexible and relatively thin catheter with a small camera and a light at the tip. The images captured by the camera are transmitted in real-time to a screen that allows examination of areas of interest [1]. The term bronchoscopy refers to a particular endoscopic technique used to visualize the inside of the airways and the lungs for diagnostic and therapeutic purposes. In this case, the instrument used is called a bronchoscope (Figure 1.1); this is similar in function to an endoscope, having a smaller outer diameter (ranging 4-8 mm). A bronchoscopy procedure is performed with the patient sitting or in supine position, and inserting the tube through the mouth or nose to the trachea and from this into the bronchial area. When the bronchoscope is at the desired point, medical instruments can be inserted through a small channel (usually 2-4 mm in diameter) of the bronchoscope and biopsies or foreign objects can be extracted or removed. Biopsy is currently the gold standard for diagnosis of lung cancer.

## 1. INTRODUCTION

---



**Figure 1.1:** Example of a standard bronchoscope.

### Imaging for Lung Cancer

Before the bronchoscopy procedure a method to identify the correct location of possible cancer nodules/lesions as well as a system to map a correct 3-dimensional (3D) path to the region of interest are required. For this reason, all patients undergo a computed tomography (CT) scan hours or days before the procedure, and this has to be properly analysed by the physician. In fact, first results from the lung cancer screening trial data show that around one third of smokers that undergo a CT scan have lung nodules that may require guided bronchoscopy and biopsy [2]. Once the analysis is completed and the physician has identified the path to follow to reach the region of interest, the bronchoscopy procedure can be performed.

### Problems with Current Approaches

One drawback of the bronchoscopy procedure is the bronchoscope's diameter which does not allow access to deeper regions of the lung where the bronchi become narrow. This is a major problem, as these locations are where many early stage cancer develop [3,4]. Moreover, a CT scan typically consists of several 2D images, the analysis of which may require a tedious inspection of individual slices in search of possible signs of disease. The performance of this method alone has a low accuracy of only 14% [5]. To help the physician overcome these problems new methods have been proposed. Among them, fluoroscopy-guided bronchocopy is one of the most widely known and remains the standard of care for lung guidance [6,7]. With this system the physician is provided with a real-time x-ray image on a screen that is coupled with the bronchoscopic video in order to identify the position of the bronchoscope within the lung. However, fluoroscopy

provides only 2D images of the inside of the body, causing possible overlapping of the different structures (see Figure 1.2). Moreover, a c-arm fluoroscope is



**Figure 1.2:** A typical chest fluoroscopy 2D image. Overlap of different structures appears evident.

required during the procedure, exposing both the patient and the clinicians to significant levels of radiations. Therefore, in recent years a new system called electromagnetic navigation bronchoscopy (ENB) has been proposed.

### **Virtual Bronchoscopy and Navigation**

Electromagnetic (EM) tracking helps to determine both the position and orientation of an object using magnetic fields. It usually uses low frequency magnetic fields ( $< 100$  kHz) which can pass freely through human tissue without significant attenuation [8]. EM tracking can be coupled with the 3D CT scan of the patient by means of a EM sensor at the tip of the bronchoscope, helping the physician to see the exact position of the bronchoscope both within the lung through the camera and in the 3D view represented by the CT image. Alignment (registration) of the patient with the CT image is required, and no radiation exposure is necessary [9–16]. Unfortunately, the minimum size of even the latest generation ultrathin bronchoscopes is around 2 mm, still too big to reach deepest peripheral sites. Hence, a new tool called virtual bronchoscopy (VB) has been proposed to further help the physician during the procedure. VB refers to a virtual 3D representations of bronchial tree and surrounding structures in which the physician can move and explore the inner part of the airway [17–24]. VB is used in conjunction with electromagnetic navigation bronchoscopy (ENB), so that the tip of the bronchoscope can be seen both on the CT image and inside the 3D

## 1. INTRODUCTION

---

model of the airway. This method can provide the physician with an automatically constructed virtual pathway to the region of interest; a sort of GPS system for the lung [24, 25]. This system have been shown to be useful in reducing the examination time when coupled with ENB [18]. To date, there are two commercially available VB systems using ENB: SuperDimension iLogic System [26] and Veran SPINDrive [27]. On the other hand, LungPoint (Broncus Medical, Mountain View, CA, USA) is the only commercially available system for VB [28]. High costs and CT resolution as well as high sensitivity to external magnetic fields, such as those that could be used as a steering mechanism or imaging (e.g., in MRI), limit these systems.

### 1.2 Thesis Objectives

This research had five main objectives:

- Development of a system to automatically detect probability of malignancy of suspect nodules and helps the physician decide whether to proceed with bronchoscopy.
- Development of a system that automatically reconstructs the best pathway to the target nodule and provides guidance during bronchoscopy.
- Development of a VB system to reproduce a virtual reconstruction of the inside and outside of the airways starting from CT, converts the tracked position of the catheter into a position in the virtual environment and guides the physician during bronchoscopy.
- Development of an open-source algorithm for airway segmentation that allows direct comparison with other methods and modifications according to personal needs and is reliable across multiple CT platforms and parameters.
- Development of a VB system that is similar to commercial ones, less cost effective, more general in terms of CT characteristics, and that reduces manual interaction as much as possible.



The primary end of this research thesis is to provide physicians with a first version of an open-source virtual navigation system for the lung to be coupled with an automatic or semi-automatic robotic ENB system. This navigation platform will automatically recognise malignancy level of possible nodules prior the procedure, determine the pathways to the nodules and provide real-time virtual navigation within the airways. At the moment, when a suspect tumour is identified, the physician visually analyses the patient's CT image to identify possible indicators of nodule's malignancy and decide whether to proceed with biopsy. However, recent studies showed that 85-90% of biopsied lung cancer nodules are benign [29]. For this reason, having a system that automatically detects lung tumours on a CT image and extracts nodule's characteristics to determine probability of malignancy is absolutely essential to save time for the physician, money for the hospital, and most of all to avoid the patient an unnecessary operation. To this end, one of the goals of the research was the development of a system that automatically determines probability of malignancy of suspect nodules and helps the physician decide whether to go ahead with the procedure.

Once the nodule is identified and considered worth of biopsy, the physician analyses the CT image to mentally reconstruct the best pathway from the trachea to the region of interest. This is a long and tedious operation, that requires the physician to also memorize the pathway to follow during bronchoscopy. For this reason, the development of a system that automatically reconstructs the best pathway to the target nodule and provides guidance during the procedure, as a type of GPS system for the airways, might be of great help for the physicians. Currently, two commercial systems of this type are available; superDimension [26] and Veran SPINDrive [27]. However, these systems have high costs, have specific requirements, such as the type of CT image that has to be used, and require a long training, due to the high user interaction necessary, before the physicians can use them. Therefore, the main goal of the research was the development of a system similar to commercial ones, but less cost effective, more general in terms of CT characteristics, and that reduces manual interaction as much as possible.

At University College of Cork (UCC), a novel electromagnetic (EM) tracking platform to identify position and orientation of the bronchoscope in real-time during the procedure has been developed. In this context, the main goal of

## 1. INTRODUCTION

---

the presented research was the development of a VB system that reproduces a virtual reconstruction of the inside and outside of the airway starting from CT, automatically reconstructs the pathway towards the targets, converts the tracked position of the catheter into the corresponding position in the virtual environment, and guides the physician during bronchoscopy.

The first step towards the creation of a VB method is represented by the creation of a 3D virtual model of the airway. To this end, the chest CT image of the patient is analysed in order to identify and isolate the airways from the rest of the lung. This process is referred to as segmentation. Several systems have been developed for airway segmentation. However, these systems are usually tested only on personal datasets, so that direct comparison is not possible, and the effect of varying parameters of the CT image have never been considered. For this reason, a final goal of the research was the development of an open-source algorithm for airway segmentation that allows direct comparison with other methods and modifications according to personal needs and is reliable across multiple CT platforms and acquisition parameters.

### 1.3 Thesis Structure

This thesis is divided into five main chapters which investigate the different aspects of the work.

Chapter 2 describes the background and the context to the research. A small introduction to lung and airway anatomy as well as to computed tomography is first presented. Then, the open-source platform 3D Slicer used throughout the research is described and a previously developed [30] EM tracking system introduced.

Chapter 3 describes the algorithm implemented to identify the likelihood of malignancy of lung nodules. Each sub-algorithm necessary to determine the important metrics that lead to a probability are detailed and a method for testing and evaluation is described.

Chapter 4 details the design and implementation of the airway segmentation algorithm. The method used to develop the algorithm as well as the theory

to support the implementation are described and the approach for testing and evaluation of the algorithm considered.

Chapter 5 covers all aspects of the virtual navigation system starting from the 3D airway model. Each part of the system, including pathway creation and image registration, is described in detail in terms of implementation and theory to support the design.

In Chapter 6, testing and evaluation of the VB system both in *ex-vivo* and *in-vivo* experiments was demonstrated. For *ex-vivo* testing, a plasticised pig lung is used as a phantom. This was navigated by nine different physicians in the field of respiratory medicine. The *in-vivo* study was conducted on two pigs, whose lungs were navigated to biopsy tumour models.

In Chapter 7, the key findings of the thesis are reviewed and recommendations for future work are presented.

## 1.4 Key Contributions

The key contributions of the presented thesis are here summarised:

- The design of a novel open-source algorithm for nodule malignancy prediction (Chapter 3). Only nodule location has to be specified. The system automatically defines nodule characteristics, such as size, location, edge shape, wall thickness and calcification presence to determine probability of malignancy. The system represents a first fundamental step for the development of a platform for automatic identification and classification of lung nodules.
- The first open-source algorithm for airway segmentation starting from chest CT images (Chapter 4). The method can be used for both human and animal (porcine, canine) images and provides a frame of reference for comparison of results using local datasets.
- The first study of effect of variation of CT parameters (slice thickness, radiation dose, convolution kernel, and level of inflation) on airway segmentation (Chapter 4).

## 1. INTRODUCTION

---

- Development of a novel method to evaluate leakage presence on segmented airways (Chapter 4). This can be easily reproduced by other teams, thus providing a general evaluation system to compare results.
- A novel open-source virtual bronchoscopy system for image-guided navigation (Chapter 5). This system has a modular structure and has been optimized for usage with the electromagnetic tracking system developed at UCC.
- The VB system provides different tools for helping during pre-procedure and navigation steps. Compared to commercial systems, it generalizes the type of CT images to be used, and reduces manual interaction as well as cost (Chapter 5).
- A new method for landmark-free registration between real and virtual environment has been proposed and validated (Chapter 5). The method improves performance of registration and drastically reduces user interaction.

# Chapter 2

## Background

### 2.1 Overview

In this chapter, a description of the research context for this work is presented. The main goal of the research was to develop a system for virtual navigation within the lung, to eventually be used by physicians during biopsy of suspect lung cancer nodules. For this reason, a brief introduction to human lung and airway anatomy is first presented, followed by characterization of lung cancer and lung diseases. For the development of a system for VB, CT images are used as a starting point. X-ray CT is described, including its main characteristics and operating principles. The open-source platform 3D Slicer, used for the development of the VB system, is then introduced, and, finally, the electromagnetic navigation platform developed at University College Cork (UCC) which is coupled with the VB to create a complete ENB system is briefly described.

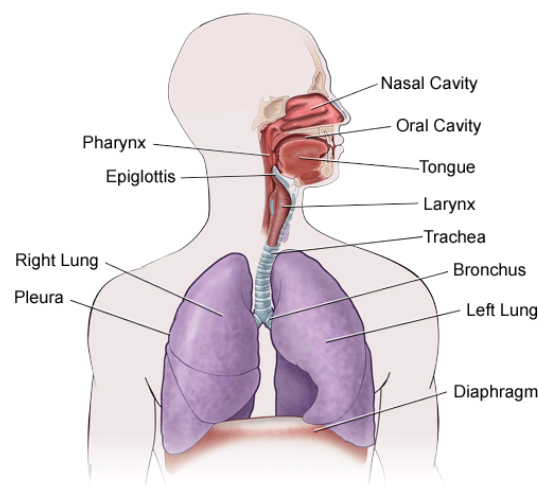
### 2.2 Human Lung and Airways Tree

The human lungs are a pair of spongy, air-filled organs which allow for the exchange of air with the external environment. They are located within the thoracic cavity of the chest, both having a conical shape and similar in appearance. However, the right lung is divided into three lobes (upper, middle, and lower) by two inter-lobular fissures (oblique and horizontal), and it is also shorter by about 2.5

## 2. BACKGROUND

---

cm than the left one, which is instead divided into two lobes (upper and lower) separated by one inter-lobular oblique fissure. The lungs are surrounded by a thin layer of tissue, called pleura, and they are connected by means of the trachea, a tube that conducts inhaled air into the two lungs through its branches, called bronchi (Figure 2.1). The bronchi then split into smaller branches (bronchioles) and end in the alveoli, a cluster of small sacs where the gas exchange takes place. The main function of the lungs is to provide oxygen to capillaries in order to oxy-



**Figure 2.1:** The human respiratory system [31].

genate the bloodstream. At the same time, through the alveoli the lungs transfer carbon dioxide, a waste product of metabolism, to the atmosphere.

The set of tubes that allows for inhalation and exhalation of the air is referred to as the pulmonary airways tree, or respiratory tract. The mouth and the nose are the normal entry and exit ports through which the air enters the body, and from here it is conducted to the trachea through the pharynx. The trachea is the biggest tube of the respiratory tract with a diameter of about 25 mm and a length of 10-16 cm. It represents the first part of the respiratory tract and it then splits into the two main branches, the right and left bronchi, in an area called the carina. The main bronchi enter the right and left lungs and progressively subdivide into two or more smaller “child” branches until the alveoli. Each

division point is called a generation and the human airway tree consists on average of 23 generations, for a total of approximately 2400 km of airways. Bronchi are typically airways surrounded by cartilaginous walls. The amount of cartilage in the walls of bronchi progressively decreases and eventually disappears by the time the bronchi divide into airways of about 1 mm diameter (after generations 12-14). The smaller airways that lack cartilage are called bronchioles [32]. The respiratory tract functions as a piping system for the air and is protected by the rib cage, spinal cord, and sternum bone.

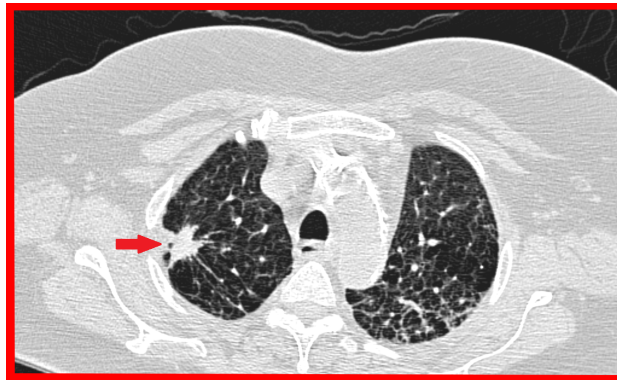
## 2.3 Lung Cancer and Diseases

The term lung cancer refers to an uncontrolled growth of abnormal cells in tissues of one or both lungs. When the abnormal cells divide and form larger tumours, the ability to provide the bloodstream with oxygen may be undermined. The most common symptoms of lung cancer are coughing, weight loss, shortness of breath, and chest pains [33]. Despite improvements in surgical, radiotherapeutic, and chemotherapeutic approaches in the last three decades, lung cancer is still the leading cause of cancer-related death and the long-term survival rate remains low [34]. According to GLOBOCAN, there were 1.8 million new global cases of lung cancer in 2012 (12.9% of the total cancer incidence). In the United States, lung cancer is the second most common cancer diagnosed cancer in men and women [35]. Other than cancer there are also several pathologies, such as airway related disease (e.g., asthma and chronic bronchitis) or chronic obstructive pulmonary disease (COPD), that can also affect the lung function. According to the World Health Organization (WHO) between 100 and 150 million people around the globe suffer from asthma and deaths from this condition have reached over 180,000 annually [36], while emphysema (one of the two main forms of COPD) is projected to be the third leading cause of death worldwide by 2020 [37].

When a lung tumour is identified, the first step is to determine whether the tumour is malignant or benign. Malignant tumours are the most dangerous and they usually spread to different parts of the body either through the bloodstream or the lymphatic system. These tumours take oxygen and nutrients from healthy cells and they destroy or reduce the ability of normal tissues to function. Typical

## 2. BACKGROUND

---



**Figure 2.2:** This figure shows an axial CT image of a patient presenting a malignant nodule (red arrow).

malignant tumours are usually large ( $> 2$  cm), located in upper or middle lobes, with big internal cavities, low calcification and with spiculated edges [38, 39]. An example of a typical malignant lung tumour can be seen in Figure 2.2. On the other hand, benign tumours are not cancerous, so they will not spread to other parts of the body and they grow slowly or they might even stop growing or shrink. Usually they do not need to be removed, as they will not invade, destroy, or replace other tissues. Automatic and early recognition of probability of malignancy of a lung tumour may help the physicians decide whether to go ahead with a procedure such as bronchoscopy to biopsy or remove the tumour itself.

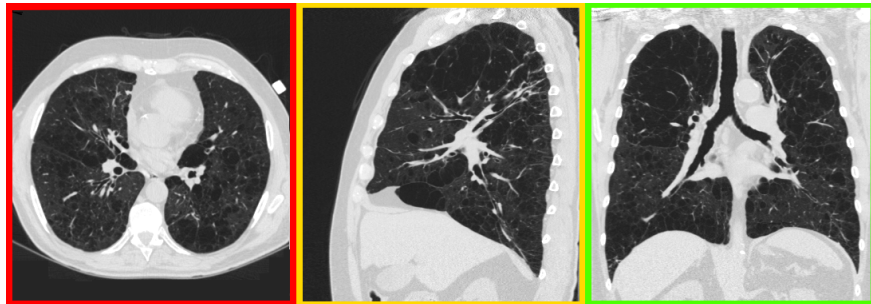
### 2.4 X-ray Computed Tomography (CT)

The most common imaging modality for lung diseases recognition is x-ray computed tomography (CT), a non-invasive system which allows a doctor to have a three-dimensional (3D) view of the patient's lung, including the complex branching structure of the airway tree [40, 41]. During a CT scan, several x-ray images of the body are taken from different angles. Digital image processing combines all the different images (defined as "slices"), to create a single 3D image. Virtually every patient with a suspect lung disease undergo a CT scan. In fact, CT is highly sensitive to pulmonary nodules and it may help better characterize COPD



## 2.4 X-ray Computed Tomography (CT)

due to tissue loss or changes in airway dimensions. First results from the lung cancer screening trial data show that around one third of smoking people that undergo a CT scan have lung nodules that may require guided bronchoscopy and biopsy [2]. Images acquired with a CT scan are provided as a set of 2D images that can be scrolled through in three different planes, that is axial, coronal, and sagittal plane. This helps the clinician examine the same region of interest from three different points of views, allowing a better analysis of possible abnormalities. Figure 2.3 shows an example of a chest CT image. Although a CT scan



**Figure 2.3:** A reconstructed CT image as shown to physicians. Axial (red), sagittal (yellow), and coronal (green) views of the same patient are shown.

requires the patients to be exposed to a certain radiation dose, advances in CT technology have made high-resolution images possible with a single breath hold at acceptable levels of radiation exposure. However, a CT scan can not be used alone for diagnosis, as false-positive findings are likely to appear [42]. Therefore, to date a histological confirmation is absolutely essential for good diagnosis. This includes biopsy at the point of interest.

### 2.4.1 Historical Background

X-ray computed tomography, was proposed for the first time in 1972 by G. N. Hounsfield and A. Cormack, who were later awarded the Nobel Peace Prize for their contributions to medicine and science [43]. CT can be considered as the first modern “slice-imaging” modality and to date is the gold standard for lung imaging. The first CT scanners were dedicated to head imaging only, but a “whole body” system was developed a few years later (1976). By 1980 CT scanners

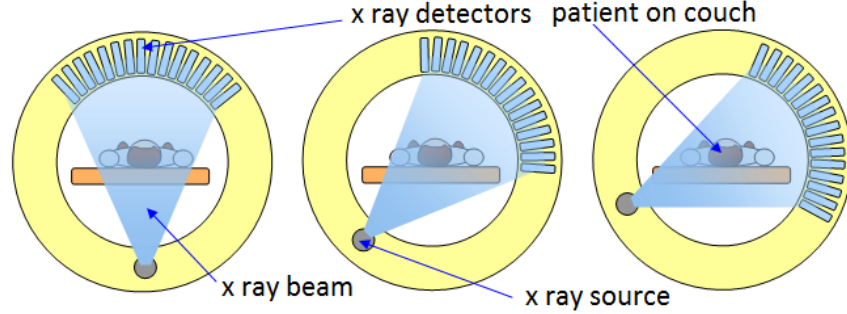
## 2. BACKGROUND

---

became widely available and at present about 30,000 scanners are installed in hospitals and private clinics worldwide. The first CT scanner was extremely slow, taking days to reconstruct a single image of a patient. New generation scanners can reconstruct a  $512 \times 512$  image from millions of data points in less than a second. For example, an entire chest (around five hundred 2 mm slices) can now be scanned in fifteen to twenty seconds, allowing the acquisition of full 3D images in a single patient breath-hold [44]. In the last two decades, CT technology has made great improvements in speed, patient comfort, and resolution. More anatomy of the body can now be scanned in a faster time that also helps eliminate possible image artifacts due to breathing and other motion. Typical CT scanners allow for the detection of bronchi up to a level between the 5th and 9th generation, with dimensions between 3.5 and 1.3 mm in luminal diameter, depending on the scan parameters chosen.

### 2.4.2 Operating Principles

The underlying basis of CT lies in the different levels of absorption of x-ray beams by the internal structures of the body. This depends on thickness, chemical composition, density and other features of the structure itself. This determines different contrast in the image between the different tissues and structures. Based on how much a structure attenuates the x-rays, a different shade of a greyscale colourmap is assigned to each pixel. As an example, bones efficiently absorb x-rays, resulting in a strong white colour level in a CT image, while soft tissue hardly absorbs any x-ray. Current scanners include an x-ray source, in which single or multiple tubes rotate around the patient emitting an x-ray beam, and an opposite array of detectors which collect the transmitted radiation (Figure 2.4). This way, a set of 1D projections are acquired at different angles, discretized, and used to generate a 2D image through a back-projection method based on the Radon transform [46]. The multiple images generated from adjacent slices are then combined to reconstruct the 3D volume. Image quality provided by CT scan has reached a very high level. This quality can vary based on several CT parameters which can be modified according to diagnostic needs and to patient characteristics. Typical parameters are slice thickness, image spacing, convolution



**Figure 2.4:** A representation of a CT scanner with x-ray source and detectors shown in three different positions [45].

kernel, and radiation dose. Radiation dose represents one of the most important parameters. High doses of ionizing radiation can increase cancer risk as well as other problems. Therefore, this limits the total radiation dose per year to which a patient can be subjected [47, 48].

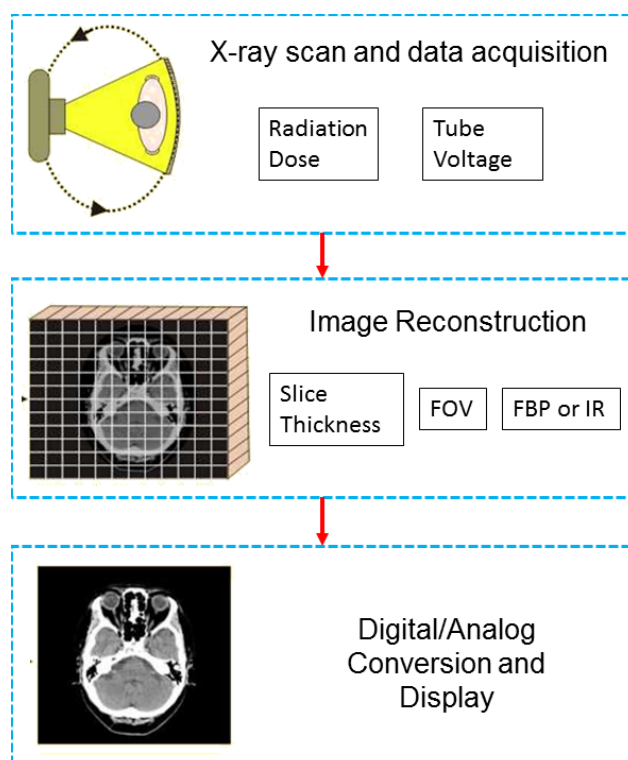
### CT Image Reconstruction

Throughout the years, several approaches have been considered to reduce CT radiation doses. A newer technique has recently become commercially available for all major CT vendors and consists in optimisation of CT image reconstruction. Currently, the most widely used reconstruction technique is filtered back-projection (FBP), an algorithm which assumes that the acquired data are free of noise. FBP is an adequate approach, but it might produce noisy images in case of low doses or obese patients [49]. Therefore, an alternative method, referred to as iterative reconstruction (IR) has been proposed [49]. With IR, dose reduction can be achieved without compromising on image quality. Different IR methods are available. However, these are vendor-specific solutions and are only provided as “black boxes” with very little information on algorithmic principles and details [50]. In general, all IR methods consist of three major steps which are repeated iteratively; a forward projection of the volumetric object estimate to create artificial raw data; the created raw data are compared to the real measured raw data in order to compute a correction term; finally, the correction term is back projected onto the volumetric object estimate [50]. As an example,

## 2. BACKGROUND

---

GE Healthcare provides two IR techniques: adaptive statistical iterative reconstruction (ASIR) and model-based iterative reconstruction (MBIR). The ASIR technique models just the photon and electronic noise statistics [51], while MBIR methods try to model the acquisition process as accurately as possible [50]. However, sufficient information on the underlying the algorithms is mostly missing. Figure 2.5 shows a block-diagram indicating the main steps and parameters for the creation of a CT image.



**Figure 2.5:** Block-diagram of the main steps for the creation of a CT image. Parameters that can be modified at every step are specified. FOV stands for field of view, FBP for filtered back-projection, while IR is used for iterative reconstruction.

### 2.4.2.1 X-ray Source and Detector

The x-ray slice image of a CT is generated using an x-ray source that rotates around the body. The x-ray beam goes through the body and reaches the x-ray detectors positioned on the opposite side of the x-ray source. The detectors

## 2.4 X-ray Computed Tomography (CT)

---

collect the non-absorbed rays and determine the different levels of contrast of the structures.

The x-ray source is composed of a vacuum tube containing a negatively charged cathode, that is a filament of tungsten with a diameter of  $\sim 200 \mu\text{m}$ , coiled to form a spiral of  $\sim 2 \text{ mm}$  in diameter and less than  $1 \text{ cm}$  in height. When a current passes through the cathode, the wire is heated up to approximately  $2200^\circ\text{C}$ . This makes the tungsten atoms able to absorb enough energy to liberate a small number electrons [52]. These “free” electrons are attracted by a positively charged anode, which contains a metal target, creating the accelerated beam of electrons. Once the accelerated electrons reach the anode, they penetrate into the metal target generating x-rays via two mechanisms: “Bremsstrahlung” or general radiation and characteristic radiation [52]. The general radiation produces about 80% of the total x-rays and it is created when an electron passes near to a tungsten nucleus and loses kinetic energy by being deflected by the attractive force of a positively charged nucleus of tungsten. Hence, this lost energy is emitted as an x-ray. The second mechanism, the characteristic radiation, produces the remaining 20% of x-rays and occurs when electrons are accelerated from the cathode and collide with a tightly bound electron in the innermost “shell” of a tungsten atom. In this case, the bound electron is ejected and the resulting “hole” is filled by another electron from an outer shell. This causes a loss of energy due to different binding energies of the inner and outer shells, which is transformed in a new x-ray. By controlling the current within the x-ray source and the potential difference between cathode and anode, it is possible to control the amount of emitted x-rays.

The second fundamental device in a CT scanner is the x-ray detector, an electronic sensor able to detect and recognize the energy of a radiation beam. The detector is connected to a computer to which it transmits the obtained data. Modern scanners use detectors placed all around the patient’s body, allowing the use of a wide beam of radiation to acquire more information in a single step (see Figure 2.4). X-ray detectors are characterized by three fundamental features: capture efficiency, absorption efficiency, and conversion efficiency. The capture efficiency indicates the capacity for receiving photons by the detectors and depends mainly on detector size and distance between detectors. Absorption

## 2. BACKGROUND

---

efficiency represents the ability of the detector to interact with x-ray photons actually captured and depends on size and thickness of the detector itself. Finally, the conversion efficiency is how well the detector converts the absorbed photon information to a digital signal for the computer. The most common detectors for CT scanners are usually xenon-filled ionization chambers. Xenon has an atomic number of 66, assuring a high probability of photoelectric interactions between the gas and the incoming x-rays [52].

### 2.4.2.2 Absorption and Hounsfield Unit

When the x-ray beam goes through the body, three main effects of distortion can take place. Some tissues, such as lung tissue or soft tissues in general, absorb little or no radiation which can pass through the body with no distortion. These x-rays are referred to as “primary radiation”. Certain tissues, instead, can alter the trajectory between the source and the detector, undergoing a phenomenon called “scattering”. Such x-rays are described as “secondary radiation”. Finally, x-rays can be absorbed completely in tissue and not reach the detector at all. This constitutes the “absorbed radiation”. Based on the degree of radiation absorption, a different contrast is created in a CT image between different structures. A computer receives the x-ray converted into a digital signal by the detector, analyses the data, and forms the final image shown to the clinician. As a first step, the linear attenuation coefficient for each voxel is converted into the Hounsfield Unit (HU) scale. On this scale, the radio density of distilled water at standard pressure and temperature is defined as 0 HU, while the radio density of air at standard pressure and temperature has a value of -1000 HU. Table 2.1 shows the typical HUs calculated for various structures of the body.

Considering the linear attenuation coefficient  $\mu_x$  of a voxel, the corresponding HU value is computed by equation (2.1).

$$HU = K \times \frac{\mu_x - \mu_{\text{water}}}{\mu_{\text{water}}} \quad (2.1)$$

In (2.1)  $\mu_{\text{water}}$  is the linear attenuation coefficient of the water and  $K$  is a constant, usually standardized as 1024 [43]. According to (2.1), a change of 1 HU

## 2.4 X-ray Computed Tomography (CT)

---

**Table 2.1:** This table shows the typical Hounsfield values of some body tissues and substances.

Tissue	HU
Air	-1000
Lung	-500
Fat	-84
Water	0
Soft Tissue	+40
Blood	+40 to +80
Bone	+700 to +3000

represents a change of 0.1% of the attenuation coefficient of water since the attenuation coefficient of air is zero. Images coming from a CT scanner are generally outputted in digital imaging and communication in medicine (DICOM) format. This is a standard for handling, storing, printing, and transmitting information in medical imaging. It includes a file format definition and a network communications protocol. The communication protocol is an application protocol that uses TCP/IP to communicate between systems. DICOM also enables the integration of scanners, servers, workstations, printers, and network hardware from multiple manufacturers into a picture archiving and communication system (PACS). The National Electrical Manufacturers Association (NEMA) holds the copyright to this standard.

### 2.4.2.3 Parameters

CT image quality depends on different parameters that can be set prior to a scan. Among them, those of most importance are slice thickness, radiation dose, and reconstruction kernel (see Table 2.2).

Slice thickness represents the width of each slice of the image and can be changed after the image acquisition according to specific user needs. Narrow slice thickness leads to better edge definition, better high resolution contrast (meaning that small objects and details can be differentiated from surrounding structures with a high accuracy), and less partial volume effects (a phenomenon that causes

## 2. BACKGROUND

---

**Table 2.2:** This table shows the typical parameters of a CT scan.

Parameter	Units	Effect
Slice Thickness	mm	Edge definition and resolution contrast
Radiation Dose	mA	Image quality and noise presence
Convolution Kernel	\	Edge definition and noise

a blurring effect across boundaries due to a loss of apparent intensity in small objects or regions because of the limited resolution), at the cost of a higher signal noise and poorer low contrast resolution (the ability to define objects and details which can be differentiated from surrounding structures with very little density difference). On the other hand, large thickness leads to less noise on the image and better low dose contrast, but it also results in poorer edge definition, worse high resolution contrast, and a higher presence of partial volume effects.

Radiation dose refers to the amount of x-rays emitted during the acquisition and has to be set before the scan starts. It is measured in mA as it represents the level of current within the x-ray source. The higher the current, the higher the amount of x-rays emitted and, thus, the dose. High radiation doses allow for better quality images, with more detail and less noise, but expose the patient to higher risks. Therefore, a good trade-off between radiation exposure to the patient and image quality which is useful for diagnostic purposes has to be considered.

The reconstruction kernel, known also as convolution kernel, is the filter or algorithm applied on the acquired data to reconstruct the final scan image. It has a significant impact on spatial frequency and noise characteristics of an image, and different scanner brands may have different kernels. In general, a reconstruction kernel varies in a range soft to sharp, with a soft kernel leading to smooth edges and reduced image noise, whereas a sharp kernel will enhance the edges at the cost of a higher image noise [53, 54]. There is no a perfect choice for CT parameters, and physicians tend to change them dependent on different patients.



## 2.5 3D Slicer

The main goal of the research was to develop a free open-source tool for virtual bronchoscopy. For this reason, the freely-available and easily extendible open-source package, 3D Slicer, has been used. 3D Slicer is a software package for visualization (including volume rendering) and image analysis (including image registration and segmentation), natively designed to be available on multiple platforms, including Windows, Linux and Mac OS X. It also supports multi-modality imaging including, MRI, CT, US, nuclear medicine, and microscopy, and standard image file formats, such as DICOM. The application integrates interface capabilities to biomedical research software and image informatics frameworks.

3D Slicer was initiated as a master's thesis project between the Surgical Planning Laboratory (SPL) at the Brigham and Women's Hospital and the MIT Artificial Intelligence Laboratory in 1998. Since then it has been continuously improved and in 2007 a completely re-architected version was released. The current version is Slicer 4.5 which was released in December 2015. To date, Slicer has been downloaded by thousands of users and developers worldwide and has enabled hundreds of academic publications. Slicer's users and developers are also part of a community (through two different mailing lists) that provides help and suggestions when problems occur.

3D Slicer consists of more than one million lines of code, mostly C++ and Python, and is distributed under a Berkeley Software Distribution (BSD) license. However, while available for clinical research, it is not FDA approved for diagnosis [55–57]. Permissions and compliance with applicable rules are the responsibility of the user. 3D Slicer is built on a set of powerful and widely used software components, such as Tool Command Language (Tcl/Tk) [58], Visualization Toolkit (VTK) [59], and Insight Segmentation and Registration Toolkit (ITK) [60–62] to which is added an application layer, incorporating a graphical user interface (GUI) which makes the system easily usable for non-programmer end-users. The main Slicer's feature is its powerful plug-in capabilities for adding and modifying new algorithms and applications. In fact, along with the standard and basic algorithms available, Slicer provides a type of free App Store, called Extensions Manager, from which it is possible to download, use or modify the Slicer

## 2. BACKGROUND

---

extensions, new algorithms added to Slicer from developers around the world in the same way as applications for a smartphone. More than 50 extensions and packages of extensions are currently available and these are in continuous improvement. The Extensions Manager also allows for upload of new extensions to Slicer, so that these can be used and tested by the community and feedback can be obtained. Thanks to the modularity of Slicer, developers can focus on their area of expertise without extensive knowledge of the larger platform. In advance of this thesis, Slicer did not provide any system for virtual bronchoscopy, as it is used mainly for brain imaging. Beside 3D Slicer, there exist other freely available imaging processing platforms. Among them, Osirix [63] and MITK [64] are probably the most popular.

### **Osirix and MITK**

Osirix is a software dedicated to DICOM images which has been specifically designed for navigation and visualization of multimodality and multidimensional images. It supports a complete plug-ins architecture that allows for the expansion of the capabilities of Osirix according to personal needs, but it currently does not provide many tools for image processing operations. Moreover, Osirix is currently available only for Apple Mac OS computers.

On the other hand, the Medical Imaging Interaction Toolkit (MITK) is an open-source platform for medical image analysis which aims at providing support for an efficient software-development of methods and applications dealing with medical images. As well as 3D Slicer, MITK is available on Windows, Mac OS X, and Linux. It is based on ITK and VTK classes, and it is not FDA approved. However, being more recent than 3D Slicer, MITK contains less basic tools for medical image processing. 3D Slicer has been chosen for the present research as a new project is currently being developed at SPL in order to create a branch of Slicer exclusively dedicated to chest imaging. This is referred to as Slicer Chest Imaging Platform, or SlicerCIP, and it is still under development, with a future release in mind.

## 2.6 Electromagnetic Navigation Systems

At present, two commercially available systems for electromagnetic navigation coupled with VB are available: Superdimension iLogic System and Veran SPIN-Drive. Here, the two different systems are briefly described. At University College Cork, a novel low-cost system for EM tracking is currently being developed. This system will be briefly described here, as it is the tracking system used for the research.

### 2.6.1 Superdimension iLogic System

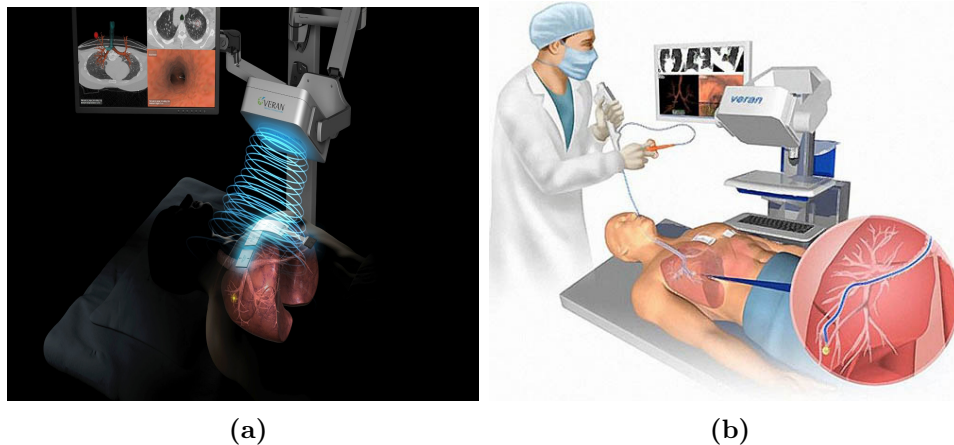
The iLogic system was developed by SuperDimension Ltd (Hertzilya, Israel) and is an example of an FDA approved electromagnetic tracking system for use in lung bronchoscopy. The basic operation of this system relies on a flat field generator board ( $47\text{cm} \times 56\text{cm} \times 1\text{cm}$ ) placed beneath the patient. A low frequency magnetic field is emitted by the board and a 6-DOF pick-up coil (1 mm in diameter and 8 mm long) placed at the tip of the instrument is used to detect the emitted field [12]. The transmitter board is shown in Figure 2.6 [26]. The tracked position is then incorporated into the preoperative CT scan of the patient, while a virtual representation of the airways is used for the navigation. The system has been reported to have a registration error of  $6.12 \pm 1.7$  mm, while it can be considered relatively safe, having rates of pneumothorax reported as low as 3.5-7.5% [12].



**Figure 2.6:** The SuperDimension transmitter board [65].

## 2. BACKGROUND

---



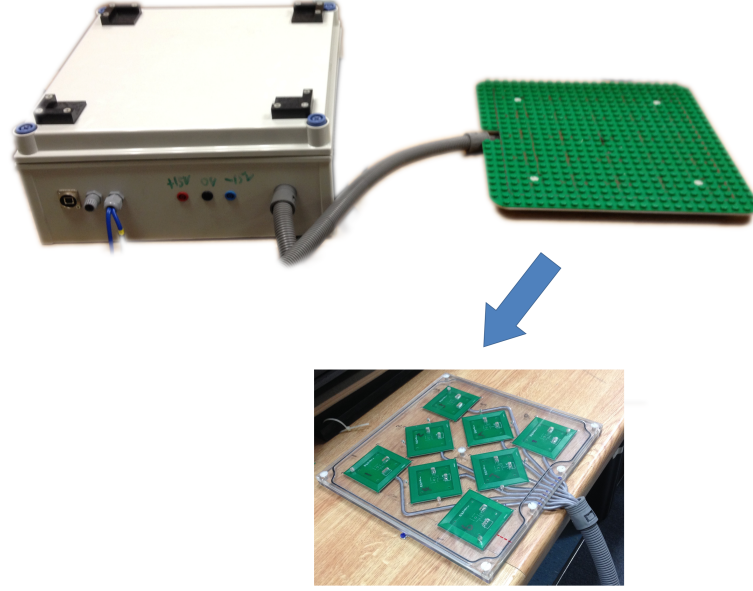
**Figure 2.7:** (a) EM transmitter and (b) working station of the Veran SPINDrive system [67].

### 2.6.2 Veran SPINDrive

The second example of FDA-approved electromagnetic tracking system for use in lung navigation is the Veran SPINDrive [27]. The magnetic field is generated by a transmitter held above the patient, as shown in 2.7(a) [66]. Specific catheters and biopsy needles containing built in EM sensors that detect the transmitted magnetic field have to be used with SPINDrive. These are provided by Veran, whose work-station is shown in Figure 2.7(b). The smallest sensor for the system measures 0.43 mm in diameter with a length of 8 mm. Secondary sensors are placed on the patient for registration and to record motion due to breathing.

### 2.6.3 Electromagnetic Navigation at University College Cork

At University College Cork (UCC), a new catheter navigation platform using EM fields to track the position of a catheter is currently being developed [8]. Currently, there exists a number of commercial EM tracking systems. However, all have high prices ( $> \text{€}10,000$ ) and limitations, such as high sensitivity to external magnetic fields. For this reason, a new platform, comparable in performance but cheaper in cost has been implemented. The system uses planar magnetic



**Figure 2.8:** The tracking system as developed at University College Cork.

coils transmitting low frequency magnetic fields ( $< 30$  kHz) and implemented on printed circuit board (PCB), as well as a miniature pick-up coil, or sensor, placed at the distal end of a catheter. An array of magnetic sources induces a voltage at various frequencies in the pick-up coil and its position and orientation can be determined by measuring this induced voltage and by solving a non-linear system of equations. An example of the hardware system is shown in Figure 2.8. It consists of multiple small transmitting coils, an 8 mm receiver coil and associated amplifiers. Software implemented in MATLAB then filters and demodulates the input signals and calculates the position and orientation. The sensor voltage as well as the current in each transmitting coil is recorded using a National Instrument USB DAQ card. Two channels were used with a sampling rate of 100 kS/s per channel.

There are different electromagnetic tracking methods described previously. However, these are typically prohibitively expensive and are also susceptible to magnetic interference [68]. Many magnetic tracking methods make use of the dipole approximation to simplify the required calculations [69, 70] and other research has investigated methods to improve this approximation [71]. However, significant errors can occur when using this approximation. These errors were

## 2. BACKGROUND

---

mitigated and accuracy was increased at UCC by directly calculating the exact magnetic fields with a filamentary conductor-based method [72]. Moreover, the use of PCB coils for position tracking had never been documented previously. Its use in position tracking has the advantage that the coils can be easily mass produced almost identically, much more than a similar set of coils wound in traditional methods. The exact position of each track can easily be determined, allowing for very accurate prediction of the generated magnetic fields with analytical methods. Finally, the sensor used at UCC is a commercial 5 degree of freedom (DOF) device. This does not allow the computation of the axial rotation angle, as the flux does not vary with rotation, but allows for navigation in smaller branches. The system accuracy has been extensively tested both *ex-vivo*, using a specifically built breathing pig lung model (Figure 2.9), and *in-vivo* through animal trials [73]. The position error from the system was found to be less than 2 mm, while system accuracy, found in the range of 1-1.5 mm, has been shown to be comparable to both commercial and research tracking systems. This level of accuracy is well suited for its application in virtual bronchoscopy [8].



**Figure 2.9:** The breathing pig lung model as used in our research.

This system paves the way for the development of a new semi-automatic robotic catheter steering platform for easier navigation within the airways and which, eventually, will allow to reach peripheral areas of the airways that are currently inaccessible. Currently, on reaching smaller branches, the clinicians navigates “blindly”. For this reason, a system of VB to be coupled with the electromagnetic navigation is of great importance. The benefits are twofold. Firstly, the physician

## 2.6 Electromagnetic Navigation Systems

---

is led in real-time to the correct region of interest through the best route, with no need to plan a priori the pathway to follow. Secondly, when reaching areas too narrow for the camera on the tip of the bronchoscope, the physician can continue the navigation following only the reconstructed model of the airways. This way, lung nodules that are unlikely to be reached with current technology, can be analysed and treated. The electromagnetic navigation platform at UCC has been used in validating the VB system developed in this thesis. Beside being prohibitively expensive, the VB systems of SuperDimension and Veran SPINDrive have specific requirements. Specific parameters for the CT images used for VB are required, and a long training is necessary for the physicians before they can start using the system, due to the high level of manual interaction with the system. Therefore, the main goal of the research is to develop a novel platform that reduces the manual input for the user, improves accuracy and robustness of the system, does not require specific CT characteristics and reduces costs.

# Chapter 3

## Solitary Pulmonary Nodules Malignancy<sup>1</sup>

### 3.1 Overview

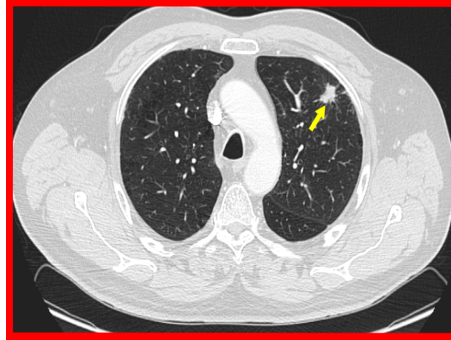
In this chapter, the design and development of the first version of a semi-automated algorithm for recognition of malignancy of solitary pulmonary nodules (SPN) is presented. As with the other algorithms described, the method is implemented as an extension of 3D Slicer [55–57, 74, 75]. The relevant background literature is briefly discussed while each subsystem composing the complete algorithm is explored and described in detail. Finally, testing methods and results are discussed. The main aspects of the algorithm presented in this chapter include:

- The first open-source algorithm entirely dedicated to determine SPN malignancy starting from a chest CT image. This allows for future modifications and improvements when new information will be available.
- At present, several calculators of probability of malignancy for SPN are available. However, they all require the physician to analyse in detail the CT image in order to input nodule characteristics, such as size, location, calcification presence, etc. This is not always an easy task. The algorithm

---

<sup>1</sup>This chapter is based on P. Nardelli, J. Pahl, S. P. Power, K. O'Regan, M. P. Kennedy, P. Cantillon-Murphy “Open-source algorithm for solitary pulmonary nodule malignancy prediction.” *Medical Image Analysis* (2015) [Under Review]





**Figure 3.1:** Example of nodule shown on a axial CT image. The nodule is indicated by the yellow arrow.

proposed requires little user interaction. The nodule to be analysed has to be selected, and patient information has to be given as input to the system. Then, the algorithm automatically computes nodule characteristics and returns a probability of malignancy.

- The algorithm helps the physician determine whether to proceed with biopsy through bronchoscopy or other systems, avoiding an invasive procedure when not strictly necessary.
- The system paves the way for potential future work aimed at automatic identification and classification of lung nodules. The sub-systems of the algorithm may be utilized as pre-processing steps for nodule identification and classification algorithms.

## 3.2 Introduction

Pulmonary nodules are small ( $\leq 3$  cm in diameter), often round- or oval-shaped lesions that grow in the lung. On CT scans, a nodule appears as a rounded or irregular opacity, well or poorly defined [76]. Figure 3.1 shows an example of nodule on an axial CT image. Nodules are potential manifestations of lung cancer and their identification, classification, and inspection is essential for diagnosis of the disease.

### 3. SOLITARY PULMONARY NODULES MALIGNANCY

---

#### 3.2.1 Nodule Classification

The main feature that indicates lung cancer is the growth rate of lung nodules. Based on their level of x-ray attenuation, soft tissue nodules may be classified as ground-glass (or non-solid), part-solid (or semi-solid) or solid. Ground-glass nodules are determined by a hazy increased attenuation in the lung that does not obliterate the bronchial and vascular margins. On the other end, a solid nodule presents a homogeneous attenuation of the soft tissue attenuation, while a part-solid nodule consists of both non-solid and solid soft tissue attenuation components [76].

Based on their position in the lung and proximity to other structures, four classes of pulmonary nodules are identified: well-circumscribed (or solitary), juxta-vascular, with pleura tail or juxta-pleural. Solitary nodules are well-margined and completely surrounded by lung parenchyma. Juxta-vascular nodules are connected to vessels, while juxta-pleural are in contact with the pleura for more than 50% of their diameter. Finally, if the nodules are connected with less than 50% of their diameter to the pleura, they are considered to have a pleural tail. When analysing lung nodules, radiologists look for changes in image intensities of tissues and abnormalities, and, oftentimes, use shape, texture and size as measures to discriminate between a healthy structure and malignant abnormalities.

#### 3.2.2 Computer-aided Detection

In recent years, several systems to support radiologists in this recognition process and enhance the quality of the diagnosis have been developed. These systems are defined as computer-aided detection (CAD) methods and try to automatically identify, segment and classify nodules in CT images. However, for different reasons this is not an easy task. In particular, some nodules may have very low CT HU values and low contrast, whereas many others may have values similar to those of blood vessels and airways, which might be included as possible nodule candidate in systems for nodule identification. For this reason, the development of CAD methods for identification and classification of pulmonary nodules is of great interest for researchers. On the other hand, several tools have recently become available to help radiologists determine probability of malignancy of pulmonary

nodules based on different clinical and radiographic characteristics [77–80]. These methods are mainly for SPNs and require the radiologists to provide all the needed information. As an example, Chest X-Ray [77] requires to specify size, location, edge smoothness, growth rate, cavity wall thickness and calcification present in the nodule, along with clinical characteristics, such as age of the patient, smoking level, previous history of malignancy, and presence of hemoptysis, to determine probability of malignancy [38, 39].

Our goal was to develop a system for semi-automatic determination of malignancy of pulmonary nodules, requiring as little user interaction as possible. Although mainly working with SPNs, the system is not restricted to this type of nodules, and paves the way for the development of a complete open-source CAD system for the identification and classification of nodules. The method automatically extracts size, location, edge smoothness, growth rate, cavity wall thickness and calcification of the analysed nodule and uses these features, combined with clinical indications, to calculate the probability of malignancy, as in [38, 39]. The algorithm has a modular structure and consists of four different steps that are executed sequentially: automatic segmentation of the lungs region, semi-automatic segmentation of the nodule of interest, automatic segmentation of lung lobular fissures, automatic segmentation of lungs’ lobes.

### 3.3 Solitary Pulmonary Nodule

A solitary pulmonary nodule is described as a well-margined, rounded nodule with a diameter of less than or equal to 3 cm that is completely surrounded by lung parenchyma and does not touch other lung structures, such as vessels, airways or pleura. The causes of SPN are many, from lung cancer and metastases to scar formation, infections, and other benign lesions. Several studies showed a prevalence of SPN on CT images from 8% to 51% [81–86] and a prevalence of malignancy from 1.1% to 12% [29]. For this reason, a good distinction between benign from malignant nodules is very important to avoid unnecessary biopsy. To this end, specific morphological characteristics of SPNs may help. In this section, a few SPN radiographic features that can be used for the distinction of benign nodules from malignant ones [87] is described.

### 3. SOLITARY PULMONARY NODULES MALIGNANCY

---

#### **Size**

Size represents the first feature to be taken into consideration when evaluating the nodule. The likelihood of malignancy in a SPN increases with the nodule diameter, and lesions larger than 3 cm (usually defined as pulmonary masses) are more likely to be malignant. However, a small size does not exclude malignancy [88, 89].

#### **Location**

If a SPN is located in the upper lobes of the lung, it is more likely to be malignant. This is due to the fact that cigarette smoking determines a higher presence of inhaled carcinogens in the upper lobes [90, 91].

#### **Edge Characteristics**

Edges of SPNs can be divided into three main categories: smooth, lobulated, and spiculated. Benign margins suggest a higher probability of a benign lesion, although this is not always certain. On the other hand, a spiculated margin is highly predictive of malignancy. A lobulated margin suggests uneven growth and a likelihood of malignancy that lies between that of smooth and spiculated SPNs [90–92].

#### **Growth Rate**

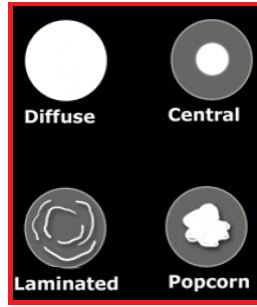
Growth of the SPN over time is another possible indicator of malignancy. Usually, volume of malignant solid nodules doubles in 20-400 days, with a majority doubling in less than 100 days. A doubling time higher than 400 days indicates slow growth, whereas a volume that doubles in less than 20 days indicates very rapid growth, usually due to infectious processes [93, 94].

#### **Cavity Wall Thickness**

Cavity wall thickness represents the presence of possible cavities inside the SPN. Cavitations can be found both in malignant and benign SPNs. However, a cavity wall thickness  $< 5$  mm points toward a benign etiology, whereas irregular cavities  $> 16$  mm are usually indicators of malignant lesions [95, 96].

### Calcification

Calcification refers to possible calcification present within the SPN. Specific patterns of calcification, such as diffuse, central, laminated or popcorn (see Figure 3.2) suggest a benign pattern. However, no specific pattern has been considered specific to malignancy [97].



**Figure 3.2:** Scheme of benign calcification patterns.

## 3.4 Literature Review

CAD systems for detection, segmentation and classification of pulmonary nodules may be of great help for the physician in order to decide whether to proceed with a biopsy test. A complete CAD system should be able to detect the nodule, classify it based on its location and connection to other structures, and ideally determine whether it is malignant or not. Despite significant progress in this area, it is difficult to find an optimal and widely used CAD scheme for lung nodule detection and classification. This is due to the great diversity in shape, size, intensity, etc., of pulmonary nodules. Moreover, connection to lung structures as well as possible noise patterns can greatly affect performance and robustness of CAD systems. Here, some of the methods proposed in the last decade are briefly introduced. Some algorithms focus only on the automatic detection of the nodule, while others are more concentrated on the segmentation of nodules. Many algorithms focus on classification of nodules, whereas there exists algorithms that try to combine all the aspects in order to develop an automatic CAD system. The final goal of the work begun in this chapter is the development of a complete CAD system for nodule classification and analysis. To this end, the presented method

### 3. SOLITARY PULMONARY NODULES MALIGNANCY

---

represents a first important step. Here some CAD systems proposed to date are first presented. This is helpful for future work toward the development of a complete CAD system. Next, some methods aiming at determining probability of malignancy of lung nodules and that are more related to the presented method, are introduced.

#### 3.4.1 CAD Methods

Okada et al [98] presented a semi-automated method able to segment both solid and non-solid lesions. Starting from a marker indicating the lesion location, the algorithm uses a model-based and multi-scale approach. In particular, nodules are approximated by ellipsoids using anisotropic Gaussian fitting. Then a volumetric measurement is accomplished from the volume of the ellipsoid. The method is promising especially for its ability to segment both solid and non-solid nodules, but it has a potential drawback in the case of nodules which are not elliptical.

De Nunzio et al [99] outlined a method for automatic detection of juxta-pleural pulmonary nodules. As a first step, the lung region is segmented and extracted exploiting the idea that in this segmented region, juxta-pleural nodules appear as small cavities. A surface of the segmented region is then obtained through triangularization, and a surface mapping algorithm is applied to map the segmented region to a sphere. High curvature regions are finally marked on the surface, indicating suspected pleural nodules.

In [100], Li et al outlined an algorithm for detection of pulmonary nodules. The key idea behind this method is the application of a multiscale selective nodule enhancement filter that enhances nodules and removes other anatomical structures, such as blood vessels and airways. After a first lung segmentation, the enhancement filter is applied to the segmented region and nodule candidates are segmented using a simple region growing approach. Several features of the segmented nodule are then extracted and an automated rule-based classifier is used to reduce the number of false positives.

Another approach for lung nodule detection is proposed by Ye et al [101]. This algorithm is meant for solid, part-solid, and non-solid nodules. First, the lung region is extracted. Then, local Gaussian and mean curvatures are used

to create a shape index map, whereas the eigenvalues of a Hessian matrix are exploited to create a “dot” map. This enhances objects having a specific shape with high spherical elements, and determines the initial nodule candidates. The candidates are then segmented by applying an adaptive thresholding and modified expectation-maximization methods. To reduce false positives, a rule-based filter followed by a weighted support vector machine (SVM) are finally employed.

Messay et al [102] presented a fully automated algorithm for detection of pulmonary nodules. The lungs are first extracted. Next, intensity thresholding and morphological process are combined to detect and segment nodules simultaneously. Finally, 245 features are extracted, and an optimal subset of features created to be used is a simple Fisher linear discriminant (FLD) classifier that detects nodules.

In [103], Farag et al try to determine the type of nodules (solitary, juxta-pleural, juxta-vascular, or with pleura-tail), using a scale invariant feature transform (SIFT) and an adaptation to Daugman’s Iris Recognition algorithm [104]. Kumar et al [105] presented a system that automatically detects and classifies lung nodules into malignant or benign. The algorithm is based on two main stages; in the first step, the image is pre-processed and the nodule region is segmented using a modified region growing method. Then, a fuzzy interference system (FIS) based on the area and brightness of the nodule region is used for the diagnosis.

Kuruvilla et al [106] presented a CAD system for lung nodule classification using artificial neural networks. Firstly, the entire lung is segmented and parameters, such as mean, standard deviation, skewness, kurtosis, fifth central moment and sixth central moment, are extracted and used for the classification. This is accomplished by using feed forward and feed forward back propagation neural networks.

Finally, Orozco et al [107] outlined a nodule classification method based on a different steps approach. First, a region of interest is extracted and a multiscale discrete wavelet transform (DWT) applied. Eleven features are then selected and combined in pairs and given as inputs to a support vector machine (SVM), which distinguishes CT images containing cancerous nodules.

### 3. SOLITARY PULMONARY NODULES MALIGNANCY

---

#### 3.4.2 Systems for Probability of Malignancy

Goal of the presented study was the development of a system for computation of probability of malignancy of lung cancer nodules. This system can be considered as a starting point for the future development of a complete CAD system. At present, only two previous studies aiming at automatically determine probability of malignancy of lung nodules have been found.

In [108], Way et al described a semi-automated system to classify benign and malignant lung nodules starting from a user-selected nodule location. First, a modified 3D active contour method is applied to segment the nodules. Then, morphological and gray-level features are extracted from the segmented image, and features from the texture around the nodule are derived using a rubber band straightening transform (RBST). The extracted features are finally used to determine malignancy of the nodule. This system showed an accuracy of 83% considering 96 lung nodules.

Anand et al [109] presented another method to predict malignancy. First, the image is filtered with a non-linear total varying denoising filter to remove random noise, and the lung region is extracted. Then, the nodules are segmented with a region growing approach and textural and geometrical features are extracted. These features are the input of a back propagation neural network classifier which determines whether the nodule is malignant or benign. The system shows an accuracy of 86.3%, but it has been tested using only 2D jpeg CT images.

In this research, a novel algorithm to automatically extract nodules characteristics to determine nodule's malignancy was developed. Characteristics to be extracted have been chosen based on the work of Gurney et al [38,39]. Gurney's method requires visual analysis of the nodule, to extract nodule characteristics which then need to be manually specified to compute nodule's malignancy. This is a long and tedious work and has a high risk of wrong analysis and diagnosis.

The main requirement for the implementation of the algorithm is the limited user interaction. For this reason, the idea is to exploit Gurney's method high reliability, while removing visual inspection of the nodule and reducing manual interaction as much as possible.



## 3.5 Algorithm Implementation

### 3.5.1 Overview

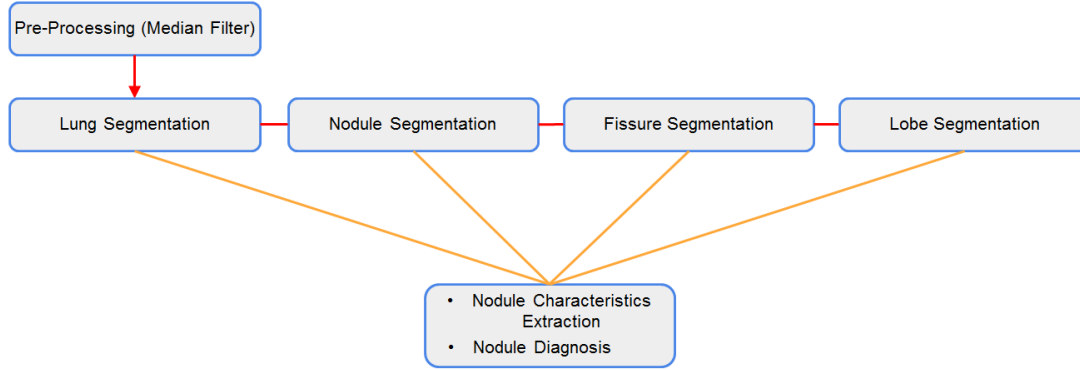
This section describes the algorithm which was implemented for determining the likelihood of SPN nodule malignancy. The idea underlying the proposed method comes from the availability of calculators of probability of malignancy which require the physician to manually specify clinical characteristics of the patient and the nodule's characteristics to compute malignancy [38,39,90,110]. Manual interaction and accuracy of the methods might be improved if nodule's characteristics can be automatically determined. The method proposed by Gurney et al. [38,39] proved one of the most reliable and was used as a base for the development of the proposed approach. The work presented here represents an important starting point for the development of a complete system which is able to automatically identify, classify and diagnose suspect lung nodules.

The system has a modular structure, described in subsequent sections, with four sub-algorithms that help automatically determine the characteristics of the nodule under inspection. Lung segmentation is the first step and helps to exclude unwanted structures from the analysis and to identify the location of the nodule; a nodule segmentation is then implemented to extract size, shape, wall thickness, and calcification presence; lung fissures are then identified by means of a lung fissure segmentation module; finally, starting from the identified fissure, the lobes are segmented by using a lobe segmentation method (as described in Section 3.5.5.1). These modules are joined together by a Python interface that requires the user to input a few clinical details of the patient and to specify with a simple mouse click the location of the nodule to analyse.

The module returns a probability of malignancy of the SPN. Figure 3.3 shows a scheme representing the algorithms involved in the nodule diagnosis extension while Table 3.1 illustrates the different modules and their main functions. Although mainly meant for SPNs, the proposed method is not strictly restricted to this type of nodule. The power of the modular structure of the system is that the separate sub-algorithms can also be used independently in different applications.

### 3. SOLITARY PULMONARY NODULES MALIGNANCY

The following sections detail the four different sub-algorithms and the Python interface that represent the complete system.



**Figure 3.3:** Modularity scheme of nodule diagnosis extension. The different tools are executed individually.

Method	Functionality
Lung Segmentation	Identify and separate lungs from surrounding structures and background air
Nodule Segmentation	Segment selected nodule and extract nodule characteristics
Lung Fissures Segmentation	Identify and segment lung fissure from the other structures of the lung region
Lung Lobe Segmentation	Separate the lung label map according to the main lung lobes
Python Interface	Execute the previous methods and determine probability of malignancy

**Table 3.1:** List of the single algorithms composing the method to determine probability of malignancy.

#### 3.5.2 Lung Segmentation

Lung segmentation consists in separating the lungs parenchyma from the surrounding tissues and thorax. Thanks to the ability to select and extrapolate the

lung tissue in chest CT images, lung segmentation has become a fundamental step in several CAD systems. In fact, having a system that automatically identifies the lung region helps to reduce computational time, as subsequent operations are restricted to this region and not to the whole volume, thus reducing the number of false positives. For this reason, systems having lung segmentation as a first step include nodule detection and segmentation algorithms [102], lung parenchyma density analysis [111], airways analysis [112], emphysema analysis [113], lung fissures detection [114], and so forth. Methods usually use a thresholding process as a first segmentation step, followed by different strategies to separate the two lungs, when necessary. Here, some of the works related to lung segmentation are briefly introduced. Implementation of the proposed method is then detailed.

### 3.5.2.1 Related Work

A large amount of research has been done in the field of lung segmentation, and a variety of methods for automatic segmentation using different strategies is currently available.

Hu et al [115] proposed a method based on three main steps. First, an optimal threshold is automatically detected and gray-level thresholding is applied. Then, anterior and posterior junctions between left and right lungs are identified on 2D axial slices and the two lungs separated. Finally, morphological operations are applied to smooth irregular boundaries. The innovative part of this work is the automatic detection of an optimal threshold to define the initial lung region. Although efficient, this technique is quite slow (23 min required to segment a 512X512X120 data set), making it not an optimal approach as a first step for other segmentation techniques (as in the case of nodule segmentation).

Leader et al [116] presented a method that removes background pixels through an image pre-processing operation, followed by a thresholding to identify the lung tissue. Finally, the initial segmented region is refined to prune incorrectly detected airways and separate fused right and left lungs. Although this approach provides flexibility, its robustness in terms of processing CT scan of other types of lung diseases remains to be determined.

### 3. SOLITARY PULMONARY NODULES MALIGNANCY

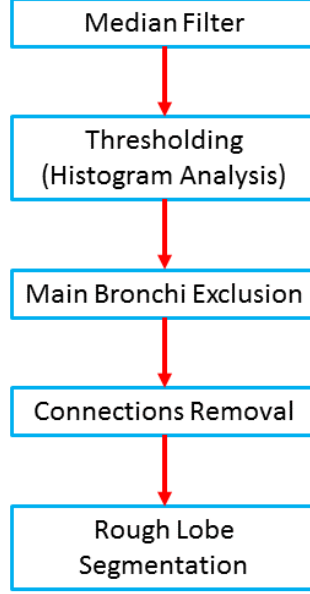
---

In their method for nodule detection, Li et al [100] implemented a lung segmentation method that first employs an interpolation technique to have size of voxels equal to 1 mm in all three dimensions. Then, a thresholding strategy that considers all the pixels between -1000 HU and - 400 HU as part of the lung region is applied. Finally, all points of the contour are checked in a clockwise fashion to close the lung region and include nodules connected to the pleura. The main drawback of this approach is the selection of a fixed threshold, that may leave out some pixels belonging to the lung. At the same time, the approach is not required to be optimal for lung segmentation as used as a first step of a nodule detection algorithm.

Yee et al [101] also utilized a lung segmentation process as a first step to a nodules detection method. This approach is based on two main steps. First, a 3D adaptive fuzzy thresholding that chooses a threshold from histogram analysis is used to obtain the segmentation. Then, a 2D post-refinement of the lung contour is applied to obtain the final mask. Although in a slightly different implementation, the idea of analysing the image histogram to determine the initial threshold for lung segmentation is exploited in the presented work. However, a different approach is used to accomplish the following refinement.

Van Rikxoort et al [117] outlined a hybrid method that combines a first conventional lung segmentation based on [115], an automatic error detection method (based on comparison with a set of statistics of correct lung segmentations and a shape consistency check), and a more sophisticated algorithm, based on multi-atlas segmentation. This method requires a seed point to start lung segmentation, while the final multi-atlas segmentation requires training of the algorithm with manually segmented images. Therefore, this approach cannot be used as first step of (semi-)automatic nodule segmentation.

Park et al [118] introduced a method for the separation of right and left lungs. The lungs are first segmented using a 2D based adaptive segmentation method and a 3D based region growing process. Then, the lungs are separated with a three-step strategy that detects connected areas in 2D slices, separates them using a guided dynamic programming process and finally classifies the two separated regions into left or right lung. This method proved efficient and reliable and was used as a basis for the presented method.



**Figure 3.4:** Block diagram of the different steps involved in lung segmentation.

In their CAD system for pulmonary nodule detection, Messay et al [102] use a method for lung segmentation based on [115] and [116]. However, they use a fixed threshold (-500 HU) combined with some morphological and topological analysis to produce the preliminary segmentation of the lung region.

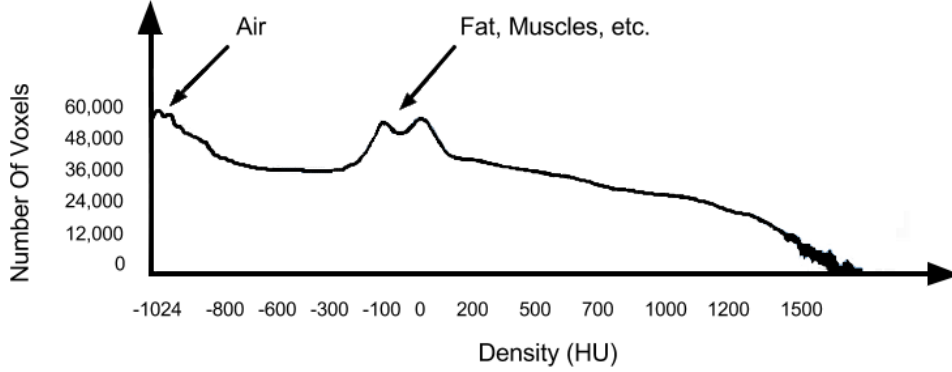
Finally, Korfiatis et al [119] introduced a method that employs a first 3D thresholding that uses a minimum error technique. This is combined with a wavelet pre-processing step to deal with the lung boundary challenges, such as anterior or posterior junction lines and juxta-pleural nodules. A 3D morphological closing is finally applied to refine segmentation. The processing time required by this method to segment a scan consisting of 50 slices is approximately 3 min. This makes this approach not optimal as a starting point for nodule segmentation.

### 3.5.2.2 Algorithm Description

The algorithm proposed here implemented and combined different commonly used techniques for lung segmentation. Figure 3.4 shows the different steps that are executed sequentially to obtain the final lung segmentation. A pre-processing operation to remove noise is followed by a thresholding operation to extract the

### 3. SOLITARY PULMONARY NODULES MALIGNANCY

---



**Figure 3.5:** Typical histogram of a chest CT image (size  $512 \times 512 \times 480$ ).

first region of the lungs. Then, the main bronchi are extracted and removed from the label, and the 2D axial slices of the lungs label are analysed in case of possible connection of the two lungs. The last step consists in a morphological closing to include nodules within the final segmentation. Each of these steps is described in detail in the following paragraphs.

#### Lung Extraction

The goal of this step is to separate the voxels corresponding to lung tissue from the surrounding voxels belonging to other anatomical structures or to the air surrounding the whole patient. To remove random noise from the image, a pre-processing step is executed. Therefore, a median filter with a  $3 \times 3 \times 3$  kernel is used. Then, the first step toward the lung extraction process involves a binarization process by means of a thresholding segmentation. Instead of using a fixed threshold for each case, a method that selects an optimal threshold for each single case is here proposed.

This approach takes into account possible variations in intensity values across different subjects. To this end, the image histogram is automatically analysed, starting from the idea presented in [101]. As shown in Figure 3.5, the histogram of a CT image presents two main peaks; the first one is usually around -1024 HU and represents the air voxels; the second peak is due to fat, muscles, vascular tree, and other structures of the lung with higher HU values. For this reason, a mean

value of these two peaks is selected as an optimal threshold for the binarization process.

All the values between -1024 HU and the determined threshold are given a value of 1, while all the others are set to 0. However, the lungs are surrounded by background air, which is included in the first binarization along with possible air in other anatomical structures, such as the bowel. These parts need to be removed from the segmented lungs. For this purpose, a connected component label is used to identify the lung voxels, and the regions that are connected to the border of the image, as well as small disconnected regions, are discarded.

Since lung segmentation is often used for analysis in which it is important to distinguish the two lungs, these have to be labelled separately. To this end, the next step in lung extraction involves using the trachea segmentation method described in Chapter 3. First, the trachea location is searched in one of the first axial slices of the binarized image as the region with minimum diameter and maximum roundness. This is used as the seed point for the region growing process that segments the trachea. The obtained label is then dilated and inverted using a pixel-wise NOT operation, and a pixel-wise AND operation is executed between the lung and the inverted trachea images. This way, the trachea and the main bronchi are discarded. In some cases this operation guarantees that the right and left lungs are separated. However, in many cases the two lungs result still connected and require a further operation for separation.

#### **Right and Left Lung Separation**

As shown in Figure 3.6(a), when viewed on axial slices, the right and left lungs may have a very thin separation in the anterior and posterior junctions. This may result in very low contrast separation between the two lungs, which causes the lung extraction operation to segment the two lungs as one (see Figure 3.6(b)). Therefore, these connection lines have to be identified and the two lungs separated.

Following the concept proposed in [118], a 2D axial search is executed to find the connection points. In particular, the idea behind the technique relies on the fact that, on two adjacent axial images, the lung regions are similar in size and shape. Hence, when the current slice is detected to contain connected lungs, the

### 3. SOLITARY PULMONARY NODULES MALIGNANCY

---

closest point between the two lungs in the previous image can be searched and used as the point in which connection is most likely.

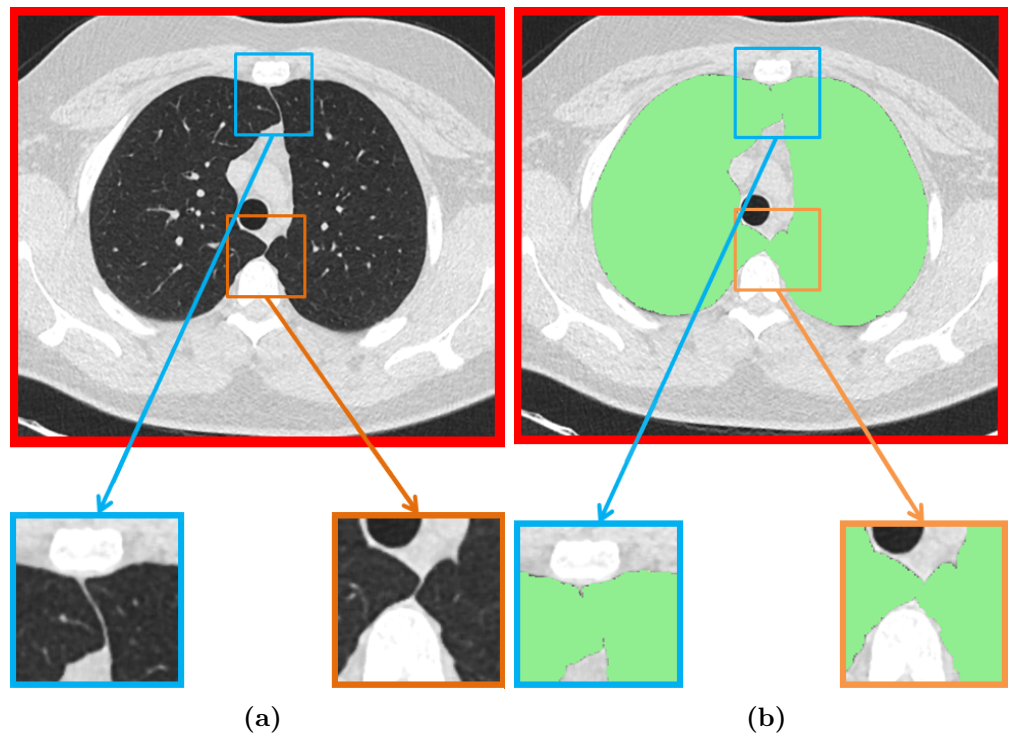
The connection point is identified by first extracting the boundaries of the two lungs. Then, moving pixel by pixel in the horizontal  $x$  direction on the axial slice (see Figure 4.8), when any pixel belonging to the boundary of one lung faces a pixel belonging to the boundary of the opposite lung, the distance between the two pixels is computed. This operation is executed for every line of pixels and the position of the mean point between the closest opposite pixels is considered. This position is used as the central point of a region of  $50 \times 80 \times 1$  pixels, which is extracted from the current image in order to remove the connection; first, an erosion process is iteratively applied to the region, with a spherical structuring element that begins with a size of  $7 \times 7 \times 1$  pixels and that increases by 2 pixels (along  $x$  and  $y$ ) until the two regions are separated. This operation is followed by dilation of the two separated labels, with a spherical structuring element of the same size as the one used for the erosion. This dilates the two labels without re-connecting them.

The region with the two separated labels is finally pasted onto the original lung slice. A second control is here executed to make sure that the two lungs are effectively separated. In fact, in some cases, a connection may appear both on the anterior and the posterior part of the lung (as shown in Figure 3.6). If this is the case, the same operations are executed again, excluding the region just separated. This way, the “new” minimum distance between the two labels is considered, and the process is repeated.

#### **Rough Lobes Subdivision**

Once the two lungs have been segmented and separated, a final morphological 2D closing operation is applied to close holes within the lung labels. Then, a rough operation of subdivision is applied to the label. This is helpful for possible future operations of lobe segmentation (see 3.5.5.1). First, a connected component labeling is used to give the two lungs a different label value and classify them as right or left lungs. Assuming that the scan is supine, head-first, the component value corresponding to the smallest  $x$  index will be the left lung and the other major component will be the right lung. If this is not the case, the image is

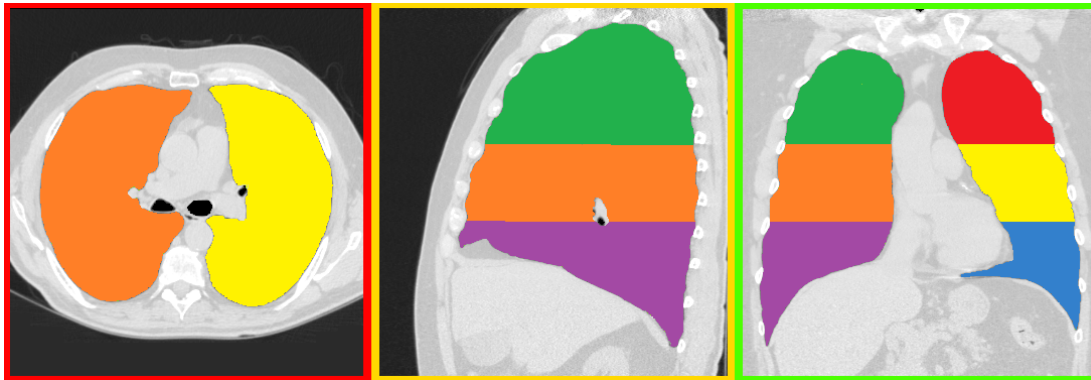




**Figure 3.6:** An example of thin lung separation in the anterior and posterior junctions. a) Shows the anterior (blue square) and posterior (orange square) junctions on a axial CT image. In b) the result after lung segmentation (green) of the same image is presented. As shown, when the junctions are thin, segmentation might consider the two lungs as one.

### 3. SOLITARY PULMONARY NODULES MALIGNANCY

---



**Figure 3.7:** Example of lung label map as roughly divided into thirds.

first flipped, and the same operation computed. At this point, the two labels are divided into thirds and a different label value is assigned to each third, according to the CIP convention (see 3.5.5.1). Figure 3.7 shows an example of the lung label map divided into thirds.

#### 3.5.3 Nodule Segmentation

Nodule segmentation represents the most important step towards the creation of a CAD system for nodule classification and diagnosis. Segmentation allows for recognition of nodules and for extraction of characteristics that can be used as indicators of malignancy. Nodule size is an important feature to be considered in nodule volumetric analysis [120], but other characteristics, such as edge shape, cavity wall thickness, and calcification may be very important [38,39]. Due to their importance, several methods for nodule segmentation have been proposed in recent years for nodule segmentation. Usually, these methods are introduced as part of more complex CAD system for nodule classification. Many methods ask the radiologist to select the nodule to analyse, while other methods try to automatically identify the nodules. However, pulmonary nodule segmentation is still a major challenge in medical imaging, due to the variety of nodules and CT image quality. Here, some of the methods developed to date are introduced. The propose method is then described in detail.

### 3.5.3.1 Related Work

Many different techniques and strategies have been proposed for pulmonary nodule segmentation.

Zhao et al [121] proposed a system that uses density and morphology to segment small nodules. An optimal threshold to separate the nodule from its surroundings using a surface gradient applied to the nodule candidates, detected at different thresholds, is determined. Then, morphological operators are used to remove vessels. The method has been validated using only 12 pulmonary nodules. Also, the choice of an appropriate threshold level step is quite complicated and often requires post-processing operations to help disconnect structures connected to the nodule.

Xu et al [122] introduced a method that works on a slice-per-slice basis to first extract 2D contours of the nodule using a dynamic programming-based algorithm that starts from a circle drawn around a user-specified point. An Expectation Maximization process is then implemented to classify and remove calcification. The main drawback of the system is the necessity of a pre-processing operation to grow a circle on each 2D slice around the user-selected nodule. This operation requires about 5 seconds per slice, making the algorithm computationally expensive.

In [123], Mullally et al extended the method described in [121] by automatically selecting the region of interest containing the nodule. Based on their attenuation levels, the regions were extracted and segmented, even when nodules were composed partially or completely of other structures. However, the task of identifying the nodules among the segmented objects has to be performed manually, increasing the risk of false positives.

Okada et al [98] focus on volumetrical and geometrical characterization of the nodules based on a model-based approach. The model is chosen as an anisotropic (non spherical) Gaussian function, which is more flexible than a spherical one. Through a multiscale analysis, a set of mean and covariance estimates are extracted and a Jensen-Shannon divergence is evaluated over multiple scales to choose the best fit for the corresponding scale-space image. The main issue of this approach is a bias due to an ellipsoidal approximation of the nodule which

### 3. SOLITARY PULMONARY NODULES MALIGNANCY

---

limits the segmentation to approximation of true tumour boundary and can be biased when the tumour possesses an irregular surface.

Diciotti et al [124] proposed a semi-automatic segmentation algorithm for solitary and juxta-vascular nodules. A volume of interest (VOI) around a nodule candidate selected by the user is first extracted. Then, a multi-scale approach is used within this VOI to detect blob-like structures, which represent nodule candidates. At this point the user is asked to select, for each candidate, whether it represents a nodule, a surrounding pulmonary structure, or an object to discard. Finally, a region growing approach based on a geodesic distance is used to segment the nodules. This method requires great manual interaction to classify all candidates in the VOI. Since goal of the research was to keep manual interaction as low as possible, this method was found not appropriate for nodule segmentation.

Dehmeshki et al [125] presented a method for segmenting different types of nodules using two different region growing approaches; fuzzy connectivity and contrast based region growing. In particular, starting from a seed point on the nodule specified by the user, a local adaptive segmentation is exploited to identify the nodule region. Then, a fuzzy connectivity map is constructed by applying fuzzy connectivity region growing, and this map is used for a sphericity-oriented contrast based region growing to get the final segmentation.

Li et al [100] proposed a method that starts from an image enhanced by means of a multi-scale filter. This helps identify nodule candidates, and for each of them an iterative region growing technique that uses the mean and standard deviation of the CT values as an inclusion criteria is performed. In the presented research, Li's method has been modified to apply the multi-scale approach only in a region of interest surrounding the user-selected nodule. This way, false positive are drastically reduced, as is computational complexity.

Ye et al [101] proposed a combination of adaptive thresholding and a modified expectation-maximization (MEM) algorithm to segment the nodules. The former determines a first coarse segmentation that is then refined with the latter considering the nodules' neighbouring intensities. The main issue of this method is that nodules could be missed if they do not include local spherical elements

or if the sizes of the elements are too small. Also, noisy images might lead to inaccurate calculation of the local shape feature.

Chen et al [126] presented a method to separate blood vessels and nodules by using Hessian matrix based line structure enhancement (LSE) and blob-like structure enhancement (BSE) filters across multiple scales. The segmentation is then performed by a front surface propagation (FSP) procedure based on a fast marching method. This method is meant for juxta-vascular nodules, while the method here described focuses on solitary pulmonary nodules.

Tan et al [127] proposed a method for segmentation of lung nodules that combines marker-controlled watershed, geometric active contours, and Markov random field (MRF) methods in a region of interest selected by the user. A preliminary segmentation is accomplished by the watershed algorithm. Then, the active contour evolution method refines the segmentation, that, in case of part- or non-solid nodules, is followed by a MRF and morphological closing operations to obtain the final segmentation. However, the applied active contours method is a local optimization method that is sensitive to the initial contour. When the watershed surface is far from the lesion boundary, the active contour is often attracted by local minimums rather than lesion boundary.

Farag et al [128] outlined an automatic algorithm that uses a variational level set approach to model the nodule image information. Next, an ellipse model represented by a signed distance map is considered and evolved to include the nodule core. This method is affected by the choice of the initialization parameters to construct the initial prior shape model. This initialization is currently executed manually.

Qiang et al [129] presented a two stage method; in the first step a freehand sketching (performed in 2D imaging slices) analysis is performed to infer information of the nodule (e.g., mass centre, density, and size); as a second step, a principal curvature analysis is used with a convex constraint to segment the nodule. The use of a freehand sketching, which requires great user interaction makes this method not appropriate for the approach presented.

Finally, Tsou et al [130] introduced an anatomy packing with hierarchical segments (APHS) method for segmentation of pulmonary nodule segmentation. The algorithm consists of two main steps; a first hierarchical segmentation tree

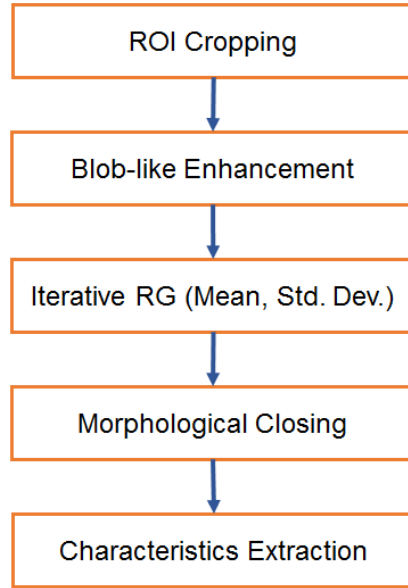
### 3. SOLITARY PULMONARY NODULES MALIGNANCY

---

(HST) construction is followed by anatomy packing that localizes individual object instances by optimizing the hierarchy conditional random field (CRF) model based on the HST. Two main aspects of this approach still need to be considered; automation of the initialization process and 3D volume measurements.

#### 3.5.3.2 Algorithm Description

As the lung segmentation module, the nodule segmentation algorithm consists in different steps that are executed sequentially and that combines different techniques available in the literature. The steps composing the algorithm are shown in Figure 3.8. First, the user is required to place a seed point to indicate the



**Figure 3.8:** Steps involved in nodule segmentation. RG stands for region growing, where ROI is the region of interest.

nodule to analyse. For this reason, the method is referred to as semi-automatic. The region around the selected point is cropped from the original image and this region is used for the following analysis. The analysis starts by enhancing the blob-like structures inside the region and then separating candidate nodule from the other anatomical structures. Then, a method similar to [100] is performed to exploit mean and standard deviation as inclusion criteria for a region growing

process. This method was chosen for its proved reliability and reproducibility, as well as for the little user interaction required. Finally, a closing operation is implemented to remove possible small holes in the label. Once the segmentation is completed, nodule characteristics are extracted. In particular, nodule size, cavity wall thickness, boundary shape, and calcification are evaluated. Here, the different steps involved in the method are outlined.

#### **Region Extraction**

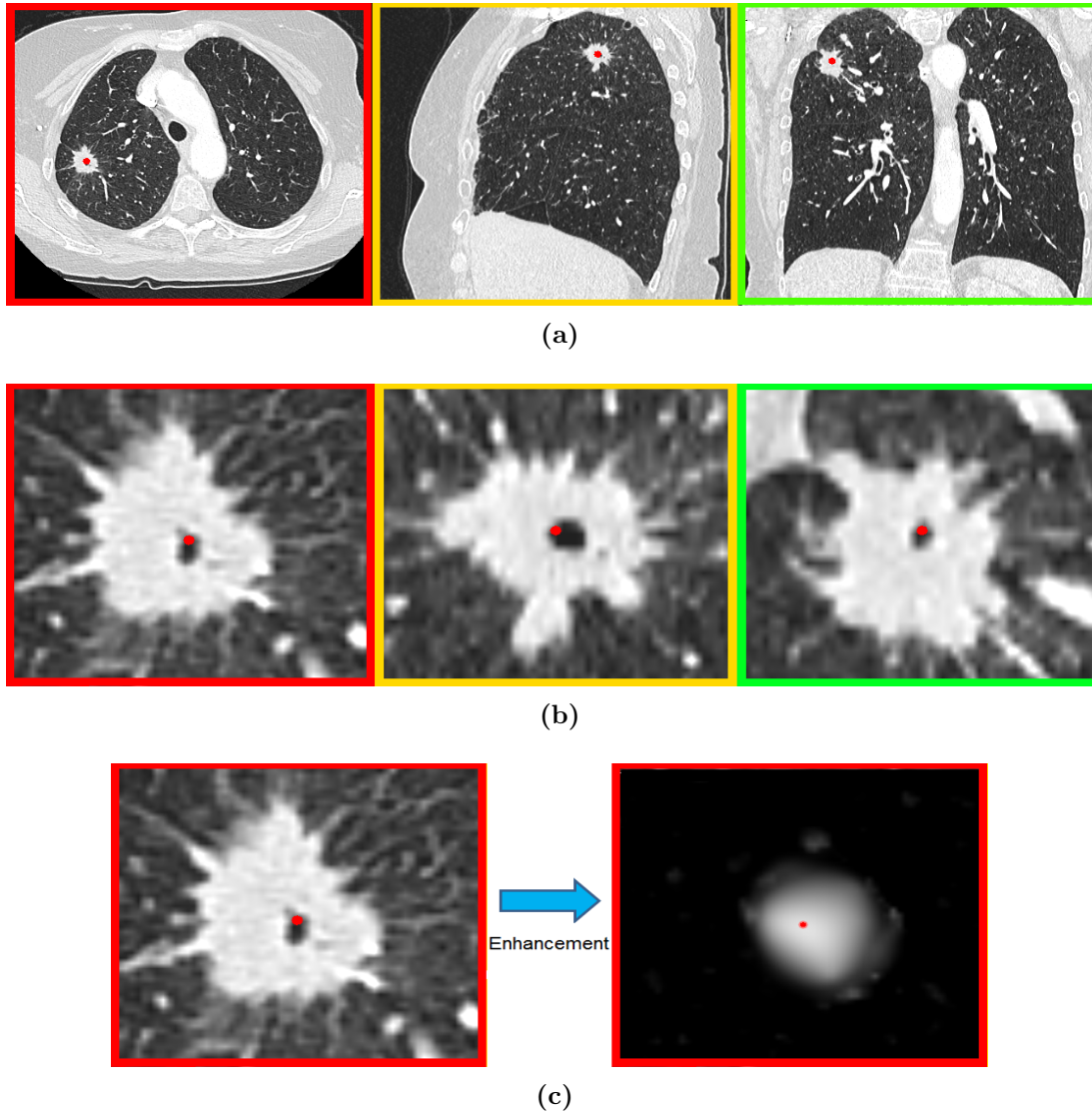
The first step of the algorithm involves the extraction of the lung region, to exclude the thorax and background air from the analysis. To this end a masking operation that sets the non-lung structures to -1024 HU (which is lower than nodule intensity values) is employed. Then, a cropping of the original CT image around the nodule selected by the user is completed. This will help to drastically decrease computational costs for nodule segmentation, and will reduce the risk of false positives. Pulmonary nodules are invariably smaller than 3 cm. Therefore, starting from the user specified point, a cubic region of  $4 \times 4 \times 4$  cm is cropped from the original CT image. This ensures that the whole nodule under inspection will be included in the segmentation. Figures 3.9(a,b) show an example of a region cropped around the user-selected nodule.

#### **Blob-like Structure Enhancement**

Once the region is extracted, structures having a blob-like shape are enhanced following the method introduced by Li et al [131]. In fact, it is easier to identify the nodule in the nodule-enhanced image than in the original image. Enhancement filters are usually used to enhance objects with a plate-like, a blob-like, or a tube-like structure in radiographs and CT images. These filters examine the multiscale second order structure of the image, called Hessian, to analyse the local behavior of the image, enhance the different objects, remove noise and background. It can be viewed as a pre-processing step for medical imaging methods. A common example of a filter of this type is the vessels enhancement filter, described for the first time by Frangi et al [132], that allows for enhancement of vessels in medical images. The idea behind the enhancement filter is to exploit the gray-scale curvature information of the different objects. These curvatures

### 3. SOLITARY PULMONARY NODULES MALIGNANCY

---



**Figure 3.9:** Example of region of interest extraction and enhancement. a) The nodule is selected by the user on the CT image (red point). b) A region of  $4 \times 4 \times 4$  cm including the whole nodule is extracted. c) The extracted region is enhanced using a blob-like multiscale enhancement.



are determined using the eigenvalues of the Hessian matrix. When analysing the local behavior of an image,  $f(\mathbf{x})$ , a common approach is to consider the second order Taylor expansion of  $f(\mathbf{x})$  about a point  $\mathbf{x} = \mathbf{x}_0 = (x_0, y_0, z_0)$ :

$$f(\mathbf{x}) \approx f(\mathbf{x}_0) + \Delta f|_{\mathbf{x}_0}(\mathbf{x} - \mathbf{x}_0) + \frac{1}{2}H(f)|_{\mathbf{x}_0}(\mathbf{x} - \mathbf{x}_0)^2 \quad (3.1)$$

where  $\Delta f|_{\mathbf{x}_0}$  represents the gradient vector of the image computed at  $\mathbf{x}_0$  and given by (3.2):

$$\Delta f = \begin{bmatrix} \frac{\partial f}{\partial x} & \frac{\partial f}{\partial y} & \frac{\partial f}{\partial z} \end{bmatrix} \quad (3.2)$$

while  $H(f)|_{\mathbf{x}_0}$  is the Hessian matrix of the image computed at  $\mathbf{x}_0$  for the six (for 3D images) independent second order derivatives:

$$H(f) = \begin{bmatrix} \frac{\partial^2 f}{\partial x^2} & \frac{\partial^2 f}{\partial x \partial y} & \frac{\partial^2 f}{\partial x \partial z} \\ \frac{\partial^2 f}{\partial y \partial x} & \frac{\partial^2 f}{\partial y^2} & \frac{\partial^2 f}{\partial y \partial z} \\ \frac{\partial^2 f}{\partial z \partial x} & \frac{\partial^2 f}{\partial z \partial y} & \frac{\partial^2 f}{\partial z^2} \end{bmatrix} = \begin{bmatrix} L_{xx} & L_{xy} & L_{xz} \\ L_{yx} & L_{yy} & L_{yz} \\ L_{zx} & L_{zy} & L_{zz} \end{bmatrix} \quad (3.3)$$

Another important aspect to consider is that objects may have different sizes on an image. For this reason, a measurement scale which varies within a certain range can be considered for a multiscale analysis. This way, the differentials are computed at all the different scales and the maximum response is usually considered. Therefore, using the concepts of linear scale space theory [133, 134], differentiation is defined as a convolution with derivatives of Gaussian kernels:

$$\frac{\partial}{\partial x} f(\mathbf{x}, \sigma) = s^\gamma f(\mathbf{x}) * \frac{\partial}{\partial x} G(\mathbf{x}, \sigma) \quad (3.4)$$

where  $\sigma$  is the scale level, and  $\gamma$  is used to define a family of normalized derivatives [135]. The Gaussian function (with mean  $\mu = 0$ ) is defined by (3.5).

$$G(\mathbf{x}, \sigma) = \frac{1}{\sigma \sqrt{2\pi}} e^{-\frac{\|\mathbf{x}\|^2}{2\sigma^2}} \quad (3.5)$$

The second derivative of the Gaussian kernel at a scale  $\sigma$  generates a new kernel that measures the contrast between the two regions (inside and outside) determined by the range  $[-\sigma, \sigma]$  in the direction of the derivative. This justifies the use of the Hessian matrix in the multiscale enhancement filters. The eigenvalue analysis of the Hessian is performed by extracting the principal directions in which the local second order structure of the image can be decomposed. If  $\lambda_k$  represents

### 3. SOLITARY PULMONARY NODULES MALIGNANCY

$\lambda_0$	$\lambda_1$	$\lambda_2$	Structure
Low	Low	Low	No noticeable structure
Low	Low	High (Neg)	Plate-like structure (bright)
Low	Low	High (Pos)	Plate-like structure (dark)
Low	High (Neg)	High (Neg)	Tube-like structure (bright)
Low	High (Pos)	High (Pos)	Tube-like structure (dark)
High (Neg)	High (Neg)	High (Neg)	Blob-like structure (bright)
High (Pos)	High (Pos)	High (Pos)	Blob-like structure (dark)

**Table 3.2:** Possible structures enhancement based on the Hessian eigenvalues  $\lambda_0$ . Neg/Pos indicates if the eigenvalue has a negative or positive value.

the eigenvalue of  $k^{\text{th}}$  normalized eigenvector,  $\hat{\mathbf{u}}_k$ , of the Hessian  $H_0$  (computed at  $\mathbf{x}_0$ ), from the definition of eigenvalues come (3.6) and (3.7).

$$H_0 \hat{\mathbf{u}}_k = \lambda_k \hat{\mathbf{u}}_k \quad (3.6)$$

$$\hat{\mathbf{u}}_k^T H_0 \hat{\mathbf{u}}_k = \lambda_k \quad (3.7)$$

From (3.7), it is clear that the eigenvalue decomposition extracts three orthonormal directions which are invariant to a scaling factor when mapped by the Hessian matrix. Therefore, different filters can be constructed based on the curvature characteristics (or eigenvalue) of the objects that have to be enhanced. Considering the relation  $|\lambda_0| \leq |\lambda_1| \leq |\lambda_2|$ , Table 3.2 reports the relations between the eigenvalues of the Hessian to be considered when different structures are to be detected (the sign is an indicator of brightness/darkness). The singular directions of the structures are represented by the respective eigenvectors:  $\hat{\mathbf{u}}_0$  indicates the direction with minimum intensity variation, while  $\hat{\mathbf{u}}_1$  and  $\hat{\mathbf{u}}_2$  form a base for the orthogonal plane. As an example, ideally a tubular object has a low eigenvalue in the parallel direction, and two strong eigenvalues in the direction perpendicular to the object. Based on this idea, various filters have been proposed for enhancement of different structures. In the proposed approach, the multi-scale Hessian-based nodule enhancement filter as described by Li et al [131] is implemented. Li's filter

is described by (3.8).

$$\varphi(\lambda_0, \lambda_1, \lambda_2) = \begin{cases} \frac{|\lambda_1|^2}{|\lambda_3|} & \text{if } \lambda_0, \lambda_1, \lambda_2 < 0 \\ 0 & \text{otherwise} \end{cases} \quad (3.8)$$

This filter is executed for each pixel at every specified scale,  $\sigma$ , and for each pixel the final output  $S$  is the maximum value from the single output at each scale, as in (3.9).

$$S = \arg \max_{\sigma} (\varphi_{\sigma}(\lambda_0, \lambda_1, \lambda_2)) \quad (3.9)$$

The number of scales and the range  $[-\sigma, \sigma]$  are determined empirically.  $N = 5$  scales, with a range of values  $[1, 6]$  was empirically found as adequate for nodule-structures enhancement. Figure 3.9(c) shows an example of a nodule in a region, cropped as describe above, enhanced using the Hessian-based nodule enhancement filter just described.

#### Region Growing Segmentation

As shown in Figure 3.9(c), the multi-scale enhancement process may enhance other round structures that can be found in the region and that usually belong to vessels or airways. For this reason, initial thresholding of the enhanced region is used, with a threshold of 40 (as described in [100]) to separate the nodule from other anatomical structures. Then, a 3D connected component filter is used to maintain only objects with a Feret diameter  $> 1$  [136] and closest to the placed seed point. The remaining object is considered as the nodule candidate.

As shown in Figure 3.9(c), the nodules in the enhanced region appear smaller than in the original image. Therefore, an iterative region growing technique, similar to that described in [100], is employed for each nodule candidate.

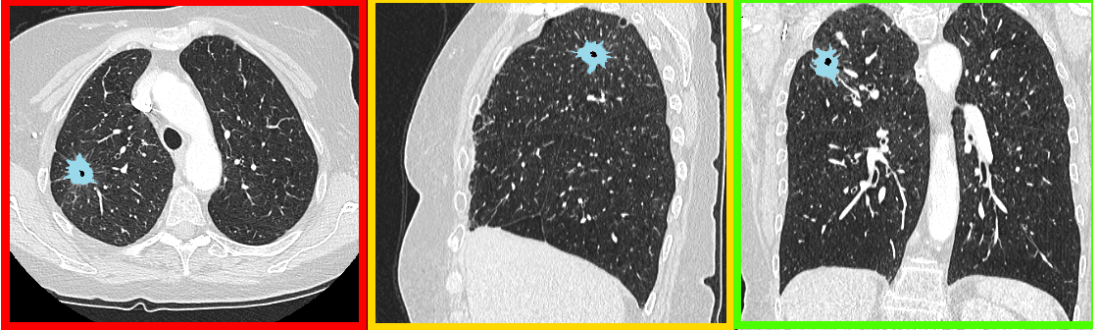
First, an operation to exclude all the voxels with an intensity lower than -500 HU (likely to belong to air) is employed. This ensures that possible cavities within the nodule are not included into the segmented region. To this end, initial thresholding is used, followed by a pixel-wise AND operation with the object region. Then, the mean and standard deviation of CT values for voxels of the original cropped region and those belonging to the enhanced objects are calculated. Next, a region growing approach using the seed point placed by the user as a starting point, and the mean  $\mu$  and standard deviation  $\sigma$  as inclusion

### 3. SOLITARY PULMONARY NODULES MALIGNANCY

---

criteria is completed. In particular, voxels are added to the segmented region if their CT values are within the range  $[\mu - 2\sigma, \mu + 2\sigma]$ .

At this point,  $\mu$  and  $\sigma$  in the new region are computed and the same process is repeated for a maximum of 10 iterations or until  $(\mu - 2\sigma > -300)$  and  $(\mu + 2\sigma < 250)$ . These two values have been empirically validated. Finally, a closing operation with a spherical structuring element with a  $3 \times 3 \times 3$  pixel volume is employed to remove small holes. Figure 3.10 shows an example of the segmented nodule starting from a chest CT image.



**Figure 3.10:** Example of nodule segmentation results. On the three CT views, the nodule label is represented in light blue and is imposed on the nodule. As shown, the cavity of the nodule is preserved (axial view). The CT image is the same as in Figure 3.9

#### Characteristics Extraction

Once the segmentation process is completed, the characteristics related to the nodule label (size, edge smoothness, cavity wall thickness, and calcification presence) are extracted. The size is computed as the label equivalent radius of the label, whereas the edge smoothness is determined by the label roundness. To calculate cavity wall thickness, holes within the nodule label are searched. Then, the minimum euclidean distance between the nodule boundary and the holes boundary is considered. To determine the presence of benign calcification within the nodule, the concept that calcification will appear as a bright region inside the nodule [137] is considered. For this reason, voxels with an intensity value higher than  $(\mu + \sigma)$  or higher than 50 HU (belonging to solid structures) are identified. This approach follows the idea from [131]. Then, to discriminate whether

the calcification has a benign pattern the number of calcification objects, their roundness, and their position is computed. This will allow to determine if the calcification has a diffuse, central, laminated, or a popcorn pattern. The computed characteristics are finally made available to the user.

### 3.5.4 Lung Fissures Segmentation

Nodule segmentation allows for the extraction of some important characteristics of the lesion under analysis. Another important feature that has to be taken into account in the process of determining whether a nodule is malignant is its location. Therefore, it is important to discriminate whether the nodule is located in the upper/middle lobe of the lung, or in the lower lobe. As described in Section 3.5.5.1, a method for lobe segmentation is part of the CIP classes. However, this method requires the user to manually select the lobe fissures, placing various seed points on each one. This may result in a very long and tedious process. For this reason, a method to automatically identify and segment the fissures may be considered as a first and very important step towards lobe segmentation. Before describing the algorithm, some of the methods for fissure recognition and segmentation that have been developed to date are here introduced.

#### 3.5.4.1 Previous Work

Lung fissures recognition for lobe segmentation has been the subject of many studies in recent years, but still remains a big challenge. This is due to the fact that fissures may not always be visible on CT images or pathological abnormalities may affect the composition of the fissures.

To overcome these issues, in their method for lobe segmentation Kuhnigk et al [138] proposed to exploit the structural knowledge of the lung anatomy and consider the fact that no vascularity is present at fissures. Therefore, vessel segmentation is first completed and the Euclidean distance from the vessels is used to enhance areas which show an absence of larger vessels. This information is then used for subsequent lobe segmentation, but the work focused on enhancing the fissures, rather than identifying them.

### 3. SOLITARY PULMONARY NODULES MALIGNANCY

---

Wiemker et al [139] compared the use of two different 3D filters to enhance plate-like structures that represent lung fissures on CT images; the first one exploits the first derivatives information of the image gray values and utilizes the eigenvalues of the local structure sensor; the second filter is based on the eigenvalue analysis of the Hessian matrix. Both filters are reported to perform equally well, with the Hessian approach being slightly faster. The idea of enhancing fissures as plate-like structures was exploited in the presented work, using the Hessian approach as shown faster.

Van Rikxoort et al [140–142] presented a method to segment fissures and other segments that can be found inside the lung area. Once the lungs region has been extracted, a supervised enhancement filter is used. This technique requires input of positive (fissures present) and negative voxels. Therefore, fissures in several images are manually segmented and their voxels used as positive examples. Negative voxels are taken in equal number from the remainder of the lung. Then, for each voxel a multiscale eigenvalue analysis of the Hessian matrix is performed to extract 9 features that are used to train a  $k$ -nearest neighbour classifier (KNNC) to be able to assign to unseen voxels a probability that they belong to a fissure. Then, fissures are segmented by means of a thresholding followed by grouping of neighbouring voxels based on their likelihood of being part of the same plane. Since goal of the research was to reduce manual interaction with the system, this method was not appropriate.

Pu et al [143, 144] outlined an automatic method that uses a marching cubes algorithm, Laplacian smoothing, and extended Gaussian image pyramids to enhance the surface shaped structures within the lung volume. Then, an anisotropic morphological filter is used for fissure surface smoothing and hole repairing. A progressive shape decomposition algorithm is used for individual fissure identification, and finally an anatomy knowledge-based fissure type classification is employed to estimate the complete fissures.

In [145], Lassen et al outlined a method for fissure segmentation based on fissure enhancement that uses an eigenvalue analysis of the Hessian matrix followed by thresholding that combines the contrast and structure information with the voxel intensity. The approach for fissure enhancement and segmentation was ex-

exploited in the presented approach, with some modifications to make the method more general and reliable.

Appia et al. [146] implemented a semi-automated method that uses a minimal path approach on CT images for fissure segmentation. Starting from a few points defined by the user on a single sagittal slice, a 2D energy function is computed using intensity, distance to the vasculature, curvature in 2D, and continuity in 3D. In this energy domain, the fissure is identified by the infimum energy path between a point on the fissure and the nearest lung boundary point. This system proved efficient and reliable, but requires a long and tedious work of manually placing the seed points on sagittal slices.

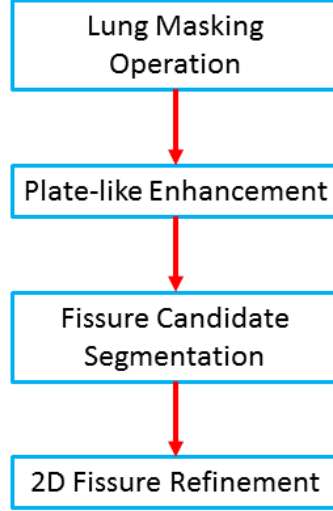
Finally, Qi et al [114] proposed a method that handles each feature separately. Potential fissure regions are first localized on sagittal slices of the image using sagittal adaptive fissure scanning (SAFS). A line enhancement filter based on the Hessian matrix analysis followed by uniform cost search (UCS) is used to extract the complete fissure line. Finally, implicit surface fitting based on radial basis functions is employed to extract the final fissure surface. The robustness of this algorithm was validated using only 14 datasets, and the approach uses a few parameters that have to be determined empirically, and might be not suitable for other datasets.

#### 3.5.4.2 Algorithm Description

For the fissure segmentation algorithm, a pre-processing step is first used to mask the lung region in order to consider only the parenchyma and to exclude other anatomical structure in the CT image. A sequence of three steps is then executed: (i) enhancement of plate-like structures by means of an eigenvalue analysis, (ii) fissure candidate segmentation considering direction and position of the voxels, (iii) final 2D fissure refinement to exclude small regions not belonging to the fissures. A block diagram of the steps involved in the algorithm is shown in Figure 3.11. The method implemented can be considered a good trade-off between complexity and reliability for lobe segmentation. Here, the different steps involved in the fissure segmentation algorithm are described.

### 3. SOLITARY PULMONARY NODULES MALIGNANCY

---



**Figure 3.11:** Steps involved in fissure segmentation.

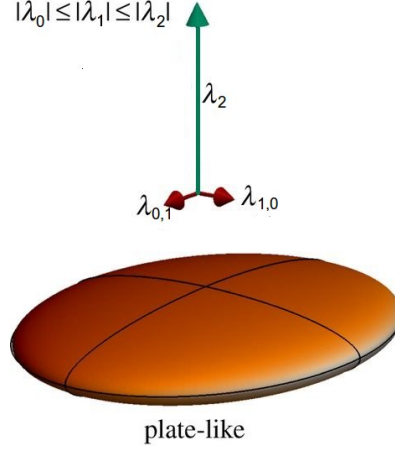
#### Fissure Enhancement

Fissure enhancement represents the first important step for fissures segmentation. Fissures on a CT image have a plate-like structure that goes through the entire image. Therefore, structures of this type inside the parenchyma can be enhanced using a multiscale Hessian eigenvalue analysis. Details about eigenvalue analysis for structures enhancement are given in Section 3.5.3. In the proposed approach, a method similar to that described in [145] was implemented, as it is automatic and proved a good trade-off between computational complexity and reliability. According to this method, a single scale ( $\sigma = 1$ ) is sufficient for fissure enhancement and considering the plate-like structure of the fissures, these can be modelled as objects with a large eigenvalue parallel to the structure and two other small eigenvalues (see Figure 3.12). Therefore, the following structure and sheet functions are introduced (with  $|\lambda_0| \leq |\lambda_1| \leq |\lambda_2|$ ) in (3.10) and (3.11), respectively.

$$F_{struc} = \begin{cases} e^{\frac{-(\lambda_2 - \alpha)^6}{\beta^6}} & \text{if } \lambda_2 < 0 \\ 0 & \text{otherwise} \end{cases} \quad (3.10)$$

$$F_{sheet} = e^{\frac{-\lambda_1^6}{\gamma^6}} \quad (3.11)$$





**Figure 3.12:** Representation of the eigenvalues of plate-like structures [147].

$F_{struct}$  rates the strength of the image structure. In [145],  $\alpha$  and  $\beta$  have been empirically set at  $\alpha = 50$  and  $\beta = 35$ . Unlike [145], a value of  $|\lambda_2|$  was found as more appropriate than  $\lambda_2$  in the definition of  $F_{struct}$ . The requirement for  $\lambda_2 < 0$  is necessary because only bright structures on a dark background (and vice versa) can be considered as fissures (see Table 3.2). On the other hand,  $F_{sheet}$  allows for the discrimination of a sheet structure from other anatomical structures with a high  $\lambda_1$  value, such as nodules and vessels.  $\gamma$  is empirically set to 25, as determined in [145]. The two functions are then combined in (3.12) to obtain the overall fissure similarity measure,  $S_{fissure}$ .

$$S_{fissure} = F_{struct} F_{sheet} \quad (3.12)$$

$S_{fissure}$  will enhance plate-like structures on the CT image, removing objects with other structures. Figure 3.13 shows an example of a sagittal slice (a) before and (b) after enhancement. The right fissures are clearly visible. However, as shown in Figure 3.13, other small regions may also appear in the fissure-enhanced image. Therefore, another step is necessary to ensure that only voxels belonging to fissures are included and to exclude the others.

### Fissure Segmentation

The first step for fissure segmentation involves the removal of voxels that are

### 3. SOLITARY PULMONARY NODULES MALIGNANCY

---



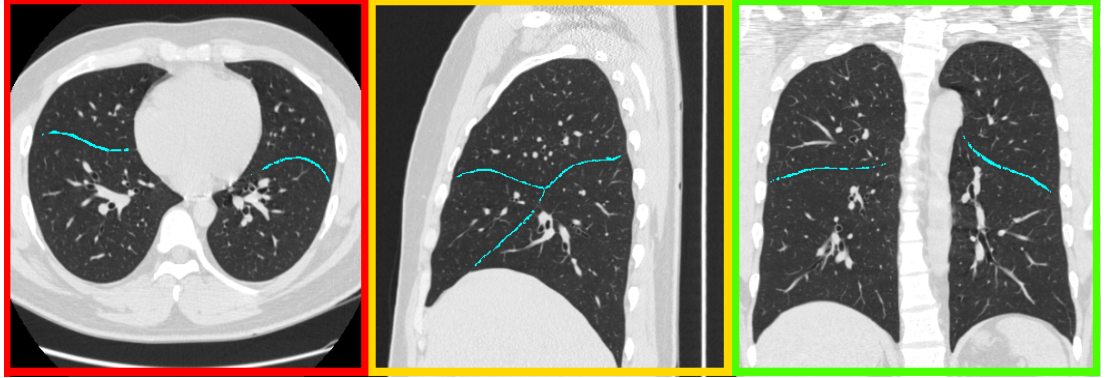
**Figure 3.13:** An example of fissure enhancement as it appears on a sagittal CT slice. The right fissures are clearly visible on the enhanced image (right). However, other structures are also still present in the enhanced image. The thorax is excluded using the lung label map previously segmented as a mask prior to the enhancement.

clearly not fissure candidates. To this end, the  $S_{fissure}$  information and the intensity of voxels in the original image are combined. Thus, voxels are considered as possible fissure voxels candidates if  $S_{fissure} > 0.1$  and  $-900 \text{ HU} < \text{pixel intensity} < -300 \text{ HU}$ , which is a typical range of intensities for lung fissures. Next, a method similar to [141, 142] is employed to discard voxels that are not discarded with the previous operation and do not belong to a plate-like structure. In particular, the idea is that, as the curvature of a fissure is low, adjacent fissure voxels have a similar eigenvector corresponding to the largest eigenvalue. In fact, this shows the orientation of a structure. For this reason, neighbouring voxels (in a  $7 \times 7 \times 7$  pixel volume) are considered to be on the same plate if they have similar direction and are not on two parallel plate structures. To check whether two voxels have similar direction, the inner product between the normalized eigenvector of the two voxels has to be close to 1.0 (inner product  $\geq 0.985$ ). On the other hand, to make sure that the two voxels are not on two different parallel plates, the outer product between the eigenvector of one voxel and the normalized difference vector between the locations of the two voxels is considered. This outer product has to be close to 1.0 (outer product  $\geq 0.985$ ) to consider two voxels as

belonging to the same plate. The result of this operation is a binarized image in which all the voxels that satisfy these two conditions are assigned a value of 1, while the remaining voxels are set to 0. Finally, a 3D connected component filter is employed to only retain objects with a size of at least 2000 pixels.

#### Final Fissure Refinement

Although the segmentation method is able to successfully identify the main lung fissures, in some cases small objects can still be included in the segmentation result. For this reason, a final refinement may be necessary. To this end, the binarized image is analysed by moving through 2D axial slices. On these slices fissures have a linear shape, although they may be visible as a cluster of small lines, due to small holes within the fissures. Therefore, for each slice a connected component filter is computed and all the objects with a roundness higher than 0.5 and a total of pixel count lower than 50 are removed. All the remaining objects are then merged together and a final 3D closing operation is employed to remove holes within the fissures. An example of fissures segmented with the described method is shown in Figure 3.14.



**Figure 3.14:** Example of a fissure segmentation result. The fissures label is imposed on the three views of the CT image in a light blue colour.

#### 3.5.5 Lung Lobes Segmentation

Once the lobe fissures are determined, the lobes of the lung can be segmented starting from the lung label. For this purpose, the method described by Ross et

### 3. SOLITARY PULMONARY NODULES MALIGNANCY

---

al [148] was used as a basis. This method proved reliable in segmenting lobes starting from a lung label map. However, it requires the user to place a few fiducial points on each fissure to obtain the final lobe segmentation. Since the algorithm should be automatic, a method to automatically distinguish the right horizontal and oblique fissures, as well as the left oblique fissure from the fissure segmentation approach described above was implemented. Points of these fissures are then used as starting inputs for lobe segmentation.

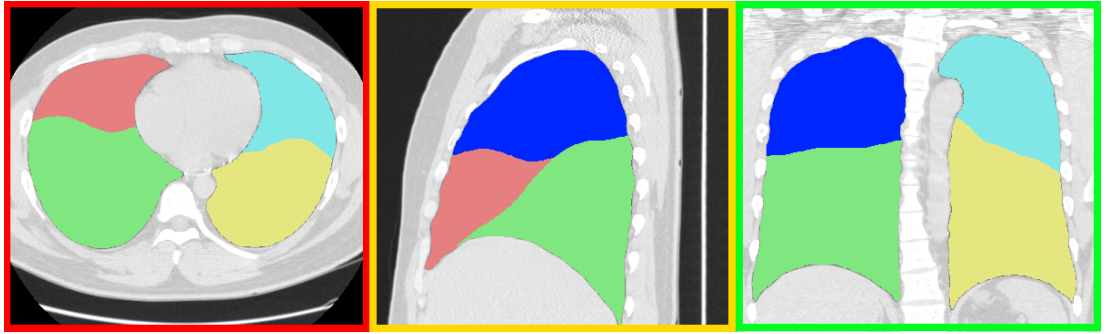
#### 3.5.5.1 Lobe Segmentation Algorithm

At the Surgical Planning Laboratory (SPL) of Brigham & Women’s Hospital, in Boston, a tool for semi-automated lobe segmentation has been developed [149]. The tool requires minimal user interaction (i.e., semi-automatic) and it allows the user to quickly, easily, and accurately generate segmentations of the left upper and lower lobes and right upper, middle, and lower lobes. As well as loading the HRCT dataset and the corresponding lung label map, the user is asked to scroll through the HRCT data and place fiducials along the three major fissures of the lung: left oblique, right oblique, and right horizontal. The algorithm uses a thin plate splines (TPS) method [150] that provides an interpolation scheme whereby a minimally curved surface is defined such that it passes through all the user-selected points. The tool has been demonstrated to be reliable over several HRCT datasets with different disease states and results are usually generated within five to six minutes, including time for seed placement. The tool is available as part of the Chest Imaging Platform (CIP) [74], a group of classes and method for chest imaging under development at SPL.

#### 3.5.5.2 Fissure Points Extraction

To distinguish the three different fissures both the subdivided lung label map as sub-divided into the three sub-parts (as described in Section 3.5.2) and the fissure label positions are exploited. In particular, all the fissure points that correspond to the upper, middle or lower left lung in the lung label map are considered as part of the left oblique fissure. On the other hand, distinction between the two right fissures is more complex. As shown in Figure 3.13, these

two fissures appear on sagittal slices as a sort of two pronged pitchfork, with the upper “prong” belonging to the horizontal fissure, and the lower one belonging to the oblique fissure. Therefore, if a point corresponds to the area of the right upper lobe in the lung label map, it is considered as a horizontal fissure point. If it lies in the right lower part, it is assigned to the right oblique fissure. For points corresponding to the right middle lobe, 2D sagittal slices are considered. Distances from the horizontal and oblique fissure points in the  $z$  direction (see Figure 4.8) are computed and the point is assigned to the closest point. The number of points for each fissure may be very high. Having too many points per fissure may affect the lobe segmentation, since lobe segmentation was developed to work with a relatively small number of points (selected by the user). Therefore, for the left fissure, a maximum of 100 points was selected, while a maximum of 200 points for each of the two right fissures is used. The three groups of points are finally passed as input to the lobe segmentation method which will create the final lobe segmentation. Figure 3.15 shows an example of lobe segmentation starting from the segmented fissures.



**Figure 3.15:** Example of a lobe segmentation result. The three different lobes are assigned a different label. Blue, red, and green represent the right upper, middle, and lower lobes, respectively. Light blue and yellow are the colour used for the labels of the left upper and lower lobes, respectively.

#### 3.5.6 Nodule Diagnosis

To compute probability of malignancy of lung nodules, the user is only required to specify location of the nodule (through a seed point), a few clinical characteristic,

### 3. SOLITARY PULMONARY NODULES MALIGNANCY

---

such as number of cigarettes smoked per year, hemoptysis, and presence/absence of history of malignancy, as well as a prior probability of malignancy, based on visual inspection. Age is automatically acquired from the DICOM information of the CT image. Then, radiographic characteristics of the selected nodule, namely size (in cm), location, edge smoothness, cavity wall thickness, and calcification pattern are automatically computed along with the calculated probability of malignancy of the nodule. While size, edge smoothness, cavity wall thickness and calcification are determined by the nodule segmentation algorithm, the location is determined based on the position of the nodule on the lobe label map. The method to determine the probability of nodule malignancy is based on the Bayesian method described by Gurney et al [38, 39]. However, Gurney's method requires visual inspection of the CT image and manual input, while the developed method starts from CT images and is automatic. In particular, the likelihood ratio for each radiographic and clinical characteristic was computed by (3.13).

$$\text{Ratio} = \frac{\text{Prob. of finding in subjects with malignancy}}{\text{Prob. of finding in subjects with benignity}} \quad (3.13)$$

$$= \frac{\text{Test sensitivity}}{1 - \text{Test specificity}} \quad (3.14)$$

$$= \frac{\text{True positive fraction}}{\text{False positive fraction}} \quad (3.15)$$

Table 3.3 reports the likelihood ratios as found by Gurney et al [38]. From the likelihood ratios, the odds of cancer are given by (3.16).

$$\text{Odds of Cancer} = \text{Prior Odds} \times \text{Likelihood Ratios} \quad (3.16)$$

Prior Odds can be subjectively estimated or based on the prevalence of malignancy of the population under analysis, and are computed using (3.17).

$$\text{Prior Odds} = \frac{\text{Prev. of malignancy}}{1 - \text{Prev. of malignancy}} \quad (3.17)$$

Finally, the probability  $P$  of malignancy is given by (3.18).

$$P = \frac{\text{Odds of Cancer}}{\text{Odds of Cancer} + 1} \quad (3.18)$$

### 3.5 Algorithm Implementation

Characteristics	Likelihood Ratio for Malignancy	Confidence Interval
<b>Size</b>		
0-1.0 cm	0.52	0.43-0.62
1.1-2.0 cm	0.74	0.66-0.82
2.1-3.0 cm	3.67	3.46-3.87
> 3 cm	5.23	5.11-5.34
<b>Edge</b>		
Smooth	0.30	0.20-0.41
Spiculated	5.54	5.46-5.63
<b>Cavity Wall Thickness</b>		
≤ 4 mm	0.07	0.03-0.14
5-15 cm	0.72	0.50-1.03
≥ 16 cm	37.97	13.07-110.30
<b>Calcification</b>		
Benign Pattern	0.01	0.0-0.03
Non-Calcified	2.20	2.14-2.26
<b>Location</b>		
Upper/Middle Lobe	1.22	0.91-1.64
Lower Lobe	0.66	0.49-0.89
<b>Age (years)</b>		
20-29	0.05	0.01-0.09
30-39	0.24	0.14-0.35
40-49	0.94	0.87-1.01
50-59	1.90	1.73-2.07
60-69	2.64	2.44-2.83
≥ 70	4.16	3.97-4.35
<b>Smoking (Packets/Years)</b>		
Never Smoked	0.17	
< 30	0.75	
30-39	2.0	
> 40	3.7	
<b>Hemoptysis</b>		
Present	5.08	3.55-7.27
<b>Previous Malignancy</b>		
Present	4.95	4.13-5.93

**Table 3.3:** Likelihood ratios for malignancy in SPNs as found in [38].

## 3.6 Algorithm Performance

### 3.6.1 Overview

In this section, the methods used to test the performance of the nodule segmentation and classification algorithms are described. One of the main issues when developing a system for automatic evaluation of malignancy probability is that performance of the algorithm is often evaluated on local datasets and results are difficult to compare. Most of the databases for lung image analysis do not report nodule follow-up. As an example, in 2009 van Ginneken et al [151] introduced the ANODE'09 challenge to compare the various methods available for automatic detection of pulmonary nodules in thoracic CT scans. Training and testing data are available, so that different methods can be compared. However, this dataset is for algorithms that aim at detecting nodules. No indication of nodule location or follow-up are provided.

The lung image database consortium (LIDC) [152] provides a wide range of lung CT data. Numerous scans are available online, but a limited number of cases report diagnosis at nodule level. Therefore, performance of the described algorithm was tested on a combination of LIDC images available online and local datasets provided by CUH. However, as the software is available online, results of different algorithms tested on local datasets can be compared with those described here. In this section, the datasets used are first described and the evaluation method implemented is then detailed. Finally, the results obtained are presented and the conclusion are drawn.

### 3.6.2 CT Datasets

For testing the algorithm, two different groups of datasets were used. The first group consisted of a selected number of images from the LIDC database. This database is intended to be a common dataset for the development of CAD systems and for comparison of performance. For each scan used from the LIDC database, annotations by four expert radiologists (each from a different institution) have been included. The radiologists drew complete outlines of all nodules between 3 and 30 mm in diameter and identified some of the specified characteristics



(subtlety, internal structure, calcification, sphericity, texture), on a 1 to 5 scale. A “blinded” and “unblinded” reviewing procedure was established. In the “blinded” stage, each radiologist individually marked the lesions. In the unblinded phase, each radiologist re-examined the cases with the additional information of the annotation of the other radiologists, although no forced consensus was imposed. For each marked nodule bigger than 3 mm, the four radiologists also provided a subjective assessment of likelihood of malignancy, on a 1 to 5 scale, with 1 indicating a nodule highly unlikely to be malignant and 5 representing a high likelihood of malignancy.

In order to evaluate probability of malignancy, radiologists were asked to assume that patients were 60 years old male smokers. At present, 1012 CT scans are available via the website of the National Biomedical Imaging Archive (NBIA) of the National Cancer Institute (NCI) [153]. Follow-up diagnosis, obtained at nodule level, has been provided for a total of 120 nodules from 107 separate scans. Diagnosis of the nodules has been obtained with one of four possible methods; (i) further review of radiological images, (ii) biopsy, (iii) surgical resection, or (iv) progression (response). However, no indication of which nodule was considered for follow-up is provided. Some images provide several nodules, making recognition of the diagnosed nodule complicated.

From the LIDC database, 95 images with a total of 108 nodules were extracted. To this end, a specific SQL database was developed. The images have varying resolution and slice thickness, with reconstruction interval ranging from 0.75 to 3 mm. This group of nodules was split into two different sets, LIDC.A and LIDC.B, for separate tests. LIDC.A consisted of 80 nodules with a consistent assessment of malignancy among the four radiologists. Of these 80 nodules, 10 were considered highly unlikely to be malignant (score = 1) by the 4 radiologists, 15 moderately unlikely (score = 2), 10 had an indeterminate likelihood (score = 3), 25 moderately suspicious for cancer (score = 4), and the last 20 cases were considered highly suspicious for cancer (score = 5). LIDC.B was extracted from 120 cases with follow-up. To properly identify the analysed nodules, all images with two or more nodules were first excluded. Then, only nodules that were bigger than 3 mm and which were identified by all four radiologists were considered. A

### 3. SOLITARY PULMONARY NODULES MALIGNANCY

---

total of 28 nodules, 12 benign and 16 malignant, were extracted from the LIDC.B dataset.

The second group of images was provided by the Cork University Hospital (CUH) in compliance with an approved ethical protocol by the Cork Research Ethics Committee. This group contained 67 nodules (40 malignant, 27 benign) from 67 patients that were acquired using different scan machines and various reconstruction parameters. For each image, location of the nodule and follow-up diagnosis were provided.

#### 3.6.3 Algorithm Testing Approach

To evaluate performance of the algorithm, three different tests were applied, one for each set of nodules. First, the probability of malignancy computed by the algorithm was compared to the radiologists' assessment, using the 80 nodules from LIDC.A. These nodules were assessed with equal probability of malignancy by all four radiologists. This approach gives a frame of reference to prove reliability of the algorithm. The developed algorithm computes a percentage for the probability of malignancy. To compare results to those from the radiologists, the percentages were divided into the LIDC 5-point scale (1-20% = 1, 21-40% = 2, 41-60% = 3, 61-80% = 4, 81-100% = 5). Radiologists' and algorithm results were normally distributed, as shown by probability plot, histogram analysis, and Shapiro-Wilk test [154] ( $p = 0.984$  and  $p = 0.923$  for radiologists' and algorithm results, respectively). An unpaired Student's t-test to assess the ability of the algorithm to match the radiologist's diagnosis was applied. To better match the radiologists' diagnosis conditions, prior probability of malignancy was set to 50%, age to 60, and the smoking parameter to 30-39 pk/year.

For the second test, the ability of the algorithm to predict nodule malignancy, as compared to the radiologists' assessment, was evaluated on the 28 cases from the LIDC.B database. A receiver-operating characteristic (ROC) curve analysis [155] was used, with the estimated area under the ROC curve (AUC) used as the parameter for algorithm accuracy. Results were compared by means of the DeLong test [156]. This approach allowed for evaluation of accuracy of the algorithm, compared with radiologists' assessment.

### 3.6 Algorithm Performance

A final test was then performed using the CT images provided by CUH. Results obtained with the described approach were compared to similar methods applied by Swensen [90] and McWilliams [110] using ROC analysis. Swensen's method requires to specify age, smoking status and history of cancer, and to indicate presence of spiculation. Probability of malignancy is then computed using (3.19).

$$\begin{aligned} \text{Probability} = & (0.0391 \times \text{Age}) + (0.7917 \times \text{Smoker}) + (1.3388 \times \text{Cancer History}) + \\ & (0.1274 \times \text{Nodule Diameter}) + (1.0407 \times \text{Spiculation}) + \\ & (0.7838 \times \text{UpperLobe}) - 6.8272 \end{aligned} \quad (3.19)$$

Conversely, McWilliams' approach assigns a value to the user-specified age, sex (0.6011), family cancer history (0 or 0.2961), emphysema (0 or 0.2953), nodule size, nodule type (-0.1276 for non-solid, 0.377 partially solid, and 0 for solid), nodule count, nodule in the upper lobe (0.6581) and spiculation (0.7729). Probability of malignancy is computed by (3.20) and (3.21).

$$\begin{aligned} \text{LogOdds} = & (0.0287 \times (\text{Age} - 62)) + \text{Sex} + \text{Lung Cancer Hx} + \text{Emphysema} - \\ & (5.3854 \times ((\frac{\text{Nodule size}}{10}) - 0.5 - 1.58113883)) + \text{Nodule Type} + \\ & \text{Upper Lung} - (0.0824 \times (\text{Nodule count} - 4)) + \text{Spiculation} - 6.7892 \end{aligned} \quad (3.20)$$

$$\text{Probability} = 100 \times \frac{e^{\text{LogOdds}}}{1 + e^{\text{LogOdds}}} \quad (3.21)$$

At present, nodule type is not determined by the presented algorithm, but is manually specified in equation 3.20 after visual inspection of each nodule.

For ROC curve analysis, the true positive rate (sensitivity) is plotted in function of the false positive rate (1-specificity). Sensitivity indicates the probability that a test result will be positive when the disease is present, while specificity determines the probability that a test result will be negative when the disease is not present. In the ROC curve, the sensitivity (true positive rate) is plotted in function of the false positive rate for different cut-off points. Each point on the ROC curve represents a sensitivity/specificity pair corresponding to a particular decision threshold. Therefore, for every possible threshold (cut-off point)

### 3. SOLITARY PULMONARY NODULES MALIGNANCY

---

selected to discriminate between the two populations, there will be some cases with the disease correctly classified as positive (true positive fraction), but some cases where the disease will be classified negative (false negative fraction). On the other hand, some cases without the disease will be correctly classified as negative (true negative fraction), but some cases without the disease will be classified as positive (false positive fraction).

#### 3.6.4 Results

Prediction of nodule malignancy was obtained for all 175 cases considered (LIDC.A + LIDC.B + CUH) with an average time of 3.55 minutes on a 2.40 GHz, 12 GB RAM PC. As shown in Table 3.4, lung and fissure segmentation were the longest processes, with an average time of 2.03 minutes and 1.23 minutes, respectively. Lung and nodule segmentations were accomplished for all nodules, whereas in twenty cases the algorithm failed fissure and lobe segmentation, for one or both lungs. This was due to presence of lung diseases, such as diffuse emphysema, which affect the structure of the fissures. In eleven cases, lobe segmentation failed in the lung not containing the nodule, so that correct nodule localization was still possible. In the remaining nine cases, nodule location was computed based on the corresponding third of the lung label map.

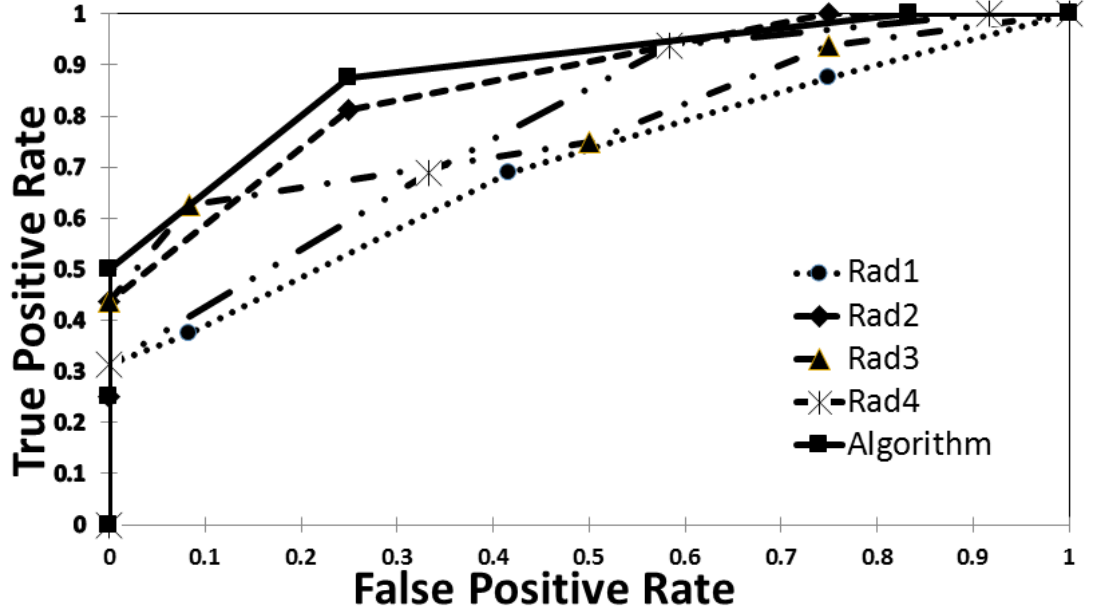
Results from the algorithm on the 80 LIDC.A nodules proved not statistically different from subjective diagnosis of the four radiologists (Student's t-test,  $p = 0.34$ ). For five cases, the described method provided high ( $> 3$ ) or low ( $<$

Process	Average Time (seconds)
Lung Segmentation	$123 \pm 15.71$
Nodule Segmentation	$3 \pm 0.98$
Fissure Segmentation	$83 \pm 20.12$
Lobe Segmentation	$25 \pm 5.25$
Malignancy Computation	$1 \pm 0.25$

**Table 3.4:** Average times to compute the different steps for prediction of likelihood of malignancy for 175 cases.

Method	AUC	95% CI
Radiologist 1	0.701	0.512-0.889
Radiologist 2	0.859	0.735-0.983
Radiologist 3	0.784	0.6150-0.952
Radiologist 4	0.776	0.612-0.940
Algorithm	0.885	0.775-0.996

**Table 3.5:** Comparison of prediction performance of radiologists and algorithm from the LIDC.B dataset.



**Figure 3.16:** ROC curves comparing the different results from the four radiologists and the described algorithm from the LIDC.B dataset.

3) probability, while radiologists gave an undetermined reading. Unfortunately, since these nodules did not have follow-up diagnosis, evaluation of these five results was not possible.

Table 3.5 shows the comparison of prediction accuracy obtained by the radiologists and by the algorithm on the 28 LIDC.B nodules with follow-up. The test ROC curves for the various predictors are shown in Figure 3.16. The cut-off points are shown, while the individual ROC outcomes for the different threshold

### 3. SOLITARY PULMONARY NODULES MALIGNANCY

	Rad1			Rad2			Rad3			Rad4			Alg.		
T	SN	SP	SN+SP	SN	SP	SN+SP	SN	SP	SN+SP	SN	SP	SN+SP	SN	SP	SN+SP
1	0.875	0.250	1.125	1.000	0.250	1.250	0.938	0.250	1.188	1.000	0.083	1.083	1.000	0.167	1.167
2	0.688	0.583	1.271	0.813	0.750	1.563	0.750	0.5	1.250	0.938	0.417	1.354	0.875	0.750	1.625
3	0.375	0.917	1.292	0.438	1.000	1.438	0.625	0.917	1.542	0.688	0.667	1.354	0.500	1.000	1.500
4	0.313	1.000	1.313	0.250	1.000	1.250	0.438	1.000	1.438	0.313	1.000	1.313	0.250	1.000	1.250
5	0.000	1.000	1.000	0.000	1.000	1.000	0.000	1.000	1.000	0.000	1.000	1.000	0.000	1.000	1.000

**Table 3.6:** Individual ROC outcomes for the first ROC curve analysis (LIDC.A). T stands for threshold, SN for sensitivity (true positive rate), and SP for specificity (1 - false positive rate).

are presented in Table 3.6. Considering the radiologist who provided the highest accuracy (radiologist 2), ROC analysis showed an area under the curve (AUC) of 0.859 (95% CI, 0.735-0.983) for radiologist 2, and 0.885 (95% CI, 0.775-0.996) for the described algorithm. Although similar to radiologist 2 ( $p < 0.05$ ), the algorithm had a higher accuracy. In one case, the algorithm predicted low probability of malignancy, while follow-up indicated malignancy of the nodule, whereas in a second case high likelihood was predicted by the algorithm for a benign nodule. In nine cases, the algorithm provided an undetermined likelihood (score = 3) to the analysed nodules.

The last tests evaluated accuracy of the algorithm on the 67 local cases with follow-up provided by CUH. ROC analysis results showed an AUC of 0.795 (95% CI, 0.712-0.877) for the described approach, 0.738 (95% CI, 0.648-0.828) for Swensen’s method, and 0.759 (95% CI, 0.671-0.846) for McWilliams’. Results are summarised in Table 3.7, while ROC curves are presented in Figure 3.17. The cut-off points are shown, while the individual ROC outcomes for the different threshold are presented in Table 3.8. In 24 cases the proposed algorithm provided uncertain probability of malignancy (score = 3). In general, these results confirm the high accuracy of the described approach, as compared to other methods.

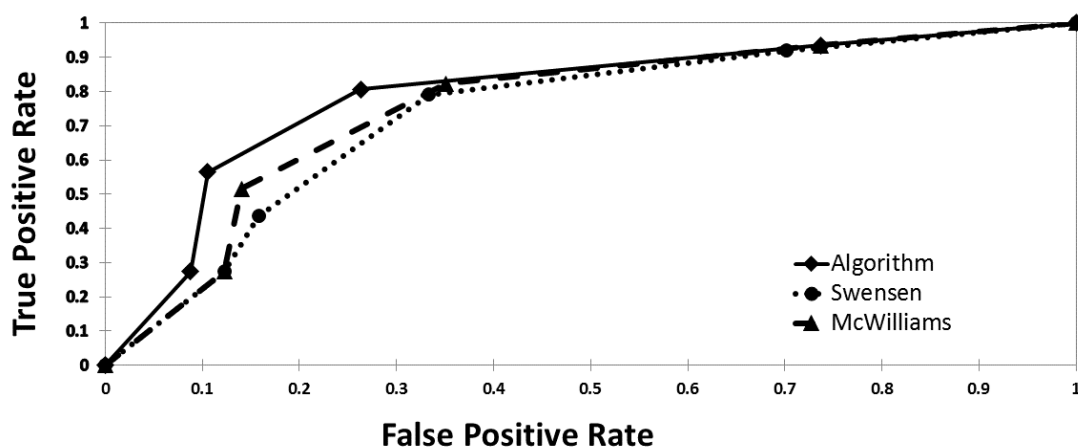
#### 3.6.5 Discussion

In this section, performance of the proposed method for nodule malignancy prediction was evaluated. Three sets of chest CT images composing 175 nodules have

### 3.6 Algorithm Performance

Method	AUC	95% CI
Swensen	0.738	0.648-0.828
McWilliams	0.759	0.671-0.846
Algorithm	0.795	0.712-0.877

**Table 3.7:** Comparison of the performance of the algorithm, compared to Swensen’s [90] and McWilliams’ [110] methods using the CUH dataset.



**Figure 3.17:** ROC curves comparing results from the algorithm compared to Swensen’s and McWilliams’ methods for the CUH dataset.

	Swensen			McWilliams			Alg.		
T	SN	SP	SN+SP	SN	SP	SN+SP	SN	SP	SN+SP
1	0.919	0.298	1.218	0.935	0.263	1.199	0.935	0.263	1.199
2	0.790	0.667	1.457	0.823	0.649	1.472	0.806	0.737	1.543
3	0.435	0.842	1.278	0.516	0.860	1.376	0.565	0.895	1.459
4	0.274	0.877	1.151	0.274	0.877	1.151	0.274	0.912	1.186
5	0.000	1.000	1.000	0.000	1.000	1.000	0.000	1.000	1.000

**Table 3.8:** Individual ROC outcomes for the second ROC curve analysis (LIDC.B). T stands for threshold, SN for sensitivity, and SP for specificity.

### 3. SOLITARY PULMONARY NODULES MALIGNANCY

---

been used for separate testing. Comparison with four radiologists' subjective assessment showed that the implemented algorithm is comparable to radiologists' performance. This test cannot be considered accurate to evaluate reliability of the algorithm, as no follow-up was provided for the images. Therefore, 28 images with clinical follow-up from the LIDC dataset were selected to assess the capability of the described approach in predicting nodule malignancy, and the algorithm's results were compared to the radiologists' subjective assessment. ROC analysis showed that the described method is accurate and improves radiologists' diagnosis. However, the data sample was small, and a larger dataset should be used in order to properly evaluate performance of the algorithm and compare it to radiologists' diagnosis. The last test showed that the described method predicts likelihood of malignancy with accuracy higher than two methods available in the literature. For the approach proposed by McWilliams et al [110], results might have been biased by visual classification of the nodule as solid, non-solid, and semi-solid. A method which computes automatic classification of the nodules may improve results obtained with this approach.

In the method proposed here, nodules' shape was classified as smooth or spiculated only, with no characterization for nodule lobulation. Future work might include the development of a method for automatic definition of nodule lobulation to help improve accuracy of the algorithm.

At present, the algorithm was tested on a limited number of images. A larger database of images providing follow-up and assessment from different radiologists should be considered for future evaluation. Assuming a study power of 80%, with a significance level of 5%, a sample size  $n = 1072$  nodules is necessary for a proper ROC curve analysis to evaluate whether the algorithm improves the radiologists' assessment. In general, the obtained results are positive and indicate that the algorithm is reliable and accurate at predicting probability of malignancy and improving radiologists' assessment and different methods' accuracy.

The described system requires user interaction in order to identify the nodules to analyse. Automatic nodule identification and classification should be investigated in the future to provide the physician with a complete and reliable CAD system to determine whether to proceed with biopsy of the nodule.



## 3.7 Summary

In this chapter, a new method for prediction of solitary pulmonary nodule malignancy starting from chest CT was described. The primary results are as follows:

- The algorithm has a modular structure, being composed of different segmentation methods that can be used independently for individual needs.
- Simple user interaction is required from the user, who has to select the nodule under analysis. Lungs, nodule, fissures, and lobes are then automatically segmented.
- Nodule radiological characteristics are automatically computed and combined with radiological features, and probability of malignancy is computed based on the method introduced by Gurney et al [38,39].
- The algorithm determines probability of malignancy with high accuracy when compared to other methods available in the literature and to radiologists' assessment.
- Improvements need to be implemented to make the algorithm more robust against affecting factors, such as lung disease. Also, tests with larger datasets should be performed.
- The algorithm is easily modified and extended, and it is a good starting point for a complete CAD system.

# Chapter 4

## Airway Segmentation\*

### 4.1 Overview

This chapter details the design and development of a semi-automated algorithm for airway segmentation starting from chest CT images. The algorithm is implemented as an extension of the open-source software 3D Slicer [74], and can be freely downloaded, used, and modified according to personal needs. Some of the most common techniques for medical image segmentation, the background theory, and the relevant literature are briefly discussed, while the implementation of the algorithm is explored in detail. The results obtained testing the algorithm on several human and animal CT images are then discussed. In particular, reliability of the algorithm in terms of CT scanner parameters is shown. Key contributions presented in this chapter include:

- The first open-source algorithm entirely dedicated to airway segmentation. This increases extendibility of the algorithm and allows for easier comparison with other algorithms.
- The algorithm requires minimal interaction by the user. One click selection at the patient trachea (easily recognizable on a CT image) is required,

---

\*This chapter is based on P. Nardelli, K. A. Khan, A. Corvò, N. Moore, M. J. Murphy, M. Twomey, O. J. O'Connor, M. P. Kennedy, R. S. J. Estépar, M. M. Maher and P. Cantillon-Murphy “Optimizing parameters of an open-source airway segmentation algorithm using different CT images.” *Biomedical Engineering Online* 14, no. 1 (2015): 62.

making the algorithm amenable to a vast range of researchers, from physicians that need specific analysis of the airways to engineers that can use the software as a starting point for other applications.

- Although not yet capable of segmenting all the airways on a CT image due to limits on CT resolution, the results obtained using the algorithm show that the method is comparable with other results.
- Unlike other algorithms present in the literature, the airway segmentation method presented here proved reliable across different types of CT scanners and parameters. Moreover, the algorithm can be easily modified, adding new options as new datasets become available.

## 4.2 Medical Image Segmentation

In computer vision, image segmentation is the process of partitioning an image into salient and non-overlapping regions to help identify, classify, analyse or simply recognize objects or other relevant information. The idea underlying this process is to assign a specific label to pixels that share a certain characteristic [157]. In this way, all the pixels with similar characteristics, such as colour, texture or intensity can be gathered into different regions in order to analyse, in an easier manner, an object of interest or a part of the image. In fact, adjacent regions can be significantly different with respect to some characteristics [158,159]. This technique is widely used in the field of medical imaging, as the resulting labels can be combined to create 3D reconstructions of the regions of interest, using algorithms that reconstruct new data points starting from a discrete set of known points, called interpolation algorithms. An example of an interpolation algorithm is the marching cubes algorithm [160], which forms an imaginary cube taking eight neighbour locations at a time. The algorithm then determines what polygon is necessary to represent the part of the isosurface passing through this cube. The individual polygons are then fused into the desired surface.

In the last three decades, several automated image segmentation techniques have been developed. An important aspect to bare in mind is that an optimal segmentation method does not exist, and each situation may require a different

## 4. AIRWAY SEGMENTATION

---

technique. In particular, the technique to be used for segmentation is specific to application, imaging modality and type of body part to be studied. As an example, brain segmentation requires methods that are different from those required in the thorax. Also, another important aspect to consider when selecting a segmentation algorithm is the possible presence of noise on the image, which may be due to partial volume effects, motion or ring artefacts, and noise related to sensors and electronic systems. Here, some of the most common techniques for segmentation used in medical imaging are briefly presented [161].

### 4.2.1 Thresholding

Thresholding represents the simplest method of image segmentation. It consists in applying an intensity threshold value and adding all the pixels with an intensity above or below this threshold. This way, the intensities of the image are binarized into two classes, with all the pixels above the threshold grouped in one class and the remaining pixels in another class [162]. This threshold can be chosen by analysing the histogram of the image, a graphical representation of the image intensities distribution. This method is suitable to segment regions or objects with intensities that stand out from the rest of the image. The main issue with this technique is that usually it is not simple to choose a single threshold to label a region and, therefore, it often requires user interaction (i.e., the threshold value has to be chosen and evaluated by the user). Therefore, thresholding is often used as a first step in more complicated segmentation techniques, in order to have a first approximate separation. A typical example of usage of this technique is as the first step in lung segmentation from CT images. This way, the soft tissue of the lung can be roughly separated from the surrounding chest structures with higher HU values (see Table 2.1) [163]. However, simple thresholding can not be used in operation such as airway segmentation, as image noise and the high number of voxels with intensities similar to air in the lung tissue (as in patients with emphysema) would not allow a proper distinction of airways from the surrounding tissues.

### 4.2.2 Edge Based Segmentation

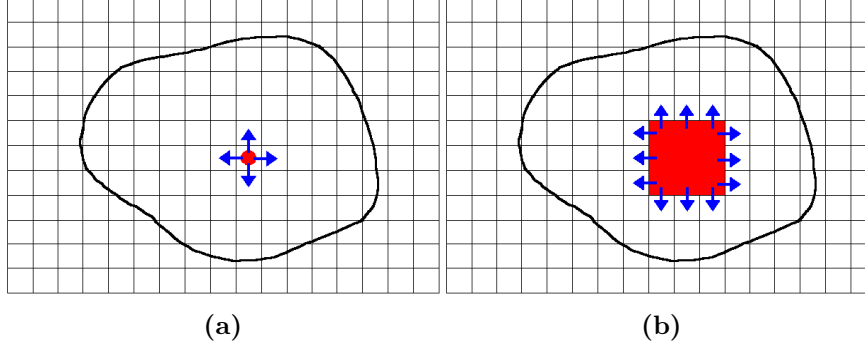
Edge based segmentation is a method based on the identification of boundaries which separate the different regions. To this end, discontinuities in grey level close to uniform grey level regions are considered edges of the region itself. Edge based algorithms use edge detecting operators based on gradient (derivative) functions, such as Prewitt, Sobel, Roberts (1st derivative), and Laplacian (2nd derivative). Problems with this technique are the possible presence of noise or weak edges that can greatly affect the segmentation results [161]. For this reason, edge-based algorithms, like thresholding techniques are often used in conjunction with other techniques for complete segmentation. Examples of edge based segmentation algorithms are edge relaxation [164] and Hough transform based [165].

### 4.2.3 Region Growing Segmentation

Region growing algorithms involve extracting pixels within an image region that are connected based on some predefined criteria [161]. The segmentation starts from an initial “seed region” (one or more pixels) and check a neighbourhood region of pixels to assess whether these neighbours satisfy the predefined condition. For 3D images, two approaches can be used to check neighbours; face connectivity and full connectivity. With a face connectivity approach, 6 neighbours connected to the seed pixels are considered (four pixels surrounding the seed on the same slice and two pixels corresponding to the seed on the previous and next slices), while with full connectivity, the 26 pixels surrounding the seed are checked. Pixels that satisfy the condition are added to the initial region and their neighbours are checked in turn. The process continues as long as new pixels are added to the region. A representation of region growing segmentation is included in Figure 4.1. There exists several region growing segmentation techniques depending on (i) the selected criteria to add a pixel to the growing region, (ii) the connectivity indicating the neighbourhood size, and (iii) the strategy used to add neighbouring pixels. The main disadvantage of this method is that, oftentimes, the seed region and the inclusion criteria have to be set manually. Moreover, if several regions need to be extracted, different region seeds must be selected. Examples of region growing segmentation methods are the “Threshold Connected”, which evaluates

## 4. AIRWAY SEGMENTATION

---



**Figure 4.1:** Region growing segmentation scheme. (a) A seed pixel (red) is selected and the algorithm starts checking neighbouring pixels (blue arrows). (b) The pixels around the grown region (red) are assessed.

if the pixels' intensity value is inside a specific interval, and “Otsu segmentation”, which tries to minimize the error of misclassification of the pixels by finding a threshold that classifies the image into two clusters. Otsu segmentation seeks to minimize the area under the histogram due to one cluster which lies on the other cluster's side of the threshold [61]. For the development of the described airway segmentation method, a region growing technique was chosen for the simple initialization process, the little user interaction required, as well as the good results showed in the literature.

### 4.2.4 Level Set Segmentation

The level set segmentation approach was proposed for the first time in 1988 [166] and refers to a numerical technique that tracks the evolution of contours and surfaces in an image. It uses and solves a partial differential equation (PDE) to facilitate the segmentation. In particular, a contour is embedded as the zero level set of a higher dimensional function called the level-set function, which is then evolved under the control of the PDE. At any time, the evolving contour can be obtained by extracting the zero level-set function from the output. This technique is widely used in medical image segmentation because of its capacity for modelling and handling complex shapes and topological changes, as well as its computational efficiency in 3D images. In a typical approach, a contour is

initialized by the user and is then evolved until it fits the form of an anatomical structure in the image. The main problem of level set methods is that choosing a proper initialization contour (speed function) may be complicated in some applications. As well as in region growing segmentation, many different implementations and variants of the level set segmentation have been proposed [167]. A typical example of a level set segmentation method is the fast marching algorithm, that starts from an initial position on the front, and systematically moves the front forward one grid point at a time, successively solving the Eikonal equation [168]. In the case of airway segmentation, a fast marching approach requires the definition of a very complicated speed function, as shown in Schlathölter et al [169], that can highly increase the computational complexity of the system.

### 4.2.5 Atlas Based Segmentation

A fourth approach to medical image segmentation is to exploit the anatomical features of the structures or region of interest with a repetitive form or geometry, using atlas based segmentation methods. If an atlas or template is available, these techniques can be very useful. The atlas is usually generated by comparing images of several subjects in order to extract a model explaining the variation in the shape of the structure itself. This generated model is then used as a reference frame for the segmentation of new images [162]. However, the creation of the atlas needs registration of all the images from several patients as well as a probabilistic representation of the registered data. Moreover, due to anatomical variability, an accurate construction of the atlas can be quite complex and expert knowledge is often required in building the database to be used for the atlas construction. Therefore, atlas based segmentation methods are generally used for the segmentation of structures that tend to remain stable over the population of study. An example of this technique lies in magnetic resonance (MR) brain imaging for different types of segmentation [170].

### 4.3 Airway Segmentation Methods: Background

#### 4.3.1 Overview

Over the last two decades, several methods for airway segmentation starting from chest CT images have been developed. Several techniques, both automatic and semi-automatic, aiming at obtaining a segmentation which is as complete as possible, have been proposed. However, the problem of airway segmentation still represents a big challenge for researchers around the world. Here the principal issues that limit image segmentation and that researchers are trying to overcome are examined. A brief introduction to different published methods for airway segmentation are then presented.

#### 4.3.2 Principal Limitations of Airway Segmentation

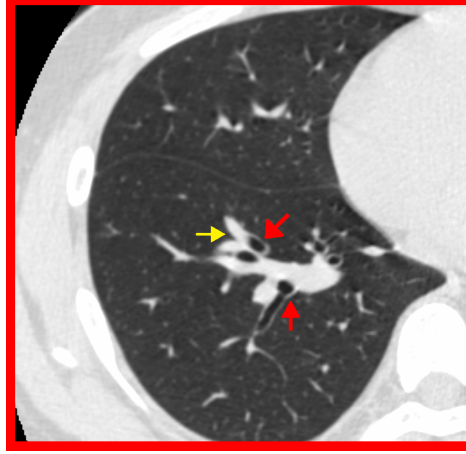
The lung airways tree presents a complex anatomy. In fact, starting from the trachea, with a diameter of about 25 mm, the bronchi continuously split into two (or more) smaller branches until the most distal bronchioles, after around 23 generations. Unlike the bronchi, which have rings of cartilage that serve to keep them open, the bronchioles are lined with muscular walls and they can be as small as 0.3-0.5 mm in diameter. This represents the first main issue when trying to segment the airways as, when bronchi are so small and with only soft muscular tissue to surround them, it becomes very difficult to distinguish them on a CT image.

The airway wall separates the inside space of the airway, or lumen, from the surrounding lung tissue. Since the airway contains air, this should appear with a low intensity on a CT image (around - 1000 HU), whereas the wall is supposed to have a higher intensity, causing a high contrast between the two regions. Furthermore, vessels usually run parallel to airways branches and they appear substantially brighter than the lung tissue. Therefore, on a CT image, airways can usually be recognized as a strong black part surrounded by a white contour and close to a uniform white circular region. Figure 4.2 shows an example of typical airways (red arrows) and vessels (yellow arrow) on a axial chest CT image. However, when the bronchi narrow and the airway walls become thinner



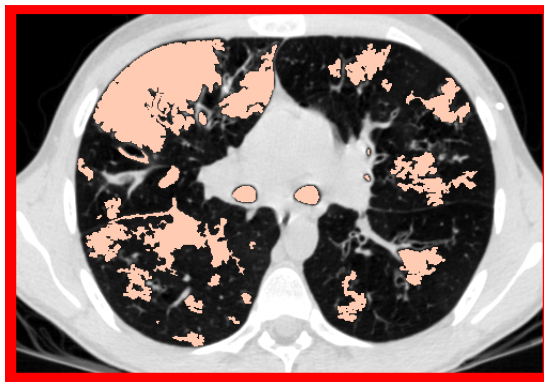
### 4.3 Airway Segmentation Methods: Background

---



**Figure 4.2:** Example of airways (red arrows) and vessels (yellow arrow) on a axial chest CT image.

and less recognizable from the lung tissue (due to similar HU value of muscular and soft tissue), a partial volume effect is more likely to appear. This leads to a blurring of the airway wall and decreases the contrast between the lumen, wall, and lung tissue. For this reason, one of the biggest risks in airway segmentation is the phenomenon referred to as leakage. This phenomenon is characterized by an “explosion” of the segmentation outside the airway tree into the lung tissue, due to similar intensity HU values in nearby tissues (see Figure 4.3). Over the



**Figure 4.3:** Example of leakage on a axial chest CT image. The segmentation (pink) “explodes” including pixels of the lung tissue surrounding the airways.

last two decades, several attempts to find a good method to segment as many

## 4. AIRWAY SEGMENTATION

---

airway branches as possible, while avoiding leakage, have been proposed.

Another main issue in the field of airway segmentation is the difficulty in comparing results from different researchers. Algorithms are commonly tested only on specific image types and their reliability is usually not proven across images acquired using different characteristics, such as slice thickness, reconstruction kernel and radiation dose. Furthermore, algorithms are normally not freely available, making comparison with other methods particularly complicated. For this reason, in 2009 a new challenge aiming to compare different algorithm performance using the same database was launched [171]. This challenge is referred to as the EXACT'09 challenge and consists of a total of 40 CT chest images publicly available. Among them, 20 cases have to be used for training of the algorithm, and the remaining 20 cases can be used for testing. The challenge is still open and authors can compare results with those of the other teams that took part in the challenge.

At the moment, results from 15 different teams are available online. To evaluate and compare results, a reference segmentation was constructed using all the correctly segmented branches of all teams as a “gold standard”. However, since 2009 this gold standard has never been made publicly available, so individual results have to be sent to the EXACT'09 authors, making a direct comparison quite complicated. Moreover, only the results of teams who took part in the challenge in 2009 are available online, while those of other teams that evaluated the performance of their software on the EXACT'09 database are not published online.

Finally, the gold standard was constructed considering only the results of the 15 initial team that presented the results in 2009 and it has not been updated since then. This gives rise to difficulties when a new method may outperform all the other 15 teams of the challenge. In this case, the new segmented branches would be detected as incorrect branches or considered as leakage, since they were not included within the original gold standard.

## 4.4 Background

Here, some of the different methods for airway segmentation starting from CT images that have been developed in the last two decades which rely on the underlying techniques discussed in Section 4.2 are examined. Computerized airway segmentation techniques are usually classified into two categories; automated and semi-automated methods. Automated methods require no user interaction and automatically try to identify the airways, whereas semi-automated algorithms may need the user to undertake some simple action before the segmentation itself initiates. As an example, in most of the semi-automated methods the user is asked to simply place a seed point inside the trachea (easily recognisable) of the CT image.

Many airway segmentation techniques rely on a region-growing approach, a fast method that requires no prior knowledge of the structure of the airway, and uses a seed voxel and an intensity threshold to separate air from tissue voxels [169,172–175]. The main problem with this technique is leakage, caused by voxels misclassified as air voxels.

To address this problem, several solutions have been proposed. One of the first methods, proposed by Mori et al. [172], used a 3D painting algorithm to directly extract the inside of the airway tree automatically increasing the intensity threshold until leakage occurs. This approach is able to stop the segmentation before leakage occurs, but is not able to segment peripheral branches. This method represents the basis of most of the methods using a region growing approach, with modifications to improve segmentation. The method proposed here is an improved version of Mori’s approach.

Schlathölter et al [169] implemented a fast marching algorithm in which wave-front propagation is used in conjunction with an anatomical model of the airway tree to implement a region growing algorithm, which ends when leakage occurs in all the directions of propagation. The main disadvantage of this method is the complexity of the specific speed function and the high computational complexity that make the algorithm not a good candidate for airway segmentation to be used with VB.

## 4. AIRWAY SEGMENTATION

---

A good trade-off between computational complexity, leakage presence and segmentation results is absolutely essential. Therefore, Lo et al [176, 177] proposed an algorithm where an airway appearance model is used in combination with a vessel tree segmentation to develop a classifier able to automatically discern between airways and surrounding tissue voxels using local descriptors. This approach provides good results, but requires the user to find an accurate training dataset which has to be large enough to be able to create the airway appearance model and properly classify the pixels.

Kiraly et al [178] proposed an algorithm using a 3D region growing method based on Mori's algorithm to segment larger airways, combined with specific morphologic operators to improve the segmentation. To avoid leakage an empirically found maximum number of allowed voxels is used. This is not an optimal solution, due to the different CT reconstruction parameters and lungs dimensions. Moreover, the algorithm is tested only on personal dataset, that are not publicly available, so that a proper comparison of results is not possible. The method presented here starts from Kiraly's idea to avoid leakage, but instead of considering a fixed maximum number of allowed voxels, this is identified based on trachea dimensions and scan parameters.

Salito et al [179] applied a simple 3D region growing, similar to Mori's algorithm, on healthy subjects and patients with severe emphysema, to evaluate the effect of emphysema on airway segmentation. This method is used to only confirm that a region growing approach is not optimal in case of patients with emphysema and can not be used for real applications, as the development of a VB system.

Graham et al [180–183] proposed a method in which a first adaptive region growing method similar to [172] is applied. An empirically found maximum number of allowed voxels is used. Afterwards, branch segments are identified considering tube-like structures. Finally, neighbouring branch segments are connected by smooth interpolated surfaces. Despite the great results obtained, this method was tested only on 23 personal cases and manual interaction is required to improve results.

Irving et al [184] extended the morphology based method proposed by Pisupati et al [185], by including a three dimensional morphological filtering and leak

## 4.5 Airway Segmentation: Implementation

---

removal using 3D dilation. Recently, a further extension of this approach has been presented [186], which proposes integration of the airway tree topology and branch shape to help identify and segment missing branches. However, this method is applicable only as a second step for airway segmentation, following an initial rough segmentation.

Rudyanto et al [187] presented an airway posterior probability model that exploits a novel multi-scale wallness measure to develop a probabilistic map that may help to optimize the cost function for region growing or fast marching-based algorithms. However, this algorithm was applied and tested only on 2D images and application to 3D images resulted difficult and computationally expensive.

Finally, Xu et al [188] proposed a hybrid multi-scale approach that combines intensity-based region growing with a morphology-based method using a multi-scale vesselness to try to segment peripheral branches while avoiding leakage. The main drawback of this system is the impossibility to compare results, as the algorithm was tested only on personal cases.

In the presented research, a novel semi-automatic algorithm for airway segmentation that uses an iterative region growing approach with voxel intensity as criteria to avoid leakage is presented. The method starts from Mori's region growing approach, improving it by modifying the stopping criteria. Unlike previous works, trachea, right and left lungs are cropped and segmented individually so that segmentation of one part does not affect the other. In order to stop the segmentation before leakage appears, a novel method to identify a maximum number of voxel based on CT and patients characteristics is introduced. Moreover, the algorithm is publicly available, facilitating comparison of results on personal datasets, and a novel study on the effect of CT parameters on airway segmentation has been accomplished.

## 4.5 Airway Segmentation: Implementation

### 4.5.1 Introduction

For the development of the algorithm used here, the freely available and easily extendible software platform, 3D Slicer, has been used [55–57, 75]. The algorithm

## 4. AIRWAY SEGMENTATION

---

has been mostly written in C++ and Python, exploiting the functionality of the ITK [60, 61] and VTK [59] classes. The described algorithm is available as an extension of Slicer and can be downloaded and tested on personal datasets. The source code is also freely available online, so that it can be modified according to different needs. The method is based on a modified 3D region growing algorithm that uses an intensity threshold as an inclusion criteria. In particular, only voxels having an intensity value below a certain threshold are considered as part of the segmented airways. To avoid leakage due to possible noise from various sources that may blur some airway walls, the threshold is iteratively modified and optimised until leakage appears. Other parameters, such as the number of voxels included in the segmented region at each iteration, have been optimised based on robustness of results across all datasets.

When using a single threshold for the segmentation, the approach might stop the segmentation too early, causing peripheral airways to be excluded from the segmented region. For this reason, the lung volume is first subdivided into three different parts; trachea, right and left lungs. This way, the three parts can be segmented individually, using three different thresholds, each of which will be specific and optimal for each airways part. Previous methods [178, 182, 189] sought to stop the segmentation before leakage appears based on an empirically pre-defined maximum number of voxels that can be included in the segmentation. This greatly limits the segmentation, especially considering the great variability in airway size and anatomy among different patients and CT images. For this reason, the proposed method determines the maximum number of voxels for the two lungs based on the number of voxels included in the trachea region.

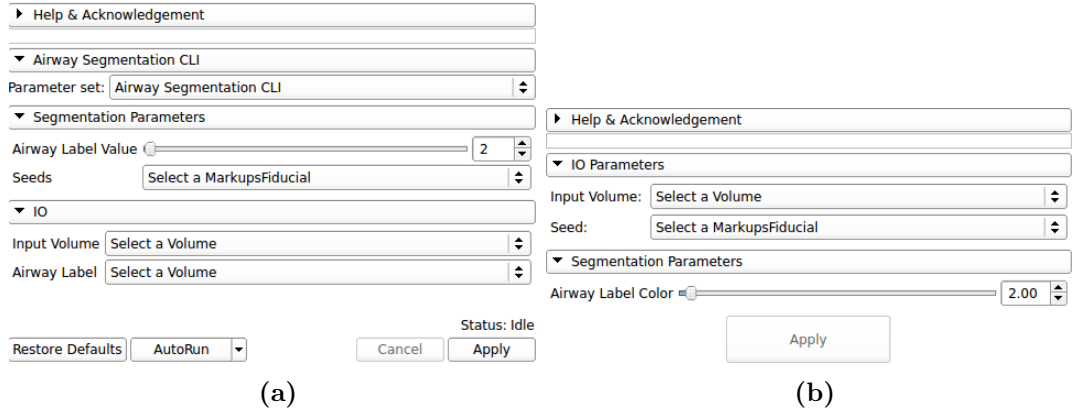
### 4.5.2 Overview of Algorithm Versions

The airway segmentation algorithm underwent three different iterations over the course of the implementation process, which involved modifications and improvements in order to obtain better results and more reliability. Reviews and questions from several users around the world helped to fix possible bugs and improve the software performance. Each version is detailed below in order of online appearance and a summary of the versions is reported in Table 4.1.

## 4.5 Airway Segmentation: Implementation

### Version 1.0

In the first version of the algorithm, the user was required to place three seed points on the CT image; one within the trachea, and the other two inside the two main bronchi. The points' positions were used to split the volume into the three different parts and as starting points for the three different segmentation processes. Also, a pre-defined maximum number of voxels was used in order to prevent leakage in the right and left lungs. The algorithm used the Slicer interface for common language interface (CLI) modules. This way, beside the three seed points, the user needed to also select the input and the label volumes to be used for the airways identification. This version of the algorithm was tested on the EXACT'09 cases, and while it showed good results in terms of leakage, the performance was not optimal in terms of segmented branches when compared to other methods [190]. Placing the two fiducials in the main bronchi was not always an easy task. Figure 4.4(a) shows an example of mode of operation of the first version of the algorithm.



**Figure 4.4:** Airway segmentation algorithm interface of (a) version 1.0 and (b) version 1.2. In (a) seeds, input and label volumes had to be created and selected. With the new version (b) Only input volume and seed point have to be selected. In both cases the label value can be manually changed (default = 2).

### Version 1.1

For the second version, the aim was to use only one seed point to be placed in the

## 4. AIRWAY SEGMENTATION

---

trachea for starting the segmentation and to obtain better results in terms of segmented branches. This was achieved exploiting the anatomical knowledge of the trachea, which can be separated from the rest of the lung volume considering the seed point position. Two segmentations of the trachea were then implemented. A first segmentation is obtained from the cropped trachea volume. Then, the point in which the trachea splits into the two main bronchi is searched and used to refine the cropping of the trachea volume. The central point of the two main bronchi labels is then used as starting point for the left and right lungs segmentation. Also, the maximum number of voxels was determined as a percentage of the number of voxels of the segmented trachea. While maintaining low leakage appearance, this version also showed good segmentation results. However, the algorithm still used a CLI interface and was not generalized for different CT scanner types and parameters.

### Version 2.1

For the final version, a new interface for the module was implemented in Python (see Figure 4.4(b)). This way, the only action required of the user is to place one seed point within the trachea and trigger the algorithm. Moreover, this new version has been extended and adapted to different types of CT scanners and parameters. The algorithm reads the DICOM metadata of the images to automatically identify kernel and slice thickness used to reconstruct the CT image and determine an optimised maximum number of voxels to avoid leakage. At the end of the segmentation process, a 3D model of the airway is automatically reconstructed and visualised on the 3D view panel of Slicer. In this way the user does not have to manually create a 3D model of the airway every time a new case is analysed and segmented. This version was tested on several clinical and *ex-vivo* cases, including the EXACT'09 cases, showing good results in terms of both leakage and segmented branches. Details of the implementation of this version are reported below.



## 4.5 Airway Segmentation: Implementation

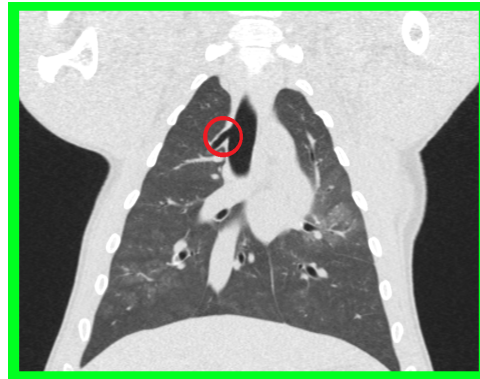
Version	User Interaction	Interface	Max Number of Voxels	Generalized
1.0	3 seed points	CLI	Empirically pre-determined	No
1.1	1 seed point	CLI	Based on trachea voxel count	No
1.2	1 seed point	Python	Based on trachea voxel count	Yes

**Table 4.1:** Airway segmentation algorithm versions.

### 4.5.3 Algorithm Implementation

#### 4.5.3.1 Overview

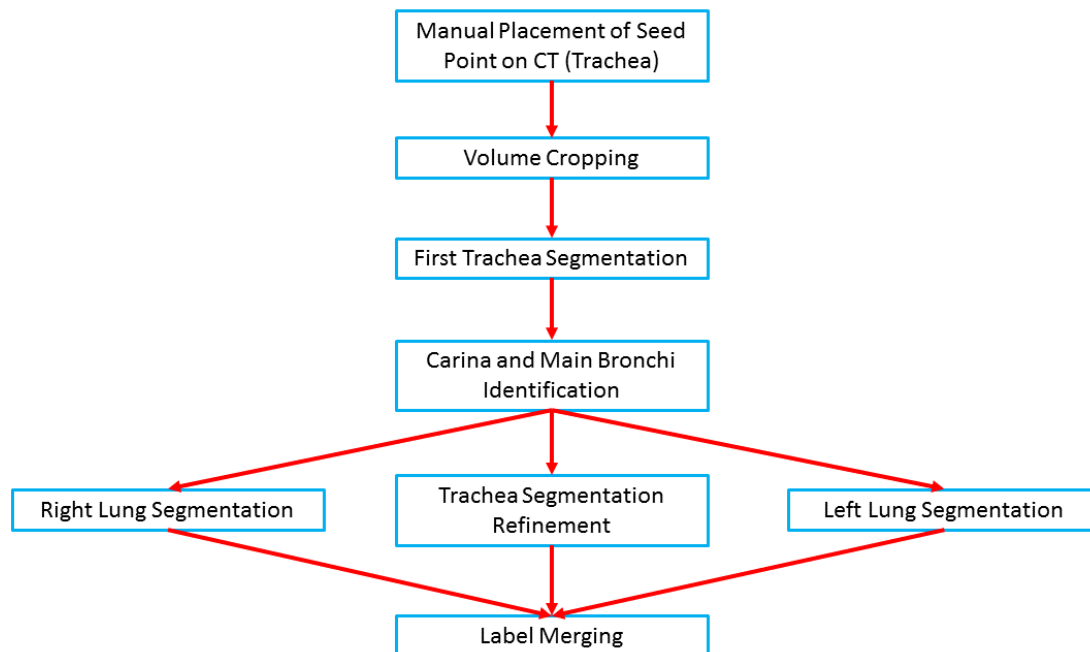
The airway segmentation method belongs to the group of methods referred to as semi-automated, as it requires the user to manually place a seed within the trachea, which is easily recognizable in an axial CT image. Different approaches, such as De Nunzio et al [191], automatically find the trachea in the first slices of the CT scan. However, these systems work only for the human trachea, while the system described here is intended to be as general as possible, considering non-human images as well. As an example, in airways which have a branch leaving the trachea above the carina, as in the case of a pig airways (see Figure 4.5), the seed point has to be placed between this branch and the carina. Therefore, manual placement of the seed point can be considered as a good trade-off between versatility and automation. Figure 4.6 shows the steps involved in the implementation of the algorithm. The different steps are here detailed.



**Figure 4.5:** Coronal CT image showing a pig lung. The additive bronchus coming out of the trachea above the carina is indicated in the red circle.

## 4. AIRWAY SEGMENTATION

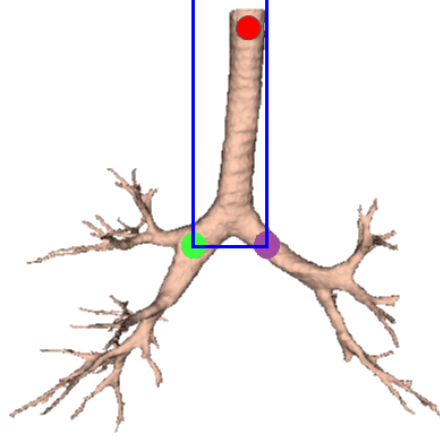
---



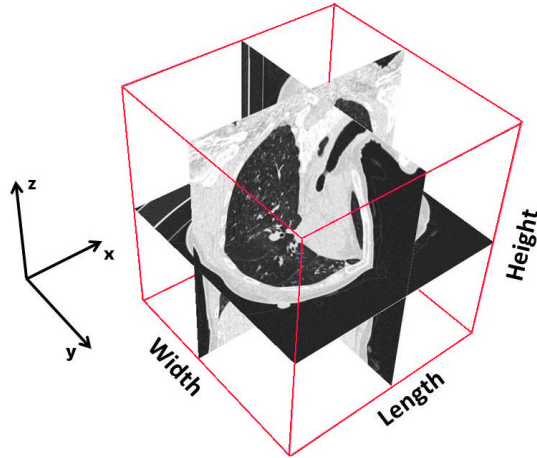
**Figure 4.6:** Scheme of the steps involved in airway segmentation.

### 4.5.3.2 Volume cropping

The algorithm's first step involves cropping the whole volume in order to extract the trachea. In version 1.0, the volume was cropped exploiting the placement of the three seed points. In particular, a fixed rectangular area that extended from the seed point in one bronchus to the next and that included the whole trachea was cropped. Figure 4.7 shows how the cropping was implemented in version 1.0. However, the placement of the points was not always easy and could hugely affect the results of the segmentation. In fact, different positions of the two points in the main bronchi in some cases could yield different results, and, in some cases, part of the trachea could be cropped out inadvertently (Figure 4.7). Therefore, the placement of only one fiducial and automatic cropping was absolutely necessary for the new versions. To this end, an average trachea length (with a safe margin), the whole volume width, and a height given by the whole volume minus a small portion of volume itself are considered starting from the seed point (for definition of depth, width and length in a 3D volume see Figure 4.8). Using this cropped volume, the initial segmentation of the trachea starting from the placed seed



**Figure 4.7:** Example of volume cropping in version 1.0 of the algorithm. The seeds point are represented by the circles, while the trachea volume as it would be cropped by the approach is showed on the blue rectangle. In this case, due to the seeds' position the entire trachea is included in the cropped volume, but a slightly different position of the purple seed might exclude some part.

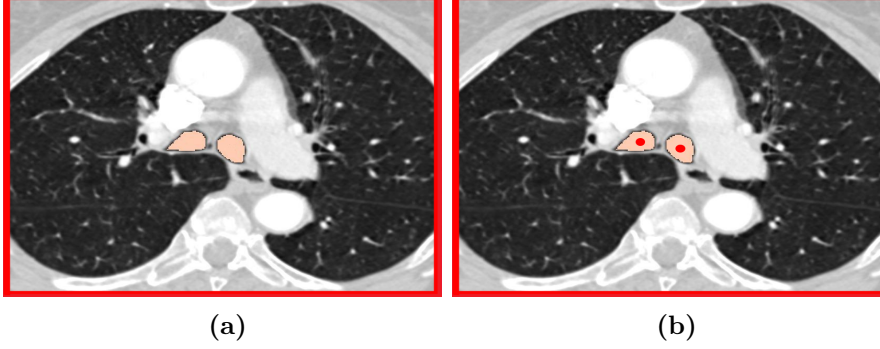


**Figure 4.8:** Representation of length, width and height in a 3D volume as utilised in this approach.

point is accomplished. Details of how trachea segmentation is performed are reported in Section 4.5.3.3. Once this first segmentation is completed, the second step involves using the obtained trachea label to improve the cropping of the trachea volume. To achieve this, the carina position is computed automatically, by scanning from the fiducial position and moving slice by slice towards the carina

## 4. AIRWAY SEGMENTATION

---

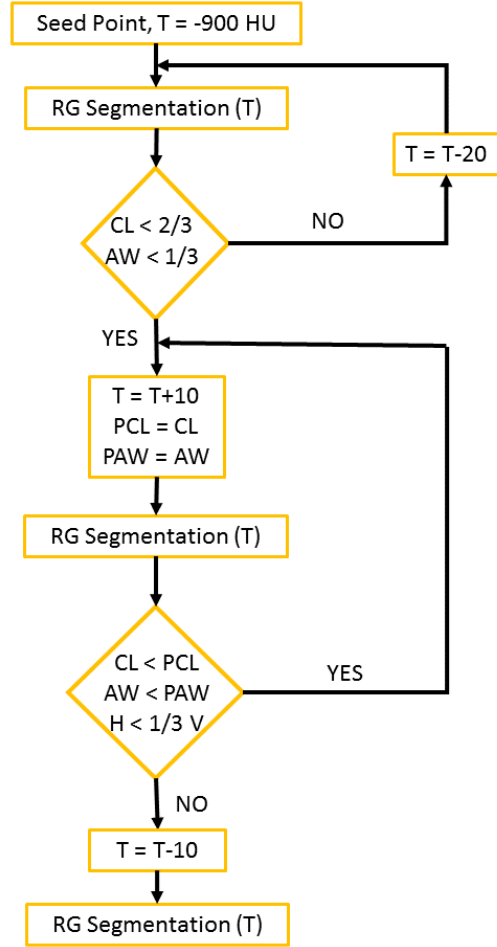


**Figure 4.9:** CT axial slice showing (a) the carina slice as found by the presented approach and (b) seed points representation (red circles) of seed points as automatically identified and placed on the main bronchi.

along the axial slices. The algorithm recognises the carina as the point in which the segmented label splits into two different parts, representing the two main bronchi. As an example, Figure 4.9(a) shows the carina position as found on an axial CT image after the first trachea segmentation. The algorithm's third step uses the carina position to compute the maximum height of the trachea, and the volume is cropped accordingly. Simultaneously with this third step, the cropping size is also updated in length, to take into account possible bends in the trachea. This is achieved by moving slice by slice along the  $z$  axis and identifying points in which the label touches the side borders of the previously cropped volume, in which case the cropping is extended in length. The fourth step involves a second and final trachea segmentation of the new cropped volume. Once the trachea label is finalised, the carina position within the trachea label is used to automatically define the seed points for the segmentation of the right and left lungs.

### 4.5.3.3 Trachea Segmentation

Figure 4.10 shows the block diagram of the implementation of trachea segmentation. The seed point placed by the user is exploited as starting point for the segmentation of the trachea. Starting from a value of  $-900$  HU, the threshold is iteratively and automatically increased until it either reaches the maximum value



**Figure 4.10:** Block diagram of the implementation of trachea segmentation.  $T$  stands for threshold,  $CL$  and  $PCL$  for coronal length and previous coronal length, while  $AW$  and  $PAW$  are used for axial width and previous axial width. Finally,  $V$  stands for volume.

## 4. AIRWAY SEGMENTATION

---

of  $-800$  HU or leakage occurs as outlined presently. At the initial threshold the volume is segmented and the width of the obtained trachea's label is computed. To this end, a small region of the axial section of the label around the seed point's position is extracted and the width is calculated. Simultaneously, a small set of coronal images of the label is also extracted and its length computed. As a check on the subsequent automatic segmentation of the trachea, these computed values are compared with the entire cropped volume of the trachea. If the label has a coronal length of less than two thirds of the whole cropped volume and an axial width less than one quarter of the whole cropped volume, it is assumed that no leakage has occurred and the two label sizes are stored. Otherwise, the threshold is repeatedly decreased in increments of  $20$  HU until leakage is no longer evident.

On the other hand, if  $-900$  HU is not high enough as an initial threshold to obtain trachea segmentation, voxels around the seed point are first evaluated as new possible starting points, and if none of the  $26$  touching voxels gives a segmentation, the threshold is increased in increments of  $50$  HU and the previously described process repeated.

At this point, the threshold is iteratively increased to check whether it is possible to obtain improved segmentation (i.e., segmentation of more peripheral branches without leakage appearance). Again, if no leakage has occurred in the previous step,  $50$  HU is added to the threshold. If leakage has previously occurred  $10$  HU is added. Hence, a new segmentation is computed and the old and new labels are subtracted. In this way, differences referring to how much trachea label has been added using the new threshold can be calculated. Width and length of these differences are computed and compared with the previously stored values. This process is repeated until either the size of the added labels is larger than the memorized sizes or the height of the label is less than one third of the height of the trachea volume. If the previous conditions on size of the added label are not satisfied, leakage is likely to occur. In this case, the threshold is repeatedly decreased in increments of  $10$  HU until a label with no leakage is obtained.

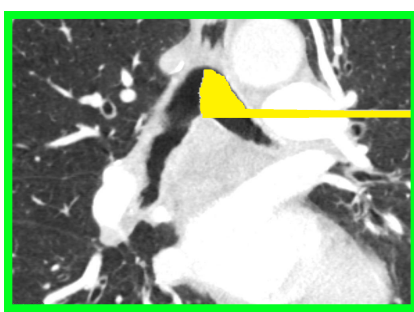
### 4.5.3.4 Right and Left Airways Segmentation

The right and left lungs have to be separated and segmented. In order to do so, the algorithm uses half of the trachea label obtained to “mask” the trachea in

## 4.5 Airway Segmentation: Implementation

---

the original CT volume. In particular, the half trachea distal from the lung to be segmented is considered. In the original image the intensity value of all the “masked” voxels inside the trachea is set to 0 HU, which is a value much higher than the threshold that will be used for the airway segmentation. In this way, it is not necessary to crop the volume again and only one lung at the time is iteratively segmented. Figure 4.11 illustrates how the left half of the trachea is “masked” to segment the right lung. The yellow part represents voxels that have been given



**Figure 4.11:** Example of “masking” as it appears on a sagittal slice. Half trachea label is used to turn values where the half trachea overlays to 0 HU (yellow voxels). In the picture, the left part of the trachea is masked, to allow segmentation of the right lung. A closing process is also used to make sure that no spreading within the left lung is obtained.

a 0 HU value. As shown in the picture, a method to “close” the opposite main bronchus has also been implemented, so that segmentation of one lung does not spread within the other one. Using half of the trachea label to mask the trachea at this stage facilitates segmentation of animal lungs, such as the pig lung, where a tracheal branch may be present above the carina. Obviously, this branch is not segmented during the trachea segmentation, due to the volume cropping, as this would lead to an incomplete segmentation. With the proposed method, the segmentation is spread into part of the trachea itself allowing the segmentation of any possible branch above the carina position. As the starting points to be used for segmentation, two seed points are automatically defined on the axial slice containing the carina. The seed points represent the respective centre points of the two parts into which the label splits, as shown in Figure 4.9(b). As was the case for the trachea, segmentation of the right and left lungs uses a 3D region

## 4. AIRWAY SEGMENTATION

---

growing method with an iteratively increased threshold. However, in this case leakage occurrence is controlled by two approaches, based on Tschirren et al [189]. Firstly, any sudden increase in the number of voxels between segmentations with two consecutive thresholds is considered leakage. Secondly, a maximum number of allowed voxels for the segmentation is also defined. In order to define when the increase between two successive segmentation steps is large enough to lead to leakage, the parameter  $g$  of (4.1) is defined.

$$g = \frac{N_{vox}}{N_{vox-1}} \quad (4.1)$$

In 4.1,  $N_{vox}$  is the number of voxel of the actual segmentation, while  $N_{vox-1}$  represents the number of segmented pixel of the previous segmentation.  $g$  is computed and compared to  $g_{max} = 1.6$ , as in [189]. A value of  $N_{vox,max} = 500,000$  for the maximum number of voxels allowed in the segmentation is proposed in [189], while in other works maximum volumes  $V_e = 50,000 \text{ mm}^3$  [178] and  $V_e = 75,000 \text{ mm}^3$  [182] were defined.

Since only part of the lung is considered, a novel idea is that  $N_{vox,max}$  be related to the number of voxels of the trachea. In particular, a specific percentage of the number of trachea voxels is used, based on the size of the trachea. This percentage can be optimised according to the different characteristics of the dataset under inspection. Table 4.2 summarizes the optimised percentages depending on the CT characteristics, such as reconstruction kernel and slice thickness. These values have been empirically calculated from the datasets available to date. Also, a general percentage for not yet inspected datasets is provided. In this sense, since datasets acquired with all the possible combination of parameters were not available, percentages have been optimised for the types of datasets available. However, since the system is open-source, parameters may be continuously updated and optimised when new datasets are considered.

As showed in the results section, the chosen percentage values are quite appropriate to achieve a good trade-off between leakage and accurate segmentation of branches and provide a reliable method across different CT scan images acquired with various parameters. Finally, once the right and left lungs' labels are obtained, they are merged with the trachea's segmentation to create a unique inseparable airway label. In some cases, the label might present some disconnected



## 4.5 Airway Segmentation: Implementation

# of Slices ( $S$ )	# of Voxels ( $N$ )	Percentage
<b>STD, B20f, B30f, B, C, FC10, FC12</b>		
$S \leq 300$	$N > 5 \times 10^4$	0.5
	$2 \times 10^4 < N \leq 5 \times 10^4$	0.75
	$N \leq 2 \times 10^4$	0.9
$300 < S \leq 400$	$N > 10^5$	0.5
	$8.5 \times 10^4 < N \leq 10^5$	0.75
	$N \leq 8.5 \times 10^4$	0.9
$S > 400$	$N > 17 \times 10^4$	0.5
	$14 \times 10^4 < N \leq 17 \times 10^4$	0.75
	$N \leq 14 \times 10^4$	0.9
<b>LUNG, B50f, FC50, FC52</b>		
$S \leq 300$	$N > 8.5 \times 10^4$	0.2
	$7.5 \times 10^4 < N \leq 8.5 \times 10^4$	0.3
	$3.5 \times 10^4 < N \leq 7.5 \times 10^4$	0.35
	$10^4 < N \leq 3.5 \times 10^4$	0.5
	$N \leq 10^4$	0.8
$300 < S \leq 400$	$N > 12 \times 10^4$	0.2
	$10^5 < N \leq 12 \times 10^4$	0.35
	$8.5 \times 10^4 < N \leq 10^5$	0.5
	$N \leq 8.5 \times 10^4$	0.7
$S > 400$	$N > 14 \times 10^4$	0.2
	$11.5 \times 10^4 < N \leq 14 \times 10^4$	0.35
	$8 \times 10^4 < N \leq 11.5 \times 10^4$	0.5
	$N \leq 8 \times 10^4$	0.75
<b>B60f, B70f, B70s, D</b>		
$S \leq 300$	$N > 9 \times 10^4$	0.35
	$6 \times 10^4 < N \leq 9 \times 10^4$	0.5
	$3 \times 10^4 < N \leq 6 \times 10^4$	0.6
	$N \leq 3 \times 10^4$	0.8
$S > 300$	$N > 12 \times 10^4$	0.25
	$8 \times 10^4 < N \leq 12 \times 10^4$	0.4
	$5 \times 10^4 < N \leq 8 \times 10^4$	0.6
	$N \leq 5 \times 10^4$	0.8
<b>Any other Kernel</b>		
$S \leq 300$	$N > 9 \times 10^4$	0.35
	$4 \times 10^4 < N \leq 9 \times 10^4$	0.55
	$N \leq 4 \times 10^4$	0.8
$S > 300$	$N > 13 \times 10^4$	0.3
	$7 \times 10^4 < N \leq 13 \times 10^4$	0.55
	$N \leq 7 \times 10^4$	0.8

**Table 4.2:** Percentage of trachea voxels used for different reconstruction kernels and slice thicknesses.  $S$  is used to take into account the different slice thicknesses. (a) Kernels: GE Medical System Standard, Siemens B20f and B30f, Philips B and C, Toshiba FC10 and FC12; (b) Kernels: GE Medical System Lung, Siemens B50f, Toshiba FC50 and FC52; (c) Kernels: Siemens B60f, B70f and B70s, and Philips D; (d) Any other kernel.

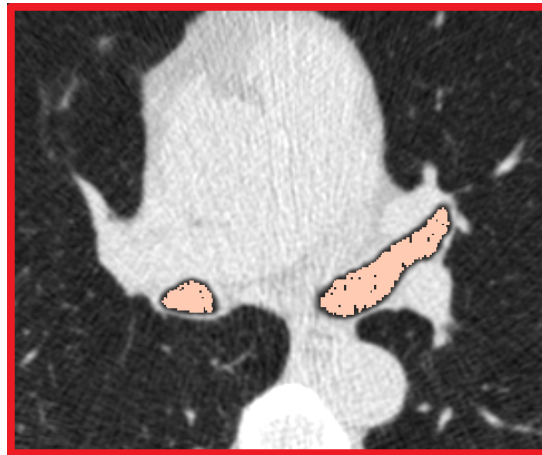
## 4. AIRWAY SEGMENTATION

---

parts. Therefore, as a final step a morphological closing and a hole filling step are used to connect these potentially disconnected parts.

### 4.5.3.5 Binary Image Closing

The airways label obtained from the previous steps can be considered as a binary image in which all the voxels identified as airways have a non-zero value and all the remaining have a value of zero. This binary image may contain some imperfections, such as small holes due to noise in the CT image (see Figure 4.12). For this reason, a morphological image processing step may help to improve

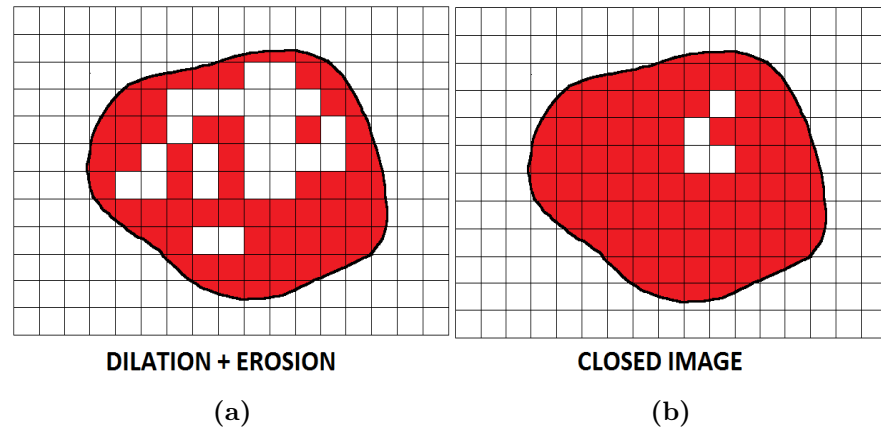


**Figure 4.12:** Example of small holes on the airways label due to noise. The label (pink) is shown overlaid on an axial CT image zoomed on the area of interest.

the quality of the image. Morphological image processing is a technique for the analysis and processing of images, which is mostly applied to binary images [192]. It consists of a collection of non-linear operations related to shape, or morphology, of the features in an image. In particular, these techniques utilise a small template called a structuring element, or kernel, which is “compared” with all the neighbouring voxels to the voxel under investigation in the image using a set operator (intersection, union, inclusion, complement). The voxels that pass the test are assigned a non-zero value. The basic operators of morphological image processing are dilation and erosion and all the other operators such as opening and closing, are a combination of these two operators. Dilation usually

## 4.5 Airway Segmentation: Implementation

uses the structuring element to gradually enlarge the boundaries of regions of non-zero voxels. Therefore, the area of the region is expanded, and holes within that region become smaller. Conversely, erosion is usually used to shrink the boundaries of regions with non-zero values. This way, the area of the region is reduced and holes become larger. Closing is another important morphological operator and, like its dual operator, opening, it is derived by a combination of erosion and dilation. In particular, a closing operation consists in a dilation followed by an erosion using the same structuring element. The effect of this operator is to remove small (i.e., smaller than the structuring element) holes and tube like structures in the interior or at the boundaries of the image. Figure 4.13 represents the scheme of a closing operation. Closing is similar in some way to dilation, as it tends to enlarge a region and reduce its holes. In order to keep the original boundary shape, the structuring element has to be “small enough”, affecting at the same time the reduction of the holes. For this reason, a structuring element with a circular shape and  $11 \times 11 \times 11$  pixels is used in this work. However, to further reduce possible holes in the binary image, the closing operation is followed by a voting fill hole filter.



**Figure 4.13:** Morphological closing scheme. (a) A region with small holes (white parts inside the red region). (b) After the closing operation the red region has grown and the holes become smaller.

## 4. AIRWAY SEGMENTATION

---

### 4.5.3.6 Binary Voting Fill Hole Filter

This filter aims at filling medium size holes and cavities (tens of voxels) inside the boundary of a binary image applying a voting operation. A squared structuring element is used to probe the image and determine if a voxel should be included in the non-zero region. The filter runs iteratively until no voxels are changed between two iterations or until a maximum number of iteration is reached. In principle, the number of iterations should be chosen based on the size of the holes to be filled in. The larger the holes expected, the higher the number iterations should be in order to fill in the full hole. In the proposed method, a neighbourhood size of  $3 \times 3 \times 3$  pixels was chosen, with 10 as maximum number of possible iterations.

## 4.5.4 Algorithm Performance

### 4.5.4.1 Overview

In this section, the method used to test algorithm performance is described. The datasets that have been used are first presented. Then, the methods used to evaluate the performance of the algorithm are described. Finally, the results obtained from the testing are shown and the conclusions are summarised.

### 4.5.4.2 CT Datasets

Many reported airway segmentation algorithms have been tested only on specific types of images, making evaluation of reliability across different platforms problematic. Parameters such as slice thickness, reconstruction kernel and radiation dose greatly affect the quality of the image, and thus the quality of segmentation may vary hugely. For these reasons, the algorithm was tested on twenty four human cases and several breathing pig lung CT scans across multiple scan parameters; slice thickness, convolution kernel, and radiation dose have been considered. For the human cases, the twenty test cases from the EXACT'09 dataset [171] were used and the proposed method was compared with the other teams who participated to the challenge. From the twenty test cases of the challenge, six cases belonging to the same subject, reconstructed using different parameters, were then extrapolated. The algorithm was also tested on four local clinical cases

## 4.5 Airway Segmentation: Implementation

---

belonging to different subjects but reconstructed with the same convolution kernel.

Since twenty four cases are not sufficient to determine true reliability of the algorithm, several CT scans of a phantom breathing pig lung were also used. These scans were all acquired from the same model varying convolution kernel, slice thickness, and radiation dose for each scan. Images from the pig lung model were acquired during simulated inspiration, expiration and half inflation. Forty-eight pig lung scans were obtained, in addition to clinical data. This is still not a sufficient number of scans, as thousands of cases would be needed, but it can be considered a sufficiently high number to assess the algorithm, especially considering the difficulty in comparing different methods.

### Human Cases

Four clinical chest CT scans were acquired at CUH using a GE Medical System scanner from four different subjects. The first two scans were acquired using a Discovery CT750 HD CT scanner, case 3 was scanned using a GE LightSpeed VCT scan, whereas the CT model for case 4 was the GE Discovery STE. The four patient scans were all provided by the Cork University Hospital (CUH) in compliance with an approved ethical protocol by the Cork Research Ethics Committee. They all belonged to patients with suspicious lung cancer and were selected from the regional multidisciplinary thoracic oncology meeting. Datasets were generated using a standard scanning protocol for lung cancer patients, i.e., asking the patient to hold a full-inspiration breath for less than 20 s to reduce motion artifacts. A voltage of 120 kVp was used for all cases, while the tube current varied from 60 to 200 mA as determined by automatic tube current modulation. Slice thickness was 1.25 mm for all the datasets. The final 3D images were all reconstructed using a lung convolution kernel and an ASIR reconstruction technique. Table 4.3 reports acquisition parameters for the CUH cases.

In order to evaluate the algorithm on a larger database, the EXACT'09 challenge [171] was considered. The datasets are publicly available and Table 4.4 presents acquisition parameters of the twenty test cases. Numbers of the cases represent the indices from the EXACT'09 project. The presented algorithm does not require any training, so the first twenty cases of the database were not used. Since the

## 4. AIRWAY SEGMENTATION

	Manufacturer	Model Name	Slice Thickness (mm)	Kernel	Tube Voltage (kVp)	Tube Current (mA)	I\ E
CUH 1	GE System	Discovery CT750 HD	1.25	LUNG	120	65	I
CUH 2	GE System	Discovery CT750 HD	1.25	LUNG	120	125	I
CUH 3	GE System	LightSpeed VTC	1.25	LUNG	120	60	I
CUH 4	GE System	Discovery STE	1.25	LUNG	120	170	I

**Table 4.3:** Acquisition parameters of the scans provided by CUH. I/E indicates full-inspiration (I) or full-expiration (E) breath-hold.

	Manufacturer	Model Name	Slice Thickness (mm)	Kernel	Tube Voltage (kVp)	Tube Current(mA)	I\ E
CASE 21	Siemens	Sensation 64	0.6	B50f	120	200.0	E
CASE 22*	Siemens	Sensation 64	0.6	B50f	120	200.0	I
CASE 23	Siemens	Sensation 64	0.75	B50f	120	200.0	I
CASE 24	Toshiba	Aquilion	1.0	FC12	120	10.0	I
CASE 25*	Toshiba	Aquilion	1.0	FC10	120	150.0	I
CASE 26	Toshiba	Aquilion	1.0	FC12	120	10.0	I
CASE 27*	Toshiba	Aquilion	1.0	FC10	120	150.0	I
CASE 28	Siemens	Volume Zoom	1.25	B30f	120	348.0	I
CASE 29*	Siemens	Volume Zoom	1.25	B50f	120	348.0	I
CASE 30	Philips	Mx8000 IDT 16	1.0	D	140	120.0	I
CASE 31	Philips	Mx8000 IDT 16	1.0	D	140	120.0	I
CASE 32	Philips	Mx8000 IDT 16	1.0	D	140	120.0	I
CASE 33	Siemens	Sensation 16	1.0	B60f	120	103.6	I
CASE 34	Siemens	Sensation 16	1.0	B60f	120	321.0	I
CASE 35	GE	LightSpeed 16	0.625	Standard	120	411.5	I
CASE 36	Philips	Brilliance 16P	1.0	C	120	206.0	I
CASE 37	Philips	Brilliance 16P	1.0	B	140	64.0	I
CASE 38*	Philips	Brilliance 16P	1.0	C	120	51.0	E
CASE 39	Siemens	Sensation 16	1.0	B70f	100	336.7	I
CASE 40	Siemens	Sensation 16	1.0	B70s	120	90.6	I

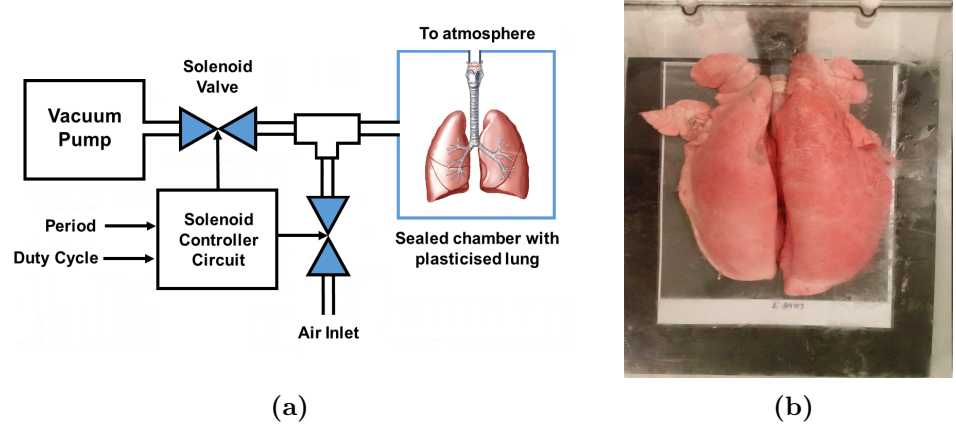
**Table 4.4:** Acquisition parameters of the twenty cases from the EXACT’09 dataset. I/E indicates full-inspiration (I) or full-expiration (E) breath-hold. Asterisk \* indicates that a scan was acquired from the same subject as the previous one.

goal of the work was also to compare clinical images reconstructed with different kernels but acquired with other CT platforms, six scans from the twenty cases of the EXACT’09 project [171] were further extrapolated and considered. In particular, three scans belonging to the same subject and acquired with the same scanner, but using different parameters, were chosen; cases 24 and 25 scanned with Toshiba Aquilion; cases 28 and 29 acquired using a Siemens Volume Zoom scanner; cases 37 and 38 that were obtained using a Philips Brilliance 16P scan.

### Breathing Pig Lung Model

To further investigate reliability of the algorithm, a breathing pig lung model was

## 4.5 Airway Segmentation: Implementation



**Figure 4.14:** Breathing pig lung model. (a) Scheme representing the breathing pig lung model. (b) Plasticised pig lung when fully inflated [30].

developed. To this end, a BioQuest Inflatable Lung kit (Nasco, Fort Atkinson, WI, USA) was used as a phantom for CT image acquisition (see Figure 4.14a). This kit consists of plasticised pig lungs (Figure 4.14b) which can be inflated to various levels as required. The lungs are placed in a vacuum chamber, with the trachea connected to atmospheric pressure. When the chamber is evacuated, the pressure differential between the outside and the inside of the lungs causes them to inflate. Venting the chamber to the atmosphere equalises the pressure which causes the lungs to collapse to an uninflated equilibrium form. The lungs were made to inflate and deflate in a programmable way to simulate standard breathing patterns. An Arduino Uno microcontroller was used to enable a set of solenoid valves (AD612 by CS Fluid Power) to control the lung inflation level. One valve connects to the vacuum pump, while another is used for venting the chamber. To set the breathing cycle, two dials are connected to the microcontroller. One dial controls the overall period of the cycle while a second one sets the inflation time as a percentage of the period. This simple low cost solution proved very effective in simulating the human breathing pattern. Using this model, 48 CT scans of the lungs were generated during inspiration, expiration and half inflation phases. For both inspiration and expiration eight different protocols were used to evaluate the effect on image quality. The scanner used to get computerized tomographic images was the GE Medical System Discovery CT750 HD with an

## 4. AIRWAY SEGMENTATION

---

ASIR reconstruction technique. The reconstruction kernel was varied between lung and standard kernels, and images were acquired at four different of slice thicknesses ranging from 5 to 0.625 mm. Three different levels of tube current and radiation exposure were used; a high radiation dose ranging from 60 to 160 mA, a medium dose of 40 mA and a low dose of 10 mA. Finally, an image at half inflation was acquired with a 0.625 mm slice thickness, high radiation dose and a standard reconstruction kernel to investigate the effect of lung inflation.

### 4.5.4.3 Evaluation Methods

To evaluate the performance of the algorithm, the airway labels from all the datasets described were generated. To this end, one seed point was manually placed in the trachea of each case exploiting the 3D Slicer functionalities. For the pig lung model images, the seed point has been carefully placed between the carina and the bronchus sus which leaves the trachea before the carina. The method has then been invoked, and the labels generated using the approach outline in Sections 4.5.3.3 and 4.5.3.4. The segmentation process took an average of 23 min to complete on a 64-bit, i7-3770, 8 GB computer.

From the generated labels, 3D models of the airways have been created leveraging the 3D Slicer model maker module, with parameters optimised for good visual results. No pre-filtering was used before the segmentation. Only in one case (for a pig breathing model that was scanned during inflation, with a 1.25 mm slice thickness, high radiation dose, and reconstructed with a lung kernel) a blur gaussian filtering was necessary to partially remove noise from the image and avoid leakage “explosion” during the segmentation.

For the evaluation of the EXACT’09 cases, the segmentation results obtained using the presented method were sent to the organizers who used the constructed reference segmentation to calculate results. The resultant performance measures are:

- Branch Count: the number of branches that were detected correctly, as compared to the gold standard described in Section 4.3.2.



## 4.5 Airway Segmentation: Implementation

---

- Percentage of Branches Detected: the fraction of branches that are correctly detected, with respect to the total number of branches present in the gold standard.
- Tree Length: the sum of the lengths of the centrelines of all correctly detected branches.
- Percentage of Tree Length Detected: the fraction of tree length in the gold standard that was correctly detected.
- Leakage Count: the number of disconnected (considering the 26 neighbours voxels) sources where leakage occurs. A leakage source is defined as “correct” voxels (relatively to the gold standard) that have at least one non-“correct” voxel within its 26-neighbours.
- Leakage Volume: the total volume of the regions that are not marked as “correct” in the gold standard
- False Positive Rate: the fraction of the total segmented volume that is not marked as “correct” compared to the gold standard.

For the remaining CUH clinical cases and the pig lung model cases, branch count, branch length, airway volume and leakage score were calculated and evaluated. For the branch count, correctly segmented branches were counted by visual inspection. The centreline of the airway label was then extracted exploiting the classes provided by the Vascular Modeling Toolkit (VMTK) [193] and this was used to compute the length of the branches. The sum of all branch lengths of a case was considered to compute the final branch length of that case. Airway volume was computed considering the number of label voxels combined with voxel geometry. Finally, the most important parameter, the leakage score, was used to determine the quality of the segmentation for each image. To this end, a new evaluation system for leakage detection was implemented. This method is detailed in Section 4.5.4.4.

For the pig lung breathing model, the correlation between segmentation metrics and CT acquisition parameters was also investigated. This analysis was possible only for the breathing pig lung model, as the clinical case data were too

## 4. AIRWAY SEGMENTATION

---

diverse for meaningful comparison. This analysis helped us further prove reliability of the algorithm across varying parameters. In particular, dose and slice thickness were included. The convolution kernel variation was not included in correlation outputs, as only two values are considered (i.e., lung and standard) and correlation was always maximum.

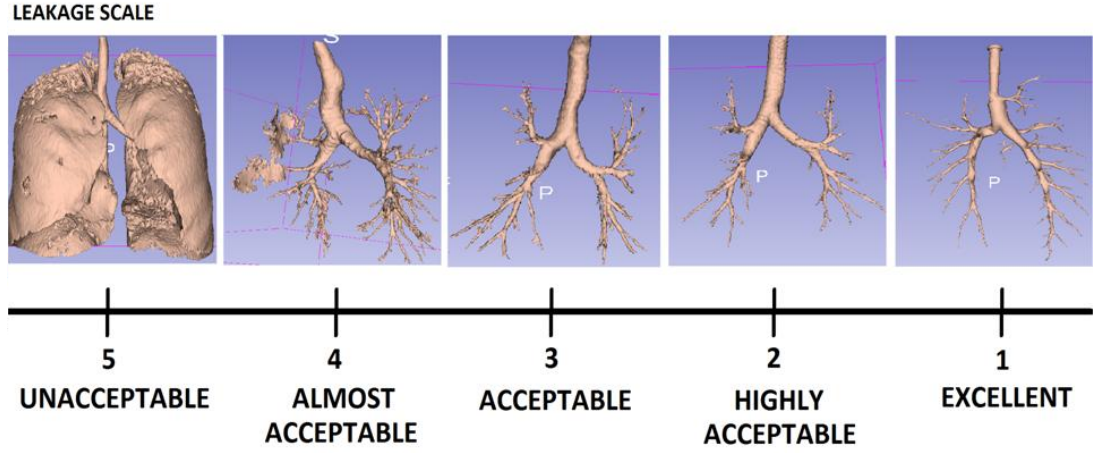
### 4.5.4.4 Leakage Evaluation Method

Leakage presence is the most important parameter to be considered once the airway is segmented. This often turns out to be a complicated task, as it may be difficult to distinguish small leakage from a correctly segmented branch. For this reason, a novel leakage evaluation system was developed which allowed expert clinicians to quantify leakage in airway segmentation results. To the best of our knowledge, an evaluation method of this type has never been considered before. Four expert clinicians from the field of respiratory medicine or radiology were instructed on what leakage is. This way, clinicians' knowledge of airway's anatomy could be exploited and a specialized assessment on leakage presence was obtained. The clinicians were then asked to analyse the 3-D reconstructed model of the airway as well as the label placed on the chest CT image and to score the segmentation ranging from 1 to 5, where 5 was a segmentation presenting significant leakage and 1 was an image with no leakage. Figure 4.15 shows the scoring scheme presented to the clinicians in order to score the images. Average scores were then used to evaluate the segmentation.

### 4.5.5 Results

In this section, the results obtained on both the clinical cases and on the breathing pig lung model are described. As an example of obtained results, Figures 4.16(a)-(f) show the 3D reconstruction obtained for six clinical cases. On the other hand, Figures 4.16(g)-(l) represent results obtained for six pig cases acquired during inspiration, with a 0.625 mm slice thickness, and varying the radiation dose. Cases shown in Figures 4.16(g)-(i) were reconstructed using a lung convolution kernel, whereas cases presented in Figures 4.16(j)-(l) were reconstructed with a standard convolution kernel.

## 4.5 Airway Segmentation: Implementation



**Figure 4.15:** Leakage scoring scheme as presented to clinical experts. A score of 5 is given to an image with significant leakage present, while 1 represents an image with no leakage.

### 4.5.5.1 Results on Clinical Cases

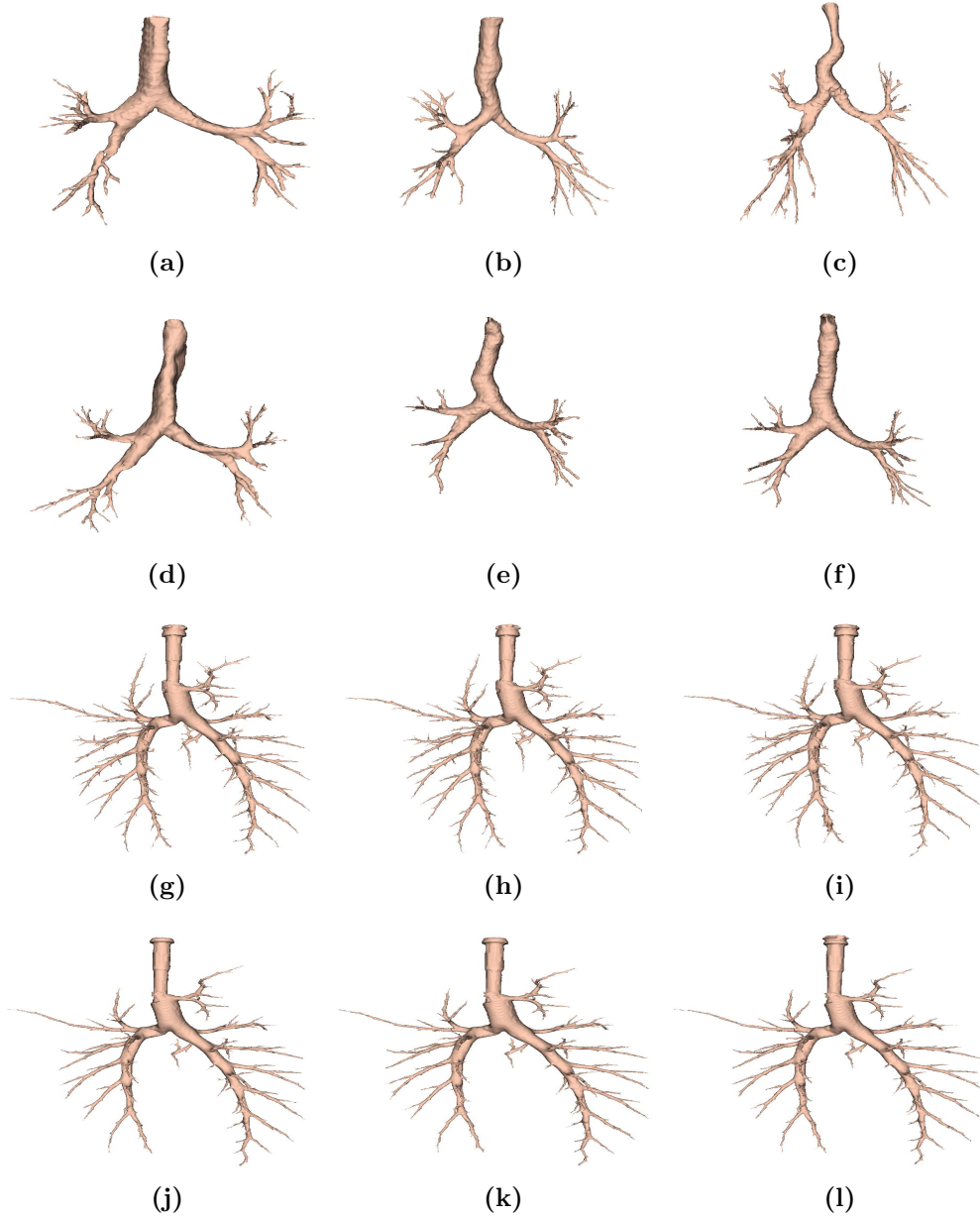
In Table 4.5 the optimal thresholds identified by the algorithm for the human cases of Tables 4.3 (CUH) and 4.4 (EXACT09) are reported. As shown in the table, in most cases, a different threshold is chosen for the segmentation of the two airways. Therefore, having a different threshold for the trachea, the right and left lungs helps to have a better segmentation in one lung, which will not be affected by the presence of leakage in the other. Table 4.6 shows the results obtained from the EXACT’09 challenge. Considering the “mean” row of the table, as compared to the other team’s mean results reported in

Table 4.7, it is evident that the method is comparable to other methods in terms of branch count and tree length, and it is reasonably placed in terms of leakage count and leakage volume as well as false positive rates. These results are also shown in Figure 4.17. In choosing a threshold for the two lungs there is a good trade-off between airway segmentation and leakage presence.

Table 4.8(a) reports the results obtained for the CUH datasets. In this case, the goal was to evaluate the reliability of the developed software across different human cases. For this reason, the most important metric to be considered is the leakage scoring, since unlike the EXACT09 dataset, for the others parameters no

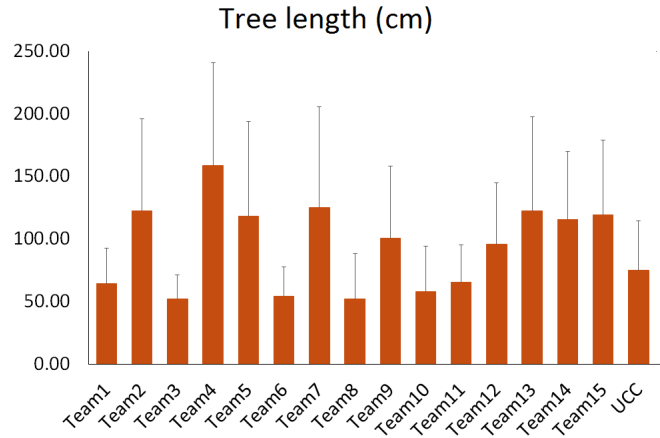
#### 4. AIRWAY SEGMENTATION

---

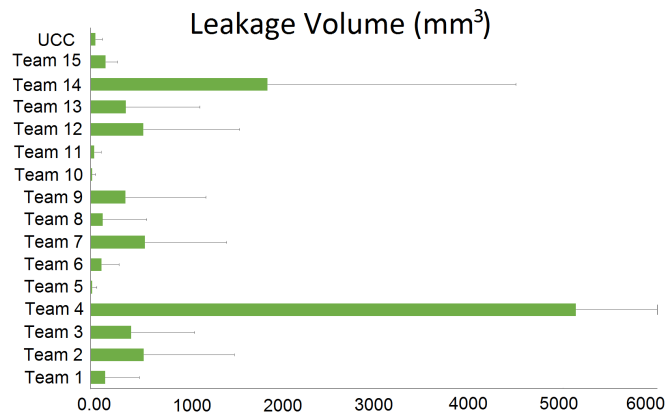


**Figure 4.16:** Representative 3D constructions of results obtained from (a-d) CUH cases (acquired with 1.25 mm slice thickness), from (e,f) EXACT'09 cases 24 and 25 (1.0 mm slice thickness), and from (g-l) six pig lung breathing model cases acquired using 0.625 mm slice thickness, during inspiration. (g-i) were reconstructed using a lung convolution kernel, varying dose from high to low, respectively. (j-l) were reconstructed with a standard convolution kernel, varying dose from high to low, respectively.

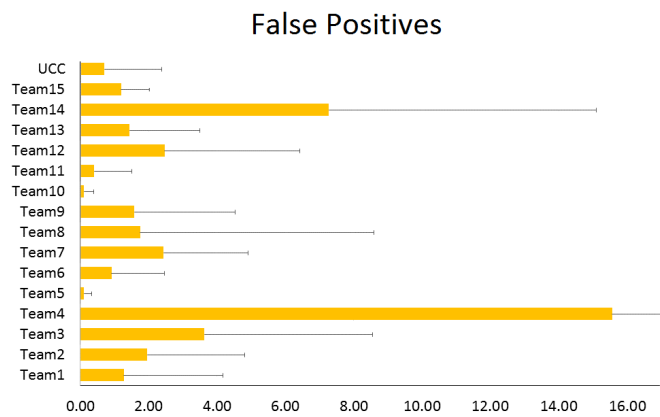
## 4.5 Airway Segmentation: Implementation



(a)



(b)



(c)

**Figure 4.17:** Results for the EXACT'09 challenge. In airway segmentation, having a good trade-off between tree length and leakage volume is essential.

#### 4. AIRWAY SEGMENTATION

---

	Trachea	Right Lung	Left Lung
CUH 1	-800	-800	-824
CUH 2	-930	-1000	-1024
CUH 3	-800	-1096	-1000
CUH 4	-800	-995	-976
CASE 21	-800	-840	-820
CASE 22*	-800	-1008	-1000
CASE 23	-820	-1003	-996
CASE 24	-820	-980	-974
CASE 25*	-800	-955	-972
CASE 26	-860	-925	-846
CASE 27*	-800	-800	-800
CASE 28	-800	-866	-835
CASE 29*	-800	-912	-930
CASE 30	-800	-825	-820
CASE 31	-800	-958	-1000
CASE 32	-800	-997	-1000
CASE 33	-800	-953	-940
CASE 34	-800	-1000	-980
CASE 35	-800	-918	-907
CASE 36	-800	-851	-825
CASE 37	-800	-889	-894
CASE 38*	-800	-800	-800
CASE 39	-800	-950	-959
CASE 40	-800	-1009	-1005

**Table 4.5:** Optimal thresholds (in HU) identified by the algorithm for airway segmentation of human cases. Thresholds are chosen independently for trachea, right and left lungs. Asterisk \* indicates that a scan was acquired from the same subject as the previous one.

gold standard is available. As shown in the table, the average score for all cases is close to 3, meaning that the clinicians considered the segmentation and the 3D reconstruction acceptable in terms of leakage presence. As a further test, the effect of changing parameters during scan acquisition on airway segmentation was assessed on six EXACT'09 cases. Table 4.8(b) shows the results for the selected cases. Results are in the same format as those reported in Table 4.6 with an added column representing the leakage score as evaluated by the four clinicians. For the case of leakage appearance, the segmentation does not seem to be particularly affected by varying parameters. However, comparing cases 28 and 29,

## 4.5 Airway Segmentation: Implementation

	Branch Count	Branch Detected (%)	Tree Length (cm)	Tree length Detected (%)	Leakage Count	Leakage Volume (mm <sup>3</sup> )	False Positive Rate (%)
CASE21	98	49.2	51.1	46.2	1	0.2	<0.01
CASE22	141	36.4	98.6	29.8	13	77.7	0.60
CASE23	126	44.4	90.5	34.8	12	119.8	1.02
CASE24	72	38.7	57.0	35.1	23	245.9	1.82
CASE25	108	46.2	82.7	32.8	5	29.2	0.20
CASE26	32	40.0	21.6	32.8	2	226.3	7.53
CASE27	41	40.6	30.1	37.1	0	0.0	0.00
CASE28	69	56.1	47.7	43.6	0	0.0	0.00
CASE29	93	50.5	62.2	45.0	1	9.0	0.12
CASE30	79	40.5	57.0	37.3	0	0.0	0.00
CASE31	99	46.3	70.3	40.0	2	73.9	0.74
CASE32	89	38.2	73.2	33.6	2	29.9	0.26
CASE33	85	50.6	62.1	42.2	0	0.0	0.00
CASE34	264	57.6	195.7	54.7	16	89.5	0.41
CASE35	146	42.4	108.9	35.2	1	23.7	0.19
CASE36	121	33.2	122.8	29.8	2	2.6	0.03
CASE37	64	34.6	54.4	30.6	1	2.7	0.03
CASE38	37	37.8	27.3	41.1	3	4.0	0.08
CASE39	113	21.7	97.6	23.8	5	92.0	1.01
CASE40	102	26.2	91.2	23.6	5	21.5	0.17
Mean	99.0	41.6	75.1	36.5	4.7	52.4	0.71
Std. dev.	50.3	9.0	39.4	7.6	6.3	73.3	1.67
Min	32	21.7	21.6	23.6	0	0.0	0.00
1st quartile	69	36.4	51.1	30.6	1	0.2	<0.01
Median	96	40.6	66.2	35.1	2	22.6	0.18
3rd quartile	126	50.5	98.6	43.6	12	92.0	1.01
Max	264	57.6	195.7	54.7	23	245.9	7.53

**Table 4.6:** Results obtained from the twenty test cases of the EXACT'09 project.

## 4. AIRWAY SEGMENTATION

---

	Branch Count	Branch Detected (%)	Tree Length (cm)	Tree length Detected (%)	Leakage Count	Leakage Volume (mm <sup>3</sup> )	False Positive Rate (%)
Team 1	91.1	43.5	64.6	36.4	2.5	152.3	1.27
Team 2	157.8	62.8	122.4	55.9	12.0	563.5	1.96
Team 3	74.2	32.1	51.9	26.9	4.2	430.4	3.63
Team 4	186.8	76.5	158.7	73.3	35.5	5138.2	15.56
Team 5	150.4	59.8	118.4	54	1.9	18.2	0.11
Team 6	77.5	36.7	54.4	31.3	2.3	116.3	0.92
Team 7	146.8	57.9	125.2	55.2	6.5	576.6	2.44
Team 8	71.5	30.9	52	26.9	0.9	126.8	1.75
Team 9	139	56	100.6	47.1	13.5	368.9	1.58
Team 10	79.3	32.4	57.8	28.1	0.4	14.3	0.11
Team 11	93.5	41.7	65.7	34.5	1.9	39.2	0.41
Team 12	130.1	53.8	95.8	46.6	5.6	559	2.47
Team 13	152.1	63	122.4	58.4	5	372.4	1.44
Team 14	161.4	67.2	115.4	57	44.1	1873.4	7.27
Team 15	148.7	63.1	119.2	58.9	10.4	158.8	1.19
UCC	99.0	41.6	75.1	36.5	4.7	52.4	0.71

**Table 4.7:** Mean results of the teams taking part in the EXACT’09 challenge. The last row reports mean results obtained with the described approach.



## 4.5 Airway Segmentation: Implementation

	Volume (mm <sup>3</sup> )	Branch Count	Branch Length(mm)	Leakage Score
CUH 1	41270.59	84	1369.69	3±1.15
CUH 2	34772.03	106	1505.25	2.50±0.58
CUH 3	41369.35	96	1610.39	3.25±0.50
CUH 4	58288.49	88	1425.97	3.25±0.50

(a)

	Branch Count	Branch Detected (%)	Tree Length (cm)	Tree length Detected (%)	Leakage Count	Leakage Volume (mm <sup>3</sup> )	False Positive Rate (%)	Leakage Score
CASE 24	72	38.7	57.0	35.1	23	245.9	1.82	2.75±0.50
CASE 25*	108	46.2	82.7	32.8	5	29.2	0.20	2.50±0.58
CASE 28	69	56.1	47.7	43.6	0	0.0	0.0	3.25±0.50
CASE 29*	93	50.5	62.2	45.0	1	9.0	0.12	3.50±0.58
CASE 37	64	34.6	54.4	30.6	1	2.7	0.03	2.50±0.58
CASE 38*	37	37.8	27.3	41.1	3	4.0	0.08	3.00±0.00

(b)

**Table 4.8:** Results obtained for human cases. (a) Cases provided by CUH. (b) Cases selected from the EXACT’09 cases. Asterisk \* indicates that a scan was acquired from the same subject as the previous ones.

that where acquired changing only the convolution kernel, the resultant airway volume, branch count, and branch length were slightly different between the two cases. In particular, the use of a sharper B50f kernel gives better segmentation than using a smoother B30f kernel. In terms of leakage, both cases were considered quite acceptable, although case 28 scored slightly better. This result was as expected, as the use of different kernels affects the quality of the image. In particular, a sharper kernel would preserve higher spatial frequencies at the expense of greater image noise, whereas a smoother kernel would decrease noise and spatial resolution, at the same time reducing the higher frequency contribution. Therefore, a sharper kernel allows for more peripheral aiway segmentation, at the cost of more leakage. In fact, the size of peripheral branches decreases going deeper into the lung, leading to a blurring effect that makes peripheral branches less recognizable from the lung parenchyma.

EXACT’09 cases 24 and 25 were also reconstructed using two different kernels. In particular, a smoother FC10 kernel was used for case 25. Therefore, as for the previous comparison, a better segmentation may be expected for case 24.

## 4. AIRWAY SEGMENTATION

---

However, as shown in Table 4.4, case 25 was acquired using a higher radiation dose. This affects the quality of the image more than kernel variation, leading to far better segmentation in terms of airway volume, branch count, and branch length. Furthermore, the leakage score was also slightly lower for case 25. In this case, this may be due to improved quality of the image which at the same time improved the quality of peripheral branches. Note that for cases 26 and 27 (acquired and reconstructed with the same parameters as cases 24 and 25, respectively) a similar situation occurs, confirming the results of the previous 2 cases. Since their reconstruction parameters were the same as that for cases 24 and 25, these cases were not reported in the table.

Analysis of segmentation for cases 37 and 38 is slightly different. Here, case 37 was scanned using a smoother kernel, but with a higher radiation dose and, more importantly, a full-inspiration breath-hold, while case 38 was acquired during a full-expiration breath-hold. In this latter case, a full-inspiration breath-hold guarantees that more airway branches will be visible on the CT image, since branches will be more expanded and the air inside them will help to increase the contrast with respect to lung tissue. For this reason, far better results are obtained for case 37 compared to case 38. This may also explain the difference in leakage score. It should be noted that the CT datasets from EXACT'09 were only used for comparative analysis of segmentation parameters, rather than comparison with any gold-standard.

In general, results obtained on human datasets are promising and show that the proposed algorithm with the optimised parameters is quite stable across varying scanning parameters. However, to avoid leakage, in some cases segmentation may stop too early, thus preventing possible segmentation of peripheral branches. In this sense, a new method for segmentation of peripheral branches to be integrated with the current algorithm may be of great benefit and should be considered in the future.

### 4.5.5.2 Results on Breathing Pig Lung Model

The breathing pig lung model was used to evaluate the effect on airway segmentation of:

## 4.5 Airway Segmentation: Implementation

Kernel	Volume (mm <sup>3</sup> )		Branch Count		Branch Length (mm)		Leakage Score	
	Inspiration	Expiration	Inspiration	Expiration	Inspiration	Expiration	Inspiration	Expiration
Standard	53025.54±213.45	41213.01±118.34	91.89±21.12	52.22±17.23	2240.55±155.90	1512.20±127.78	1.89±0.28	2.67±0.35
Lung	54374.74±251.21	44516.82±210.53	94.73±35.78	89.00±28.01	2320.74±175.10	2008.65±201.61	2.04±0.50	2.69±0.32

**Table 4.9:** Results obtained on the breathing pig lung model for kernel variation in inspiration and expiration.

Parameters			Results			
Slice Thickness (mm)	Dose	Kernel	Volume (mm <sup>3</sup> )	Branch Count	Branch Length (mm)	Leakage Score
0.625	H	STD	48171.31	87	2186.95	2

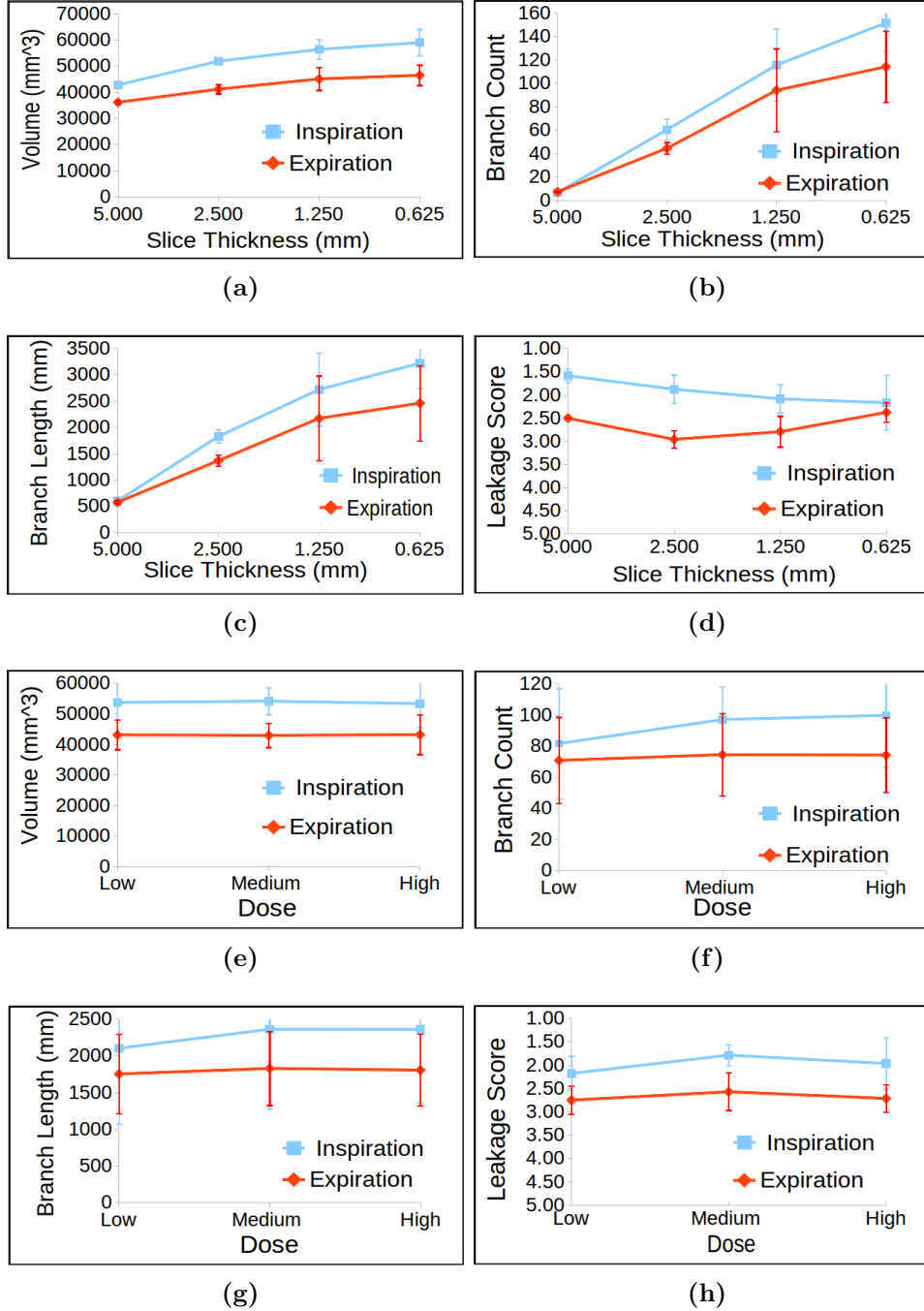
**Table 4.10:** Parameters and results for pig lung breathing model during half-inflation.

- Slice thickness
- Reconstruction kernel
- Radiation dose
- Level of inflation

In order to evaluate the half-inflation case, a slice thickness of 0.625 mm, high radiation dose and a standard kernel have been chosen. Figure 4.18 reports the average results obtained across slice thickness and radiation dose for inspiration and expiration phases. Results are obtained considering a specific slice thickness or dose and computing the average value among the other parameters. As an example, the value obtained for a slice thickness of 0.625 mm is given by the average of the results obtained varying dose and kernel for that thickness.

Table 4.9 shows results obtained varying the convolution kernel (computing the average values among dose and slice thickness), whereas in Table 4.10, parameters and results for the half-inflation dataset are presented. Although airway segmentation for images acquired during an inspiration phase shows improved segmentation compared to that obtained on expiration datasets, in both cases slice thickness is the parameter most affecting the segmentation. In fact, as shown in Figures 4.18(a)-(c), airway volume, branch count and branch length all increase when thickness is reduced. This result is expected, as less fine details

#### 4. AIRWAY SEGMENTATION



**Figure 4.18:** Results for the breathing pig lung model during inspiration (blue) and expiration (red), when varying (a-d) slice thickness (computing the average values among dose and kernel) and (e-h) radiation dose (computing the average values among slice thickness and kernel).

## 4.5 Airway Segmentation: Implementation

---

are preserved with thicker slices. At the same time, during inspiration, leakage is more likely when thickness is reduced (see Figure 4.18(d)). This is probably due to the higher number of branches segmented, which makes automatic recognition of leakage more complicated. However, it is worth pointing out that, in general, the presence of leakage was insignificant during inspiration, as confirmed by the fact that for a slice thickness of 0.625 mm, an average score around 2 was given to the segmented image.

As for the expiration phase, leakage appeared more often than in the inspiration dataset. This is due to the minor presence of air inside the lung, which makes the airways less recognizable from the lung tissues on a CT image. Furthermore, in Figure 4.18(d) leakage increases for a 2.5 mm slice thickness relative to the 5 mm slice thickness image. However, when thickness is further decreased, the perception of the degree of leakage decreased as well. In this case, the result is thought due to the combination of the thinner slices used (i.e., an image with a better quality) resulting in a smaller number of branches segmented with respect to the inspiration phase. In fact, better quality images enables the segmentation of more branches. At the same time, the segmentation is stopped quite early in this case, thus reducing the probability of leakage.

On the other hand, tube current and radiation dose does not particularly affect airway segmentation, as shown in Figure 4.18(e)-(h). In this case, for both inspiration and expiration, none of the considered metrics present significant variation across the different doses. In particular, the segmented volume does not seem to vary when changing the dose. Branch count and length are slightly increased with increased dose, while leakage occurrence is quite stable.

Finally, variation of the convolution kernel used for the reconstruction only slightly affects segmentation for the inspiration phase. As shown in Table 4.9, a lung kernel allows segmentation of more peripheral branches, at the cost of leakage. However, in general the algorithm can be considered quite stable with kernel variation during an inspiration phase. On the expiration phase, a lung kernel gives better results in terms of volume, branch count and branch length, whereas the kernel choice does not seem to greatly affect the leakage probability. Good results have also been obtained for half inflation images, as shown in Table

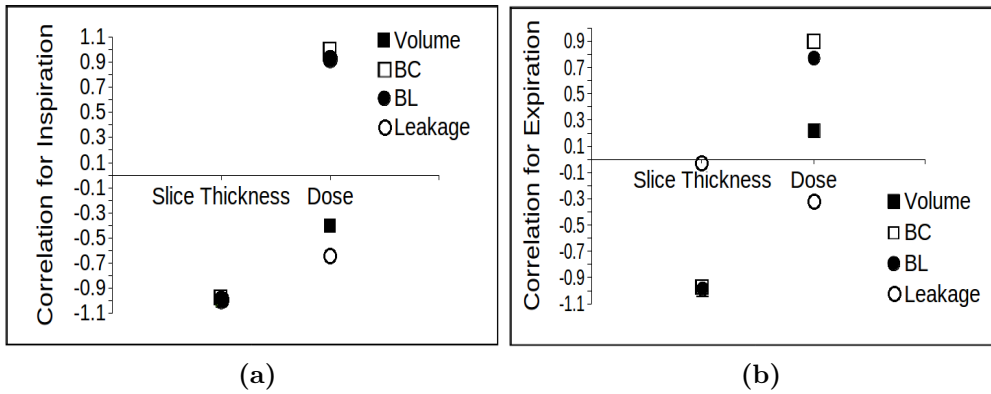
## 4. AIRWAY SEGMENTATION

4.10. In this case, airway segmentation was similar to that obtained for a full-inspiration phase.

In general, the results obtained for the breathing pig lung model are quite encouraging and show that the algorithm proposed here can be considered reliable and stable across the different CT acquisition parameters. As expected, slice thickness is the parameter that has the greatest effect on airway segmentation. However, this is due to the fact that less details are recognizable on the image when thickness is higher. In terms of leakage score, the images were largely considered highly acceptable, indicating that the algorithm is able to segment as many branches as possible among those recognizable on the CT scans, while avoiding the leakage appearance.

### 4.5.5.3 Correlation Between Segmentation Metrics and CT Acquisition Parameters

To improve quantitative analysis of results, the considered metrics were correlated with the different acquisition parameters. Radiation dose and slice thickness were included, while the convolution kernel variation was not considered, as only two values are considered, i.e., lung and standard, and correlation is always maximum as is evident from Table 4.9. In fact, all the segmentation measures improved



**Figure 4.19:** Correlation between image quality and metrics for the breathing pig lung model during (a) inspiration and (b) expiration phases.

when a lung kernel was used, although the improvement was not significant.

## 4.5 Airway Segmentation: Implementation

---

Figure 4.19(a) shows the correlation for the inspiration case, whereas in Figure 4.19(b) correlation during expiration is represented.

As seen in Figure 4.19(a), all the segmentation metrics strongly correlated with slice thickness variation for inspiration, confirming the great effect of thickness variation on airway segmentation. In particular, when slice thickness decreased, airway volume, branch count, branch length and leakage increased, giving a correlation value of approximately  $-1$  ( $R \leq -0.97$  for all the metrics). This result confirms those discussed above. Moreover, as already stated in Section 4.5.5.2, the segmented volume correlated poorly with radiation dose ( $R = 0.378$ ) during inspiration, while branch count and length improved in the same way with dose ( $R = 0.99$  and  $R = 0.92$ , respectively).

Leakage occurrence is only slightly correlated to dose variation ( $R = 0.723$ ). For the expiration case, again slice thickness strongly correlated with volume, branch count, and branch length ( $R \leq -0.97$ ). However, there is no significant correlation with leakage presence ( $R = -0.02$ ).

In terms of dose variation, the metrics correlated similarly to the inspiration case, with branch count and length following the change of dose more closely than the segmented volume ( $R = 0.91$  for branch count,  $R = 0.85$  for branch length, and  $R = 0.21$  for volume). As was the case for the slice thickness, leakage was not greatly dependent on the chosen radiation dose ( $R = -0.31$ ). Therefore, these results further confirm that the airway segmentation algorithm proposed here can be considered stable across radiation dose and convolution kernel variations. Again, the segmentation greatly depends on the chosen slice thickness, as this substantially affects the quality of the image and the number of branches visible on the CT scan.

Finally, scanning of a real pig lung has been accomplished during two animal studies for testing the virtual bronchoscopy (see Chapter 6). For both studies, 0.625 mm slice thickness, 60 mA radiation dose, and standard convolution kernel were used. This allowed for evaluation of reliability of the algorithm on real images. Results are shown in Chapter 6.

## 4. AIRWAY SEGMENTATION

---

### 4.5.6 Discussion and Future Work

In this Chapter, the implementation of a new semi-automated algorithm for airway segmentation starting from chest CT images has been described. The algorithm is freely available and can be downloaded and used within the 3D Slicer environment. This is the first freely available system for airway segmentation and will help new research teams compare their results with those presented here.

The optimization of parameters of the algorithm in order to have as general an algorithm as possible was described. The method proved to be reliable and stable across varying CT parameters while comparable with other teams' methods. As expected, slice thickness is the parameter which most affects segmentation, whereas variation in radiation dose and convolution kernel do not significantly affect airway segmentation.

A CT scan acquired during a full-inspiration breath-hold guarantees a higher contrast between airway and lung tissue, leading to better segmentation, as shown in both clinical and pig phantom cases. The method is able to cease the segmentation before significant leakage appears. Although not optimised to maximise branch detection as other algorithms proposed in literature, the proposed method allows the segmentation of one lung's airways regardless of possible leakage appearance in the other. This feature appears novel and avoids early and unnecessary stoppage of the algorithm due to leakage. In previous works [178, 182, 189] a pre-determined maximum number of voxels or a maximum volume were used as stopping criteria for the segmentation. A maximum number of allowed voxels can be determined case by case based on the number of voxels of the trachea segmentation, giving more flexibility and adaptability to the algorithm. However, in some cases the segmentation does not allow to segment deeper branches, as once the region growing encounters the stopping criteria, the segmentation is not further increased. Therefore, the method might benefit from the integration of the region growing approach with other segmentation techniques, as in [183, 194, 195].

Future improvements may seek to use different thresholds for different volumes of interest within the same lung. Also, performance of the algorithm should be considered on more human CT images and on CT images belonging to patients affected by different pulmonary diseases. However, being the first open-source



airway-segmentation algorithm available, the proposed approach enables other teams to have a frame of reference for comparison of segmentation results using personal datasets. Alternatively, the algorithm could be considered as a starting point for new airway segmentation algorithms that seek to segment narrow peripheral bronchial branches. The final goal is to obtain a method that is stable across all available scanners and allow stable and reliable segmentation regardless of the parameters chosen for scanning.

## 4.6 Summary

In this chapter, a new open-source method for semi-automatic airway segmentation starting from chest CT images was described. The primary results are as follows:

- The algorithm is the first open-source minimal user interaction algorithm of its kind and is as general as possible. It can be used for both human and animal (porcine, canine) chest CT images.
- A method to split the volume into three different parts to be segmented separately without affecting computation time has been introduced.
- A novel method to evaluate leakage presence on the segmented images has been presented. This is quite simple and can be re-used by other teams to compare results.
- The described algorithm is reliable across different clinical CT cases, providing results that are comparable with those of other teams.
- The algorithm is reliable also across different CT scanners and parameters, as proven using a breathing pig lung model.
- The algorithm is easily modified and extended, making it a good starting point for new airway segmentation methods.

# Chapter 5

## Virtual Bronchoscopy\*

### 5.1 Overview

This chapter presents the implementation of a novel open-source method for virtual bronchoscopy (VB) to be used in combination with the UCC electromagnetic tracking system [8, 16]. This VB method is available online as an extension of 3D Slicer and is composed of different sub-systems that can be used independently for other purposes. First, the relevant literature and background to VB systems is introduced. Then, implementation of the algorithm and its sub-parts is presented in detail. The tool consists of a Python module composed of six different parts; three methods to be used as pre-processing steps prior to the virtual navigation procedure, a step dedicated to real-time navigation, and two final methods for operations that facilitate the navigation procedure. The main aspects presented in this chapter are:

- Development of the first open-source method for VB navigation starting from airway segmentation of CT images.
- Optimization of the algorithm for an EM tracking system developed at UCC. However, the system can be coupled with any EM system for lung

---

\*This chapter is based on P. Nardelli, H. A. Jaeger, C. O'Shea, K. A. Khan, M. P. Kennedy and P. Cantillon-Murphy, "Open-source Virtual Bronchoscopy in Pre-clinical Validation Using 3D Slicer", *International Journal of Computer Assisted Radiology and Surgery* (2016), [Under Review]

navigation tracking.

- Automatic creation of pathways from the lung trachea toward selected regions of interest. These pathways will guide physicians during navigation.
- Development of a method for image registration during the navigation. This compensates for the use of 5 DOF sensors, helping to avoid possible roll-rotation misalignment with the real view.
- Providing the user with a complete system that facilitates navigation toward a region of interest. To this end, six different views showing the position of the probe inside the lung are simultaneously presented to the user, who can then choose the easiest and most helpful to follow.

## 5.2 Introduction

When a patient is diagnosed with a suspiciously malignant lung cancer, the physician may decide to proceed with biopsy or cancer exportation. To do so, the CT image of the patient is analysed and anatomy of the airways is mentally reconstructed from the stack of 2D images to identify the best path toward suspect nodule. This is then followed by a physical bronchoscopy to evaluate or biopsy the nodule. However, image guidance based on CT images alone is tedious, due to image noise, low image quality, or the complex structure of the different regions. Moreover, standard bronchoscopes do not reach thin peripheral airways. For this reason, in the last two decades the idea of using a virtual environment that reconstructs the lung anatomy and helps the physician during bronchoscopy procedures has emerged as a potential solution. This concept has been called virtual bronchoscopy (VB) and simulates the inside of the airway during navigation similar to those from a real bronchoscope, allowing for virtual exploration of the inside of the lung.

Combined with a CT image, VB can also provide information about the real position of the probe within the lung, as well as information of structures that may not be visible on a CT image. Moreover, thanks to VB systems, an "optimal" pathway, or road map, toward the lung cancer can be automatically reconstructed

## 5. VIRTUAL BRONCHOSCOPY

---

and presented to the user, allowing the physician to focus on the procedure, without the need to memorize the path. This approach, combined with the real video captured from the bronchoscope when available, will also help choose the correct path at branching points and avoid mistakes due to unexpected movements of the patients, such as coughing.

Finally, the end goal of the development of a VB system is to help the physician reach peripheral airways, which are small and narrow and therefore not reachable using a standard bronchoscope. Currently the operator has to reach these areas “blindly”. A VB system will follow the information provided by the virtual environment to navigate, biopsy and, eventually, treat cancer in these areas. At present, there are three commercially available systems that implement virtual navigation. As described in Chapter 2, superDimension [26] and Veran SPINDrive [27] use electromagnetic navigation coupled with virtual reconstruction of the inside of the airways. Bronchus LungPoint [28] uses a different approach. Instead of trying to identify the correct position of the bronchoscope within the lung using EM tracking, an image-based synchronization technique is used to align the virtual images obtained from the CT scan of the patient with the anatomy seen in the live bronchoscopic video. However, all these systems have the drawback of high costs.

This chapter describes an open-source method for virtual bronchoscopy starting from chest CT images for accessing and sampling pulmonary peripheral lesions. The system has a modular structure and is composed of different methods that can also be used for different applications. It has been optimized for a specific EM tracking system developed at UCC, but it can be easily adapted to be used with a different technology. A virtual navigation platform of this kind for use within the lung paves the way for potential future work with a complete system for safe and reliable diagnosis.

### 5.3 Literature Review

In the last decade, several approaches have been proposed for virtual bronchoscopy. These aim at localising the actual position of the bronchoscope in-

side the lung in a virtual environment. The most common approaches apply EM tracking, real-virtual image matching, or a combination of both.

#### **EM Tracking Methods**

EM tracking systems use a small sensor mounted on the tip of the bronchoscope (or inserted in the bronchoscope channel) to determine location and orientation of the tip in real time. These systems require calibration and registration between the real and the virtual environments before each bronchoscopic session [196]. Calibration and registration can be achieved either by using fiducial markers placed near the bony structure [196] or using anatomical landmarks of the airways, such as carina and main bronchi [10]. However, the EM field can be distorted due to the presence of ferromagnetic material around the EM system, while accuracy of EM tracking can be affected by unexpected movement of the patient and respiration during bronchoscopy.

#### **Real-virtual Images Matching**

Real-virtual matching tracking techniques, on the other hand, seek to track the position of the scope by finding the best match between the real image from the bronchoscope with the rendered view of the airways. The similarity between the two images can be accomplished using approaches that are either intensity-based or geometry-based.

Intensity-based methods [197,198] compare the intensities between the two images. Bricault et al. [197] proposed a method that renders the virtual bronchial views using a ray tracing technique, while in [198], a novel approach that uses photo-realistic rendering has been proposed. However, intensity-based techniques are really sensitive to small local intensity variations and illumination artefacts and may often require continuous manual lighting adjustment of the virtual camera.

Conversely, geometry-based approaches [199–201] consist in extracting anatomical structures from the two images to find the best match. Deligianni et al. [199–201] presented a method that uses a linear local shape-from-shading (SFS) algorithm derived from the unique camera/lighting constraints of the endoscope to extract surface normal and accomplish a  $pq$  space-based 2D/3D registration

## 5. VIRTUAL BRONCHOSCOPY

---

process. The system also incorporates a patient-specific airway deformation model that permits accounts for deformation of the airways due to breathing and coughing. This approach proved more robust to illumination artefacts and tissue deformation than intensity-based techniques. However, recovering geometrical structures from the bronchoscope video can be challenging, due to the fact that conventional methods to extract the structure, such as the SFS, assume orthogonal projection and light source at infinity. However, these assumptions can not be used in the bronchoscopic scenario. To overcome this problem, Shen et al [202] recently proposed a method which first extracts depth information of the bronchoscopic image using a SFS approach based on the assumption that the light source is near the surface. Next, depth information from CT data is recovered by linearisation of depth buffering from perspective projections of the CT model. Finally, the camera position is then estimated as that which maximises the similarity between the two extracted depth maps.

### Hybrid Methods

Virtual bronchoscopy can also be achieved using an hybrid approach that combines EM tracking and image registration. An hybrid method that combines EM tracking and intensity-based image registration has been proposed by Mori et al [203]. The approximate position and orientation of the bronchoscope in the coordinate system of the CT image is determined using EM tracking. This is used as a starting point for an intensity-based registration between the real bronchoscopic image and the virtual image generated with a highly-optimized software-based volume rendering. A similar approach has been developed by Luo et al [204]. This system is based on three main steps. First, a camera and hand-eye calibration to obtain intrinsic parameters of the bronchoscopic camera and to perform sensor-camera alignment is undertaken. Then, a rigid registration between EM and CT tracking coordinates is performed. Finally, an intensity-based image registration is combined with the result of the EM system to improve the camera tracking. Another methodology using both EM tracking and image registration, based on differential surface analysis in a  $pq$  space, was outlined by Soper et al [205, 206]. As part of that framework, the positional and orientational error between the CT and EM tracking system is adaptively estimated by

means of Kalman filtering. The local deformation at each video frame is then intra-operatively estimated to compensate for respiratory motion. Such hybrid methods improve the performance of the registration, but have the drawback to complicate the registration algorithm and the sensor calibration.

One of the biggest issue is due to the high time consumption of image registration. For this reason, methods that use motion prediction have also been proposed to achieve faster convergence during registration. Higgins et al. [207] investigated an approach that estimates the optical-flow from the bronchoscope video and uses the tracked 3D trajectory to assist localisation in the virtual world. This allows for tracking of the 3D motion of the bronchoscope. A different approach that employs a Kalman filter to predict the 3D motion of the bronschoscope has been proposed by Nagao et al. [208]. However, the final image registration still relies on the matching between real and virtual images, as the 3D motion prediction from 2D video images may not be accurate enough.

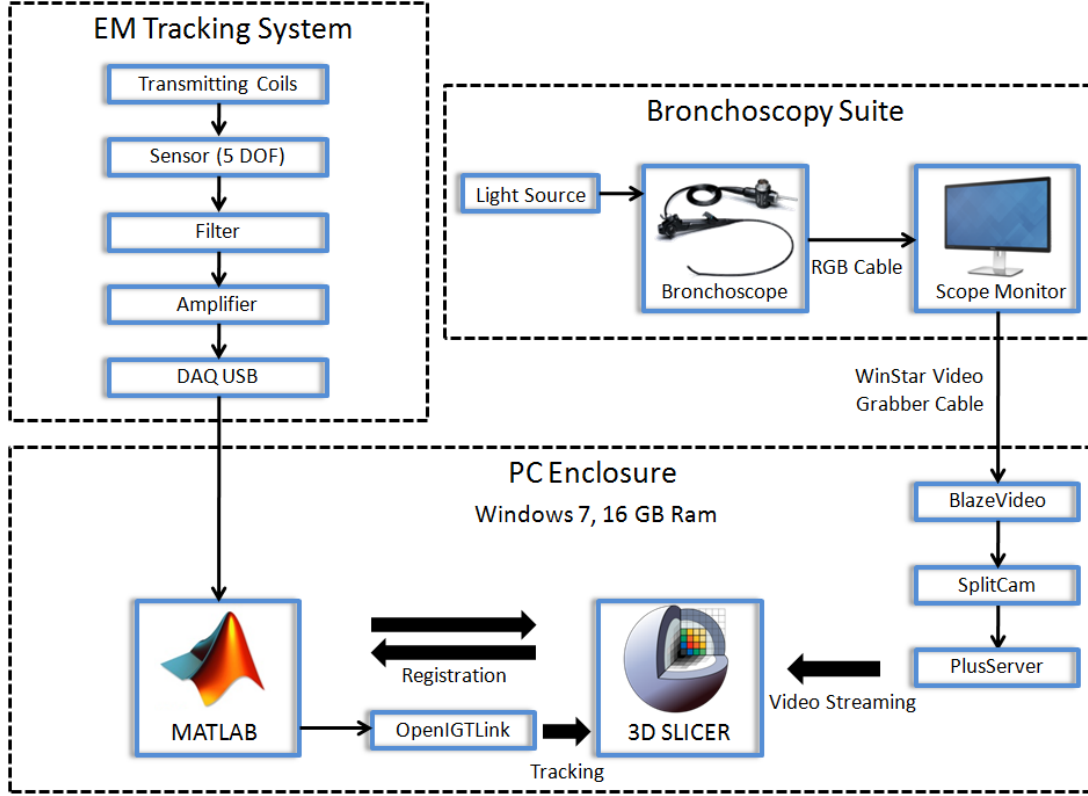
In this research, an hybrid method that combines EM tracking of 5 DOF sensing and intensity-based image registration has been investigated. A novel landmark-free registration approach for EM tracking is proposed. The 5 DOF sensor inserted through the bronchoscope channel allows for navigation in peripheral branches, but does not provide information about roll rotation of the scope. For this reason, an intensity-based image registration based on multi-scale pyramid registration is employed to compensate for possible roll-rotation misalignment.

## 5.4 Algorithm Implementation

### 5.4.1 Overview

In this section, the implementation of an open-source system for VB coupled with EM tracking is detailed. This approach was chosen to (i) minimise registration delays and (ii) facilitate VB in the outer airways where the bronchoscope cannot pass due to the airway narrow lumen. The VB method can be used for (1) real navigation, but also (2) procedural simulation and planning. The system has a modular structure, enables direct pre-operative CT-based procedure planning and

## 5. VIRTUAL BRONCHOSCOPY



**Figure 5.1:** Block diagram of system hardware.

provides direct guidance during bronchoscopy. A 3D representation of the target is provided. This virtual target changes colour once the bronchoscope reaches the desired region. Distance information between the current location and the biopsy site is interactively provided as the physician advances the bronchoscope. Since the system was used in combination with EM tracking using a 5 DOF sensing, video image registration between the real and the virtual camera has been implemented to compensate for possible roll angle misalignment. The centreline of the 3D rendered airway view is extracted and used to avoid registration issues between the real and virtual environments. Figure 5.1 shows a block diagram of the system hardware. A desktop Windows 7 computer, with 16 GB RAM is used as the main CPU. A WinStar frame grabber [209] connects the bronchoscope monitor to one of the PC's USB ports. The grabber is enabled by the BlazeVideo grabber software [210] which transmits the real image of the bronchoscope to the PC. The SplitCam software [211] is used to connect the video grabber to the



## 5.4 Algorithm Implementation

Pre-Procedure Operations	
Algorithm	Functionality
Centreline Extraction	Extract the airway model's medial axis
Procedure Planning	Create pathways toward target regions of interest
Registration	Register real and virtual environments
(a)	
Image-guided Operations	
Algorithm	Functionality
Centreline Compensation	Compensate for registration errors
Roll Rotation Compensation	Compensate for 5 DOF tracking
Distance to Target	Real-time distance to the region of interest
Video Streaming	Streams video into 3D Slicer
(b)	

**Table 5.1:** Summary of algorithms involved in the VB procedure. (a) Pre-procedure operations. (b) Operations for image-guided navigation.

open-source Public Software Library for Ultrasound Imaging (PLUS) research framework [212, 213]. PLUS is a toolkit for data acquisition, pre-processing, and calibration in navigated image-guided interventions which was originally developed for ultrasound-guided interventions. However, it is now widely used in all kinds of interventions, with and without ultrasound imaging. In the case of the proposed algorithm, PLUS was used to stream the video from the bronchoscope into 3D Slicer. The PC is also connected to the EM tracking system, with tracking implemented using MATLAB (Mathworks Corp, Natick, MA) [8, 16]. MATLAB is also used to register the real and virtual environments created from 3D Slicer. To read the sensor position tracked by the EM system in 3D Slicer, the open-source OpenIGTLink software, available as 3D Slicer extension, is used [214]. The system works in two main steps; (1) a pre-procedure step followed by (2) an image-guided bronchoscopy step. The pre-procedure step involves centreline airway extraction, real-virtual registration and procedure planning (with paths to target creation). The second step represents the operations involved during the procedure, including intensity-based image registration. The methods are written mostly in C++ (using ITK classes) and Python and are run through a

## 5. VIRTUAL BRONCHOSCOPY

---

Python graphical user interface. Table 5.1(a) reports the pre-procedure operations for VB, while in Table 5.1(b) the operations executed during navigation are summarised.

The remainder of the chapter details the different algorithms involved in the VB procedure.

### 5.4.2 Centreline Extraction

#### 5.4.2.1 Overview

The first pre-processing operation is the extraction of the centreline of the 3D model. This is a very important operation as the centreline is used during image-guided navigation to correct possible registration errors. Centreline (or “skeleton”) extraction refers to the process of computing the central axes of the label of tubular structures. In the described application, this involves taking the extracted airways and applying some mathematical operations of erosion and thinning until only the skeleton of the label remains.

Numerous methods exist for centreline extraction of tubular structures which aim to be robust and accurate without requiring human interaction. Algorithms should preserve the general anatomy of the structure and be computationally efficient.

Swift et al [215] introduced a semi-automatic algorithm that generates a series of airway-tree axes starting directly from CT images, with no prior segmentation required. The method is based on an adaptive 3D searching technique to find set of central axes for the major airways and on a subsequent cubic-spline analysis and contour finding procedure. The approach is focused on assessing major airway obstructions.

In their method for 3D path planning for VB, Kiraly et al [216] defined a skeletonization algorithm that combines two chamfer distance metrics and a 3D thinning operation.

Yu et al [217] used a method that combines the segmented image and the original CT image to derive a sub-voxel-level polygonal surface. Differential geometry is then employed to determine the set of central axes and branch points of a vascular tree.

In their methods for VB, Higgins et al [207] and Gibbs et al [218] combined these three approaches of 3D thinning, B-spline analysis, and differential geometry to extract the central axes of the segmented airways.

A different centreline tracking approach that uses the Hessian matrix to identify intensity ridges in 2D and 3D images was presented by Aylward et al [219]. This approach does not need prior segmentation.

Bitter et al [220] proposed a minimal-path approach that starts with a coarse approximation of a 3D skeleton which determines a graph. A weight is then assigned to each edge of the graph, based on a combination of the Euclidean distance from a user-defined source node and Euclidean distance from the boundary of the object. The Dijkstra's shortest path algorithm is applied on this graph to extract the final centreline.

Lee et al [221] presented an approach that implements a thinning algorithm to iteratively delete the border points of an object until a smaller set of connected points is acquired. Euler characteristics and connectivity are preserved to guarantee invariance of the object's topological requirements, such as cavities, holes, and connections to the original object.

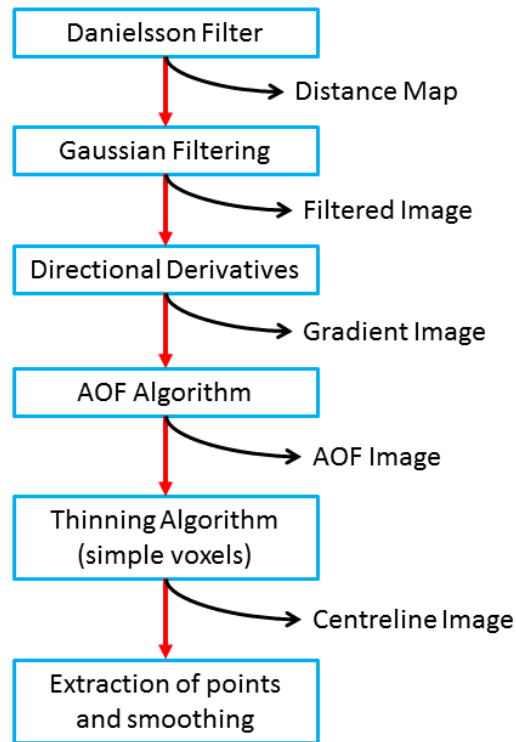
Lastly, an approach which is most closely related to the one implemented here was presented by Bouix et al [222]. This method implements fully automated centreline extraction that first utilises an average outward flux (AOF) measure to distinguish skeletal points from non-skeletal ones and then combines this information with a topology preserving thinning procedure. The strategy is to thin the medial surface to obtain a structure composed only of curves and to prune the result to obtain the skeleton. In this section, the method, based on such a thinning operation, to extract the centreline of the segmented airway tree is described.

### 5.4.2.2 Centerline Extraction Method

The method for centreline extraction implements the algorithm described in [222]. This approach was chosen as it is based on theoretical properties that have been previously thoroughly justified [223] and because the algorithm is completely automatic, the approach finds all centreline paths in volumetric tubular structures

## 5. VIRTUAL BRONCHOSCOPY

---



**Figure 5.2:** Block-diagram of the steps involved in centreline extraction. For each step the resulting image is shown.

with arbitrary topologies unlike most of the methods in literature that find a single centreline at the time and have very complex numerical implementation. Other methods require user interaction to select at least the end points of a particular centreline path. Since the main goal of the research was to reduce user interaction as much as possible, this approach was found appropriate. Moreover, this represents the first implementation of the algorithm for centreline extraction of an entirely segmented airway tree.

The steps composing the algorithm are shown in the block diagram of Figure 5.2. The algorithm extracts the centreline of the specified airway label using an AOF implementation of the label followed by a thinning of the medial surface to obtain a structure with only one curve, defined as the medial curve, and a pruning operation to obtain the final centreline. To this end, the first step is the computation of the distance map of the label. This operation is executed

using a signed Danielsson distance map filter [224]. This way, the distance map of the input image is computed as an approximation, with pixel accuracy, to the Euclidean distance [224]. The distance map is then filtered with a Gaussian filter, and the gradient vector,  $\nabla D$ , of the image is calculated. The result is used as input to the AOF algorithm, which is computed using (5.1),

$$\text{AOF}(\mathbf{x}) = \frac{1}{n} \sum_{i=1}^{26} \langle \mathbf{n}_i, \nabla D(\mathbf{x}_i) \rangle \quad (5.1)$$

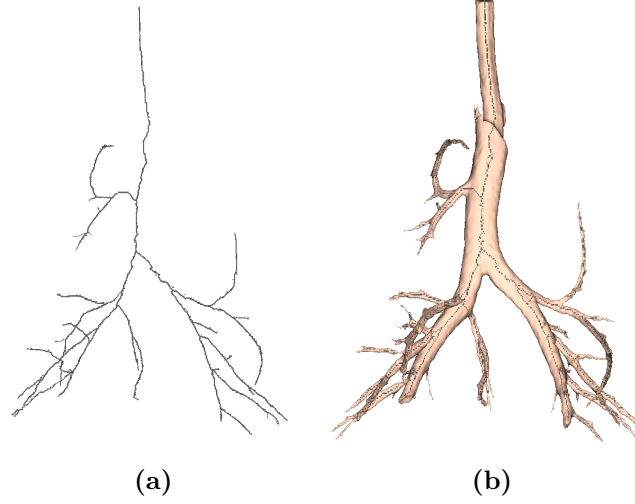
where  $\mathbf{x}_i$  is a 26-neighbour of  $\mathbf{x}$  and  $\mathbf{n}_i$  is the outward normal at  $\mathbf{x}_i$  of the unit sphere centred at the voxel  $\mathbf{x}$ . This operation is repeated for each pixel in the interior of the object.

Once the AOF algorithm ends, the centreline is extracted by thinning the medial surface to obtain a structure composed only of curves, defined as the medial curve. To this end, if the removal of a voxel does not create a hole, does not create a cavity, and does not disconnect a connected component, it is considered as a simple voxel, as its removal does not affect the object's overall topology. This is defined in accordance to the voxel's categorization introduced by Malandain et al [225]. Therefore, the strategy involves guiding the thinning operation by the AOF measure over a very small neighbourhood, while ensuring that only simple voxels are removed. This operation ends when all the simple voxels are removed or when the AOF has an average below a user-defined threshold. In the described application, a threshold of 0 was found as the optimal choice in order to extract the complete airway model centreline. The thinning operation creates a medial curve of the original surface. The output of the filter is a binary image containing the centreline of the input structure.

To complete the process, the algorithm requires a few minutes (an average of 3-4 minutes on a  $512 \times 512 \times 600$  image with a standard desktop PC). The end goal of the centreline extraction operation is to use the centreline as a tool to correct possible registration errors. To this end, the centreline is used to maintain the virtual probe inside the 3D model environment, helping the guidance system. The ideal is to remove this step when an optimal registration process is available. However, in order to use the centreline to correct the position of the probe, a 3D model of the centreline itself is created starting from the binary image.

## 5. VIRTUAL BRONCHOSCOPY

---



**Figure 5.3:** Example of centreline extraction from a pig lung 3D model. a) Shows the extracted centreline alone, whereas in b) the centreline is imposed on the lung model.

An example of a centreline model extracted from a pig CT airway label is shown (a) alone and (b) fused on the airway model in Figure 5.3. This model consists of many thousands of voxels, which would computationally burden the navigation if all voxels are considered. Therefore, the next step involves the extraction of part of the points of the centreline, followed by iterative smoothing to better align these points. Particular care needs to be taken for this operation, as points in the 3D model are ordered following their position in the axial slices. Therefore, points belonging to separated branches may appear one after the other in the points order of the 3D model. For this reason, a technique that recognizes the previous and following closest points to the considered one in the list of points of the 3D model is implemented. The central point's position is then moved to be more aligned with the previous and following points using (5.2),

$$\mathbf{p} = \rho[0.5(\mathbf{pp} + \mathbf{np}) - \mathbf{p}] \quad (5.2)$$

where  $\rho$  is a relaxation term empirically set to 0.5,  $\mathbf{p}$  is the central point,  $\mathbf{pp}$  the previous point, and  $\mathbf{np}$  the next point. The position of these points are then saved in a list of positions to be used during image-guidance.

### 5.4.3 Procedure Planning

#### 5.4.3.1 Overview

Once the centreline has been extracted, the next step involves procedure planning, that is the phase where the physician analyses the CT images and selects the biopsy target to be reached during navigation. Different tools have been provided on the Slicer user interface to aid the physician during image analysis and to improve path creation, when necessary. Different strategies have also been used for procedure planning in image-guided bronchoscopy, most of which exploit the extracted centreline to create the path to target [181,183,215,218,226]. The field of robotics has also focused much attention on the path planning problem [227], including determination of navigated device movements to reach a target site within the airway tree model [228]. Other approaches have required interactive path generation and knowledge of start/end points [229]. In this section, the approach used to create the route from the trachea to the selected targets of regions of interest is discussed.

#### 5.4.3.2 Route Extraction Implementation

In the described system, some of the classes provided by the VMTK toolkit [193] were exploited. This is an open-source toolkit that provides a collection of libraries and tools for 3D reconstruction, geometric analysis, mesh generation, and surface data analysis of 3D models of tubular structures. Most of these methods have been optimized for applications on the vascular tree. A group of these classes allows for the centreline extraction of a 3D vascular model using two end-points, defined as source and target points, provided by the user. This method was employed for the implementation of the described system and was optimized for pathway creation from an airway model. The method was also chosen considering that the trachea starting point can be used as source point, while the target location is already provided by the physician on the CT image to compute the nodule's probability malignancy with the system described in Chapter 3. This position is automatically converted by Slicer into a position within the 3D model, and no further manual interaction is required. Only in case

## 5. VIRTUAL BRONCHOSCOPY

---

the position to reach is outside the segmented airways the user is required to also select the label point closest to the target.

The algorithm extracts the centreline as the weighted shortest path traced between the two points. In order to ensure that the final lines are in fact central, the path is bound to run on the Voronoi diagram [230] of the 3D model. Voronoi diagrams can be thought of as the place where the centres of maximal inscribed spheres are defined. A sphere inscribed in an object is said to be maximal when there is no other inscribed sphere that contains it. So, for every point belonging to the Voronoi diagram, a sphere is centred on that point which is a maximal inscribed sphere. A Voronoi diagram can be very noisy. However, this noise does not affect the centreline. Centrelines are determined as the paths defined on the Voronoi diagram which minimize the integral of the radius of the maximal inscribed spheres along the path, which is equivalent to finding the shortest path in the radius. In order to do so, a wave is propagated from the selected source point using the inverse of the radius as the wave speed. The wave arrival time at all the points of the Voronoi diagram is then recorded, and finally the line from the indicated target point down along the gradient of arrival times is back-traced. The propagation is described by an Eikonal equation and is computed using the Fast Marching Method [167]. This operation is implemented for all the target points specified by the user.

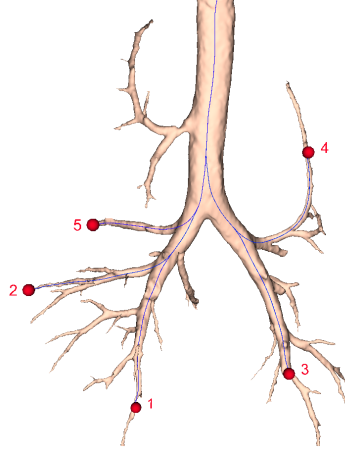
In case the area to reach is outside the 3D model, a final spline interpolation of the specified points is finally accomplished. The output of the method is a 3D model that is automatically fused to the airway model. An example of routes to different targets created using this method is presented in Figure 5.4.

### 5.4.4 Registration

#### 5.4.4.1 Overview

Registration is the last pre-processing step of the VB system implemented. Registration refers to the process of transforming a set of points in one coordinate frame of reference to another frame of reference. In the described application, this involves taking the position and orientation data from the real-time EM tracking system and transforming this data to the frame of the navigation environment,





**Figure 5.4:** Example of routes as created from an pig airway model. The different routes are shown in blue. The red dots represent 5 different targets selected by the user.

represented by the 3D rendered airway model. The registration is computed considering a rotation matrix, translation vector, and if required a scaling factor to transform the EM tracking frame into the virtual frame.

Registration allows for visualization of the position relative to the lung within the 3D model in real-time. The simplest and most common method for registration is landmark-based registration, also called rigid registration, and consists in selecting a set of points (usually 4 to 8) on the CT image of the patient, and physically touching with the probe at corresponding points in the patient. The two sets of point can then be aligned using a geometric transformation (rotation plus translation).

Solomon et al [196] presented a landmark-based registration using landmarks which are visually identified inside the lung. A similar method is also used by Schwartz et al [9] when describing the superDimension system.

A different approach to registration involves matching the video image of the bronchoscope with the 3D CT data [231]. Mori et al [203] outlined a hybrid registration method to improve an initial landmark-based registration with an image registration process. A hybrid registration algorithm was also proposed by Soper et al [205, 206]. The first landmark-based registration is followed by the implementation of a Kalman filter strategy applied to the video frame. This

## 5. VIRTUAL BRONCHOSCOPY

---

approach compensates for possible errors associated with the first registration, making the process more robust.

In general, landmark-based registration often results in a difficult and problematic approach due to difficulty in accurately obtaining registration data. Klein et al [232] demonstrated that a fiducial free approach provides better accuracy. Using in-volume-maximization (IVM) which aims at minimizing the number of points outside the airway model after acquisition of a set of probe points. In order to do so, a simulated annealing [233] is used to search for the best rotation and translation. This method provides a good registration, but is also computationally expensive.

In different studies, Mori et al [234] and Deguchi et al [235, 236] proposed landmark-free registration algorithms. Instead of using landmarks, the probe is simply moved in the patient's lungs while at the same time probe points are iteratively aligned with the virtual model through a iterative closest point (ICP) algorithm. This exploits the information for the current position in the real lungs to align the probe data with the correct bronchi regions using the 3D model's centreline. Luo et al [237] outlined a landmark-free registration that reduces the distance between rough probe points and the centreline extracted from the CT image. Lastly, Hofstad et al [238] proposed a different registration technique that uses a modified version of an ICP algorithm and combines both position and orientation of the bronchoscope to relate it to the running direction of the airway model centreline.

In this research, a novel landmark-free registration approach based on balanced surveillance bronchoscopy has been implemented. This helps improve accuracy of the algorithm and reduce the manual interaction required.

### 5.4.4.2 Landmark-free Registration

Landmark-based registration methods may oftentimes be tedious, time consuming and problematic, due to issues in picking corresponding points in the real environment. In some cases, the landmarking process needs to be repeated until a good registration is obtained. For this reason, a new landmark-free registration method that is easier and more feasible was investigated. This method uses the

probe data information acquired during a pre-procedure balanced bronchoscopy (balanced survey). The physician is asked to move the bronchoscope through the trachea and the two main bronchi, which are easily recognizable. The probe is tracked by the EM tracking system using a sensor placed at the tip of the bronchoscope [8,16,239,240]. This creates a cloud of points which is then registered to the corresponding airway model centreline points. To this end, an ICP algorithm is used. First, the mathematical tools used in the development of the algorithm are described, before implementation, testing and results of the algorithm are presented.

### Iterative Closest Point

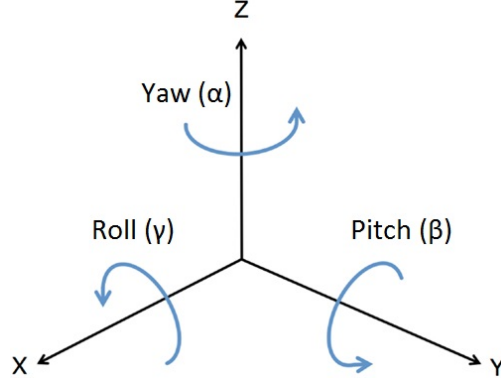
ICP is an algorithm employed to find the best transformation (in terms of rotation and translation) that aligns a source point cloud to a fixed target [241]. It is an iterative algorithm, that, in its simplest form, follows four main steps:

1. For each point in the source point cloud, the closest point in the target point cloud is identified; the closest point represents the target.
2. Root mean squared distance (RMSD) is minimised to find the optimal transformation aligning the source point cloud to the target point cloud.
3. The optimal transformation is applied to the source point cloud.
4. Step 1 is repeated until convergence is reached.

### Rotations Definition

A rotation matrix is defined by three angles:  $\alpha$ ,  $\beta$  and  $\gamma$ .  $\alpha$  is referred to as yaw rotation and defines the counterclockwise rotation around the  $z$  axis (for a definition of  $x$ ,  $y$ , and  $z$  axes, see Figure 5.5). The second angle,  $\beta$  is defined as pitch rotation and describes the counterclockwise rotation around the  $y$  axis. Finally, the  $\gamma$  angle determines a counterclockwise rotation around the  $x$  axis, and is addressed as roll rotation. These rotations are defined by (5.3) to (5.5).

$$\mathbf{R}_z(\alpha) = \begin{bmatrix} \cos \alpha & -\sin \alpha & 0 \\ \sin \alpha & -\cos \alpha & 0 \\ 0 & 0 & 1 \end{bmatrix} \quad (5.3)$$



**Figure 5.5:** Scheme representing yaw, pitch, and roll rotations.

$$\mathbf{R}_y(\beta) = \begin{bmatrix} \cos \beta & 0 & \sin \beta \\ 0 & 1 & 0 \\ -\sin \beta & 0 & \cos \beta \end{bmatrix} \quad (5.4)$$

$$\mathbf{R}_x(\gamma) = \begin{bmatrix} 1 & 0 & 0 \\ 0 & \cos \gamma & -\sin \gamma \\ 0 & \sin \gamma & \cos \gamma \end{bmatrix} \quad (5.5)$$

The single rotation matrix which embodies the three rotations is then formed by multiplying the yaw, roll and pitch rotation matrices as (5.6).

$$\mathbf{R}(\alpha, \beta, \gamma) = \mathbf{R}_z(\alpha)\mathbf{R}_y(\beta)\mathbf{R}_x(\gamma) \quad (5.6)$$

### Registration Algorithm

The algorithm takes as input the probe data acquired with EM tracking during a balanced surveillance bronchoscopy, the corresponding centreline branches and the carina position in both point clouds (used during a first rough alignment). The carina position inside the centreline is manually identified, while the carina position in the real lungs is acquired by requesting the physician to physically touch it with the probe. The points belonging to the trachea, and to left and right main bronchi are automatically labelled both on the virtual centreline points and on the physical probe data, with three different labels. The points belonging to the trachea branch are assigned the same index both on the centreline and in the probe data, as are the points of the two main bronchi. While in the landmark-based registration, at least 3 points must be selected and precision is essential. In this algorithm only the carina position must be approximately detected, as

alignment between the real and the “virtual” carina is automatic. Therefore, the registration procedure can be defined as landmark-free. The proposed algorithm works as follows. First, the two point clouds are centred (translation) with respect to the origin of the three labels. Next, an iteration process composed of 2 steps is employed. These steps are sequentially repeated until convergence is reached using a RMSD cost function defined by (5.7).

$$\text{RMSD} = \frac{1}{N} \sum_{i=1}^N \sqrt{\|\mathbf{p}_i - \mathbf{c}_i\|^2} \quad (5.7)$$

In (5.7)  $N$  is the number of points,  $\mathbf{p}_i$  is a probe point and  $\mathbf{c}_i$  is the centreline point closest to  $\mathbf{p}_i$ . The first step focuses on searching for the optimal rotation that minimises the RMSD between the two point clouds. To this end, an ICP method is implemented. Since only rotation is considered, a Kabsch algorithm [242] is used. The source points are defined by the positions acquired with the probe, whereas target points are determined by the centreline’s closest points. Searching of these closest points represents the key enabler for the algorithm and is accomplished by taking into account only points having the same label. As an example, if the trachea is assigned a label of 1, only centreline points with that index are considered. In this way, local minima (e.g. registration of the left bronchus as the right one) are avoided. This step is repeated until the rotation matrix  $\mathbf{R}$  converges. Absolute convergence is reached when  $\mathbf{R}$  is an identity matrix. Once the first step is complete, a second step of searching for the optimal translation that minimises the RMSD between the two clouds of points is employed. As in the previous step, ICP is also used to find the translation that minimises the RMSD. In this case, a local optimization algorithm is used. Again, labels of the different regions are considered to avoid local minima. This step is necessary as the carina is manually detected, causing possible misalignment between the position of the two clouds. The problem to be solved is represented by (5.8):

$$\mathbf{t}_{opt} = \arg \min_{\mathbf{t}} \left\{ \sum_{i=1}^N \sqrt{\|\mathbf{p}_i + \mathbf{t} - \mathbf{c}_i\|^2} \right\} \quad (5.8)$$

where  $N$  is the number of samples,  $\mathbf{t}=(t_x, t_y, t_z)$  the translation vector,  $\mathbf{p}_i$  the probe point, and  $\mathbf{c}_i$  the closest centreline point. The two steps are iteratively

## 5. VIRTUAL BRONCHOSCOPY

---

computed, and at the end of every iteration, the difference between the two RMSDs is computed. After the iteration process, an optimal  $\mathbf{R}$  and an optimal  $\mathbf{t}$  are found. These are used as initial conditions for an optimization algorithm that computes the final  $\mathbf{R}$  and  $\mathbf{t}$  by solving (5.9).

$$(\alpha_f, \mathbf{t}_{f,opt}) = \arg \min_{\alpha_f, \mathbf{t}_f} \left\{ \sum_{i=1}^N \sqrt{\|\mathbf{R}_f \mathbf{p}_i + \mathbf{t}_f - \mathbf{c}_i\|^2} \right\} \quad (5.9)$$

In (5.9)  $\alpha_{sa}$  is the vector containing the yaw, pitch, and roll angles,  $\mathbf{R}_{sa}$  the rotation matrix, and  $\mathbf{t}_{sa}$  is the translation vector. This step increases the probability of convergence to a global minimum. The transformation function,  $\mathbf{T}_{sa}$ , found using the optimization is a matrix defined by (5.10).

$$\mathbf{T}_f = \begin{bmatrix} \mathbf{R}_f & \mathbf{t}_f^\top \\ 0 & 1 \end{bmatrix} \quad (5.10)$$

Lastly, the final transformation matrix  $\mathbf{T}_r^v$  is given by the multiplication of the matrices found at each stage of the registration procedure, using (5.11).

$$\mathbf{T}_r^v = \mathbf{T}_x \mathbf{T}_f \left( \prod_{j=0}^{N-j} \mathbf{T}_j \right) \mathbf{T}_i \quad (5.11)$$

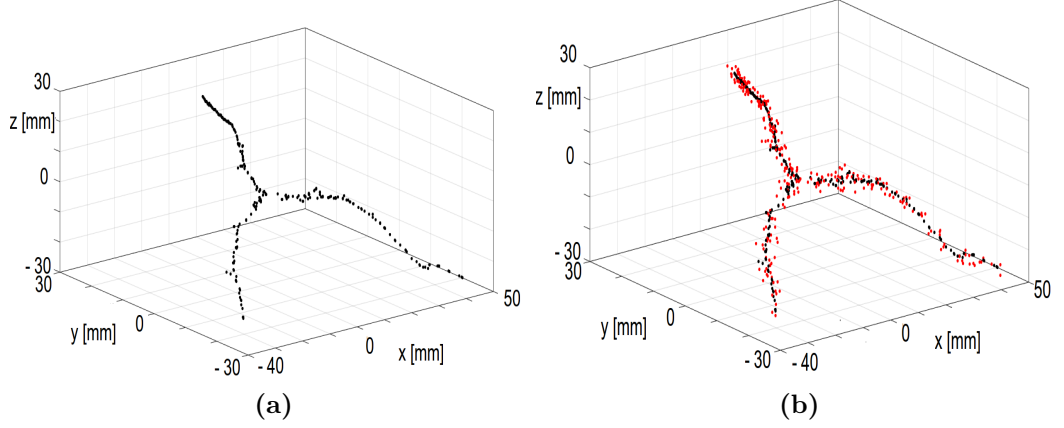
Here  $\mathbf{T}_i$  is the transformation matrix to translate the probe points to the origin and is defined by (5.12):

$$\mathbf{T}_i = \begin{bmatrix} 1 & 0 & 0 & -C_{px} \\ 0 & 1 & 0 & -C_{py} \\ 0 & 0 & 1 & -C_{pz} \\ 0 & 0 & 0 & 1 \end{bmatrix} \quad (5.12)$$

where  $C_{px}$ ,  $C_{py}$ , and  $C_{pz}$  are the coordinates of the carina position in the real world, while  $\mathbf{T}_z$  represents the transformation matrix to translate the probe points to the virtual coordinate system:

$$\mathbf{T}_z = \begin{bmatrix} 1 & 0 & 0 & C_{vx} \\ 0 & 1 & 0 & C_{vy} \\ 0 & 0 & 1 & C_{vz} \\ 0 & 0 & 0 & 1 \end{bmatrix} \quad (5.13)$$

with  $C_{vx}$ ,  $C_{vy}$ , and  $C_{vz}$  indicating the coordinates of the carina position in the virtual world. The algorithm has been implemented in MATLAB (Mathworks Corp, Natick, MA), and a graphical user interface has been designed to facilitate user interaction during the registration.



**Figure 5.6:** The model used for the first test. In a) the portion of centreline used to run the registration is shown. In b) the centreline (black) and the point cloud (red) generated by adding random values are presented. The origin of the reference system is represented by the carina centreline.

### Algorithm Testing Methods

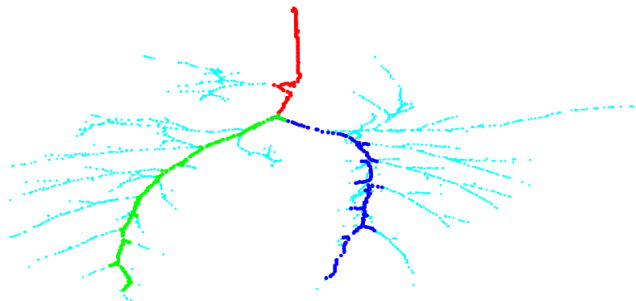
The described algorithm was tested with both simulated and real data, acquired with EM tracking data using three different test methods: the first one using simulated data obtained from the centreline obtained using the chest CT image of a pig lung. A second test was conducted on a perspex model that reproduced the airway structure. Finally, the last test was accomplished in a pre-clinical setting using the breathing pig lung phantom described in Chapter 3.

#### *Simulated Data Testing*

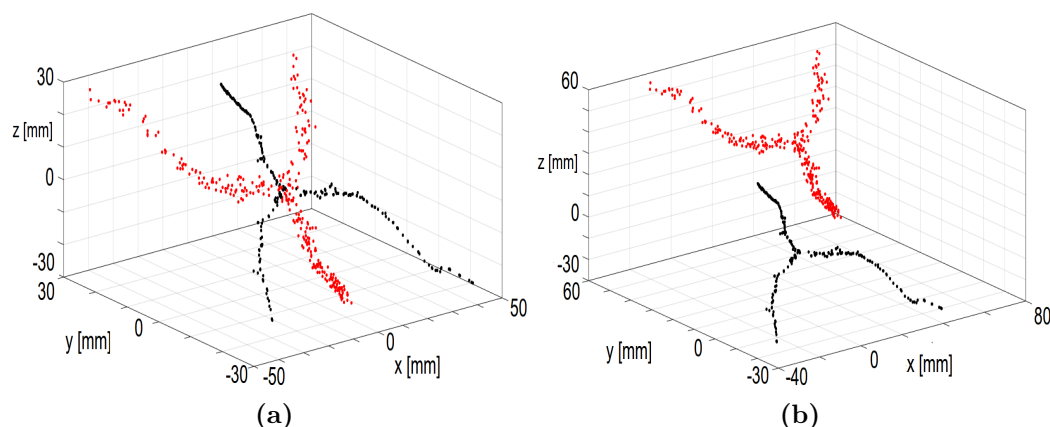
The first technique consisted in simulating real data. The approach exploits the portion of the airway centreline associated with the balance survey to generate data that simulates probe data. In particular, 299 points of the centreline extracted from the airway model obtained from a pig lung chest CT image was considered. This is shown in Figure 5.6(a). Each region of the centreline is then automatically assigned a different label, as shown in Figure 5.7. Next, the method to generate the simulated probe data was triggered. This consists in three different steps. First, a random noise (in a range  $[-5, 5]$  mm) is added to each coordinate of each centreline point, maintaining the label previously determined

## 5. VIRTUAL BRONCHOSCOPY

---



**Figure 5.7:** Portion of centreline extracted for the registration algorithm. Different labels are automatically associated with trachea, left main bronchus and right main bronchus, shown in red, green and blue, respectively.



**Figure 5.8:** Generation of simulated probe data. In (a) the centreline (black) and the generated point cloud after a rotation of yaw = roll = pitch =  $\pi$  is applied. (b) Shows the centreline (black) and the point cloud generated after an arbitrary translation is applied. The origin of the reference system is the original carina centreline.

(Figure 5.6(b)). The random values were recomputed for each trial. Next, a rotation is applied to the points cloud, using a rotation matrix with random yaw, pitch and roll (in the range  $[0, 2\pi]$ ). An example is given in Figure 5.8(a). Finally, a random translation (in a previously defined range) is applied (see Figure 5.8(b)).

The new point cloud was used as a simulated probe data points cloud. The



carina positions in the centreline points were manually identified in the centreline points used for all the tests. On the other hand, the carina position of the generated points cloud was found by adding a random value to each coordinate of the centreline carina. The carina centreline was also used as origin for the centreline's reference frame. These values were chosen in a range between  $[-20, 10]$  mm and the translation of the point cloud is defined by a vector whose elements have the same values, in the range between  $[-200, 200]$  mm.

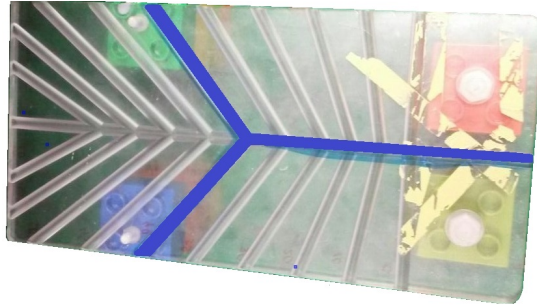
Several trials of registration achieved between the centreline and the simulated point clouds were used to evaluate performance of the algorithm, in terms of accuracy and convergence time. Accuracy was measured by comparing the RMSD between the centreline points and the generated points (1) after adding the random value and (2) after the registration process. If the RMSD obtained after registration was higher than the previously computed one, the registration result was assumed to be close enough to a global minimum.

Five hundreds trials were used to test the algorithm: 100 trials using the whole point clouds, 100 using 50% of the total points, 100 with 30% of the points, 100 considering 25% of the points, and a final 100 trials in which 20% of the total points were used. This way, accuracy was tested for cases where the number of points acquired with the probe is lower than the number of points composing the centreline. For each trial, RMSD was computed after adding the random value to the generated data and at the end of registration. Convergence time as well as values used to generate the point cloud were calculated.

Before testing the algorithm with the generated data, a simpler set of tests was carried out. In this case, the probe data points were generated without adding the first random value. Hence, the registration problem has to be solved between the centreline and a simply translated and rotated version of it. This way, the first RMSD is equal to 0 mm, as no random value was added, and the RMSD computed at the end of the registration can be interpreted as registration error. Hence, the registration error is expected to be close to zero in this set of trials. This test provides a preliminary quantitative measure of algorithm accuracy. In fact, assuming that the tip of the bronchoscope is moved close to the medial axis of the airway during the balanced survey, generating probe data starting from

## 5. VIRTUAL BRONCHOSCOPY

---

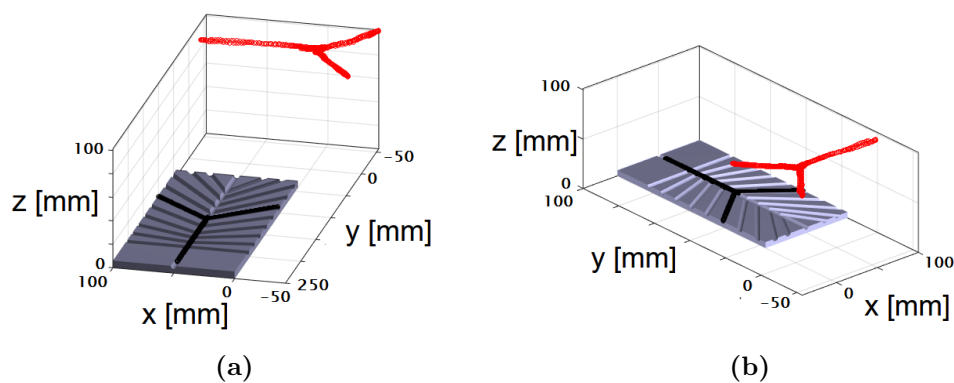


**Figure 5.9:** The perspex model used for the second test. The blue line highlights the path followed to simulate a balanced survey.

the centreline puts us in the optimal position to evaluate whether the algorithm is correctly generated.

### *Rigid Airway Model Testing*

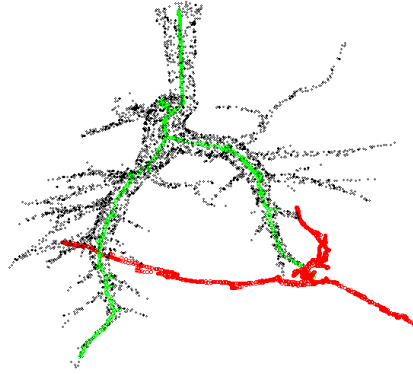
A second test was conducted using a perspex model reproducing the airway anatomy. The model is shown in Figure 5.9. The path followed with the probe is highlighted in blue. This represents the points cloud of the balanced survey. A 3D virtual model of the blue path was created and the centreline extracted using VMTK [193] classes. Fig. 5.10 shows the initial conditions of the problem. The centreline consisted of 510 points, while 1500 probe data points were tracked.



**Figure 5.10:** Two different views of initial conditions for registration testing with the plastic phantom model. Centreline points are shown in black, while probe data points are shown in red.

### *Breathing Lung Model Testing*

The last test evaluated performance using the data acquired from a breathing pig lung model. An expert pulmonologist was asked to execute a balanced surveillance bronchoscopy inside the breathing model, while the tracked probe data was recorded. The lung model was then scanned with a GE System Discovery CT750 HD scan (0.625 mm slice thickness, 60 mA radiation dose, LUNG reconstruction kernel), the airway segmented and the airway model created as described in Chapter 3. The centreline of the airway was extracted using the approach described in Section 5.4.2.2, and used for the registration process. Due to mechanical deformation of the breathing lung model, reproducing the same airway tree used to acquire the scan during the balance survey is challenging. The initial condition to this registration problem is shown in Figure 5.11. The 3D model is shown in black, the centreline is pictured in green, while the experimentally recorded probe data are shown in red.



**Figure 5.11:** Initial condition for registration testing with data acquired using a balanced surveillance bronchoscopy. The airway 3D model is shown in black, whereas centreline points are shown in green and experimentally recorded probe points are shown in red.

### Registration Testing Results

Results achieved for the probe data simulated without adding the random noise are summarized in Table 5.2. Table 5.3 shows results obtained for probe data simulated with random values added. After 500 trials, only in 9 cases was the

## 5. VIRTUAL BRONCHOSCOPY

RMSD measured after registration larger than that measured after adding random noise. In these nine cases, average differences between initial and final RMSD

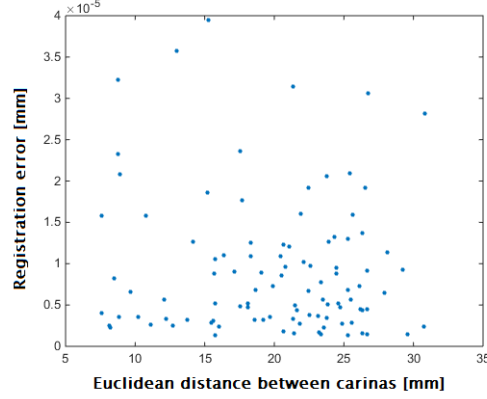
Num. of points	Average Registration Error (mm)	Maximum Registration Error (mm)	Average Time to Convergence (s)
299	$9 \times 10^{-6}$	$3.94 \times 10^{-5}$	20.30
149	$1.02 \times 10^{-5}$	$7.33 \times 10^{-5}$	14.16
99	$9.40 \times 10^{-6}$	$3.07 \times 10^{-5}$	11.95
74	$8.48 \times 10^{-6}$	$4.89 \times 10^{-5}$	10.89
59	$1.03 \times 10^{-5}$	$4.17 \times 10^{-5}$	9.70

**Table 5.2:** Registration trials between the centreline extracted from the pig (299 points) and the point clouds generated with the method proposed without adding the random values.

Num. of points	Average Time to Convergence (s)	Num. of Trials with $\text{RMSD}_f > \text{RMSD}_i$
299	19.63	1
149	15.72	0
99	13.52	3
74	12.31	3
59	10.27	2

**Table 5.3:** Registration trials between the centreline extracted from the pig (299 points) and the simulated point clouds.  $\text{RMSD}_f$  is the RMSD computed after registration, while  $\text{RMSD}_i$  represents the initial RMSD.

was  $0.02 \pm 0.02$  mm. The longest trial took 28.76 seconds on a 1.6 GHz, 4 GB RAM PC. As shown in Fig. 5.12, registration error of the algorithm is not correlated to the Euclidean distance between the position of the carina of the two clouds at the beginning of the registration. So, while human input is required, this input does not affect the results. Figure 5.13 gives an example of registration between the



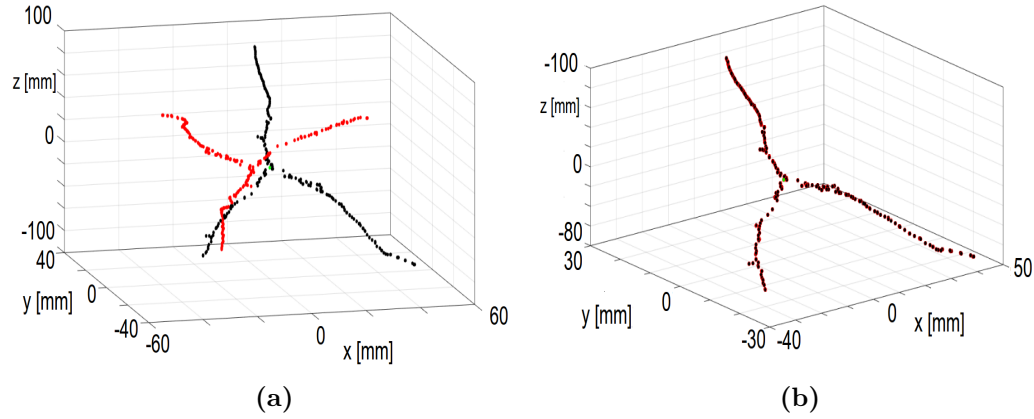
**Figure 5.12:** Correlation between Euclidean distance at the beginning of registration and the registration accuracy, achieved in 100 different trials.

centreline and a point cloud generated by adding a rotation of yaw =  $\pi$ , roll =  $\pi$ , and pitch = 0 (centreline and point clouds both consisting of 299 points). Figure 5.13(a) shows this specific initial condition. Here the carina of the two clouds are not in the same position (Euclidean distance between the two was 8.6 mm). The registration error obtained in this example was  $5.40 \times 10^{-4}$  mm, achieved in 9.88 seconds.

Table 5.4 shows the different registration results obtained on ten different cases. Initial conditions (distance and relative rotation between the carina positions in the two different point clouds), registration accuracy and time of convergence are reported. Both clouds were composed of 299 points.

Figure 5.14 shows the registration results achieved using the perspex model. In this case, time to convergence was 41.67 seconds, with RMSD = 2.09 mm. Since precision of the sensor is in the range [1, 1.5] mm, this can be considered a near optimal result. The percentage of points inside the whole model was 93.43%. Klein et al [232] analysed the performance of different registration algorithm with a similar phantom model, in terms of percentage of points within the model. Only one algorithm was reported to obtain a percentage of points bigger than 93% (97% in the best scenario). The comparison between the percentage achieved in the test presented here and the ones detailed in [232] show that the proposed registration algorithm may be considered a positive step forward. However, to

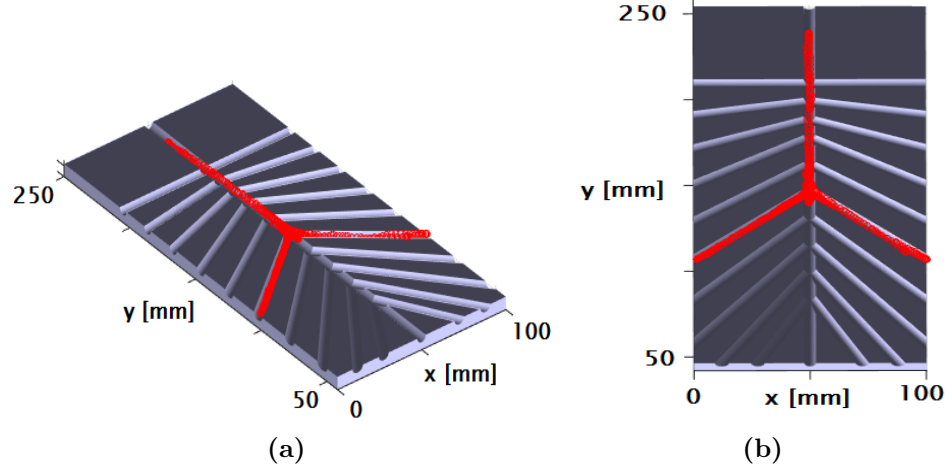
## 5. VIRTUAL BRONCHOSCOPY



**Figure 5.13:** Example of registration trial between the centreline (black) and a point cloud (red) generated without adding the initial random value. (a) Shows the initial condition: the Euclidean distance between the two carinae is 8.6 mm. (b) Shows the registration achieved. The process took 9.88 seconds, with an error of  $5.40 \times 10^{-4}$  mm.

Euclidean Distance of Carinas (mm)	Yaw (rad)	Roll (rad)	Pitch (rad)	Time of Convergence (s)	Registration Error mm
17.52	3.84	3.54	0.05	22.12	$7.50 \times 10^{-6}$
20.39	1.63	4.44	4.43	25.98	$2.00 \times 10^{-6}$
13.99	2.79	5.71	0.41	26.04	$3.89 \times 10^{-6}$
22.75	1.83	3.11	4.57	23.53	$1.43 \times 10^{-6}$
10.14	3.68	1.63	0.97	18.34	$2.16 \times 10^{-5}$
22.87	3.35	4.66	2.35	24.49	$1.16 \times 10^{-5}$
9.39	5.26	2.64	0.97	16.59	$5.25 \times 10^{-6}$
19.67	5.37	4.16	4.39	23.00	$6.37 \times 10^{-6}$
23.70	4.24	0.38	2.60	28.41	$1.28 \times 10^{-5}$
22.88	3.36	4.09	5.50	23.34	$1.36 \times 10^{-5}$

**Table 5.4:** Ten different registration problems. Initial condition, registration error and time of convergence are reported.

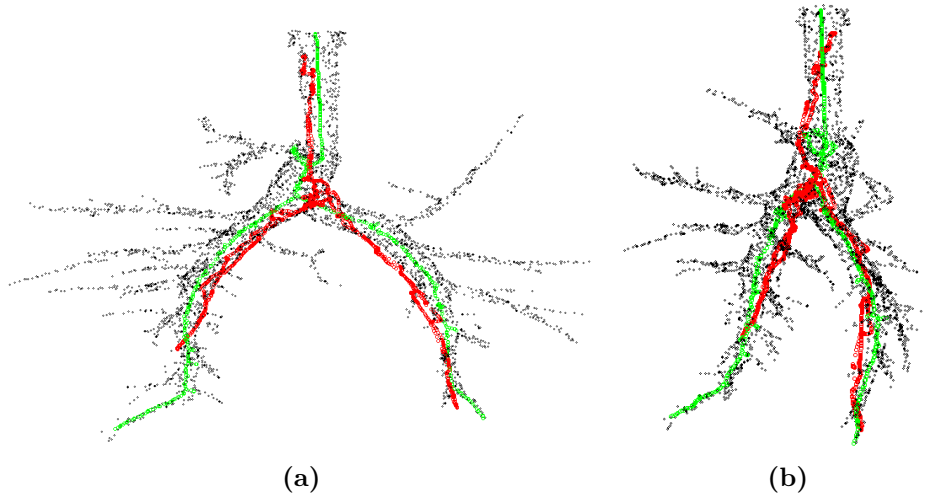


**Figure 5.14:** Two different views of result achieved using the perspex model. Centreline points are shown in black, while probe points are shown in red.

obtain a more objective comparison the same phantom model should be used for the registration.

Finally, results obtained on the breathing pig lung model are shown in Figure 5.15. In this case, time to converge was 168.03 seconds, using a centreline of 799 points and a probe data cloud of 1000 points.

In general, the algorithm may represent an improvement over the state of the art in electromagnetic navigation bronchoscopy. Although minimal user interaction is still required, the system is easy to use and increases the autonomy of the registration results. Performance of the algorithm was validated with three different test methods; simulated data, balanced survey on a perspex model, and balanced survey on a breathing pig lung model. At present, the inputs required from the user are necessary to assign different indices, or labels, to the different branches used for registration, to avoid local minima. Unlike landmark-based approaches, these inputs do not have to be precise, but just provide a rough indication of the position of the three branches. However, the end goal is to obtain an algorithm that reduces and removes all user interaction. To this end, future work will seek to automatically detect the three branches used in registration (carina, left and right main bronchi).



**Figure 5.15:** Registration results achieved on the breathing pig lung model. Two views from two different perspective are shown.

### 5.4.5 Image-Guided Bronchoscopy

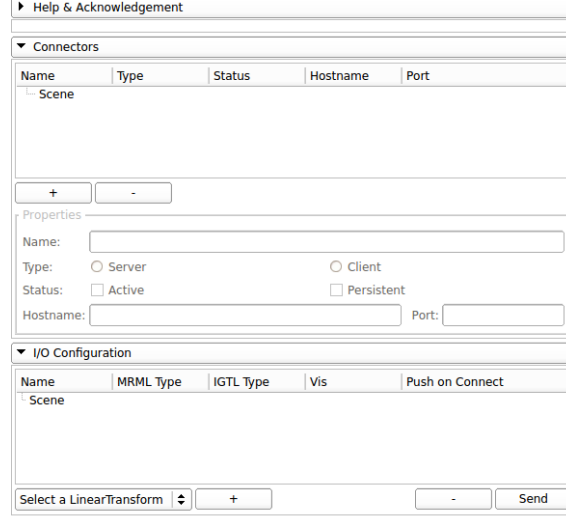
#### 5.4.5.1 Overview

The pre-procedure step ends with registration. Once the real airways are registered to the virtual airways created in Slicer, image-guided bronchoscopy begins. When the operator is ready, the tracking system sending position and orientation information from MATLAB to Slicer can be activated. The button “Track Sensor” on the interface will allow for visualization of real-time actual probe position in the airways model. For this to happen, several operations are involved, including connecting Slicer to MATLAB, compensating for possible registration or tracking errors, and correcting for roll rotation of the scope. In this section, the technique implemented to stream real video frames from the bronchoscope to 3D Slicer is also described.

#### 5.4.5.2 MATLAB-Slicer Bridge Connection

As stated above, the EM tracking system utilises a code implemented in MATLAB to track the position of the probe in the real world and to transform this information into a position in the virtual world using the registration process [30].





**Figure 5.16:** The OpenIGTLink extension interface as it appears in 3D Slicer.

After this is complete, the position of the probe is identified by a transformation matrix  $\mathbf{T}$  defined, as described above by (5.14).

$$\mathbf{T} = \begin{bmatrix} & \mathbf{R} & & \mathbf{t} \\ 0 & 0 & 0 & 1 \end{bmatrix} \quad (5.14)$$

In (5.14)  $\mathbf{R}$  represents the  $3 \times 3$  rotation matrix and  $\mathbf{t}$  is the translation vector of the probe. The first step toward the visualization of the actual probe position inside the virtual environment is communication between Slicer and MATLAB. For this purpose, a Slicer extension referred to as OpenIGTLink [214,243,244] is used. This is a network communication protocol specifically designed and developed for research on image-guided and computer-assisted interventions. It provides a standardized mechanism for communications among computers and devices for a wide variety of image-guided therapy (IGT) applications. OpenIGTLink is a set of messaging formats and rules (protocol) used for data exchange on a local area network (LAN). The extension is shown in Figure 5.16. Once installed, OpenIGTLink allows the user to create a new server with a specific hostname and a unique port number within Slicer. These can then be used to connect any other application to send real-time information to Slicer. Alternatively, the same mechanism can also be used to send information from Slicer to over devices. In the proposed application, this strategy was used to both send the transformation

## 5. VIRTUAL BRONCHOSCOPY

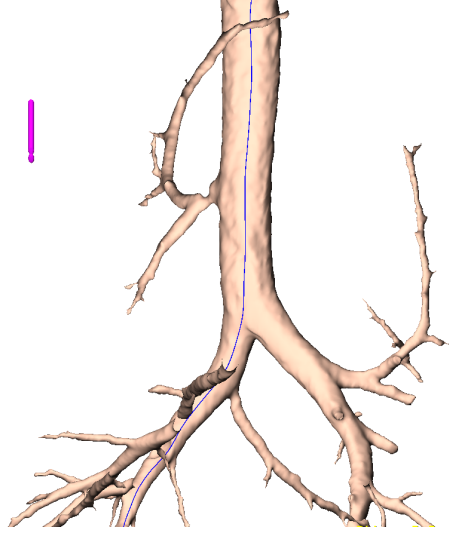
---

matrix containing the probe information from MATLAB to Slicer, and to send the video frames captured by the bronchoscope's camera to Slicer.

Once the information is available in Slicer, the “Transforms” tool is used for editing  $\mathbf{T}$ , when necessary, and to visualize the actual position of the probe in the virtual environment. With this tool, the transformation is applied to the 3D model of the probe, which is then translated and rotated according to the information received. The same transformation is then applied to the virtual camera in one of the two 3D views presented to the user. In this view, the camera is also placed at the tip of the probe model, with a focal point on the long axis of the probe. In this way, when the probe moves inside the lung, a virtual reproduction of the inside of the airways is shown to the user. The second view presented to the user shows the 3D airway model, the probe, and the planned path from a panned position. In this case, the camera is aligned with the  $z$  position (see Figure 4.8) of the probe tip. Also, according to the position of the probe, the camera zooms in or out to magnify airway details when smaller branches are reached. Finally, a second endobronchial 3D view enabling the user to follow the probe at a proximal displacement as the bronchoscope moves is available. The camera is then placed at a later side of the probe, to provide a different view that may be helpful in peripheral airways.

### 5.4.5.3 Centreline Compensation

One of the main issues when developing a system for image-guided bronchoscopy is the registration process. If the two frames of reference are not properly registered, virtual navigation will be corrupted. If a landmark-based registration process is utilised, difficulties lay in finding the correct corresponding points in the real and virtual airways. In addition, if the operator is not an expert, using a lung phantom may create confusion in distinguishing the right bronchus from the left. An example result of incorrect registration is shown in Figure 5.17. In this figure, the probe (purple marker) is completely outside of the model, whereas the bronchoscope is clearly inside. The novel landmark-free registration method developed helps improve accuracy of the registration process and therefore reduce possible misalignments. However, errors may still occur, especially in cases where

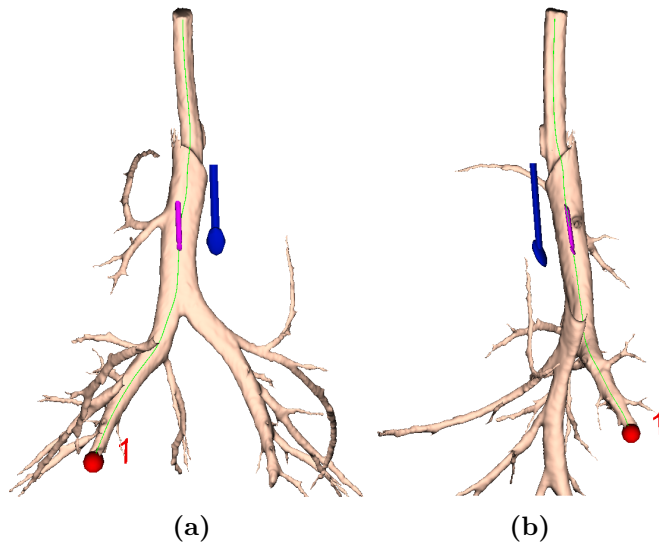


**Figure 5.17:** If registration is not adequately executed, the probe model position (indicated by the purple marker) will be completely outside the airways model.

the lungs can be deformed after the CT scan (as in the case of the lung phantom at UCC). For this reason, an interim method to compensate for misalignments to help improve accuracy of the navigation was developed. The idea underlying the method is to exploit the fact that physicians tend to move the bronchoscope on the medial axis of the airways. Therefore, assuming that registration errors are not excessive, the centreline of the airway model can be exploited. To this end, the translation vector,  $\mathbf{t}$ , of the transformation matrix is analysed and, when needed, modified. In particular,  $\mathbf{t}$  is compared to the centreline points list (extracted during the pre-processing step) and the centreline position with smallest Euclidean distance to the actual position is used as the new position. In this way,  $\mathbf{t}$  is modified with the new value. An example of corrected probe position is shown in Figure 5.18. The blue marker represents the current probe position received from MATLAB. The purple marker indicates the corrected position of the probe, when compensating for errors using the centreline extraction. However, using the Euclidean distance as a method to compensate registration errors may cause issues when branches become smaller and closer to each other. In this case, even a small registration error may cause to choose a wrong point on the centreline. This can cause a discontinuity in the compensated probe position

## 5. VIRTUAL BRONCHOSCOPY

---



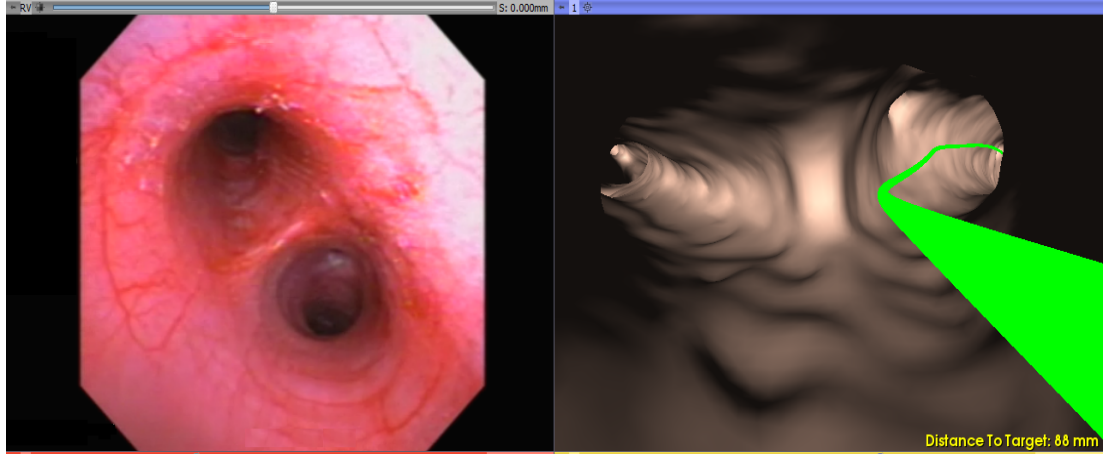
**Figure 5.18:** Representation of the centreline compensated navigation. Two views of the same frame from two different perspective are shown. The blue stick indicates the actual position as received from the tracking system. The purple stick represents the corrected position of the probe.

from one branch to another. For this reason, future work should seek to identify an optimal registration strategy.

### 5.4.5.4 Roll Rotation Compensation

The EM tracking system used to track the current position of the scope currently utilises 5 DOF sensing. This means that along with the three components of the translation  $\mathbf{t}$ , only the yaw and pitch rotations can be tracked. This adversely affects virtual navigation, because as the physician rotates the scope the virtual and real images may become misaligned (Figure 5.19). This consideration is particularly important at branching points, where a decision on the direction to follow within the virtual model is made. It is worth noting that commercial systems such as superDimension [26] and Veran SPINDrive [27] use 6 DOF sensors with in their tracking systems, at the expense of larger instruments. However, this eliminates the issue of roll misalignment.

As VB has become of general interest in research, numerous strategies of image

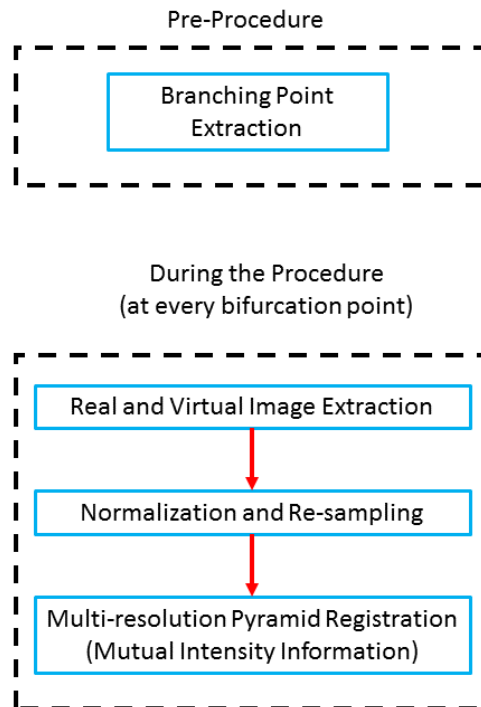


**Figure 5.19:** Example of roll misalignment between the real and virtual video frames. On the left side the actual view from the bronchoscope is presented, while the picture on the right side shows the virtual image. The green line indicates the path to reach the selected target.

registration for VB have been proposed. Some techniques try to correct videobronchoscopic distortion caused by the scope camera [245, 246], while other approaches use the video image as a real-virtual registration tool either in hybrid registration methods or as unique approaches [203, 218]. A third method uses image registration as a tracking system to determine the actual position of the scope and reproduce it inside rendered views of the airway model [196, 202]. Methods for image registration can be divided in two main categories; intensity-based and geometry-based methods. The former method compares image intensities to find the best match between the compared images [197, 198]. Geometry-based methods compare anatomical structures extracted from the real video images and the images of the airway model. Recovering geometrical structures from video images can be challenging [199, 200]. Another main drawback of image registration is that it can be time consuming (e.g.,  $> 1$  second per frame [203]). Therefore, methods that incorporate motion prediction have also been investigated to achieve faster convergence for registration [208, 247]. Although not optimised, an intensity-based image registration that geometrically aligns the video frame from the virtual camera to the corresponding video frame captured from the bronchoscope is proposed. The method requires approximately 0.25 seconds to complete.

## 5. VIRTUAL BRONCHOSCOPY

---

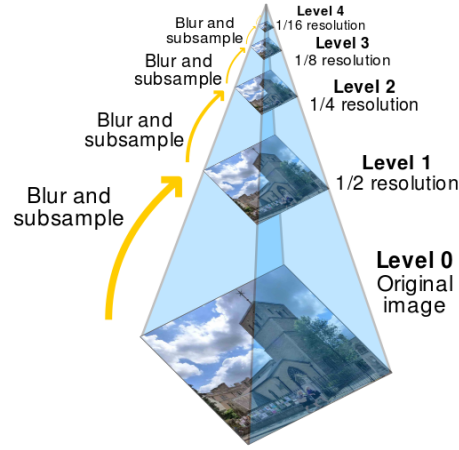


**Figure 5.20:** Block diagram of the roll rotation compensation steps. Extraction of branching points is computed prior to the procedure, while registration steps are executed at every bifurcation during navigation.

Although quite fast, the method is still too slow to be useful to track every probe position. This may cause delays and confusion during navigation. Therefore, image registration is employed only when the scope reaches a branching point. Figure 5.20 shows a block-diagram of the main steps involved in the implementation of the algorithm. In the following paragraphs the method to compute the airway model's branching points is described and then the algorithm implemented for image registration is detailed.

### Branching Points Extraction

To identify the branching points (bifurcations) of the airways model, the extracted centreline is used. This algorithm was implemented in MATLAB and is executed during the registration process. After the centreline labelling process is computed, the algorithm calculates the distance between every point of the centreline and



**Figure 5.21:** Scheme of the multiresolution pyramid method [248].

all the points of the other branches with a different label. If the reference point is close enough to one or more points belonging to a different branch, then the reference point index is stored as a bifurcation point. The threshold that defines if two points are close enough was empirically set to 3 mm. This operation determines a cloud of points at every airway bifurcation. The bifurcation positions are then saved to a .txt file which is read by Slicer when the image registration process begins.

### Image Registration Implementation

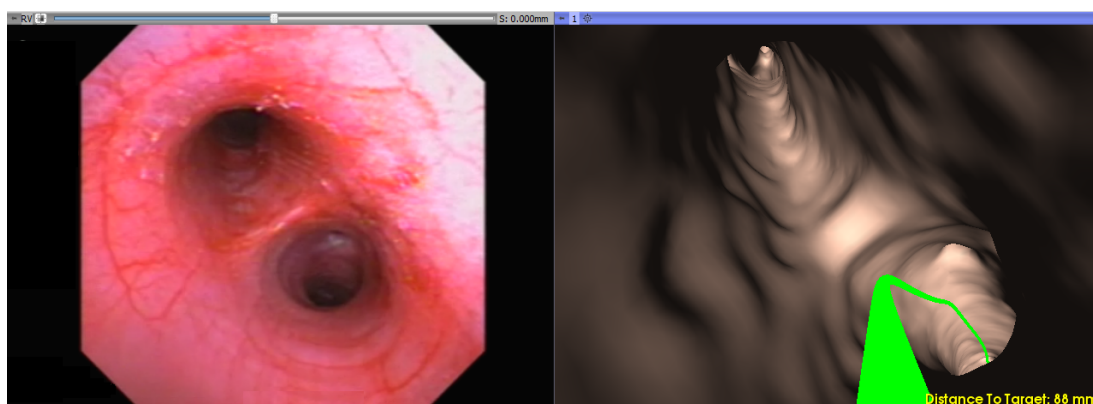
When the physician moves the scope inside the lung, the probe position is compared with the stored bifurcations points. When the probe is at a specified distance (between 3 and 6 mm) from the bifurcation, the image registration algorithm is automatically triggered. The range of distances has been empirically defined and decreases when the scope moves closer to smaller branches. Also, to avoid unwanted delays between one registration and the following one, a three second time limit on consecutive registrations is imposed. The algorithm starts recording the real video image and the virtual projection of the 3D airway model. The two images are then normalized and the virtual image is re-sampled to match the resolution size of the real image. At this point, the images are registered, estimating the virtual camera pose that maximizes the similarity between them. In

## 5. VIRTUAL BRONCHOSCOPY

---

the proposed approach, registration of the relative rotation between the two images is the key point. To do so, a multi-resolution pyramid registration method that uses mutual intensity information as the similarity measure is employed. An exhaustive optimizer is utilised to find the rotation that defines the optimal match between the two images [61]. In particular, the multi-resolution pyramid is a multi-scale signal representation in which a sequence of copies of the original image is obtained decreasing both sample density and image resolution. An interpolation is then applied to create the sub-sampled versions of the image. Figure 5.21 shows representation of the pyramid filter. To obtain the different resolution levels, the image is low pass-filtered and down-sampled by a factor of 2 to obtain the first pyramid level. The same operation is then repeated, until all the required levels are obtained. Image details and patterns may be more visible at one level rather than at another. For this reason, using a pyramid representation of the real and virtual images provides for improved comparison. In the described approach, four pyramid levels are used. For each level, the down-sampled version of the two images is compared by computing a transform that determines rotation of an image around a chosen centre. The pyramid version of the virtual image is rotated around the pyramid version of the real image and the rotation angles optimized. As a measure of similarity of the two images, the Mattes mutual information is used [249]. Considering complete  $2\pi$  rotation for comparison may require up to 1 minute to reach convergence, which is too long for VB procedures. Therefore, empirical investigation led to 36 rotations, one every 10 degrees, as a good trade-off between registration accuracy and computational time. The optimal angle that determines the best match between the real and the virtual image is then considered, and the airway 3D model is rotated accordingly. Figure 5.22 shows the real and virtual frame images after image registration is employed. This method was tested both on pre-clinical *in-vitro* and *in-vivo* studies. However, a future solution that allows for continuous image registration may further improve the guidance experience. An alternative method may be to use this approach in combination with a physical instrument to determine the roll rotation of the bronchoscope or the use of 6 DOF sensing.





**Figure 5.22:** After the image registration process, the virtual image is rotated to match the real image.

#### 5.4.5.5 Video Streaming

As shown in Figure 5.1, during the procedure the bronchoscope is connected to a screen that shows the real-time video frames. However, having the real frame next to the virtual image may further help the physician choose a correct path. For this reason, the real video is streamed into Slicer, in a window next to the virtual image. For this purpose, a WinStar video grabber [209] connects the scope screen to the PC. BlazeVideo [210] is then used to visualize the transmitted images on the PC. The PC is then connected via SplitCam [211] to allow visualization of the images for different applications. To transmit the image to Slicer the functionalities of the OpenIGTLink extension are exploited, using the open-source software PLUSServer. PLUS supports numerous video capture devices, allowing for the creation of a local server where the video can be transmitted. Orientation, frame size and video format are adjustable, as well as the local server parameters which have to be specified. Once this is complete, the system starts streaming the endobronchial video stream.

## 5.5 Summary

In this chapter, the implementation of a new open-source method for VB to be used in combination with EM tracking has been described. The method offers

## 5. VIRTUAL BRONCHOSCOPY

---

image-guidance navigation during bronchoscopy, and paves the way for potential future work with virtual navigation for safe and reliable airway disease diagnosis. The system is defined by two main parts, one pre-procedural, and the second one for virtual navigation. The key components of the system are:

- An open-source method that extracts the airways centreline starting from an airways label.
- A method for procedure planning, that provides different tools for the selection of the target biopsy, nodule or airway, and constructs the optimal path for navigation.
- Distance to target is updated in real-time and presented to the user.
- During the navigation, real and virtual images are shown and the CT image is automatically aligned to the actual position of the probe to facilitate navigation.
- Probe position compensation to the closest centreline position to overcome possible registration errors.
- An image registration process that compares the real and virtual images at every branching point of the airway model, rotating the virtual image to match the real one. This compensates for the use of 5 DOF tracking sensors.

# Chapter 6

## Pre-clinical Testing and Results

### 6.1 Overview

In this chapter the testing that was carried out on the VB system coupled with the EM tracking to verify performance and accuracy is described. The testing methodology used is described and the results are outlined.

The system was tested on both *in-vitro* and *in-vivo* pre-clinical animal studies. This serves as a precursor for future clinical work on human trials. First, the VB technology was tested *in-vitro* in a breathing lung model to verify performance in a simulated setting. Next, to further evaluate VB in a realistic setting, multiple animal studies were carried out. This chapter details the different study parameters, evaluation methods, and the results of navigation through the airways. The following summarises the main results obtained:

- Using a VB system, pathways toward pre-defined targets were correctly created.
- Using VB, targets were generally reached by the users, both by expert and non-expert pulmonologists.
- System usability was measured using standard usability scales. User feedback after using the system was very satisfactory.

## 6. PRE-CLINICAL TESTING AND RESULTS

---

- Pre-clinical *in-vivo* studies identified that few modifications need to be made to the system towards the definition of an accurate and reliable method for image-guided bronchoscopy.

### 6.2 Breathing Lung Model Evaluation

In this section, evaluation with a breathing pig lung model was explored. The tests were conducted at the Irish Thoracic Society (ITS) Conference [250], that took place in Cork, Ireland, in November 2015. Nine different specialist physicians in the field of respiratory medicine were asked to navigate through the model lungs in order to reach three pre-defined physical targets. The VB system was presented on screen to the physicians who had to follow the different paths created in the virtual environment to reach the regions of interest. At the end of the procedure, a questionnaire was presented to the physicians to evaluate their general experience. Time to reach the targets was recorded.

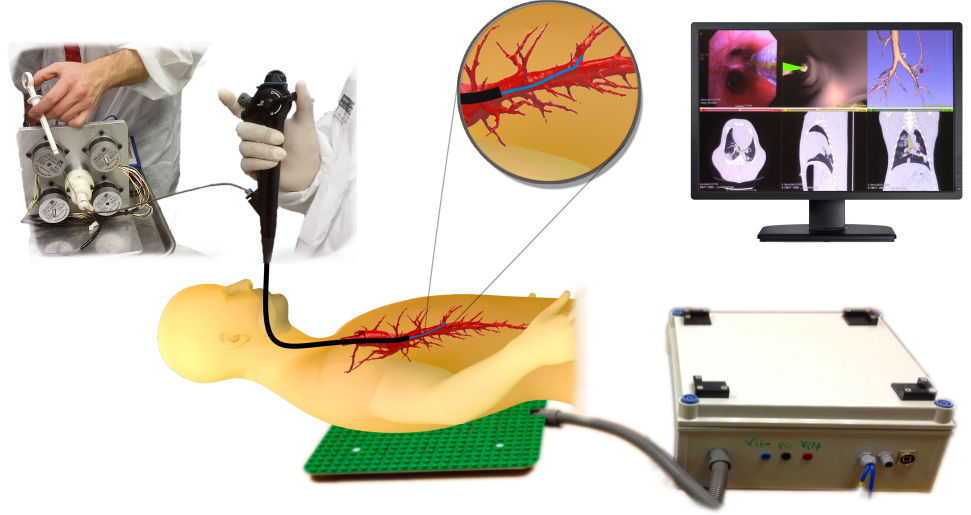
In this section, the tools used for the experimental setup are introduced. Results of airway navigation through the airways are also described.

#### 6.2.1 Bronchoscope

An Olympus 1T160 bronchoscope was used for the breathing lung tests. The unit has a 6 mm OD with an instrument channel diameter of 2.8 mm. The EM position tracking probe was inserted through the bronchoscopes instrument channel for testing. The probe was connected to the EM tracking system, which communicated probe position and orientation of the probe to a 3.6 GHz, 16 GB RAM PC where both MATLAB and Slicer were running. Figure 6.1 provides a diagram of the system setup.

#### 6.2.2 EM Tracker

The transmitter board of the tracking system was mounted directly below the lung vacuum chamber during the tests. The transmitter was rigidly aligned with the vacuum chamber to reduce errors after registration due to relative motion between the chamber and the transmitter. Once in place, the transmitter and



**Figure 6.1:** Diagram of the system in the operating setup. In the figure, the automated navigation system described in Section 6.3.1.6 is also shown. This was not used for testing with the breathing pig lung model.

sensors were first calibrated [8, 16] and then the registration was implemented. To reduce registration errors, a landmark-based registration using eight easily identifiable fiducials was used.

### 6.2.3 Airways 3D Model

The inflatable lung model used for the testing is the same used for the airway segmentation testing as described in Chapter 4. To use the VB system, the airways of the phantom were segmented and a 3D virtual model reconstructed prior to the procedure. To achieve this, the airway segmentation described in Chapter 4 was used. Optimal CT parameters (0.625 mm slice thickness, 60 mA radiation dose, and LUNG convolution kernel) were used to scan the phantom with a GE Discovery CT750 CT scanner. The model was kept inflated inside the vacuum chamber during scanning to simulate a patient breath-hold. The setup for scanning can be seen in Figure 6.2.

To further reduce artefacts in the CT scan, a low density packing foam was

## 6. PRE-CLINICAL TESTING AND RESULTS

---



**Figure 6.2:** GE Discovery CT750 CT scanner with the inflated pig lung model.

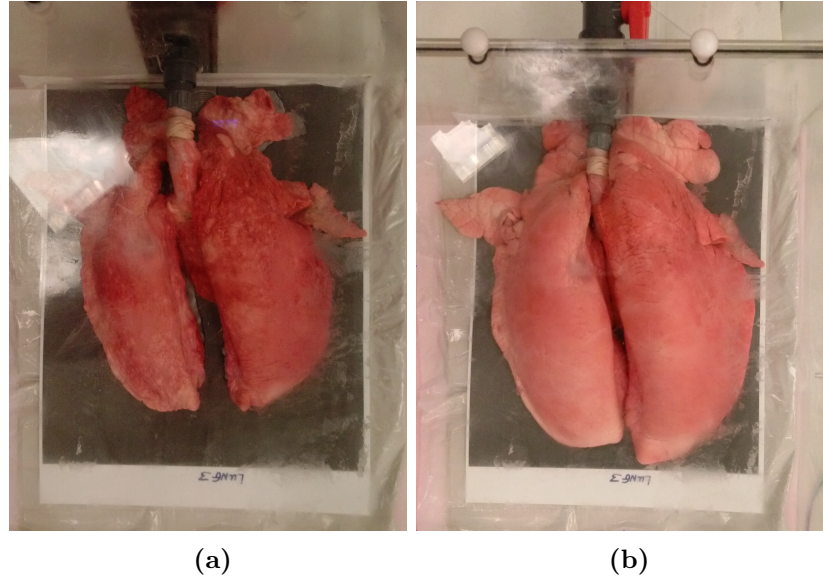
used to raise the lungs away from the high density perspex box. To ensure that the lung model matches the CT scan as much as possible when used for the procedure, a photograph of the lungs in their uninflated position was taken. This image was then printed to scale, laminated and placed at the base of the vacuum chamber. This way, every time the lungs were placed in the perspex chamber, the uninflated lungs were positioned to match the scanning position. This requirement is significantly relaxed by the automated registration approach defined in Section 5.4.4.2. While the lungs should nominally be in the same position during testing as during the CT scan, over time the lung's will deform due to wear and tear. Therefore, to reduce errors, the CT scan should be taken as close to the experiment time as possible. Ideally the experiment would take place directly after the scan, without moving the lungs.

Figure 6.3 shows the vacuum chamber with the breathing lung model before the CT scan in both the (a) deflated and (b) inflated state. Below the lungs, the laminated figure can be seen.

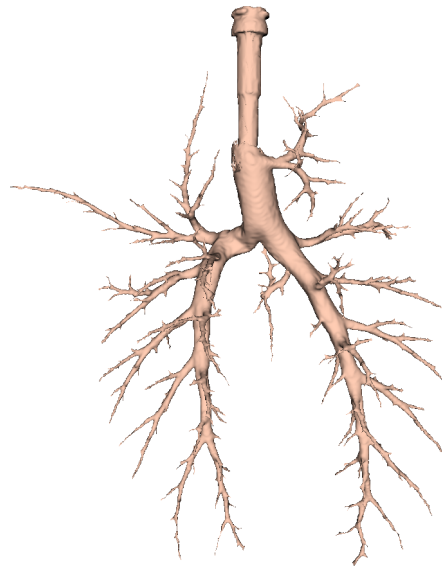
Starting from the generated CT scan, 3D Slicer and the extension described in Chapter 3 were used to generate the 3D virtual model of the phantom airways. Figure 6.4 shows an example of 3D model obtained from the pig lung phantom.

## 6.2 Breathing Lung Model Evaluation

---



**Figure 6.3:** The inflatable lung model setup for the CT scan when (a) inflated and (b) deflated. Below each lung there is a laminated scaled image of the deflated lungs used for lining up the model in a repeatable manner.



**Figure 6.4:** 3D model of the inflated pig lung model (0.625 slice thickness, 60 mA radiation dose, LUNG convolution kernel).

## 6. PRE-CLINICAL TESTING AND RESULTS

---

### 6.2.4 Breathing Lung Model

During testing, the lung model was alternated between an inflated and deflated state, to simulate breathing of the lung and create a more realistic test environment. The pressure was adjusted until it matched the level during the CT scan of the lung, and then decreased, to create a breathing cycle set to 5.3 seconds, where simulated inhalation was enabled for 27% of the period, and exhalation occupied the remaining time.

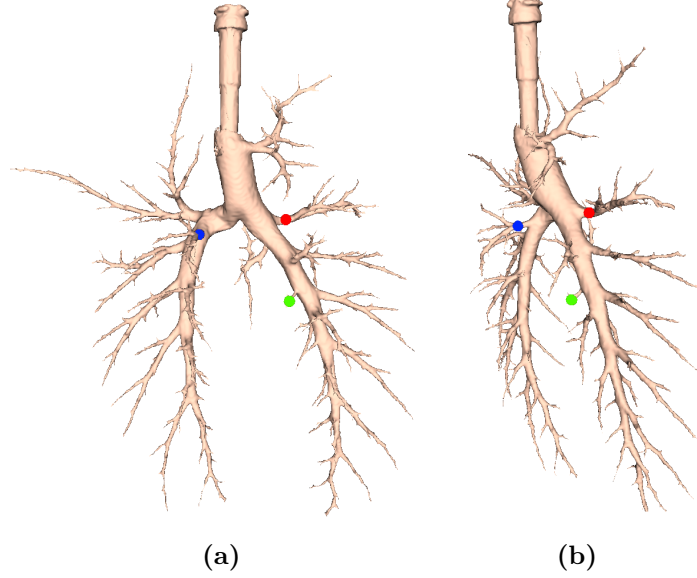
### 6.2.5 Virtual Bronchoscopy: Pre-Processing

The Slicer environment was set-up for virtual navigation and the video frame from the bronchoscope's camera streamed as described in Section 5.4.5.5. Next, three different targets were selected in order of difficulty (red, blue and green). The position of the three targets are shown in Figure 6.5. Physical targets made of Blu-Tack<sup>TM</sup> (volume  $< 5\text{mm}^3$ ) were placed within the model at the corresponding positions. These simulated the presence of endobronchial nodules within the airway. The first target was used for training with the image-guided navigation system. For this reason, the target was placed in easy reach in the first branching point of the right main bronchus (red dot in Figure 6.5). The second target was placed at the second branching point of the left main bronchus (blue dot in Figure 6.5). Finally, the last target, the most challenging for navigation, was placed inside a small branch by the fifth bifurcation in the right main bronchus (green dot in Figure 6.5). Routes to these target were automatically generated in Slicer and all computed paths and VB images evaluated to ensure that no artefacts were present, as determined by visual inspection of the CT image.

### 6.2.6 Virtual Bronchoscopy: Image-Guided Navigation

All nine participants were right handed volunteers of different ages and medical experience in the field of respiratory medicine. Table 6.1 summarizes details of the participants in terms of age, sight corrected vision, training grade and number of previous bronchoscopies performed. Before the procedure, the goal of the research was explained to all volunteers and they were briefly instructed





**Figure 6.5:** Position of the three targets inside the airways. Two different views are shown. The first, second, and third targets are indicated in red, blue, and green, respectively. First and third targets were placed in the right lung. The second target was in the left lung.

Participant ID	Age	Right Handed	Sight Corrected Vision	Training Grade	# of Previous Bronchoscopies Performed
V1	< 40	Yes	Yes	SHO	0
V2	35	Yes	No	1	> 50
V3	37	Yes	Yes	Faculty	> 50
V4	30	Yes	Yes	3 (SHO)	0
V5	38	Yes	No	2 (Reg)	< 20
V6	40	Yes	No	2 (Reg)	< 20
V7	50	Yes	Yes	5	> 50
V8	52	Yes	Yes	5	> 50
V9	35	Yes	No	5	> 50

**Table 6.1:** Details of volunteers participating to the VB system test. SHO stands for senior house officer, while Reg indicates registrar physician (junior clinical fellow).

## 6. PRE-CLINICAL TESTING AND RESULTS

---

in the methodology used. They were then required to navigate, one at a time, towards the different targets. They were not aware of the target's location, but to reach the region of interest they had to follow the created path on the virtual environment. Once in place, the virtual target placed on the 3D model, initially red, changed colour to light blue, to help realize that the target was reached. The physical Blu-Tack target (visible on the real video from the bronchoscope) was touched to consider the navigation concluded. When one target was reached, the next one was shown along with the corresponding path and the procedure repeated until all three targets were navigated. For each target, time required for guiding the physician to reach the region of interest was recorded.

### 6.2.7 System Usability Scale Questionnaire

After the procedure was completed, all participants were asked to complete a questionnaire to evaluate their experience and usability of the VB system. Each was asked five questions about the overall system usability and value:

- How was the overall ease of use of the system? (Poor to excellent)
- Does the system accurately replicate the clinical setting? (Not at all to excellent)
- How valuable do you consider the system as a training tool? (Not at all to extremely valuable)
- How valuable do you consider the system as a clinical tool? (Not at all to extremely valuable)
- Would you use image-guided navigation in bronchoscopy? (Yes-No)

The second part of the questionnaire concerned the system usability. The system usability scale (SUS) [251, 252] method was used to evaluate usability. This is a simple, ten-part scale giving a global view of subjective assessments of usability. The ten questions are characterized by five response options; from strongly agree to strongly disagree:

1. I think that I would like to use this system frequently.

2. I found the system unnecessarily complex.
3. I thought the system was easy to use.
4. I think that I would need the support of a technical person to be able to use this system.
5. I found the various functions in this system were well integrated.
6. I thought there was too much inconsistency in this system.
7. I would imagine that most people would learn to use this system very quickly.
8. I found the system very cumbersome to use.
9. I felt very confident using the system.
10. I needed to learn a lot of things before I could get going with this system.

All statements required a response and if a user felt that they could not respond to a particular item, they were asked to mark the centre point of the scale. Every option for each item is assigned a particular score, from 0 to 4. For items 1, 3, 5, 7, and 9 the score contribution is the scale position minus 1. For items 2, 4, 6, 8, and 10, the contribution is 5 minus the scale position. However, scores for particular items are not meaningful on their own. To calculate the SUS score, first all the score contributions from each item has to be summed. Then, the sum of the scores must be multiplied by 2.5 to obtain the overall value of system usability. SUS scores have a range of 0 to 100, but this is not a percentage. Based on research, a SUS score above a 68 would be considered above average and anything below 68 is below average. However, the best way to interpret the results involves “normalizing” the scores to produce a percentile ranking [253].

## 6. PRE-CLINICAL TESTING AND RESULTS

Participant ID	Target 1	Target 2	Target 3
V1	58	80	40
V2	20	17	17
V3	45	34	36
V4	59	82	241
V5	200	82	130
V6	40	20	32
V7	25	15	68
V8	10	18	40
V9	57	55	62
<b>Average</b>	58.2	44.8	74.0
<b>Std. Dev.</b>	56.5	30.04	70.7

**Table 6.2:** Time (in seconds) required to each participant to reach the three targets.

### 6.2.8 Results

All targets were reached by the users. Table 6.2 shows the times required to every user to reach the three targets. On average, target one was reached in  $58.2 \pm 56.5$  seconds, target two in  $44.8 \pm 30.04$  seconds, and target three in  $74.0 \pm 70.7$  seconds. As expected, target three was the most complicated to reach, while the high time required to reach target one (placed in a quite easy to reach position), can be explained by the fact that participants were familiarizing with the bronchoscope and the system. In general, considering that volunteers had never tried the system previously and could not analyse the CT image or the lungs prior to the procedure, this can be considered as a positive result, indicating the help that the image-guided system can provide. Moreover, even participants who never performed a bronchoscopy before were able to reach targets in reasonable clinical time frames, indicating that the image-guided system helps choose the correct path without any previous experience or image analysis. Comparison with blind navigation, namely navigation without help of the VB system, would give a better indication of the help the system could provide in a blinded comparative study. However, this was not possible in the present study to to the small

cohort and as the results would be biased by the participants already knowing the position of the target. The end points of the study were technical feasibility rather than comparative analysis. While a blinded study is certainly something to be included in the future, the limited cohort number meant that such analysis was difficult to achieve to date. Table 6.3 reports the results in terms of overall satisfaction of the participants. In particular, having a virtual reconstruction of the interior of the airways seems to help the user navigate within the lung without the need to be an expert of the field, when compared to standard bronchoscopy. An important aspect to consider is that the test was performed to evaluate the entire system (EM tracking with VB) and not only VB. As shown, the VB system has been considered easy to use and accurate in replicating the clinical setting. Also, participants evaluated the system as valuable both as a training and as a clinical tool. All the volunteers stated that they would use the system during a bronchoscopy procedure.

Finally, individual results obtained on system usability are reported in Table 6.4. Sixty-eight resulted as the 20<sup>th</sup> percentile for this test, indicating that 80% of participants found the system usable above average. In fact, as shown by Table 6.4 only two participants scored the system below 68, with V6 close to the usability limit. Furthermore, comments of the participants report that most of them preferred to follow the path in the virtual environment to move the bronchoscope, rather than looking at the real image. The results obtained in the pre-clinical setting are promising and show that an image-guided system coupled with electromagnetic tracking to recognize the current position of the scope inside the lung may be of great benefit for diagnosis and assessment of pathological conditions in the lung.

## 6.3 Tests in Live Animal Setting

Two live animal studies evaluated the VB algorithm. Both tests were approved by both the Irish Department of Health and UCC Animal Experimentation Ethics Committee and followed similar protocols, with incremental improvements to instrumentation between studies. As well as testing the VB system, the two tests were also used to evaluate performance of a novel semi-automated robotic

## 6. PRE-CLINICAL TESTING AND RESULTS

---

Participant ID	Q1	Q2	Q3	Q4	Q5 (Y/N)
V1	4	4	5	4	Yes
V2	4	4	2	4	Yes
V3	4	4	4	4	Yes
V4	2	4	5	5	Yes
V5	4	5	5	5	Yes
V6	5	4	4	4	Yes
V7	4	3	5	5	Yes
V8	5	4	4	3	Yes
V9	4	3	5	4	Yes
<b>Average</b>	4	3.89	4.33	4.22	//
<b>Std. Dev.</b>	0.87	0.6	1	0.67	//

**Table 6.3:** Results of overall satisfaction of participants. For all questions a score 1-5 was requested. For question 1 (Q1), 1 represented poor and 5 excellent. For Q2, 1 was not at all, whereas 5 stood for excellent. For Q3 and Q4 scores ranged from not at all (1) to extremely valuable. The test aimed at evaluating the entire system, composed of both the EM tracking and VB. In this sense, physical setup deficiencies cannot be addressed separately to VB.

### 6.3 Tests in Live Animal Setting

Participant ID	Q1	Q2	Q3	Q4	Q5	Q6	Q7	Q8	Q9	Q10	Usability
V1	4	2	5	4	4	2	5	1	4	2	77.5
V2	4	1	4	2	4	2	5	2	3	2	77.5
V3	3	2	4	2	4	4	2	2	3	3	57.5
V4	5	2	3	3	4	3	5	2	4	3	70
V5	5	2	5	2	5	1	5	1	4	2	90
V6	4	1	4	4	4	2	3	3	4	3	65
V7	4	1	4	1	4	2	3	2	4	3	75
V8	5	1	5	4	3	2	3	1	5	4	72.5
V9	4	1	4	5	4	1	2	2	4	1	70
<b>Average</b>	4.22	1.44	4.22	3.00	4.00	2.11	3.67	1.78	3.89	2.56	72.78
<b>Std. Dev.</b>	0.67	0.53	0.67	1.32	0.5	0.93	1.32	0.67	0.6	0.88	9.05

**Table 6.4:** System usability for all participants. Each question was given a score from 1 to 5, with 1 indicating strongly disagree, and 5 strongly agree. Final usability score for each volunteer was given by multiply by 2.5 the sum of individual scores. Scores higher than 68 indicate usability above average.

navigation method, compared to manual navigation, and to investigate novel radiopaque tumour models [254]. In both tests, tumour models were placed in different positions of the animals' lungs and image-guided navigation was tested. Navigation success, defined as correctly guiding the physician to the final pre-defined target was undertaken. Tumour model samples from the target's positions were extracted to validate the navigation. Finally, time required to guide the physician to the different regions of interest was recorded. Animal studies were achieved using the same bronchoscope and the EM tracking system used for the pre-clinical testing. Protocol and methods were similar for both studies, and the procedure was refined with preceding studies. Here the protocol and methods used for the two studies are first described. Results achieved using the VB system compared to standard bronchoscopy are then presented.

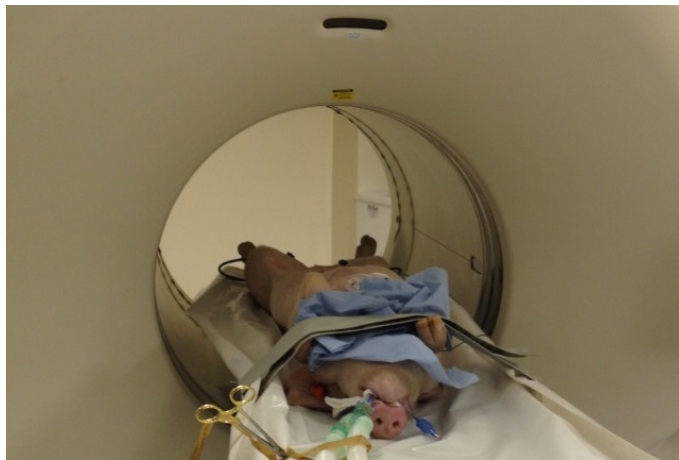
#### 6.3.1 Protocol and Methods

The first test was carried out using a 40 kg male Landrace pig, while during the second test a 22 kg female Landrace swine was used. In both cases, the animal was sedated, intubated and anaesthetised. Tracheal intubation was achieved

## 6. PRE-CLINICAL TESTING AND RESULTS

---

with a 8.5 mm endotracheal tube (Blue Line SACETT tracheal tube from Smiths Medical International, UK). After being intubated, the pig was subject to CT scanning with a GE 64 slice Discovery VTC scanner. CT scan parameters were: 0.625 mm slice thickness, 60 mA radiation dose (at 120 kV) and standard convolution kernel. Figure 6.6 shows the pig during the scanning process. This pre-scan was used as a comparison image to evaluate the contrast on CT images of different tumour models placed in the pig lungs.



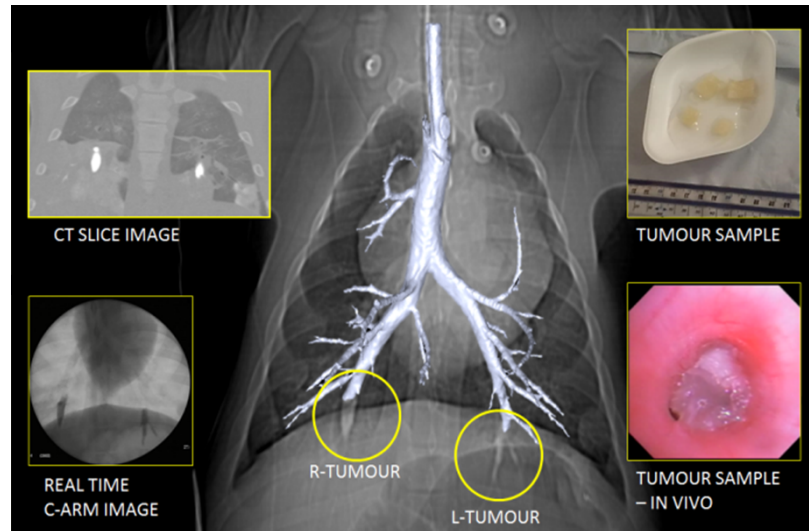
**Figure 6.6:** The pig during one of the scanning processes.

### 6.3.1.1 Endoscopic Placement of Tumour Models

To create targets for navigation, two different tumour models were investigated. These models were tested on the breathing pig phantom described in Chapter 3 prior to the animal study. Beef tripe proved the optimal tumour model [254]. The tumour model was created using fresh beef tripe segments saturated overnight in 300 mg I/ml Omnipaque solution with injection of Omnipaque and food colouring into the segments immediately prior endoscopic injection. For the first study, seven separate tripe samples were placed in the lungs (two in the upper right lobe, two in the lower right lobe and three further positioned in the upper left lobe), while during the second study six tumour models were considered (one in the right medium lobe, one in the bronchus sus, one in the left upper lobe, one in the left lower lobe, one in the right lower lobe, and a final one in the



right upper lobe). The tumours were endoluminally advanced by bronchoscope and endoscopic forceps. Each tripe segment measuring less than 1 cm<sup>3</sup> and CT fluoroscopy was used to confirm placement position. Figure 6.7 gives an example of some tripe-based tumour models as they appear on a CT scout image. A coronal CT slice containing the models, c-arm x-ray image taken in real time during placement of the tumours, and images of the tripe models prior to insertion and positioned *in-vivo* are also shown. The 3D airway model of the pig's lungs is overlaid on the fluoroscopy image to better indicate position of the tumour models.



**Figure 6.7:** Tripe tumour models visible in lower right and left lobes. A coronal CT slice, a C-arm X-ray image taken in real time while placing the models, and images of the tripe models prior to insertion and positioned *in-vivo* are shown. The 3D airway model is also visible overlaid to the CT scout image [254].

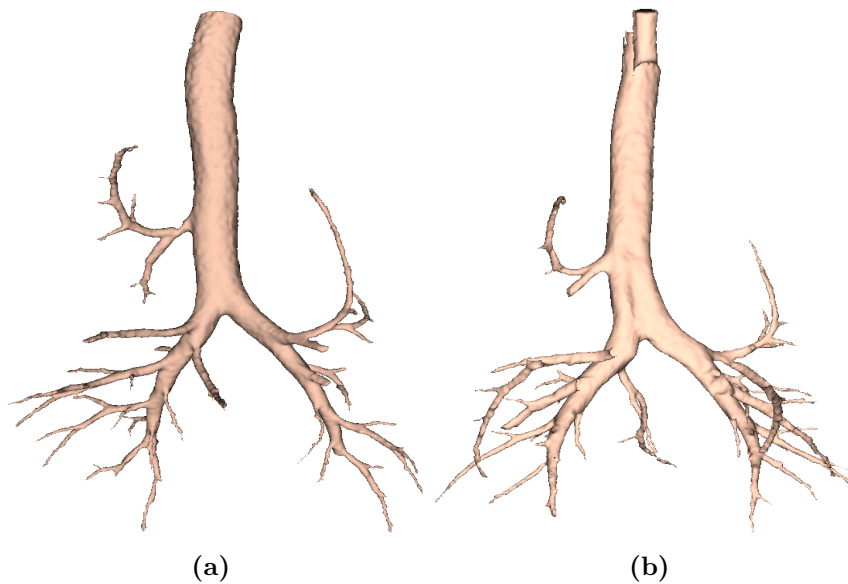
#### 6.3.1.2 Airways Segmentation

Following the placement of the tumour markers, a second CT with identical scan parameters to the first was undertaken. This facilitated visualisation of the endoluminal tumour models within the airways and enabled 3D segmentation in the Slicer platform. Airway segmentation and 3D model reconstruction was accomplished by placing a seed point within the trachea in the CT image and using

## 6. PRE-CLINICAL TESTING AND RESULTS

---

the method described in Chapter 3. During the first study, segmentation was achieved in 6 minutes on a Dell Precision M4800 with i7 Intel quad-core processor operating at 3.6 GHz, with 8 GB of RAM. For the second study, airway segmentation was achieved in 2.38 minutes on the same machine, with an improved 16 GB of RAM. Figure 6.8(a) shows the 3D airway model obtained from segmentation of the airways in the first study, while Figure 6.8(b) shows the airway model obtained from the second pig.



**Figure 6.8:** The 3D rendered airway model as obtained during (a) the first and (b) the second study.

### 6.3.1.3 Pre-Procedure

Before starting bronchoscopy navigation, a number of pre-procedure steps were executed. First, the VB system was opened in 3D Slicer, the airway label and 3D model were selected and the airway's centreline extracted. This operation required 11 minutes in the first study and 9.45 minutes in the second, on the same machine used for airway segmentation. An expert physician individually identified the tumour models by visual inspection of the CT image. Seven and six independent tumour model targets were identified in both lungs during the first

### 6.3 Tests in Live Animal Setting

Target ID	Distance to Target (mm)	Location
T1	91	Right Middle Lobe
T2	65	Left Upper Lobe
T3	76	Right Lower Lobe
T4	89	Right Lower Lobe
T5	104	Left Lower Lobe
T6	212	Left Upper Lobe
T7	163	Right Middle Lobe

(a)

Target ID	Distance to Target (mm)	Location
T1	171	Right Middle Lobe
T2	120	Bronchus Sus
T3	166	Left Upper Lobe
T4	202	Left Lower Lobe
T5	208	Right Lower Lobe
T6	148	Right Upper Lobe

(b)

**Table 6.5:** Distance (in mm) of the targets from the bronchus sus and location in the pig lungs for the (a) first and (b) second study.

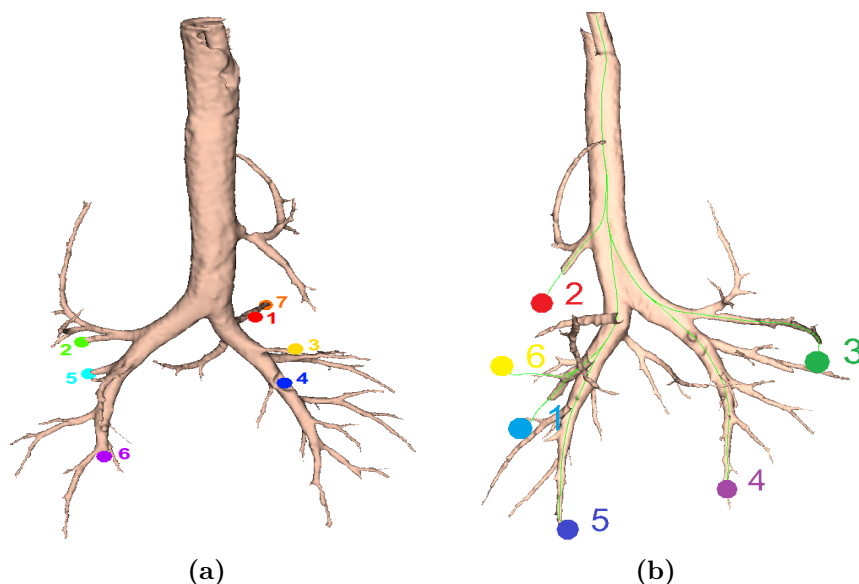
and second study, respectively. These were marked with manually placed virtual fiducials in 3D Slicer. Table 6.5 reports distances from bronchus sus and location of the targets for both studies, whereas in Figure 6.9 the airway models with the overlaid markers are presented. Finally, virtual navigation pathways were created for all targets.

#### 6.3.1.4 Registration

For both studies a landmark-based registration method was utilised. Five virtual landmarks placed in different positions were used; one in the bronchus sus, one in

## 6. PRE-CLINICAL TESTING AND RESULTS

---



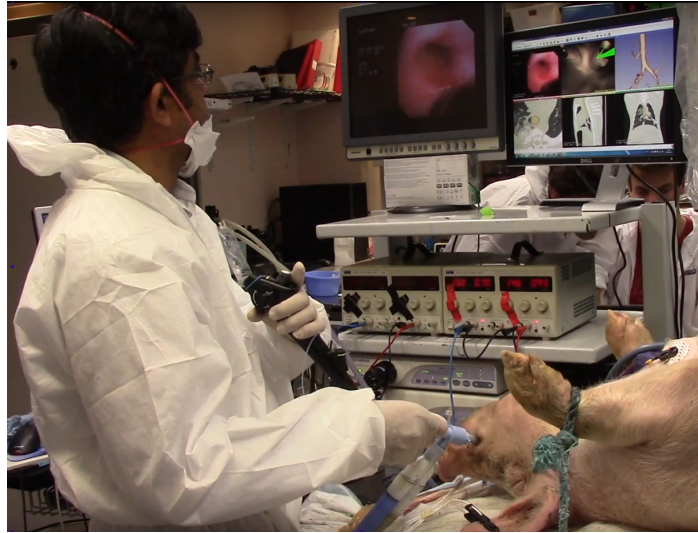
**Figure 6.9:** A 2D view of the airway model showing the position of the placed tumour markers for the (a) first and (b) second study. The different colours are used here to distinguish the targets.

the main carina, two in the secondary and tertiary left carinae, and the last one in the right secondary carina. These positions were manually identified and touched with the sensor placed at the tip of the bronchoscope via the scope instrument channel, while the same points were manually identified and marked in the virtual 3D airways. Registration was then performed in MATLAB.

### 6.3.1.5 Image-Guided Navigation to Targets

During the first study, after the pre-procedure steps, a second expert physician undertook manual navigation towards the targets. The EM tracking sensor was inserted in the bronchoscope working channel and each target was successfully identified and navigated using manual bronchoscopic steering. At the end of the procedure, automated navigation, described in Section 6.3.1.6, and biopsy was attempted for targets 1 and 5. During the second study, a second expert physician undertook only automated navigation for all targets.

As in the breathing pig lung model, once reached and touched the virtual tar-



**Figure 6.10:** The VB system as used by the physician during the first animal study.

gets changed colour from red to light blue. Roll rotation compensation, described in Chapter 5, was utilised only during the second study, after being optimised. Figure 6.10 shows the VB system as used by the physician during the procedure, while in Figure 6.11 the semi-automated system used by the physician in combination with VB during the second animal trial is presented. For each navigated target, the physician was required to take a tissue sample of the tumour model using a pulmonary biopsy forceps (2 mm Radial Jaw 4 forceps from Boston Scientific, see Figure 6.12) inserted through the bronchoscope instrument channel.

### 6.3.1.6 Automated Navigation

Figure 6.13 shows the physician using the joystick to navigate inside the lung and reach the target. The automated navigation system consists of a catheter specifically designed for use with flexible bronchoscopes incorporating a 1.5 mm working lumen for endoscopic instruments and 2.65 mm outer diameter. The catheter tip incorporates the tracking sensor and allows for continuous tracking regardless of the inserted instrument type or exchange. The catheter is connected to a motorised actuation system. The proximal end of the catheter contains

## 6. PRE-CLINICAL TESTING AND RESULTS

---



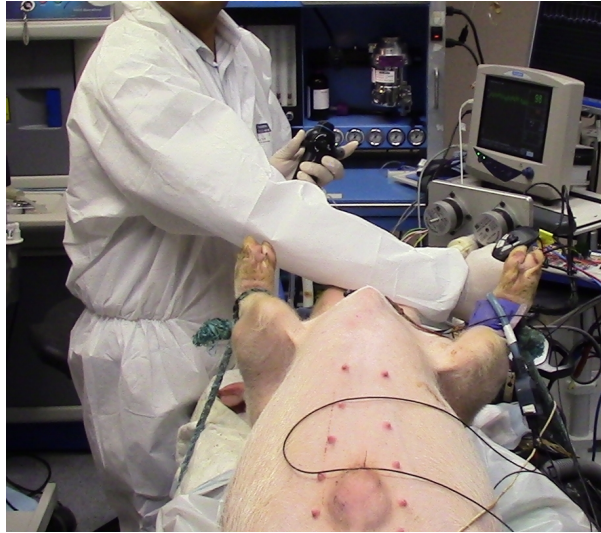
**Figure 6.11:** The semi-automated joystick-based navigation system as used by the physician in combination with VB.



**Figure 6.12:** Example of forceps as utilised to biopsy the different targets.

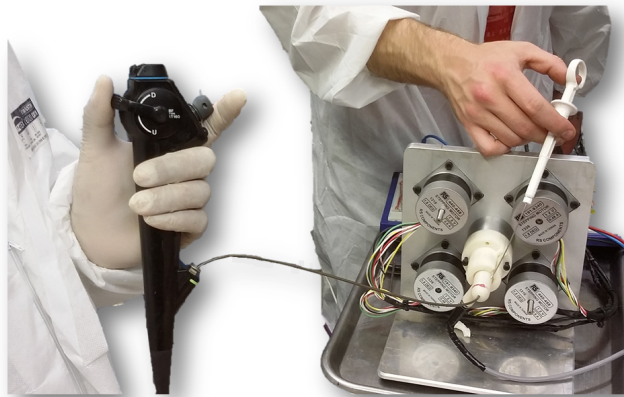
four pull wires whose tension can be monitored through individual force sensing loadcells on each wire member (see Figure 6.14). A joystick connected to the loadcells allows for different forces on each of the wires to steer the catheter's





**Figure 6.13:** The physician used the joystick to navigate inside the lung.

tip. As well as the tumour models, also the catheter automation system was



**Figure 6.14:** The catheter is connected to a motorised system where four force sensing loadcells apply a different tension on the four wires connected to the catheter's tip based on the position of the joystick.

tested in the breathing lung model prior to the animal study [73]. During the trial *ex-vivo*, the automated joystick control was used for catheter manipulation to the tumour target following positioning of the bronchoscope approximately 5 cm from the target. Once the navigated catheter was at the tumour target,

## 6. PRE-CLINICAL TESTING AND RESULTS

---

biopsy was achieved with the same pulmonary biopsy forceps used during manual navigation inserted through the central lumen of the automated catheter.

### 6.3.2 Results: First Study

During the first study, all the tumour models were successfully navigated using manual bronchoscopic steering with virtual navigation. An average time of 9.71 seconds was necessary for navigation to the targets. Table 6.6 reports the specific time required for each target. For each tumour model, a tissue sample was extracted and visually inspected to confirm successful targeting of the region of interest. Tumour 1 and 5 were also successfully navigated with automated navigation, as confirmed by biopsy of the tumour models. User satisfaction at the system was noted, although it was noted that registration between the real and virtual world should be improved. In deeper branches the centreline compensation method is not sufficient to guarantee accurate guidance. Real and virtual frame images were often mismatched when the bronchoscope was rotated. Therefore, a method to compensate for the use of 5 DOF sensing should be implemented to help align the two images.

Target ID	Time to Reach Target (sec)
T1	18
T2	14
T3	10
T4	8
T5	6
T6	7
T7	5
Average Time	9.71
Std. Dev.	4.71

**Table 6.6:** Time (in seconds) required to reach every target using VB.



### 6.3.3 Results: Second Study

During the second study, four targets were successfully navigated, whereas targets 3 and 6 were not reached, with the physician trying for more than 5 minutes. This was probably due to the fact that targets 3 and 6 were found to have moved from their original location. Table 6.7 reports the time required to reach every target. An average time to target of 45.75 seconds was required. In terms of image intensity, the placed tumour models proved more representative of real tumours on CT scans.

This study aimed at testing the robotic navigation system with VB. During navigation, the image registration approach successfully aligned real and virtual images at branching points and improved user satisfaction with the VB system was noted. However, the study outlined a few aspects to be improved for future work. First, the sensor at the tip of the catheter is fragile and easy to break. Design of the catheter should be modified to guarantee higher reliability. Also, the physician noted mis-matching between joystick movements and catheter orientation. To this end, a label indicating how to insert the catheter into the bronchoscope's channel may help. Finally, landmark-based registration did not provide true alignment between real and virtual images, and centreline compensation cannot be considered a long-term solution. Removing the centreline extraction stage would also reduce time required in pre-procedural planning. For this purpose, an optimized landmark-free registration, such as the one described in Chapter 5, represents a possible solution. Accurate testing for this method should be carried out with animal studies to evaluate the benefits which the approach brings to VB. A comparison between the two registration methods should be performed.

### 6.3.4 Conclusions

The procedure for the two animal studies described was refined by means of preceding studies, used mainly to evaluate the EM tracking system. The VB system described in Chapter 5 was tested as applied to the EM tracking system developed at UCC, both with manual navigation of the bronchoscope (first animal study) and automated navigation (second trial).

## 6. PRE-CLINICAL TESTING AND RESULTS

---

Target ID	Time to Reach Target (sec)
T1	115
T2	20
T3	Not reached
T4	25
T5	23
T6	Not reached
Average Time	45.75
Std. Dev.	46.21

**Table 6.7:** Time (in seconds) required to reach every target using robotic steering and VB. Targets 3 and 6 were not reached.

Compared to standard bronchoscopy, advantages of having a system that automatically creates a virtual reconstruction of the inside and outside of the airways tree are multiple. With standard bronchoscopy, the physician is provided only with the video from the camera at tip of the bronchoscope. Therefore, the video is used to “guess” the current location and move toward the desired region. This is a difficult operation that requires training and high experience. The VB system described here works as a GPS system for the lung, which automatically creates and provides pathways toward the target regions of interest. Beside guiding the user during navigation, the automatic creation of the pathway also avoids the physician the tedious operation of analysing the patient’s CT scan by scrolling through 2D images to mentally reconstruct the pathway. Moreover, the system updates and presents in real-time the distance to target, so that the physician is always aware of the exact location of the bronchoscope. This would help blind biopsy, especially in peripheral regions that are not reachable with the current technology.

The two animal studies proved the usability and accessibility of the developed VB system. Although direct comparison with commercial systems is not possible, the system seems to improve some key aspects. Reconstruction of the airways 3D model does not require specific CT parameters, as shown in Chapter 4, and manual interaction is kept as low as possible. Therefore, the system paves the

### 6.3 Tests in Live Animal Setting

---

way for the development of an optimized VB system that allows for automatic navigation and blind biopsy of peripheral lung nodules. To this end, improvements to the overall system are required. Among them, the registration process and roll rotation compensation should be improved and optimized and pathways should be created in real time during navigation.

# Chapter 7

## Summary and Future Work

### 7.1 Summary of Thesis Contributions

This thesis presents the development of the first open-source virtual bronchoscopy system for image-guided navigation. The system has been developed exploiting the functionalities of the freely available software package 3D Slicer. A system for nodule malignancy prediction starting from CT images has been developed and validated on clinical cases. This method paves the way for the development of a complete CAD system to detect and classify nodules and help the physician decide whether to proceed with biopsy.

An airway segmentation method has been implemented to create a 3D rendered model of airways starting from chest CT images. Performance of the system has been evaluated on clinical cases, compared to other groups' results and tested on a breathing pig lung model and live animal evaluation. This is the first fundamental step to the development of a system for virtual navigation inside the airways. This method has been developed, tested, and evaluated both in the pre-clinical and clinical settings, in combination with an electromagnetic navigation platform.

The novel contributions of this thesis are summarised here.

- The design of a novel open-source algorithm for nodule malignancy prediction has been presented (Chapter 3). The system requires the user to specify the nodule location and automatically defines nodule characteristics, such as

size, location, edge shape, wall thickness and calcification presence. These characteristics are then combined with clinical characteristics to determine probability of malignancy. Reliability of the system has been validated on real clinical cases. The system paves the way for potential future work aimed at automatic identification and classification of lung nodules.

- The first open-source algorithm for airway segmentation starting from chest CT images has been proposed (Chapter 4). The method can be used for both human and animal (porcine, canine) images and provides a frame of reference for comparison of results using local datasets. Also, the algorithm can be easily modified and extended according to local needs.
- The airway segmentation method has proven comparable with other teams' methods, as validated by participating in the EXACT'09 challenge, and is reliable across varying CT parameters, as verified using the breathing pig lung model (Chapter 4).
- A novel method to evaluate leakage presence on segmented airways has been designed (Chapter 4). This can be easily reproduced by other teams, thus providing a general evaluation system to provide a better method to compare results.
- A novel open-source virtual bronchoscopy system for image-guided navigation has been implemented and described (Chapter 5). This system has a modular structure and has been optimized for usage with an electromagnetic tracking system.
- The VB system provides different tools for helping during pre-procedure and navigation steps. Pathways towards the user-specified regions of interest can be easily defined, and methods for compensation of registration errors as well as for roll rotation of the bronchoscope have been designed and optimized (Chapter 5).
- A new method for registration between real and virtual environment has been proposed and validated (Chapter 5). The method improves performance of registration and drastically reduces user interaction.

## 7. SUMMARY AND FUTURE WORK

---

- Finally, the use of the VB system has been tested and evaluated in the pre-clinical setting, using the breathing pig lung phantom, and in live animal studies (Chapter 6). During different pre-clinical tests, landmark-based registration was used. The breathing model was successfully navigated by nine physicians from respiratory medicine, and usability of the system was validated with two live studies.

## 7.2 Proposals for Future Work

### 7.2.1 CT Images Noise Removal

A fundamental limitation of airway segmentation algorithms is the presence of noise on chest CT images, due to multiple causes. The noise may cause a blurring effect of narrow airways that may be confused with the surrounding parenchyma. For this reason, algorithms are currently unable to segment more than 5-6 airway generations of the 23 composing the lungs. Reducing noise on chest CT images may help improve the segmentation results. Toward this end, the use of a non-local means (NLM) filter that uses a multiscale approach aimed at enhancing airways on the image may be a possible solution. Similar approaches have been successfully proposed for magnetic resonance images (MRI) [255] and could be extended to CT images.

### 7.2.2 Airway Segmentation Improvement

As describe in Chapter 3, the proposed airway segmentation method is comparable with other teams' algorithms and is reliable across different CT parameters. However, the algorithm is not reliable for segmenting deeper branches, that become too narrow to be safely distinguished from the parenchyma, causing leakage. Also, the algorithm is semi-automatic, requiring the user to specify a seed point within the trachea. A first improvement may automatically find the trachea on the CT image, by searching for a round-shaped area with low intensity values ( $< -800$  HU) on the first axial images of the CT scan. A point inside this area may be used as a seed point for region growing segmentation. The algorithm

currently splits the volume into trachea, right, and left lungs, that are segmented separately to improve segmentation results. A further improvement may be splitting the volume into smaller regions (e.g., at every bifurcation point) and segment each volume independently. Alternatively, the proposed algorithm could be used as a starting point for a more sophisticated method aimed at segmenting peripheral branches. The development of a method to automatically identify and eliminate leakage during and after the segmentation may be of great help in this goal.

### 7.2.3 Registration Improvement

A fundamental limitation of many image-guided systems based on EM tracking is registration between the real and virtual environment. As described in Chapter 5, a novel and simple method that improves performance of a landmark-based registration was proposed. However, this system is affected by possible deformation over time of the lungs and by breathing of the patient. In fact, CT scans of the patients are generally acquired at full inspiration. Also, the method requires minimal user interaction, consisting in indicating the branches position and executing a balanced survey. Improvements to this method may involve automatic labelling of the branches and more sophisticated breathing compensation. For this purpose, a respiratory gated registration system may be examined. This consists in using a second sensor placed on the patient's chest to take into account the respiratory phases of the patient and track the probe's positions during the inhalation phase only. Moreover, integration of a lung deformation model should be taken into account for the future. Beside helping future testing with the breathing pig lung model, this model might help improve the registration process when executed days or months after the CT scan.

### 7.2.4 5 DOF Sensor Compensation

An important issue observed during virtual navigation is the mis-alignment, in terms of roll-rotation, between the real and virtual camera. This is due to the 5 DOF sensor used for the tracking, that does not provide roll information. An

## 7. SUMMARY AND FUTURE WORK

---

intensity-based image registration method that finds the optimal rotation angle between the real and virtual frame was proposed. However, this method is relatively slow compared to the tracking speed and is affected by the image quality. Therefore, the method is triggered only at bifurcations, where branch characteristics are easily visible. Besides hardware solutions, such as the use of sensor to be placed on the bronchoscope to identify the applied roll rotation, an improvement to image registration may involve using a computationally efficient inverse-compositional formulation as proposed by Merritt et al. [256]. This method was introduced to register real-time the real and virtual world, but a similar approach may be implemented to reduce computational costs of image registration and avoid delays. Another option consists in using a features-based image registration, to be combined with the intensity-based approach. The main drawback of this idea is that extraction of the characteristics from the two images may not be straightforward.

### 7.2.5 Real-time Pathway Updating

A challenge noted during image-guided navigation is the static nature of the virtual pathway model. The creation of the pathway is completed before the procedure starts, as it is relatively computationally expensive. During the procedure, if the virtual camera's focal point is not aligned with the the pathway, it may disappear from the screen. Hence, a method to provide real-time updates of the path computation should be examined. Toward this end, one option is the creation of an additional piece of pathway every time the original pathway exits the virtual screen. This added path would guide the physician toward the original path. Alternatively, a new method that uses the created path to compute all possible viewing directions before the procedure may be computed. However, this approach may add time to the pre-procedure phase.

### 7.2.6 Nodule Computer-aided Detection System

In Chapter 7, a semi-automatic algorithm for nodule malignancy prediction was described. The system requires indication of the nodule's location and automatically extracts radiographic characteristics. The end goal of the research is to help



the physician identify the nodule and decide whether to proceed with biopsy. Toward this end, a complete CAD system that automatically identifies and classifies the nodule should be developed. A common approach for nodule detection and classification involves using machine learning algorithms, exploiting artificial neural networks. Once the nodule is properly identified and classified, the proposed method might be employed to determine nodule malignancy. However, one of the main aspects to investigate is computational costs, as CT images usually consists of around 500 image whose analysis may require high computation costs.

# Bibliography

- [1] H. W. Dremel, “General principles of endoscopic imaging,” *Principles and Practice of Interventional Pulmonology*, pp. 13–25, 2013.
- [2] D. R. Aberle, A. M. Adams, C. D. Berg, W. C. Black, J. D. Clapp, R. M. Fagerstrom, I. F. Gareen, C. Gatsonis, P. M. Marcus, and J. D. Sicks, “Reduced lung-cancer mortality with low-dose computed tomographic screening,” *The New England Journal of Medicine*, vol. 365, no. 5, pp. 395–409, 2011.
- [3] F. J. F. Herth, R. Eberhardt, and A. Ernst, “The future of bronchoscopy in diagnosing, staging and treatment of lung cancer,” *Respiration*, vol. 73, no. 4, pp. 399–409, 2006.
- [4] C. Gilbert, J. Akulian, R. Ortiz, H. Lee, and L. Yarmus, “Novel bronchoscopic strategies for the diagnosis of peripheral lung lesions: Present techniques and future directions,” *Respirology*, vol. 19, no. 5, pp. 636–644, 2014.
- [5] M. Y. Dolina, D. C. Cornish, S. A. Merritt, L. Rai, R. Mahraj, W. E. Higgins, and R. Bascom, “Inter-bronchoscopist variability in endobronchial path selection: a simulation study,” *CHEST Journal*, vol. 133, no. 4, pp. 897–905, 2008.
- [6] R. A. Clark, P. Grech, A. Robinson, and R. H. Townsend, “Limitations of fibre-optic bronchoscopy under fluoroscopy in the investigation of peripheral lung lesions,” *British Journal of Radiology*, vol. 51, pp. 432–436, 1978.

- [7] C. S. White, E. A. Weiner, P. Patel, and E. J. Britt, "Transbronchial needle aspiration: guidance with CT fluoroscopy," *CHEST Journal*, vol. 118, no. 6, pp. 1630–1638, 2000.
- [8] K. O'Donoghue, D. Eustace, J. Griffiths, M. O'Shea, T. Power, and P. Cantillon-Murphy, "Catheter position tracking system using planar magnetism and closed loop current control," *IEEE Transactions on Magnetics*, vol. 50, no. 7, pp. 1–9, 2014.
- [9] Y. Schwarz, A. C. Mehta, A. Ernst, F. Herth, A. Engel, D. Besser, and H. D. Becker, "Electromagnetic navigation during flexible bronchoscopy," *Respiration*, vol. 70, no. 5, pp. 516–522, 2003.
- [10] H. D. Becker, F. Herth, A. Ernst, and Y. Schwarz, "Bronchoscopic biopsy of peripheral lung lesions under electromagnetic guidance: a pilot study," *Journal of Bronchology and Interventional Pulmonology*, vol. 12, no. 1, pp. 9–13, 2005.
- [11] H. Hautmann, A. Schneider, T. Pinkau, F. Peltz, and H. Feussner, "Electromagnetic catheter navigation during bronchoscopy: validation of a novel method by conventional fluoroscopy," *CHEST Journal*, vol. 128, no. 1, pp. 382–387, 2005.
- [12] Y. Schwarz, B. Greif, H. Becker, A. Ernst, and A. C. Mehta, "A real-time electromagnetic navigation bronchoscopy to peripheral lung lesions using overlaid CT images: the first human study," *CHEST Journal*, vol. 129, no. 4, pp. 988–994, 2006.
- [13] T. R. Gildea, P. J. Mazzone, D. Karnak, M. Meziane, and A. C. Mehta, "Electromagnetic navigation diagnostic bronchoscopy: a prospective study," *American Journal of Respiratory and Critical Care Medicine*, vol. 174, no. 9, pp. 982–989, 2006.
- [14] T. S. Weiser, K. Hyman, J. Yun, V. Little, C. Chin, and S. J. Swanson, "Electromagnetic navigational bronchoscopy: a surgeon's perspective," *The Annals of Thoracic Surgery*, vol. 85, no. 2, pp. S797–S801, 2008.

## BIBLIOGRAPHY

---

- [15] R. Eberhardt, D. Anantham, F. Herth, D. Feller-Kopman, and A. Ernst, “Electromagnetic navigation diagnostic bronchoscopy in peripheral lung lesions,” *CHEST Journal*, vol. 131, no. 6, pp. 1800–1805, 2008.
- [16] K. O’Donoghue, A. Corvo, P. Nardelli, C. O’Shea, K. A. Khan, M. Kennedy, and P. Cantillon-Murphy, “Evaluation of a novel tracking system in a breathing lung model,” *36th Annual International Conference of the IEEE Engineering in Medicine and Biology Society (EMBC)*, pp. 4046–4049, 2014.
- [17] D. J. Vining, K. Liu, R. H. Choplin, and E. F. Haponik, “Virtual bronchoscopy : relationships of virtual reality endobronchial simulations to actual bronchoscopic findings,” *CHEST Journal*, vol. 109, no. 2, pp. 549–553, 1996.
- [18] R. M. Summers, D. F. Feng, S. M. Holland, M. C. Sneller, and J. H. Shelhamer, “Virtual bronchoscopy: segmentation method for real time display,” *Radiology*, vol. 200, no. 3, pp. 857–862, 1996.
- [19] W. E. Higgins, K. Ramaswamy, R. D. Swift, G. McLennan, and E. A. Hoffman, “Virtual bronchoscopy for three-dimensional pulmonary image assessment: state of the art and future needs,” *Radiographics*, vol. 18, no. 3, pp. 761–778, 1998.
- [20] D. J. Vining, K. Liu, R. H. Choplin, and E. F. Haponik, “Automated anatomical labeling of the bronchial branch and its application to the virtual bronchoscopy system,” *IEEE Transactions on Medical Imaging*, vol. 19, no. 2, pp. 103–114, 2000.
- [21] H. G. Colt, S. W. Crawford, and O. G. III., “Virtual reality bronchoscopy simulation: a revolution in procedural training,” *CHEST Journal*, vol. 120, no. 4, pp. 1333–1339, 2001.
- [22] H. G. Colt, S. W. Crawford, and O. G. III., “Grading airway stenosis down to the segmental level using virtual bronchoscopy,” *CHEST Journal*, vol. 125, no. 2, pp. 704–711, 2004.

- [23] Y. Onodera, T. Omatsu, S. Takeuchi, N. Shinagawa, K. Yamazaki, T. Nishioka, and K. Miyasaka, “Enhanced virtual bronchoscopy using the pulmonary artery: improvement in route mapping for ultraselective trans-bronchial lung biopsy,” *American Journal of Radiology*, vol. 184, no. 4, pp. 1103–1110, 2004.
- [24] A. P. Kiraly, J. P. Helferty, E. A. Hoffman, G. McLennan, and W. E. Higgins, “Three-dimensional path planning for virtual bronchoscopy,” *IEEE Transactions on Medical Imaging*, vol. 23, no. 11, pp. 1365–137, 2004.
- [25] P. Nardelli, K. A. Khan, A. Corvó, N. Moore, M. J. Murphy, M. Twomey, O. J. O’Connor, M. P. Kennedy, R. S. J. Estépar, M. M. Maher, and P. Cantillon-Murphy, “Optimizing parameters of an open-source airway segmentation algorithm using different CT images,” *Biomedical Engineering Online*, vol. 14, no. 1, p. 62, 2015.
- [26] R. Eberhardt, D. Anantham, F. Herth, D. Feller-Kopman, and A. Ernst, “Electromagnetic navigation diagnostic bronchoscopy in peripheral lung lesions,” *CHEST Journal*, vol. 131, no. 6, pp. 1800–1805, 2007.
- [27] A. Chen, N. Pastis, B. Furukawa, and G. A. Silvestri, “The effect of respiratory motion on pulmonary nodule location during electromagnetic navigation bronchoscopy,” *CHEST Journal*, vol. 147, no. 5, pp. 1275–1281, 2015.
- [28] R. Eberhardt, N. Kahn, D. Gompelmann, M. Schumann, C. P. Heussel, and F. J. F. Herth, “LungPoint-a new approach to peripheral lesions,” *Journal of Thoracic Oncology*, vol. 5, no. 10, pp. 1559–1563, 2010.
- [29] M. M. Wahidi, J. A. Govert, R. K. Goudar, M. K. Gould, and D. C. McCrory, “Evidence for the treatment of patients with pulmonary nodules: when is it lung cancer? ACCP evidence-based clinical practice guidelines,” *CHEST Journal*, vol. 132, no. S3, pp. 94S–107S, 2007.
- [30] K. O’Donoghue, *Electromagnetic Tracking and Steering for Catheter Navigation*. PhD thesis, University College Cork, 2014.

## BIBLIOGRAPHY

---

- [31] <https://www.aireurbano.com>. Accessed: 2015-12-23.
- [32] K. E. Barrett, H. Brooks, S. Boitano, and S. M. Barman, *Pulmonary function. Ganong's Review of Medical Physiology*. McGraw-Hill, 2009.
- [33] G. V. Scagliotti, "Symptoms, signs and staging of lung cancer," *European Respiratory Monograph*, vol. 6, pp. 86–119, 2001.
- [34] R. Siegel, D. Naishadham, and A. Jemal, "Cancer statistics, 2012," *CA: A Cancer Journal For Clinicians*, vol. 60, no. 1, pp. 10–29, 2012.
- [35] J. Ferlay, I. Soerjomataram, M. Ervik, R. Dikshit, S. Eser, C. Mathers, M. Rebelo, D. M. Parkin, D. Forman, and F. Bray, "GLOBOCAN 2012 v1.0, cancer incidence and mortality worldwide: IARC CancerBase," *International Agency for Research on Cancer, Lyon, France*, vol. 11, 2013. Available from: <http://globocan.iarc.fr>. Accessed: 2015-10-28.
- [36] "World Health Organization, Fact sheet 206." <http://www.who.int/mediacentre/factsheets/fs206/en/>. Accessed: 2015-10-28.
- [37] A. Gulsvik, "The global burden and impact of chronic obstructive pulmonary disease worldwide," *Monaldi Archives for Chest Disease*, vol. 56, no. 3, pp. 261–264, 2001.
- [38] J. W. Gurney, "Determining the likelihood of malignancy in solitary pulmonary nodules with bayesian analysis. Part I. Theory," *Radiology*, vol. 186, pp. 405–413, 1993.
- [39] J. W. Gurney, D. M. Lyddon, and J. A. McKay, "Determining the likelihood of malignancy in solitary pulmonary nodules with bayesian analysis. Part II. Application," *Radiology*, vol. 186, pp. 415–422, 1993.
- [40] H. O. Coxson and R. M. Rogers, "Quantitative computed tomography of chronic obstructive pulmonary disease," *Academic Radiology*, vol. 12, no. 11, pp. 1457–1463, 2005.

- [41] I. Sluimer, A. Schilham, M. Prokop, and B. V. Ginneken, “Computer analysys of computed tomography scans of the lung: a survey,” *IEEE Transactions on Medical Imaging*, vol. 25, no. 4, pp. 385–405, 2006.
- [42] J. Croswell, J. Miller, B. S. Kramer, A. R. Kreimer, P. C. Prorok, J.-L. Xu, S. G. Baker, R. Fagerstrom, T. L. Riley, J. D. Clapp, C. D. Berg, J. K. Gohagan, G. L. Andriole, D. Chia, T. R. Church, E. D. Crawford, M. N. Fouad, E. P. Gelmann, L. Lamerato, D. J. Reding, and R. E. Schoen, “Cumulative incidence of false-positive results in repeated, multimodal cancer screening,” *The Annals of Family Medicine*, vol. 7, no. 3, pp. 212–222, 2009.
- [43] G. N. Hounsfield, “Computerized transverse axial scanning (tomography): Part 1. description of system,” *The British Journal of Radiology*, vol. 46, no. 552, pp. 1016–1022, 1973.
- [44] W. A. Kalender, W. Seissler, E. Klotz, and P. Vock, “Spiral volumetric CT with single-breath-hold technique, continuous transport, and continuous scanner rotation,” *Radiology*, vol. 176, no. 1, pp. 181–183, 1990.
- [45] <https://www.schoolphysics.co.uk>. Accessed: 2015-12-23.
- [46] J. Radon, “Über die bestimmung von funktionen durch ihre integralwerte längs gewisser mannigfaltigkeiten,” *Berichte Sächsische Akademie der Wissenschaften, Leipzig, Math.-Phys. Klasse*, vol. 69, pp. 262–267, 1917.
- [47] A. N. Desmond, K. O’Regan, C. Curran, S. McWilliams, T. Fitzgerald, M. M. Maher, and F. Shanahan, “Crohn’s disease: factors associated with exposure to high levels of diagnostic radiation,” *Gut*, vol. 57, no. 11, pp. 1524–1529, 2008.
- [48] R. Fazel, H. M. Krumholz, Y. Wang, J. S. Ross, J. Chen, H. H. Ting, N. D. Shah, K. Nasir, A. J. Einstein, and B. K. Nallamothu, “Exposure to low-dose ionizing radiation from medical imaging procedures,” *New England Journal of Medicine*, vol. 361, no. 9, pp. 849–857, 2009.

## BIBLIOGRAPHY

---

- [49] M. J. Willemink, P. A. de Jong, T. Leiner, L. M. de Heer, R. A. J. Nieuvelstein, R. P. J. Budde, and A. M. R. Schilham, “Iterative reconstruction techniques for computed tomography. Part 1: technical principles,” *European Radiology*, vol. 23, no. 6, pp. 1623–1631, 2013.
- [50] M. Beister, D. Kolditz, and W. A. Kalender, “Iterative reconstruction methods in X-ray CT,” *Physica Medica*, vol. 28, no. 2, pp. 94–108, 2012.
- [51] S. Sarabjeet, M. K. Kalra, M. D. Gilman, J. Hsieh, H. H. Pien, S. R. Digmurthy, and J.-A. O. Shepard, “Adaptive statistical iterative reconstruction technique for radiation dose reduction in chest CT: a pilot study,” *Radiology*, vol. 259, no. 2, pp. 565–573, 2011.
- [52] A. Webb, *Introduction to Biomedical Imaging*. Wiley-Interscience, 2003.
- [53] O. Masaki, S. Wada, A. Kayugawa, T. Matsumoto, and K. Murao, “Image filtering as an alternative to the application of a different reconstruction kernel in CT imaging: feasibility study in lung cancer screening,” *Medical Physics*, vol. 38, no. 7, pp. 3915–3923, 2011.
- [54] K. J. Jang, J. W. Choi, D. C. Kweon, J. W. Lee, E. H. Goo, K. R. Dong, J. S. Lee, G. H. Jin, and S. B. Seo, “Measurement of image quality in CT images reconstructed with different kernels,” *Journal of the Korean Physical Society*, vol. 58, no. 2, pp. 334–342, 2011.
- [55] D. T. Gering, A. Nabavi, R. Kikinis, W. E. L. Grimson, N. Hata, P. Everett, F. Jolesz, and W. M. Wells, “An integrated visualization system for surgical planning and guidance using image fusion and interventional imaging,” *Medical Image Computing and Computer-Assisted Intervention-MICCAI*, pp. 809–819, 1999.
- [56] S. Pieper, M. Halle, and R. Kikinis, “3D Slicer,” *3rd IEEE International Symposium on Biomedical Imaging: Nano to Macro, 2004.*, pp. 632–635, 2004.



- [57] S. Pieper, B. Lorensen, W. Schroeder, and R. Kikinis, “The NA-MIC kit: ITK, VTK, pipelines, grids and 3D Slicer as an open platform for the medical image computing community,” *3rd IEEE International Symposium on Biomedical Imaging: Nano to Macro, 2006.*, pp. 698–701, 2006.
- [58] “Tcl/tk.” <https://www.tcl.tk/>. Accessed: 2015-10-28.
- [59] “Visualization Toolkit.” <https://www.vtk.org/>. Accessed: 2015-10-28.
- [60] L. Ibanez, W. Schroeder, L. Ng, and J. Cates, “The insight segmentation and registration toolkit.” <https://www.itk.org/>. Accessed: 2015-10-28.
- [61] L. Ibanez, W. Schroeder, L. Ng, and J. Cates, *The ITK Software Guide: Second Edition Updated for ITK 2.4*. Kitware, Inc., 2005.
- [62] “CMake: Cross Platform Make.” <https://www.cmake.org/>. Accessed: 2015-10-28.
- [63] “Osirix viewer.” <https://www.osirix-viewer.com/>. Accessed: 2016-03-11.
- [64] “The medical imaging interaction toolkit (mitk).” <https://mitk.org/wiki/MITK>. Accessed: 2016-03-11.
- [65] S. Leong, H. Ju, H. Marshall, R. Bowman, I. Yang, A.-M. Ree, C. Saxon, and K. M. Fong, “Electromagnetic navigation bronchoscopy: a descriptive analysis,” *Journal of Thoracic Disease*, vol. 4, no. 2, pp. 173–185, 2012.
- [66] “Veran Medical, SPINDrive 2.0.” <http://www.veranmedical.com/healthcare-professionals/products/spin-drive>. Accessed: 2015-10-28.
- [67] “Veran Medical, “SPINDrive 2.0”.” <http://www.veranmedical.com/healthcare-professionals/products/spin-drive>. Accessed: 2015-12-23.

## BIBLIOGRAPHY

---

- [68] E. Wilson, Z. Yaniv, D. Lindisch, and K. Cleary, “A buyer’s guide to electromagnetic tracking systems for clinical applications,” *Medical Imaging. International Society for Optics and Photonics*, p. 69182B, 2008.
- [69] D. Roetenberg, P. Slycke, A. Ventevogel, and P. H. Veltink, “A portable magnetic position and orientation tracker,” *Sensors and Actuators A: Physical*, vol. 135, no. 2, pp. 426–432, 2007.
- [70] A. Zikmund and P. Ripka, “A magnetic distance sensor with high precision,” *Sensors and Actuators A: Physical*, vol. 186, pp. 137–142, 2012.
- [71] E. Paperno and A. Plotkin, “Cylindrical induction coil to accurately imitate the ideal magnetic dipole,” *Sensors and Actuators A: Physical*, vol. 112, no. 2-3, pp. 248–252, 2004.
- [72] C. L. W. Sonntag, M. Spre, E. A. Lomonova, J. L. Duarte, and A. J. A. Vandenput, “Accurate magnetic field intensity calculations for contactless energy transfer coils,” *Proceedings of the 16th International Conference on the Computation of Electromagnetic Fields*, 2007.
- [73] K. A. Khan, P. Nardelli, K. O’Donoghue, A. Corvo, A. Jaeger, C. O’Shea, P. Cantillon-Murphy, and M. P. Kennedy, “The design and validation of a novel semiautomatic lung navigation platform,” *Irish Journal of Medical Sciences*, vol. 184, pp. S475–S547, 2015.
- [74] “3D Slicer.” <http://www.slicer.org>. Accessed: 2015-10-28.
- [75] A. Fedorov, R. Beichel, J. Kalpathy-Cramer, J. F. J. C. Fillion-Robin, S. Pujol, C. Bauer, D. Jennings, F. Fennessy, M. Sonka, J. Buatti, S. R. Aylward, J. V. Miller, S. Pieper, and R. Kikinis, “3D Slicer as an image computing platform for the quantitative imaging network,” *Magnetic Resonance Imaging*, vol. 30, no. 9, pp. 1323–1341, 2012.
- [76] D. M. Hansell, A. A. Bankier, H. MacMahon, T. C. McLoud, N. L. Muller, and J. Remy, “Fleischner society: glossary of terms for thoracic imaging 1,” *Radiology*, vol. 246, no. 3, pp. 697–722, 2008.

- [77] “Chest X-ray.” <http://www.chestx-ray.com/index.php/calculators/spn-calculator>. Accessed: 2015-11-5.
- [78] “MedScape.” <http://reference.medscape.com/calculator/>. Accessed: 2015-11-5.
- [79] A. McWilliams, M. C. Tammemagi, J. R. Mayo, H. Roberts, G. Liu, K. Soghrati, K. Yasufuku, S. Martel, F. Laberge, M. Gingras, and S. A. Khattra, “UpToDate.” <http://www.uptodate.com/contents/>. Accessed: 2015-11-5.
- [80] “NucMed.” <http://www.nucmed.com/nucmed/>. Accessed: 2015-11-5.
- [81] S. Diederich, D. Wormanns, M. S. Lenzen, M. Semik, M. Thomas, and P. E. Peters, “Screening for asymptomatic early bronchogenic carcinoma with low dose CT of the chest,” *Cancer*, vol. 89, no. S11, pp. 2483–2484, 2000.
- [82] C. I. Henschke, D. F. Yankelevitz, D. M. Libby, D. McCauley, M. Pasmantier, N. K. Altorki, J. P. Smith, and O. S. Miettinen, “Early lung cancer action project: annual screening using single-slice helical CT,” *Annals of the New York Academy of Sciences*, vol. 952, pp. 124–134, 2001.
- [83] T. Nawa, T. Nakagawa, S. Kusano, Y. Kawasaki, Y. Sugawara, and H. Nakata, “Lung cancer screening using low-dose spiral CT: results of baseline and 1-year follow-up studies,” *CHEST Journal*, vol. 122, no. 1, pp. 15–20, 2002.
- [84] C. I. Henschke, D. F. Yankelevitz, D. P. Naidich, D. I. McCauley, G. McGuinness, D. M. Libby, J. P. Smith, M. W. Pasmantier, and O. S. Miettinen, “CT Screening for Lung Cancer: Suspiciousness of Nodules according to Size on Baseline Scans 1,” *Radiology*, vol. 231, no. 1, pp. 164–168, 2004.
- [85] J. Gohagan, P. Marcus, R. Fagerstrom, P. Pinsky, B. Kramer, and P. Prorok, “Baseline findings of a randomized feasibility trial of lung cancer screening with spiral CT scan vs chest radiograph: the Lung Screening Study of

## BIBLIOGRAPHY

---

- the National Cancer Institute,” *CHEST Journal*, vol. 126, no. 1, pp. 114–121, 2004.
- [86] F. Li, S. Sone, H. Abe, H. MacMahon, and K. Doi, “Malignant versus benign nodules at CT screening for lung cancer: Comparison of thin-section CT findings 1,” *Radiology*, vol. 233, no. 3, pp. 793–798, 2004.
- [87] V. K. Patel, S. K. Naik, D. P. Naidich, W. D. Travis, J. A. Weingarten, R. Lazzaro, D. D. Gutterman, C. Wentowski, H. B. Grosu, and S. Raoof, “A practical algorithmic approach to the diagnosis and management of solitary pulmonary nodules: part 1: radiologic characteristics and imaging modalities,” *CHEST Journal*, vol. 143, no. 3, pp. 825–839, 2013.
- [88] E. A. Zerhouni, F. P. Stitik, S. S. Siegelman, D. P. Naidich, S. S. Sagel, A. V. Proto, J. R. Muhm, J. W. Walsh, C. R. Martinez, and R. T. Heelan, “CT of the pulmonary nodule: a cooperative study,” *Radiology*, vol. 160, no. 2, pp. 319–327, 1986.
- [89] H. MacMahon, J. H. M. Austin, G. Gamsu, C. J. Herold, J. R. Jett, D. P. Naidich, E. F. P. Jr, and S. J. Swensen, “Guidelines for management of small pulmonary nodules detected on CT scans: a statement from the fleischner society 1,” *Radiology*, vol. 237, no. 2, pp. 395–400, 2005.
- [90] S. J. Swensen, M. D. Silverstein, D. M. Ilstrup, C. D. Schleck, and E. S. Edell, “The probability of malignancy in solitary pulmonary nodules: application to small radiologically indeterminate nodules,” *Archives of Internal Medicine*, vol. 157, no. 8, pp. 849–855, 1997.
- [91] H. T. Winer-Muram, “The solitary pulmonary nodule,” *Radiology*, vol. 239, no. 1, pp. 34–39, 2006.
- [92] C. V. Zwirewich, S. Vedal, R. R. Miller, and N. L. Mller, “Solitary pulmonary nodule: high-resolution CT and radiologic-pathologic correlation,” *Radiology*, vol. 179, no. 2, pp. 469–476, 1991.

- [93] P. B. Bach, G. A. Silvestri, M. Hanger, and J. R. Jett, "Screening for lung cancer: ACCP evidence-based clinical practice guidelines," *CHEST Journal*, vol. 132, no. 3S, pp. 69S–77S, 2007.
- [94] A. O. Soubani, "The evaluation and management of the solitary pulmonary nodule," *Postgraduate Medical Journal*, vol. 84, no. 995, pp. 459–466, 2008.
- [95] J. J. Woodring, A. M. Fried, and V. P. Chuang, "Solitary cavities of the lung: diagnostic implications of cavity wall thickness," *American Journal of Roentgenology*, vol. 135, no. 6, pp. 1269–1271, 1980.
- [96] J. J. Woodring and A. M. Fried, "Significance of wall thickness in solitary cavities of the lung: a follow-up study," *American Journal of Roentgenology*, vol. 140, no. 3, pp. 473–474, 1983.
- [97] D. F. Yankelevitz and C. I. Henschke, "Derivation for relating calcification and size in small pulmonary nodules," *Clinical Imaging*, vol. 22, no. 1, pp. 1–6, 1998.
- [98] K. Okada, D. Comaniciu, and A. Krishnan, "Robust anisotropic Gaussian fitting for volumetric characterization of pulmonary nodules in multislice CT," *IEEE Transactions on Medical Imaging*, vol. 24, no. 3, pp. 409–423, 2005.
- [99] G. D. Nunzio, A. Massafra, L. Martina, R. Cataldo, S. Maglio, M. Quarta, A. Retico, and L. Bolanos, "Lung uniformization for juxta-pleural nodule detection," *Nuclear Science Symposium Conference Record, NSS'08*, pp. 4429–4432, 2008.
- [100] Q. Li, F. Li, and K. Doi, "Computerized detection of lung nodules in thin-section CT images by use of selective enhancement filters and an automated rule-based classifier," *Academic radiology*, vol. 15, no. 2, pp. 165–175, 2008.
- [101] X. Ye, X. Lin, J. Dehmeshki, G. Slabaugh, and G. Beddoe, "Shape-based computer-aided detection of lung nodules in thoracic CT images," *IEEE Transactions on Biomedical Engineering*, vol. 56, no. 7, pp. 1810–1820, 2009.

## BIBLIOGRAPHY

---

- [102] T. Messay, R. C. Hardie, and S. K. Rogers, “A new computationally efficient CAD system for pulmonary nodule detection in CT imagery,” *Medical Image Analysis*, vol. 14, no. 73, pp. 390–406, 2010.
- [103] A. Farag, S. Elhabian, J. Graham, A. Farag, and R. Falk, “Toward precise pulmonary nodule descriptors for nodule type classification,” *Medical Image Computing and Computer-Assisted Intervention-MICCAI*, pp. 626–633, 2010.
- [104] J. Daugman, “How Iris Recognition works,” *IEEE Transactions on Circuits and Systems for Video Technology*, vol. 14, no. 1, pp. 21–30, 2004.
- [105] S. A. Kumar, J. Ramesh, P. T. Vanathi, and K. Gunavathi, “Robust and automated lung nodule diagnosis from CT images based on fuzzy systems,” *Process Automation, Control and Computing (PACC), International Conference On*, pp. 1–6, 2011.
- [106] J. Kuruvilla and K. Gunavathi, “Lung cancer classification using neural networks for CT images,” *Computer Methods and Programs in Biomedicine*, vol. 113, no. 1, pp. 202–109, 2014.
- [107] H. M. Orozco, O. O. V. Villegas, V. G. C. Snchez, H. de Jess Ochoa Dominguez, and M. de Jess Nandayapa Alfaro, “Automated system for lung nodules classification based on wavelet feature descriptor and support vector machine,” *Biomedical Engineering Online*, vol. 14, no. 1, p. 9, 2015.
- [108] T. D. Way, L. M. Hadjiiski, B. Sahiner, H.-P. Chan, P. N. Cascade, E. A. Kazerooni, N. Bogot, and C. Zhou, “Computer-aided diagnosis of pulmonary nodules on CT scans: segmentation and classification using 3D active contours,” *Medical Physics*, vol. 33, no. 7, pp. 2323–2337, 2006.
- [109] S. K. V. Anand, “Segmentation coupled textural feature classification for lung tumor prediction,” *IEEE International Conference on Communication Control and Computing Technologies (ICCCCT)*, pp. 518–524, 2010.

- [110] A. McWilliams, M. C. Tammemagi, J. R. Mayo, H. Roberts, G. Liu, K. Soghrati, K. Yasufuku, S. Martel, F. Laberge, M. Gingras, and S. A. Khattra, “Probability of cancer in pulmonary nodules detected on first screening CT,” *New England Journal of Medicine*, vol. 369, no. 10, pp. 910–919, 2013.
- [111] L. W. Hedlund, R. F. Anderson, P. L. Goulding, J. W. Beck, E. L. Effmann, and C. E. Putman, “Two methods for isolating the lung area of a CT scan for density information,” *Radiology*, vol. 144, no. 2, pp. 353–357, 1982.
- [112] I. Amirav, S. S. Kramer, M. M. Grunstein, and E. A. Hoffman, “Assessment of methacholine-induced airway constriction by ultrafast high-resolution computed tomography,” *Journal of Applied Physiology*, vol. 75, no. 5, pp. 2239–2250, 1993.
- [113] R. Uppaluri, T. Mitsa, M. Sonka, E. A. Hoffman, and G. McLennan, “Quantification of pulmonary emphysema from lung computed tomography images,” *American Journal of Respiratory and Critical Care Medicine*, vol. 156, no. 1, pp. 248–254, 1997.
- [114] S. Qi, H. J. van Triest, Y. Yue, M. Xu, and Y. Kang, “Automatic pulmonary fissure detection and lobe segmentation in CT chest images,” *Biomedical Engineering Online*, vol. 13, no. 1, p. 59, 2014.
- [115] S. Hu, E. Hoffman, and J. M. Reinhardt, “Automatic lung segmentation for accurate quantitation of volumetric X-ray CT images,” *IEEE Transactions on Medical Imaging*, vol. 20, no. 6, pp. 490–498, 2001.
- [116] J. K. Leader, B. Zheng, R. M. Rogers, F. C. Sciurba, A. Perez, B. E. Chapman, S. Patel, C. R. Fuhrman, and D. Gur, “Automated lung segmentation in X-ray computed tomography: development and evaluation of a heuristic threshold-based scheme,” *Academic Radiology*, vol. 10, no. 11, pp. 1224–1236, 2003.

## BIBLIOGRAPHY

---

- [117] E. M. van Rikxoort, B. de Hoop, M. A. Viergever, M. Prokop, and B. van Ginneken, “Automatic lung segmentation from thoracic computed tomography scans using a hybrid approach with error detection,” *Medical Physics*, vol. 36, no. 7, pp. 2934–2947, 2009.
- [118] S. C. Park, J. K. Leader, J. Tan, G. S. Lee, S. H. Kim, I. S. Na, and B. Zheng, “Separation of left and right lungs using 3D information of sequential CT images and a guided dynamic programming algorithm,” *Journal of Computer Assisted Tomography*, vol. 35, no. 2, p. 280, 2011.
- [119] P. Korfiatis, S. Skiadopoulos, P. Sakellaropoulos, C. Kalogeropoulou, and L. Costaridou, “Combining 2D wavelet edge highlighting and 3D thresholding for lung segmentation in thin-slice CT,” *The British Journal of Radiology*, 2014.
- [120] A. P. Reeves, A. B. Chan, D. F. Yankelevitz, C. Henschke, B. Kressler, and W. J. Kostis, “On measuring the change in size of pulmonary nodules,” *IEEE Transactions on Medical Imaging*, vol. 25, no. 4, pp. 435–450, 2006.
- [121] B. Zhao, A. P. Reeves, D. F. Yankelevitz, and C. I. Henschke, “Three-dimensional multicriterion automatic segmentation of pulmonary nodules of helical computed tomography images,” *Optical Engineering*, vol. 38, no. 8, pp. 1340–1347, 1999.
- [122] N. Xu, N. Ahuja, and R. Bansal, “Automated lung nodule segmentation using dynamic programming and EM-based classification,” *Medical Imaging. International Society for Optics and Photonics*, pp. 666–676, 2002.
- [123] W. Mullally, M. Betke, J. Wang, and J. P. Ko, “Segmentation of nodules on chest computed tomography for growth assessment,” *Medical Physics*, vol. 31, no. 4, pp. 839–848, 2004.
- [124] S. Diciotti, G. Picozzi, M. Falchini, M. Mascalchi, N. Villari, and G. Valli, “3D segmentation algorithm of small lung nodules in spiral CT images,” *IEEE Transactions on Information Technology in Biomedicine*, vol. 12, no. 1, pp. 7–19, 2008.



- [125] J. Dehmeshki, H. Amin, M. Valdivieso, and X. Ye, "Segmentation of pulmonary nodules in thoracic CT scans: a region growing approach," *IEEE Transactions on Medical Imaging*, vol. 27, no. 4, pp. 467–480, 2008.
- [126] B. Chen, T. Kitasaka, H. Honma, H. Takabatake, M. Mori, H. Natori, and K. Mori, "Automatic segmentation of pulmonary blood vessels and nodules based on local intensity structure analysis and surface propagation in 3D chest CT images," *International Journal of Computer Assisted Radiology and Surgery*, vol. 7, no. 3, pp. 465–482, 2012.
- [127] Y. Tan, L. H. Schwartz, and B. Zhao, "Segmentation of lung lesions on CT scans using watershed, active contours, and markov random field," *Medical Physics*, vol. 40, no. 4, p. 043502, 2013.
- [128] A. A. Farag, H. E. A. E. Munim, J. H. Graham, and A. A. Farag, "A novel approach for lung nodules segmentation in chest CT using level sets," *IEEE Transactions on Image Processing*, vol. 22, no. 12, pp. 5202–5213, 2013.
- [129] Y. Qiang, Q. Wang, G. Xu, H. Ma, L. Deng, L. Zhang, J. Pu, and Y. Guo, "Computerized segmentation of pulmonary nodules depicted in CT examinations using freehand sketches," *Medical Physics*, vol. 41, no. 4, p. 041917, 2014.
- [130] C.-H. Tsou, K.-L. Lor, Y.-C. Chang, and C.-M. Chen, "Anatomy packing with hierarchical segments: an algorithm for segmentation of pulmonary nodules in CT images," *Biomedical Engineering Online*, vol. 14, no. 1, p. 42, 2015.
- [131] Q. Li, S. Sone, and K. Doi, "Selective enhancement filters for nodules, vessels, and airway walls in two-and three-dimensional CT scans," *Medical Physics*, vol. 30, no. 8, pp. 2040–2051, 2003.
- [132] A. F. Frangi, W. J. Niessen, K. L. Vincken, and M. A. Viergever, "Multiscale vessel enhancement filtering," *Medical Image Computing and Computer-Assisted Intervention-MICCAI*, pp. 130–137, 1998.

## BIBLIOGRAPHY

---

- [133] J. J. Koenderink, "The structure of images," *Biological Cybernetics*, vol. 50, no. 5, pp. 363–370, 1984.
- [134] L. M. J. Florack, B. M. ter Haar Romeny, J. J. Koenderink, and M. A. Viergever, "Scale and the differential structure of images," *Image and Vision Computing*, vol. 10, no. 6, pp. 376–388, 1992.
- [135] T. Lindeberg, "Edge detection and ridge detection with automatic scale selection," *International Journal of Computer Vision*, vol. 30, no. 2, pp. 117–156, 1998.
- [136] C. Y. Kuo, J. Frost, J. Lai, and L. Wang, "Three-dimensional image analysis of aggregate particles from orthogonal projections," *Transportation Research Record: Journal of the Transportation Research Board*, vol. 1526, pp. 98–103, 1996.
- [137] A. N. Khan, H. H. Al-Jahdali, C. M. Allen, K. L. Irion, S. A. Ghanem, and S. S. Koteyar, "The calcified lung nodule: What does it mean?," *Annals of Thoracic Medicine*, vol. 5, no. 2, p. 67, 2010.
- [138] J.-M. Kuhnigk, H. Hahn, M. Hindennach, V. Dicken, S. Krass, and H.-O. Peitgen, "Lung lobe segmentation by anatomy-guided 3D watershed transform," *Medical Imaging. International Society for Optics and Photonics*, pp. 1482–1490, 2003.
- [139] R. Wiemker, T. Blow, and T. Blaffert, "Unsupervised extraction of the pulmonary interlobar fissures from high resolution thoracic CT data," *International Congress Series*, vol. 1281, pp. 1121–1126, 2005.
- [140] E. M. van Rikxoort, B. V. Ginneken, M. Klik, and M. Prokop, "Supervised enhancement filters: application to fissure detection in chest CT scans," *IEEE Transactions on Medical Imaging*, vol. 27, no. 1, pp. 1–10, 2008.
- [141] E. M. van Rikxoort, B. D. Hoop, S. V. D. Vorst, M. Prokop, and B. V. Ginneken, "Automatic segmentation of pulmonary segments from volumetric chest CT scans," *IEEE Transactions on Medical Imaging*, vol. 28, no. 4, pp. 621–630, 2009.

- [142] E. M. van Rikxoort, M. Prokop, B. D. Hoop, M. Viergever, J. P. Pluim, and B. V. Ginneken, “Automatic segmentation of pulmonary lobes robust against incomplete fissures,” *IEEE Transactions on Medical Imaging*, vol. 29, no. 6, pp. 1286–1296, 2010.
- [143] J. Pu, J. K. Leader, B. Zheng, F. Knollmann, C. Fuhrman, F. C. Sciurba, and D. Gur, “A computational geometry approach to automated pulmonary fissure segmentation in CT examinations,” *IEEE Transactions on Medical Imaging*, vol. 28, no. 5, pp. 710–719, 2009.
- [144] J. Pu, C. Fuhrman, J. Durick, J. K. Leader, A. Klym, F. C. Sciurba, and D. Gur, “Computerized assessment of pulmonary fissure integrity using high resolution CT,” *Medical Physics*, vol. 37, no. 9, pp. 4661–4672, 2010.
- [145] B. Lassen, J.-M. Kuhnigk, O. Friman, S. Krass, and H.-O. Peitgen, “Automatic segmentation of lung lobes in CT images based on fissures, vessels, and bronchi,” *IEEE International Symposium on Biomedical Imaging: From Nano to Macro*, pp. 560–563, 2010.
- [146] V. Appia, U. Patil, and B. Das, “Lung fissure detection in CT images using global minimal paths,” *SPIE Medical Imaging, International Society for Optics and Photonics*, pp. 76231P–76231P, 2010.
- [147] I. C. Campbell, B. Coudrillier, J. Mensah, R. L. Abel, and C. R. Ethier, “Automated segmentation of the lamina cribrosa using frangi’s filter: a novel approach for rapid identification of tissue volume fraction and beam orientation in a trabeculated structure in the eye,” *Journal of the Royal Society Interface*, vol. 12, no. 104, p. 20141009, 2015.
- [148] J. C. Ross, R. S. J. Estpar, G. Kindlmann, A. Daz, C.-F. Westin, E. K. Silverman, and G. R. Washko, “Automatic lung lobe segmentation using particles, thin plate splines, and maximum a posteriori estimation,” *Medical Image Computing and Computer-Assisted Intervention-MICCAI*, pp. 163–171, 2010.

## BIBLIOGRAPHY

---

- [149] J. C. Ross, R. S. J. Estpar, A. Daz, C.-F. Westin, R. Kikinis, E. K. Silverman, and G. R. Washko, “Lung extraction, lobe segmentation and hierarchical region assessment for quantitative analysis on high resolution computed tomography images,” *Medical Image Computing and Computer-Assisted Intervention-MICCAI*, pp. 690–698, 2009.
- [150] F. L. Bookstein, “Principal warps: thin-plate splines and the decomposition of deformations,” *IEEE Transactions on Pattern Analysis & Machine Intelligence*, no. 6, pp. 567–585, 1989.
- [151] B. van Ginneken, S. G. Armato, B. de Hoop, *et al.*, “Comparing and combining algorithms for computer-aided detection of pulmonary nodules in computed tomography scans: the ANODE09 study,” *Medical Image Analysis*, vol. 14, no. 6, pp. 707–722, 2010.
- [152] S. G. Armato, G. McLennan, L. Bidaut, *et al.*, “The lung image database consortium (LIDC) and image database resource initiative (IDRI): a completed reference database of lung nodules on CT scans,” *Medical Physics*, vol. 38, no. 2, pp. 915–931, 2011.
- [153] “National Biomedical Imaging Archive.” <https://ncia.nci.nih.gov/ncia>. Accessed: 2015-12-23.
- [154] S. S. Shapiro and M. Wilk, “An analysis of variance test for normality (complete samples),” *Biometrika*, pp. 591–611, 1965.
- [155] C. E. Metz, “ROC methodology in radiologic imaging,” *Investigative Radiology*, vol. 21, no. 9, pp. 720–733, 1986.
- [156] E. R. DeLong, D. M. DeLong, and D. L. C. Pearson, “Comparing the areas under two or more correlated receiver operating characteristic curves: a nonparametric approach,” *Biometrics*, vol. 1, pp. 837–845, 1988.
- [157] L. G. Shapiro and G. C. Stockman, *Computer Vision*. New Jersey: Prentice-Hall, 2001.

- [158] N. R. Pal and S. H. Pal, “A review on image segmentation techniques,” *Pattern Recognition*, vol. 26, no. 9, pp. 1277–1294, 1993.
- [159] R. C. Gonzalez and R. E. Woods, *Digital Image Processing*. New Jersey: Pearson Education, 2004.
- [160] W. E. Lorensen and H. E. Cline, “Marching cubes: a high resolution 3D surface construction algorithm,” *ACM Siggraph Computer Graphics*, vol. 21, no. 4, pp. 163–169, 1987.
- [161] N. Sharma and L. M. Aggarwal, “Automated medical image segmentation techniques,” *Journal of Medical Physics/Association of Medical Physicists of India*, vol. 35, no. 1, pp. 3–14, 2010.
- [162] D. L. Pham, C. Xu, and J. L. Prince, “Current methods in medical image segmentation,” *Annual Review of Biomedical Engineering*, vol. 2, no. 1, pp. 315–337, 2000.
- [163] S. Zhou, Y. Cheng, and S. Tamura, “Automated lung segmentation and smoothing techniques for inclusion of juxtapleural nodules and pulmonary vessels on chest CT images,” *Biomedical Signal Processing and Control*, vol. 13, pp. 62–70, 2014.
- [164] E. R. Hancock and J. Kittler, “Edge-labeling using dictionary-based relaxation,” *IEEE Transactions on Pattern Analysis and Machine Intelligence*, vol. 12, no. 2, pp. 165–181, 1990.
- [165] H. Kalviainen, P. Hirvonen, L. Xu, and E. Oja, “Probabilistic and non-probabilistic Hough transforms: overview and comparisons,” *Image and vision computing*, vol. 13, no. 4, pp. 239–252, 1995.
- [166] S. Osher and J. A. Sethian, “Fronts propagating with curvature-dependent speed: algorithms based on Hamilton-Jacobi formulations,” *Journal of computational physics*, vol. 79, no. 1, pp. 12–49, 1988.
- [167] J. A. Sethian, *Level Set Methods and Fast Marching Methods*. Cambridge University Press, 1996.

## BIBLIOGRAPHY

---

- [168] A. R. Bruss, “The Eikonal equation: Some results applicable to computer vision,” *Journal of Mathematical Physics*, vol. 23, no. 5, pp. 890–896, 1982.
- [169] T. Schlathölter, C. Lorenz, I. C. Carlsen, S. Renisch, and T. Deschamps, “Simultaneous segmentation and tree reconstruction of the airways for virtual bronchoscopy,” *IEEE Transactions on Medical Imaging*, pp. 103–113, 2002.
- [170] M. Cabezas, A. Oliver, X. Llad, J. Freixenet, and M. B. Cuadra, “A review of atlas-based segmentation for magnetic resonance brain images,” *Computer methods and programs in biomedicine*, vol. 104, no. 3, pp. e158–e177, 2011.
- [171] P. Lo, B. V. Ginneken, J. M. Reinhardt, *et al.*, “Extraction of airways from CT (EXACT’09),” *IEEE Transactions on Medical Imaging*, vol. 31, no. 11, pp. 2093–2107, 2012.
- [172] K. Mori, J. Hasegawa, J. Toriwaki, H. Anno, and K. Katada, “Recognition of bronchus in three-dimensional X-ray CT images with applications to virtualized bronchoscopy system,” *Proceedings of the 13th International Conference on Pattern Recognition*, vol. 3, pp. 528–532, 1996.
- [173] T. Kitasaka, K. Mori, Y. Suenaga, J. Hasegawa, and J. Toriwaki, “A method for segmenting bronchial trees from 3D chest X-ray CT images,” *Medical Image Computing and Computer-Assisted Intervention-MICCAI*, pp. 603–610, 2003.
- [174] J. Tschirren, E. Hoffman, G. McLennan, and M. Sonka, “Intrathoracic airway trees: segmentation and airway morphology analysis from low-dose CT scans,” *IEEE Transactions on Medical Imaging*, vol. 12, no. 11, pp. 1529–1539, 2005.
- [175] K. Lai, P. Zhao, Y. Huang, J. Liu, C. Wang, H. Feng, and C. Li, “Automatic 3D segmentation of lung airway tree: a novel adaptive region growing approach,” *Bioinformatics and Biomedical Engineering-ICBBE, 3rd International Conference on*, pp. 1–14, 2009.

- [176] P. Lo, C. Pau, J. Sporring, and M. de Bruijne, "Multiscale vessel-guided airway tree segmentation," *The Second International Workshop on Pulmonary Image Analysis*, pp. 323–332, 2009.
- [177] P. Lo, J. Sporring, H. Ashraf, J. J. H. Pedersen, and M. de Bruijne, "Vessel-guided airway tree segmentation: a voxel classification approach," *Medical image analysis*, vol. 14, no. 4, pp. 527–538, 2010.
- [178] A. P. Kiraly, W. E. Higgins, G. McLennan, E. A. Hoffman, and J. M. Reinhardt, "Three-dimensional human airway segmentation methods for clinical virtual bronchoscopy," *Academic Radiology*, vol. 9, no. 10, pp. 1153–1168, 2002.
- [179] C. Salito, L. Barazzetti, J. C. Woods, and A. Aliverti, "3D airway tree reconstruction in healthy subjects and emphysema," *Lung*, vol. 189, no. 4, pp. 287–293, 2011.
- [180] M. W. Graham, J. D. Gibbs, and W. E. Higgins, "Robust system for human airway-tree segmentation," *Medical Imaging. International Society for Optics and Photonics*, pp. 69141J–69141J, 2008.
- [181] J. D. Gibbs, M. W. Graham, and W. E. Higgins, "3D MDCT-based system for planning peripheral bronchoscopic procedures," *Computers in biology and medicine*, vol. 39, no. 3, pp. 266–279, 2009.
- [182] M. W. Graham, J. D. Gibbs, D. C. Cornish, and W. E. Higgins, "Robust 3D airway tree segmentation for image-guided peripheral bronchoscopy," *IEEE Transactions on Medical Imaging*, vol. 29, no. 4, pp. 982–997, 2010.
- [183] M. W. Graham, J. D. Gibbs, and W. E. Higgins, "Computer-based route-definition system for peripheral bronchoscopy," *Journal of Digital Imaging*, vol. 25, no. 2, pp. 307–317, 2012.
- [184] B. Irving, P. Taylor, and A. Todd-Pokropek, "3D segmentation of the airway tree using a morphology based method," *Proc. of Second International Workshop on Pulmonary Image Analysis*, pp. 297–307, 2009.

## BIBLIOGRAPHY

---

- [185] C. Pisupati, L. Wolff, E. Zerhouni, and W. Mitzner, “Segmentation of 3D pulmonary trees using mathematical morphology,” *Mathematical Morphology and its Applications to Image and Signal Processing*, pp. 409–416, 1996.
- [186] B. Irving, P. Goussard, R. Gie, A. Todd-Pokropek, and P. Taylor, “Segmentation of obstructed airway branches in CT using airway topology and statistical shape analysis,” *IEEE International Symposium on Biomedical Imaging: From Nano to Macro*, pp. 447–451, 2011.
- [187] R. D. Rudyanto, A. Munoz-Barrutia, A. Diaz, J. Ross, G. R. Washko, C. O. de Solorzano, and R. S. J. Estépar, “Modeling airway probability,” *IEEE 10th International Symposium on Biomedical Imaging - ISBI*, pp. 378–381, 2013.
- [188] Z. Xu, U. Bagci, B. Foster, and D. J. Mollura, “A hybrid multi-scale approach to automatic airway tree segmentation from CT scans,” *IEEE 10th International Symposium on Biomedical Imaging - ISBI*, pp. 1308–1311, 2013.
- [189] J. Tschirren, T. Yavarna, and J. M. Reinhardt, “Airway segmentation framework for clinical environments,” *Proceedings of Second International Workshop on Pulmonary Image Analysis*, pp. 227–238, 2013.
- [190] P. Nardelli, R. S. J. Estepar, and P. Cantillon-Murphy, “Semi-automated airway segmentation for lung CT datasets,” *27th International Congress and Exhibition in Computer Assisted Radiology and Surgery (CARS)*, 2013.
- [191] G. D. Nunzio, E. Tommasi, A. Agrusti, R. Cataldo, I. D. Mitri, M. Favetta, S. Maglio, A. Massafra, M. Quarta, M. Torsello, I. Zecca, R. Bellotti, S. Tangaro, P. Calvini, N. Camarlinghi, F. Falaschi, P. Cerello, and P. Oliva, “Automatic lung segmentation in CT images with accurate handling of the hilar region,” *Journal of Digital Imaging*, vol. 24, no. 1, pp. 11–27, 2011.
- [192] J. P. Serra, *Image Analysis and Mathematical Morphology*. Academic Press Inc., 1982.



- [193] “The Vascular Modeling Toolkit (vmtk).” <http://www.vmtk.org>. Accessed: 2015-10-30.
- [194] D. Gao, X. Gao, C. Ni, and T. Zhang, “MGRG-morphological gradient based 3D region growing algorithm for airway tree segmentation in image guided intervention therapy,” *Bioelectronics and Bioinformatics-ISBB, International Symposium on*, pp. 76–79, 2011.
- [195] C. Zhu, S. Qi, H. V. Triest, S. Wang, Y. Kang, and Y. Yue, “Automatic 3D segmentation of human airway tree in CT image,” *Biomedical Engineering and Informatics-BMEI, 3rd International Conference on*, vol. 1, pp. 132–136, 2010.
- [196] S. B. Solomon, P. White, C. M. Wiener, J. B. Orens, and K. P. Wang, “Three-dimensional CT-guided bronchoscopy with a real-time electromagnetic position sensor: a comparison of two image registration methods,” *CHEST Journal*, vol. 118, no. 6, pp. 1783–1787, 2000.
- [197] I. Bricault, G. Ferretti, and P. Cinquin, “Registration of real and CT-derived virtual bronchoscopic images to assist transbronchial biopsy,” *IEEE Transactions on Medical Imaging*, vol. 17, no. 5, pp. 703–714, 1998.
- [198] A. J. Chung, F. Deligianni, P. Shah, A. Wells, and G.-Z. Yang, “Patient-specific bronchoscopy visualization through brdf estimation and disocclusion correction,” *IEEE Transactions on Medical Imaging*, vol. 25, no. 4, pp. 503–513, 2006.
- [199] F. Deligianni, A. Chung, and G.-Z. Yang, “pq-space based 2D/3D registration for endoscope tracking,” *Medical Image Computing and Computer-Assisted Intervention-MICCAI*, pp. 311–318, 2003.
- [200] F. Deligianni, A. Chung, and G.-Z. Yang, “Patient-specific bronchoscope simulation with pq-space-based 2D/3D registration,” *Computer Aided Surgery*, vol. 9, no. 5, pp. 215–226, 2004.

## BIBLIOGRAPHY

---

- [201] F. Deligianni, A. Chung, and G.-Z. Yang, “Nonrigid 2-D/3-D registration for patient specific bronchoscopy simulation with statistical shape modeling: Phantom validation,” *IEEE Transactions on Medical Imaging*, vol. 25, no. 11, pp. 1462–1471, 2006.
- [202] M. Shen, S. Giannarou, and G.-Z. Yang, “Robust camera localisation with depth reconstruction for bronchoscopic navigation,” *International Journal of Computer Assisted Radiology and Surgery-CARS*, pp. 1–13, 2015.
- [203] K. Mori, D. Deguchi, K. Akiyama, T. Kitasaka, C. R. M. Jr, Y. Suenaga, H. Takabatake, M. Mori, and H. Natori, “Hybrid bronchoscope tracking using a magnetic tracking sensor and image registration,” *Medical Image Computing and Computer-Assisted Intervention-MICCAI*, pp. 543–550, 2005.
- [204] X. Luo, M. Feuerstein, T. Sugiura, T. Kitasaka, K. Imaizumi, Y. Hasegawa, and K. Mori, “Towards hybrid bronchoscope tracking under respiratory motion: evaluation on a dynamic motion phantom,” *SPIE Medical Imaging, International Society for Optics and Photonics*, pp. 76251B–76251B, 2010.
- [205] T. D. Soper, D. R. Haynor, R. W. Glenney, and E. J. Seibel, “Validation of CT-video registration for guiding a novel ultrathin bronchoscope to peripheral lung nodules using electromagnetic tracking,” *SPIE Medical Imaging, International Society for Optics and Photonics*, pp. 72610C–72610C, 2009.
- [206] T. D. Soper, D. R. Haynor, R. W. Glenney, and E. J. Seibel, “In vivo validation of a hybrid tracking system for navigation of an ultrathin bronchoscope within peripheral airways,” *IEEE Transactions on Biomedical Engineering*, vol. 57, no. 3, pp. 736–745, 2010.
- [207] W. E. Higgins, J. P. Helferty, K. Lu, S. A. Merritt, L. Rai, and K.-C. Yu, “3D CT-video fusion for image-guided bronchoscopy,” *Computerized Medical Imaging and Graphics*, vol. 32, no. 3, pp. 159–173, 2008.
- [208] J. Nagao, K. Mori, T. Enjouji, D. Deguchi, T. Kitasaka, Y. Suenaga, J. ichi Hasegawa, J. ichiro Toriwaki, H. Takabatake, and H. Natori, “Fast and

- accurate bronchoscope tracking using image registration and motion prediction,” *Medical Image Computing and Computer-Assisted Intervention-MICCAI*, pp. 551–558, 2004.
- [209] “WinStar.” <http://www.win-star.com/>. Accessed: 2015-11-25.
- [210] “BlazeVideo.” <http://www.blazevideo.com>. Accessed: 2015-11-25.
- [211] “SplitCamera.” <http://splitcamera.com/>. Accessed: 2015-11-25.
- [212] A. Lasso, T. Heffter, A. Rankin, C. Pinter, T. Ungi, and G. Fichtinger, “PLUS: Open-source toolkit for ultrasound-guided intervention systems,” *IEEE Transactions on Biomedical Engineering*, no. 10, pp. 2527–2537, 2014.
- [213] “PLUSServer.” <https://www.assembla.com/spaces/plus/>. Accessed: 2015-11-25.
- [214] “OpenIGTLink Software.”
- [215] R. D. Swift, A. P. Kiraly, A. J. Sherbondy, A. L. Austin, E. A. Hoffman, G. McLennan, and W. E. Higgins, “Automatic axis generation for virtual bronchoscopic assessment of major airway obstructions,” *Computerized Medical Imaging and Graphics*, vol. 26, no. 2, pp. 103–118, 2002.
- [216] A. P. Kiraly, J. P. Helferty, E. A. Hoffman, G. McLennan, and W. E. Higgins, “Three-dimensional path planning for virtual bronchoscopy,” *IEEE Transactions on Medical Imaging*, vol. 23, no. 11, pp. 1365–1379, 2004.
- [217] K.-C. Yu, W. E. Higgins, and E. L. Ritman, “3D model-based vascular tree analysis using differential geometry,” *IEEE International Symposium on Biomedical Imaging: Nano to Macro, 2004*, pp. 177–180, 2004.
- [218] J. D. Gibbs, M. W. Graham, R. Bascom, D. C. Cornish, R. Khare, and W. Higgins, “Optimal procedure planning and guidance system for peripheral bronchoscopy,” *IEEE Transactions on Biomedical Engineering*, vol. 61, no. 3, pp. 638–657, 2014.

## BIBLIOGRAPHY

---

- [219] S. R. Aylward and E. Bullit, “Initialization, noise, singularities, and scale in height ridge trasversal for tubular objects centerline extraction,” *IEEE Transactions on Medical Imaging*, vol. 21, no. 2, pp. 61–75, 2002.
- [220] I. Bitter, A. E. Kaufman, and M. Sato, “Penalized-distance volumetric skeleton algorithm,” *IEEE Transactions on Visualization and Computer Graphics*, vol. 7, no. 3, pp. 195–206, 2001.
- [221] T.-C. Lee, R. L. Kashyap, and C.-N. Chu, “Building skeleton models via 3-d medial surface axis thinning algorithms,” *CVGIP: Graphical Models and Image Processing*, vol. 56, no. 6, pp. 462–478, 1994.
- [222] S. Bouix, K. Siddiqi, and A. Tannenbaum, “Flux driven automatic center-line extraction,” *Medical Image Analysis*, vol. 9, no. 3, pp. 209–221, 2005.
- [223] K. Siddiqi, B. B. Kimia, and C. Shu, “Geometric shock-capturing ENO schemes for sub-pixel interpolation, computation and curve evolution,” *CVGIP: Graphical Models and Image Processing*, vol. 59, no. 5, pp. 278–301, 1997.
- [224] P. E. Danielsson, “Euclidean distance mapping,” *Computer Graphics and Image Processing*, vol. 14, no. 3, pp. 227–248, 1980.
- [225] G. Malandain, G. Bertrand, and N. Ayache, “Topological segmentation of discrete surfaces,” *International Journal of Computer Vision*, vol. 10, no. 2, pp. 183–197, 1993.
- [226] A. P. Kiraly, J. P. Helferty, E. A. Hoffman, G. McLennan, and W. E. Higgins, “Three-dimensional path planning for virtual bronchoscopy,” *IEEE Transactions on Medical Imaging*, vol. 23, no. 11, pp. 1365–1379, 2004.
- [227] R. Gayle, P. Segars, M. C. Lin, and D. Manocha, “Path planning for deformable robots in complex environments,” *Robotics: Science and Systems*, vol. 2005, pp. 225–232, 2005.

- [228] M. Kukuk, “Modeling the internal and external constraints of a flexible endoscope for calculating its workspace: application in transbronchial needle aspiration guidance,” *Medical Imaging, International Society for Optics and Photonics*, pp. 539–550, 2002.
- [229] J. D. Westwood, “Interactive navigation and bronchial tube tracking in virtual bronchoscopy,” *Medicine Meets Virtual Reality: The Convergence of Physical & Informational Technologies: Options for a New Era in Healthcare*, vol. 62, p. 130, 1999.
- [230] G. Voronoi, “Nouvelles applications des paramtres continus la thorie des formes quadratiques. premier mmoire. sur quelques propriets des formes quadratiques positives parfaites,” *Journal fr die reine und angewandte Mathematik*, vol. 133, pp. 97–178, 1908.
- [231] S. X. Liu, L. F. Gutierrez, and D. Stanton, “Quantitative evaluation for accumulative calibration error and video-CT registration errors in electromagnetic-tracked endoscopy,” *International Journal of Computer Assisted Radiology and Surgery*, vol. 6, no. 3, pp. 407–419, 2011.
- [232] T. Klein, J. Traub, H. Hautmann, A. Ahmadian, and N. Navab, “Fiducial-free registration procedure for navigated bronchoscopy,” *Medical Image Computing and Computer-Assisted Intervention-MICCAI*, pp. 475–482, 2007.
- [233] S. Kirkpatrick, “Optimization by simulated annealing: Quantitative studies,” *Journal of Statistical Physics*, vol. 34, no. 5, pp. 975–986, 1984.
- [234] K. Mori, D. Deguchi, T. Kitasaka, Y. Suenaga, Y. Hasegawa, K. Imaizumi, and H. Takabatake, “Improvement of accuracy of marker-free bronchoscope tracking using electromagnetic tracker based on bronchial branch information,” *Medical Image Computing and Computer-Assisted Intervention-MICCAI*, pp. 535–542, 2008.

## BIBLIOGRAPHY

---

- [235] D. Deguchi, M. Feuerstein, T. Kitasaka, Y. Suenaga, I. Ide, H. Murase, K. Imaizumi, Y. Hasegawa, and K. Mori, “Real-time marker-free patient registration for electromagnetic navigated bronchoscopy: a phantom study,” *International Journal of Computer Assisted Radiology and Surgery*, vol. 7, no. 3, pp. 359–369, 2012.
- [236] D. Deguchi, K. Ishitani, T. Kitasaka, K. Mori, Y. Suenaga, H. Takabatake, M. Mori, and H. Natori, “A method for bronchoscope tracking using position sensor without fiducial markers,” *Medical Imaging, International Society for Optics and Photonics*, p. 65110N, 2007.
- [237] X. Luo, “A bronchoscopic navigation system using bronchoscope center calibration for accurate registration of electromagnetic tracker and CT volume without markers,” *Medical Physics*, vol. 41, no. 6, p. 061913, 2014.
- [238] E. F. Hofstad, H. Sorger, H. O. Leira, T. Amundsen, and T. Lang, “Automatic registration of CT images to patient during the initial phase of bronchoscopy: A clinical pilot study,” *Medical Physics*, vol. 41, no. 4, p. 041903, 2014.
- [239] K. O’Donoghue and P. Cantillon-Murphy, “Planar magnetic shielding for use with electromagnetic tracking systems,” *IEEE Transactions on Magnetics*, vol. 51, no. 2, pp. 1–12, 2015.
- [240] K. O’Donoghue and P. Cantillon-Murphy, “Low cost super-nyquist asynchronous demodulation for use in EM tracking systems,” *IEEE Transactions on Instrumentation and Measurement*, vol. 64, no. 2, pp. 458–466, 2015.
- [241] P. J. Besl and N. D. McKay, *Method for registration of 3-D shapes*. Schenker, Ed., 1992.
- [242] W. Kabsch, “A solution for the best rotation to relate two sets of vectors,” *Acta Crystallographica Section A: Crystal Physics, Diffraction, Theoretical and General Crystallography*, vol. 32, no. 5, pp. 922–923, 1976.

- [243] J. Tokuda, G. S. Fischer, X. Papademetris, Z. Yaniv, L. Ibanez, Patrick, C. H. Liu, J. Blevins, J. Arata, A. J. Golby, T. Kapur, S. Pieper, E. C. Burdette, G. Fichtinger, C. M. Tempny, and N. Hata, “OpenIGTLink: an open network protocol for imageguided therapy environment,” *The International Journal of Medical Robotics and Computer Assisted Surgery*, vol. 5, no. 4, pp. 423–434, 2009.
- [244] S. Tauscher, J. Tokuda, G. Schreiber, T. Neff, N. Hata, and T. Ortmaier, “OpenIGTLink interface for state control and visualisation of a robot for image-guided therapy systems,” *International Journal of Computer Assisted Radiology and Surgery*, vol. 10, no. 3, pp. 285–292, 2015.
- [245] J. P. Helferty, C. Zhang, G. McLennan, and W. E. Higgins, “Videoendoscopic distortion correction and its application to virtual guidance of endoscopy,” *IEEE Transactions on Medical Imaging*, vol. 20, no. 7, pp. 605–617, 2001.
- [246] S. N. Kalitzin, J. Staal, B. M. ter Haar Romeny, and M. Viergever, “A computational method for segmenting topological point-sets and application to image analysis,” *IEEE Transactions on Pattern Analysis and Machine Intelligence*, vol. 23, no. 5, pp. 447–459, 2001.
- [247] L. Rai, J. P. Helferty, and W. E. Higgins, “Combined video tracking and image-video registration for continuous bronchoscopic guidance,” *International Journal of Computer Assisted Radiology and Surgery*, vol. 3, no. 3, pp. 315–329, 2008.
- [248] [https://commons.wikimedia.org/wiki/File:Image\\_pyramid.svg#/media/File:Image\\_pyramid.svg](https://commons.wikimedia.org/wiki/File:Image_pyramid.svg#/media/File:Image_pyramid.svg). Accessed: 2015-12-23.
- [249] D. Mattes, D. R. Haynor, H. Vesselle, T. K. Lewellyn, and W. Eubank, “Nonrigid multimodality image registration,” *Medical Imaging International Society for Optics and Photonics*, pp. 1609–1620, 2001.
- [250] “Irish Thoracic Society.” <http://www.irishthoracicsociety.com/its-conference/its-asm-2015>. Accessed: 2015-12-02.

## BIBLIOGRAPHY

---

- [251] “System Usability Scale.” <http://www.usability.gov/how-to-and-tools/methods/system-usability-scale.html>. Accessed: 2015-11-30.
- [252] J. Brooke, “SUS-A quick and dirty usability scale,” *Usability Evaluation in Industry*, vol. 189, no. 194, pp. 4–7, 1996.
- [253] A. Bangor, P. Kortum, and J. Miller, “Determining what individual SUS scores mean: Adding an adjective rating scale,” *Journal of Usability Studies*, vol. 4, no. 3, pp. 114–123, 2009.
- [254] C. M. O’Shea, K. A. Khan, P. Nardelli, A. Jaeger, M. P. Kennedy, and P. Cantillon-Murphy, “Evaluation of endoscopically deployed radiopaque tumour models in bronchoscopy.” Accepted for Publication, 2015.
- [255] A. Tristán-Vega, V. García-Pérez, S. Aja-Fernández, and C.-F. Westin, “Efficient and robust nonlocal means denoising of MR data based on salient features matching,” *Computer Methods and Programs in Biomedicine*, vol. 105, no. 2, pp. 131–144, 2012.
- [256] S. Merritt, R. Khare, R. Bascom, and W. Higgins, “Interactive CT-video registration for the continuous guidance of bronchoscopy,” *IEEE Transactions on Medical Imaging*, vol. 32, no. 8, pp. 1376–1396, 2013.